



Universitat Autònoma de Barcelona

**ADVERTIMENT.** L'accés als continguts d'aquesta tesi queda condicionat a l'acceptació de les condicions d'ús establertes per la següent llicència Creative Commons:  [http://cat.creativecommons.org/?page\\_id=184](http://cat.creativecommons.org/?page_id=184)

**ADVERTENCIA.** El acceso a los contenidos de esta tesis queda condicionado a la aceptación de las condiciones de uso establecidas por la siguiente licencia Creative Commons:  <http://es.creativecommons.org/blog/licencias/>

**WARNING.** The access to the contents of this doctoral thesis it is limited to the acceptance of the use conditions set by the following Creative Commons license:  <https://creativecommons.org/licenses/?lang=en>

PhD Thesis

---

Thermal transport in semiconductors:  
first principles and phonon hydrodynamics

---

**Author:**

Pol Torres Alvarez

**Directors:**

Francesc Xavier Àlvarez Calafell  
and  
Xavier Cartoixa Soler

Doctoral Program in Physics  
Universitat Autònoma de Barcelona  
Facultat de Ciències, Departament de Física  
Bellaterra

September 19, 2017



*A la família i amics*

*”...nunca olvides que nos ayuda a luchar  
el saber que aún queda gente que ve el principio  
donde todos creen que está el final...”*



# Acknowledgments

During this three years of work on thermal transport I have met a lot of great researches that I would like to acknowledge in these lines.

First of all I want to show my gratitude to my supervisors Dr. F. Xavier Alvarez and Dr. Xavier Cartoixa for their great guidance on teaching, advise and revise all my steps. This work reflects a part of their knowledge transferred to me and shaped as good as I could.

In second place I would like to acknowledge all the Statistical Physics group of the UAB and specially to Dr. Juan Camacho, Dr. Javier Bafaluy, Dr. David Jou and Àlvar Torelló for their collaboration in the development of the heat transport model presented in this thesis.

Also I appreciate the hospitality of Prof. Ali Shakouri, Dr. Atsushi Togo and Prof. Isao Tanaka to invite me to their research groups and share fruitful discussions really useful to improve this work. This has also allowed me to meet other experts on thermal transport like Dr. Amir Ziabari and Prof. Singh.

In addition, the external collaborations with Dr. Marisol Martín and Dr. Miguel Muñoz from IMM and Dr. Myers's group from CRM with Marc Calvo and Dr. Hennessy has been really useful as well to improve on the study of thermal transport in small systems.

Finally, from the scientific point of view I would also like to thank all the people from NanoTherm project for the nice work carried on and give me the opportunity to collaborate with them.

No work is possible without adequate resources, and in this aspect I gratefully acknowledge the financial support of the PIF program of the Universitat Autònoma de Barcelona and also Spain's Ministerio de Economía y Competitividad research grants nanoTHERM CSD2010-00044, TEC2015-67462-C2-2-R (MINECO/FEDER) and TEC2015-67462-C2-1-R (MINECO/FEDER).

Des del punt de vista personal, vull agrair a tota la gent que m'ha acompanyat aquests anys de vida acadèmica, començant per la gent de física (Rocky, Miguel, Juan, Ferran i Sergio) fins als grans científics madrilenys Alex i Quique, passant pels capis Dani i Quim. També, òbviament, a tota la gent de La Plana, Piera i voltants que hem compartit el dia a dia durant tants anys: Roberto, Guillem, Gerard, Batlle, Primo, Guita, Xurri, Ruben, Lidia, Kala, Aitor, Gery, Brenda, Calabuig, Carolina, Sayago, Solà, Kate, Tamy, Vis, Mariano, Ferran, Elena, Eloi, Deivid, Carafí, Tiris, Mada, Herranz i un llarg etc.

Finalment, com no pot ser d'altra manera, vull donar les gràcies a la meva família per aguantar-me durant tota la vida, als meus pares Manel i Carme, als meus germans Adrià i Elisa, i especialment a la Marta pels bons moments i estar al meu costat aquests tres anys.

# Abstract

In this thesis, thermal transport is analyzed from the bulk to the nanoscale under different approaches using *first principles*. On one side, the bulk thermal conductivity is studied in the general kinetic-collective framework, where the Boltzmann Transport Equation (BTE) for phonons is solved under the Guyer and Krumhansl (GK) model and maximizing the entropy of the system. This solution is known as Kinetic Collective Model (KCM). On one side, the KCM, which splits the thermal conductivity into a kinetic and a collective contribution, has allowed obtaining the thermal conductivity of a large number of semiconductors, with excellent agreement to experimental results. On the other side, for reduced size samples, two approaches have been considered. In the first case, the GK boundary approach considers the boundaries as a microscopic scattering mechanism in the kinetic regime while in the collective contribution their effects are included from a hydrodynamic basis. The limitation of this approach for complex geometries has prompted the development of the second case: a full hydrodynamic thermal transport framework. A hydrodynamic thermal transport equation has been developed based in the combination with the GK model and the Extended Irreversible Thermodynamics (EIT) framework and using a general hydrodynamic slip boundary condition. This has allowed to use the hydrodynamic KCM equation in finite elements calculations to study complex geometries. Finally, an analysis of the phonon spectrum and its importance to deal with transient transport regimes is included.

Comparison of the KCM results with other current solutions concerning all the topics of the thesis are discussed.

Parallel to the development of the hydrodynamic model, the KCM expressions from the kinetic-collective boundary approach as well as hydrodynamic parameters have been implemented in an open source code. Sharing the model as a tool to predict thermal transport phenomena will allow bridging the physics of the heat transport from the microscopic to the macroscopic point of view.





# Contents

<b>Acknowledgments</b>	<b>v</b>
<b>Abstract</b>	<b>vii</b>
<b>Contents</b>	<b>viii</b>
<b>List of Figures</b>	<b>x</b>
<b>Introduction</b>	<b>1</b>
<b>1 Thermal transport</b>	<b>5</b>
1.1 Boltzmann Transport Equation . . . . .	6
1.2 Solutions to the LBTE . . . . .	8
1.3 Thermal transport beyond Fourier . . . . .	20
1.4 Thermal boundary resistance . . . . .	31
1.5 Thermal measurements . . . . .	32
1.6 Thermoelectric properties . . . . .	35
1.7 Note on phonon drag . . . . .	36
<b>2 First principles calculations</b>	<b>39</b>
2.1 Total energy calculations . . . . .	39
2.2 Interatomic force constants . . . . .	45
2.3 Phonon scattering mechanisms . . . . .	50
2.4 <i>Ab initio</i> KCM expressions . . . . .	59
2.5 Calculation methodologies . . . . .	62
2.6 System modeling . . . . .	63
2.7 Computational methods . . . . .	66
<b>3 Thermal transport of bulk semiconductors in the KCM</b>	<b>71</b>
3.1 Dispersion relations and density of states . . . . .	72
3.2 Scattering rates and mean free times . . . . .	76
3.3 Kinetic slowdown . . . . .	80

---

3.4	Thermal conductivity of bulk materials . . . . .	83
3.5	Graphene . . . . .	92
3.6	Thermal conductivity in other models . . . . .	94
<b>4</b>	<b>Low dimension thermal conductivity in the KCM</b>	<b>99</b>
4.1	Kinetic-collective boundary approach . . . . .	100
4.2	Hydrodynamic KCM approach . . . . .	105
4.3	Boundary effects in other models . . . . .	112
<b>5</b>	<b>Phonon spectrum and transient regimes in the KCM</b>	<b>115</b>
5.1	Phonon spectrum . . . . .	115
5.2	Transient regimes . . . . .	127
5.3	The role of low energy phonons . . . . .	131
5.4	Relaxation times from the full scattering matrix . . . . .	133
<b>6</b>	<b>Geometric effects in complex experiments</b>	<b>135</b>
6.1	1D heat propagation . . . . .	136
6.2	2D heat propagation . . . . .	139
6.3	Steady state and transient heat transport . . . . .	141
6.4	Effective modeling of KCM . . . . .	146
<b>7</b>	<b>Conclusions</b>	<b>149</b>
<b>A</b>	<b>Generalization of the KCM equations</b>	<b>153</b>
<b>B</b>	<b>Hydrodynamic heat flow in two dimensions</b>	<b>155</b>
<b>C</b>	<b>Longitudinal heat transport in a thin film</b>	<b>159</b>
	<b>Bibliography</b>	<b>163</b>

# List of Figures

1.1	Sketch of the kinetic and collective transport regimes . . . . .	14
1.2	Resistive and total KCM relaxation times. . . . .	19
1.3	Sketch of Brownian motion, Lévy flight and ballistic transport . . .	21
1.4	Heat flux profile with slip boundary condition . . . . .	25
1.5	Accumulated thermal conductivity for silicon . . . . .	28
1.6	Renormalized mean squared displacement for Si, SiGe and InGaAs .	31
1.7	Frequency dependence of thermal boundary resistance from TDTR.	32
2.1	Sketch of a pseudopotential (PS) and all-electrons (AE) functions . .	43
2.2	Cubic supercell sketch . . . . .	44
2.3	Feynman diagram and sketch of 3-phonon scattering processes . . .	52
2.4	Sketch of typical sample geometries . . . . .	56
2.5	Relaxation times and experimental thermal conductivity for silicon .	56
2.6	Effective thermal conductivity as a function of the Knudsen number	57
2.7	Work flow of <i>ab initio</i> calculations . . . . .	63
2.8	Total energy <i>versus</i> lattice constant for a 2-atoms silicon primitive cell.	64
2.9	Total energy <i>versus</i> $\mathbf{q}$ -point grid sampling for a 2-atoms silicon . . .	65
2.10	Total energy <i>versus</i> kinetic energy cutoff for a 2-atoms silicon . . .	65
2.11	KCM thermal transport program example . . . . .	68
2.12	Primitive and conventional diamond-like cell for silicon . . . . .	69
2.13	First Brillouin and irreducible Brillouin zone for cubic conventional (8-atoms) and primitive (2-atoms) cell of the FCC structure. . . . .	69
2.14	Normal and umklapp relaxation times from different cells . . . . .	70
3.1	Crystal structures of the different studied materials. . . . .	72
3.2	Dispersion relations of Si, Ge, C and GaAs along high symmetry directions. . . . .	73
3.3	Density of states of silicon, germanium, diamond and gallium arsenide.	74
3.4	Density of states for different $\text{Si}_{1-x}\text{Ge}_x$ alloys . . . . .	75
3.5	Density of states for different $\text{In}_x\text{Ga}_{1-x}\text{As}$ alloy concentration. . . .	75

3.6	Dispersion relations along high symmetry directions and density of states of PbTe. . . . .	76
3.7	Dispersion relations along high symmetry directions and density of states of $\alpha$ -quartz. . . . .	77
3.8	Dispersion relations along high symmetry directions and density of states of Bi <sub>2</sub> Te <sub>3</sub> . . . . .	77
3.9	Umklapp and normal silicon relaxation times. . . . .	78
3.10	Umklapp and normal bismuth telluride relaxation times. . . . .	79
3.11	Impurity relaxation time for Si, Ge, C, Ge, PbTe, $\alpha$ -quartz and Bi <sub>2</sub> Te <sub>3</sub> as a function of frequency in a 20x20x20 $\mathbf{q}$ -point grid. . . . .	80
3.12	Temperature dependent relaxation times for bulk silicon. . . . .	81
3.13	Frequency dependent relaxation times for bulk Si. Comparison of RTA, KCM, kinetic (resistive) and collective relaxation times. . . . .	82
3.14	Thermal conductivity of bulk Si, Ge, C and GaAs in terms of temperature. . . . .	84
3.15	Switching factor $\Sigma$ for Si, Ge, GaAs and C in terms of temperature. . . . .	84
3.16	Kinetic and collective contributions to thermal conductivity of diamond in terms of temperature. . . . .	86
3.17	Thermal conductivity of bulk bismuth telluride. . . . .	87
3.18	Thermal conductivity of PbTe and $\alpha$ -quartz . . . . .	88
3.19	Lattice parameter and alloy term $\Gamma$ for Si <sub>1-x</sub> Ge <sub>x</sub> alloy as a function of germanium concentration $x$ . . . . .	89
3.20	Thermal conductivity of $L_{\text{eff}} = 7\text{mm}$ rods in terms of alloy concentration $x$ at 300 K for Si <sub>1-x</sub> Ge <sub>x</sub> and In <sub>x</sub> Ga <sub>1-x</sub> As. . . . .	90
3.21	Switching factor $\Sigma$ corresponding to Fig. 3.20. . . . .	91
3.22	Crystal structure of graphene obtained with XCrySDen . . . . .	92
3.23	Dispersion relations and density of states of graphene. . . . .	93
3.24	Thermal conductivity of graphene in terms of temperature. . . . .	93
3.25	Thermal conductivity of natural bulk silicon and diamond. Comparison of KCM and other models. . . . .	95
3.26	Collision operator split in normal and resistive processes. . . . .	96
3.27	Thermal conductivity of natural bulk natural diamond as a function of temperature for D-LBTE, KCM and altered solutions. . . . .	97
4.1	Heat transport profile sketch. . . . .	101
4.2	Thermal conductivity of silicon thin films and nanowires. . . . .	101
4.3	Switching factor $\Sigma$ for bulk silicon, 2.8 mm rod, 830 nm film and 56 nm wire as a function of temperature. . . . .	102
4.4	Thermal conductivity at 300K of Bi <sub>2</sub> Te <sub>3</sub> nanowires and a thin film. . . . .	104
4.5	Thermal conductivity in terms of temperature for Si <sub>1-x</sub> Ge <sub>x</sub> at different alloy concentration $x$ . . . . .	105

4.6	Sketch of roughness parameters. . . . .	107
4.7	Thermal conductivity, non-local length and relaxation time of bulk silicon as a function of temperature. . . . .	109
4.8	Thermal conductivity of silicon nanowires as a function of temperature with full hydrodynamic KCM. . . . .	110
4.9	Effective heat flux profile for different values of slip condition in a wire. . . . .	111
4.10	Thermal conductivity of $\text{Si}_{1-x}\text{Ge}_x$ nanowires as a function of temperature for different diameters and concentrations $x$ . . . . .	111
4.11	Theoretical predictions and experimental data for thermal conductivity of silicon wires . . . . .	114
5.1	Normal, umklapp, impurity and boundary relaxation times for $L_{\text{eff}} = 2.8$ mm and $L_{\text{eff}} = 115$ nm silicon at 50 K and 300 K. . . . .	116
5.2	Kinetic and collective mean free times (MFT) for $L_{\text{eff}} = 2.8$ mm and $L_{\text{eff}} = 115$ nm silicon at 50 K and 300 K in terms of temperature . . . . .	117
5.3	Thermal conductivity spectral distribution and mode kinetic and collective MFP in terms of frequency for bulk silicon at $T=300\text{K}$ . . . . .	118
5.4	Thermal conductivity accumulation function in terms of MFP for bulk silicon at $T=300$ K . . . . .	119
5.5	Thermal conductivity accumulation function for alloys. . . . .	121
5.6	Thermal conductivity spectral distribution and thermal conductivity accumulation function in terms of frequency for $\text{Si}_{0.82}\text{Ge}_{0.18}$ and $\text{In}_{0.53}\text{Ga}_{0.47}\text{As}$ for $L_{\text{eff}} = 7$ mm rods at $T=300$ K. . . . .	122
5.7	Thermal conductivity accumulation function (TCAF) for natural Si and $\text{Si}_{0.82}\text{Ge}_{0.18}$ at 300 K and $L_{\text{eff}} = 7$ mm. . . . .	122
5.8	Spectral and accumulated thermal conductivity for a $4\ \mu\text{m}$ film, 300 nm and 25 nm wires of $\text{Bi}_2\text{Te}_3$ at 300 K. . . . .	124
5.9	<i>First principles</i> relaxation times and thermal conductivity accumulation function for PbTe. . . . .	125
5.10	<i>First principles</i> relaxation times and thermal conductivity accumulation function for $\alpha$ -quartz. . . . .	126
5.11	Phonon relaxation times for graphene. . . . .	127
5.12	Spectral and accumulated thermal conductivity of natural graphene. . . . .	127
5.13	Fractal thermal conductivity in the KCM framework for silicon. . . . .	129
5.14	Fractal diffusivity for $\text{In}_{0.53}\text{Ga}_{0.47}\text{As}$ and $\text{Si}_{0.82}\text{Ge}_{0.18}$ . . . . .	130
5.15	Umklapp and impurity/alloy <i>first principles</i> relaxation times for Si, $\text{In}_{0.53}\text{Ga}_{0.47}\text{As}$ and $\text{Si}_{0.82}\text{Ge}_{0.18}$ at 300 K. . . . .	131
5.16	Umklapp relaxation times at 300 K, 100 K and 50 K for natural silicon. . . . .	132
5.17	<i>First principles</i> total relaxation times for silicon and diamond under the RTA, R-LBTE and KCM models. . . . .	134

---

6.1	Effective decay rate as a function of the inverse grating length scale.	137
6.2	Thermal grating simulations from different models. . . . .	138
6.3	Effective thermal resistivity as a function of the heater width $L$ with periodicity $4L$ on top of silicon. . . . .	140
6.4	Experimental setup of TDTR imaging . . . . .	141
6.5	Temperature profile of TDTR measurement on silicon with a $1 \mu\text{m}$ (left) and $400 \text{ nm}$ gold heating line (right). . . . .	142
6.6	Temperature profile of TDTR measurement on silicon with a $200 \text{ nm}$ gold heating line, 2D temperature profile based on KCM and color representation of the angle between $\mathbf{Q}$ and $-\nabla T$ . . . . .	142
6.7	TDTR imaging for a $10 \mu\text{m}$ and $2 \mu\text{m}$ heating lines on $\text{In}_{0.53}\text{Ga}_{0.47}\text{As}$ .	144
6.8	Temporal response of different width heating lines on $\text{In}_{0.53}\text{Ga}_{0.47}\text{As}$ .	145
6.9	Effective thermal conductivity from a Fourier representation of the KCM solution. . . . .	146
6.10	Temperature profile on $\text{In}_{0.53}\text{Ga}_{0.47}\text{As}$ for $W=200 \text{ nm}$ , $W=400 \text{ nm}$ and $W=10 \mu\text{m}$ . . . . .	147
6.11	Best anisotropic fit to experimental $\text{In}_{0.53}\text{Ga}_{0.47}\text{As}$ temperature profile with $W=500 \text{ nm}$ . . . . .	148
C.1	Correction coefficient $f$ as a function of $\zeta h/2$ for different values of $h/\ell$ and for boundary conditions: $C = 0$ and $C = 1$ . . . . .	161

# Introduction

Most of the daily life devices and electronic tools have components based on semiconductor materials. These have been traditionally used for a wide range of applications, from transistors to photovoltaic or thermoelectric energy sources. The improvement of these devices can be only achieved from the proper knowledge of the physics involved in their operation. In recent years, the technology industry has evolved to the nanotechnology world in an attempt to reduce the size of the devices to dimensions as small as allowed by manufacturing. The problem that this reduction has faced is that the properties of semiconductors at these new scales have turned out to be different from those at larger scales. A lot of phenomena can appear in semiconductors when the size of the materials is reduced, such as quantum confinement, boundary effects or the appearance of correlations. In addition, the temperature has an important effect on the properties of the material, and this can influence its performance. In the specific case of heat transport, heat dissipation has become a new challenge in order to reduce the size of the components. A model able to predict these new properties at all time and length scales will also reduce the time, human and economic resources from the design point.

There are two different approaches that can be used to face the thermal transport phenomena at the nanoscale, microscopic and macroscopic. The first approach consists in obtaining the microscopic magnitudes describing the behavior of the participating heat carriers, while the second one consists in obtaining the relations between the thermodynamic magnitudes involved. The connection between these two approaches is the key goal of statistical physics. This has been extensively developed for equilibrium or local equilibrium in the last century and high predictability has been achieved. In contrast, far from equilibrium obtaining a reliable solution is not that easy. When large thermodynamic inhomogeneities appear, the distribution of the heat carriers becomes very complex. Spatial and temporal dependence appear on the system and memory and non-localities are needed for their correct description. To find the microscopic connection in these situations a proper thermodynamic framework is necessary.

In the last years the numerical capabilities of computer clusters have made



it possible to improve the microscopic approach. Nowadays it is possible to introduce all the relevant microscopic information into a very large Hamiltonian and try to solve the transport equations directly. Despite of this, its complexity can make the computational time needed to obtain a single solution huge. This means that the combination with macroscopic approaches finding symmetries and conservation laws of the system can allow simplifying the problem and obtaining a very good approximation in less computational time. So, although microscopic models based on a Hamiltonian are the only way to obtain an exact solution, in practice actual calculations must always reduce the amount of microscopic information used, providing thus a non-exact solution. If the error of approximating the problem to a simpler one by using a conservation law is of the same order as the errors introduced in practical solutions of the microscopic approach, the latter can be more useful. The benefit of this approach is that it can give a deeper physical insight and can show the appearance of new phenomena that can be hidden in the complexity of microscopic approaches.

The validity of the Fourier law has been demonstrated to be broken at the nanoscale and the formulation of a new equation valid at this scale is pursued. Its generalization is studied through the solution of the Boltzmann Transport Equation (BTE). The main problem of this equation is its extreme complexity. This forces the use of simplifications in order to obtain some approximate solutions.

In this thesis the Kinetic Collective Model (KCM) is proposed as a framework to solve the BTE and as a generalization of Fourier's law [1, 2, 3] to include memory and non-local effects in order to describe heat transport at small size and time scales. In the KCM, thermal conductivity is split into a kinetic and a collective regime. In the first regime all the phonons interact between them and the boundaries independently. In the collective regime a global interaction of the phonons due to the momentum conservation of certain collisions takes place, leading to the appearance of a hydrodynamic-like heat flow.

This dissertation is organized as follows. First, in **Chapter 1** thermal transport is introduced from current solutions of the BTE for phonons to recent heat transport formulations based on superdiffusive and hydrodynamic regimes. In **Chapter 2**, the *first principles* framework used to obtain phonon properties is introduced, and the equations of thermal transport in the KCM are detailed. In addition, computational details of *ab initio* calculations are also discussed. In the following chapters, the KCM framework is applied to the study of thermal transport in different systems and compared to other current solutions. In **Chapter 3**, the thermal conductivity of bulk materials is studied. In **Chapter 4**, systems from nano to micrometer characteristic size like nanowires and thin films are considered for the study of thermal conductivity. In this case, solutions are provided from a kinetic-collective boundary approach based on Guyer

and Krumhansl's derivation, and from a full hydrodynamic model. The transport properties in transient regimes and the phonon spectrum of the presented samples is discussed in **Chapter 5**. Finally, in **Chapter 6** complex experiments where diffusive heat transport can not be applied are studied within the hydrodynamic KCM framework, before summarizing the conclusions in **Chapter 7**.



# Chapter 1

## Thermal transport

A common way to understand the heat transfer is by considering that energy is transferred by a quantum called phonon. A phonon is a pseudo-particle with energy  $\hbar\omega$  and crystalline momentum  $\hbar\mathbf{q}$  obtained from the solution of the equations of motion of the atoms in a periodic crystal lattice. With this building blocks the first picture of thermal transport is that of phonons moving randomly at their constant group velocity in a Brownian motion. The macroscopic consequence of this microscopic picture is a diffusive heat transport governed by the Fourier law. This law has been successfully used in the last two centuries, but in the last decades divergences from classical behavior at reduced time and length scales have been observed. The first approach to understand these deviations was using an effective thermal conductivity depending on the characteristic length of the samples, but still relying in the Fourier equation. This approach has also been overtaken in the last years using more advanced techniques. Some examples are ultra-fast laser techniques measuring the effective thermal conductivity using heaters with different sizes or working at different excitation frequency ranges [4, 5, 6, 7, 8, 9, 10]. In these new setups an explicit generalization of the Fourier law should be used because the effective thermal conductivity approach does not provide good results. In consequence, other transport phenomena such as ballistic transport, superdiffusive regime or collective flow have appeared [3, 11, 12, 13, 14].

Different proposals that have tried to modify the diffusive behaviour from the microscopic point of view through a change in the collisions relaxation times. In situations where Fourier law is applicable, these models are able to predict the thermal conductivity with excellent performance, but in non-homogeneous situations the anharmonic nature of the phonon collisions makes it difficult to find reliable results. Some of the proposed explanations are based on kinetic models considering anisotropy or using phonon suppression functions, but none of them seems fully satisfactory. The difficulty to explain these experiments

from a classical kinetic point of view [10, 14] has prompted the emergence of new proposals based on including memory or non-locality like superdiffusive or hydrodynamic models.

From a microscopic point of view, at reduced time and spatial scales the Truncated Lévy Flight (TLF) model has emerged in recent years as a framework to describe heat transport [11, 12]. The TLF model is able to capture the coexistence of ballistic and diffusive heat transport that can appear when the sample size and/or temporal scale is reduced. Parallel to the microscopic formulation, in the last half of the past century some authors [14, 15, 16, 17] have established a description from a hydrodynamic point of view. In this case the phonons behave like a fluid, emerging the so-called phonon hydrodynamics. This formulation allows defining a hydrodynamic heat transport equation in which boundary conditions can be imposed in order to solve complex geometry systems. While the thermal conductivity of an infinite material can be computed from a mechanical formulation, for real systems is more suitable the use of hydrodynamic heat transport due to the finite size. In addition, this formalism allows to account for memory and non-local effects able to reproduce recent experimental observations of deviations from Fourier heat transport [4, 5, 6, 7, 8, 9, 10].

In this chapter the different models used to obtain the thermal evolution of a system using *first principles* magnitudes are introduced. The separation of conserving and non-conserving momentum collisions is shown to be key in order to predict the thermal conductivity in bulk materials.

To avoid mix-up in the present work  $\mathbf{Q} = (Q_x, Q_y, Q_z)$  is used for the heat flux and  $\mathbf{q} = (q_x, q_y, q_z)$  is used for the phonon wave vector.

## 1.1 Boltzmann Transport Equation

When studying thermal transport, phonons have been widely used as energy carriers. In equilibrium, the distribution function of such pseudo-particles is the Bose-Einstein distribution, which gives information about the number of phonons in momentum space

$$n_{\mathbf{q}\nu}^0(\omega, T) = \frac{1}{e^{\hbar\omega_{\mathbf{q}}/\kappa_B T} - 1}, \quad (1.1)$$

where  $\mathbf{q}_\nu$  denotes a phonon with wave vector  $\mathbf{q}$  and branch  $\nu$  with frequency  $\omega_{\mathbf{q}}$ .  $T$  is the equilibrium temperature and  $k_B$  and  $\hbar$  are the Boltzmann and reduced Planck constants respectively.

Eq. (1.1) shows that in equilibrium the description of the system can be achieved by using a single thermodynamic magnitude  $T$ , but, when the system is perturbed from its equilibrium state, the phonon distribution changes and inhomogeneities and temporal evolution appear.

In 1892, Ludwig Boltzmann introduced his kinetic theory of gases [18] to describe the evolution of the distribution function in these situations. This equation is called since then the Boltzmann Transport Equation (BTE). Out of equilibrium the distribution function will evolve due to two mechanisms. First, the presence of mechanical or thermodynamic forces in the system generates inhomogeneities. Second, the collisions of the phonons among themselves and with other particles will tend to restore the equilibrium. The temporal evolution of the distribution function is described by balancing both effects

$$\left(\frac{dn_{\mathbf{q}}}{dt}\right)_{\text{drift}} = \left(\frac{\partial n_{\mathbf{q}}}{\partial t}\right)_{\text{scattering}}. \quad (1.2)$$

The general form of the drift operator in the phonon basis is

$$\left(\frac{dn_{\mathbf{q}}}{dt}\right)_{\text{drift}} \equiv \frac{\partial n_{\mathbf{q}}}{\partial t} + \mathbf{v}_{\mathbf{q}} \frac{\partial n_{\mathbf{q}}}{\partial \mathbf{r}} + \mathbf{F} \frac{\partial n_{\mathbf{q}}}{\partial \mathbf{v}}, \quad (1.3)$$

where  $\mathbf{v}_{\mathbf{q}}$  is the group velocity of the mode  $\mathbf{q}$  and  $\mathbf{F}$  the force that particles experience due to external fields. Opposite to electrons, phonons can not be influenced by external forces, and the last term is not necessary.

In this representation the drift operator is diagonal and consequently the most important complexity of the BTE lies in the collision term. This depends on the type of collisions that are considered. It includes products of the distribution function of the particles involved in the collision, having at least an incoming and an outgoing phonon. This makes this term non-linear and renders its solution extraordinarily difficult. In the case of phonons the most complex collision term is the anharmonic phonon-phonon scattering. It includes at least three phonons. In this case, the collision term has the form:

$$\left(\frac{\partial n_{\mathbf{q}}}{\partial t}\right)_{\text{scatt}} = \int \int [n_{\mathbf{q}} n_{\mathbf{q}'} (n_{\mathbf{q}''} + 1) - \frac{1}{2} n_{\mathbf{q}} (n_{\mathbf{q}'} + 1) (n_{\mathbf{q}''} + 1)] \Omega_{\mathbf{q}, \mathbf{q}', \mathbf{q}''} \frac{d\mathbf{q}' d\mathbf{q}''}{(2\pi)^3}, \quad (1.4)$$

where  $\Omega_{\mathbf{q}, \mathbf{q}', \mathbf{q}''}$  is the transition probability of the collision of two phonons  $\mathbf{q}$  and  $\mathbf{q}'$  giving an outgoing phonon  $\mathbf{q}''$ .

As a non-linear integro-differential equation, the ability to solve the BTE depends on the simplifications used. A very useful approach when the perturbation is not very large is the linearization.

### 1.1.1 Linearization of the BTE

The linearized BTE (LBTE) is the equation obtained from the linearization of the perturbation. The distribution function can be expressed as the equilibrium

term and a deviation from it

$$n_{\mathbf{q}} = n_{\mathbf{q}}^0 + \Delta n_{\mathbf{q}} . \quad (1.5)$$

The deviation from equilibrium can be expressed in first order of certain perturbation  $A$  as:

$$\Delta n_{\mathbf{q}} = \frac{\partial n_{\mathbf{q}}}{\partial \epsilon_{\mathbf{q}}} \frac{\partial \epsilon_{\mathbf{q}}}{\partial A} \nabla A \cdot \Delta \mathbf{r} = \frac{\partial n_{\mathbf{q}}}{\partial \epsilon_{\mathbf{q}}} \Phi_{\mathbf{q}} = \frac{n_{\mathbf{q}}^0 (n_{\mathbf{q}}^0 + 1)}{k_B T} \Phi_{\mathbf{q}} , \quad (1.6)$$

where  $\Phi_{\mathbf{q}}$  accounts for the deviation from equilibrium. In the simplest situation,  $A$  can be just the temperature  $T$  and Fourier transport is obtained by solving the LBTE. In more complex cases, the perturbation can also depend on the heat flux  $\mathbf{Q}$  and Fourier transport is no longer valid to describe the heat transport in all situations. With a little algebra, using Eqs. (1.5)-(1.6) in the scattering operator (Eq. (1.4)), an expression of the collision term as a function of the deviation from equilibrium can be obtained [19]:

$$\left( \frac{\partial n_{\mathbf{q}}}{\partial t} \right)_{\text{scatt}} = \int \int [\Phi_{\mathbf{q}} - \Phi_{\mathbf{q}'} - \Phi_{\mathbf{q}''}] P_{\mathbf{q},\mathbf{q}',\mathbf{q}''} \frac{d\mathbf{q}' d\mathbf{q}''}{(2\pi)^3} , \quad (1.7)$$

where  $P_{\mathbf{q},\mathbf{q}',\mathbf{q}''}$  is the equilibrium transition rate. This change simplifies enormously the equation as the product of distributions disappears. This makes Eq. (1.1) linear and consequently can be written in matrix form. Despite of this, the diagonalization of the LBTE is still complex. Simplifying the solution of the scattering operator by choosing the best basis to work with has been the focus of great efforts in the last decades.

## 1.2 Solutions to the LBTE

The linearization of the BTE allows to express the LBTE in operator form as:

$$\mathbf{Dn} = \mathbf{Cn} , \quad (1.8)$$

where  $\mathbf{n}$  corresponds to the phonon distribution function and  $\mathbf{D}$  and  $\mathbf{C}$  are the drift and collision operator respectively. The solution of the LBTE should be obtained by inverting the drift or the collision operators, that is, obtaining the eigenstates and eigenfunctions of

$$\mathbf{n} = \mathbf{D}^{-1} \mathbf{Cn} \text{ or } \mathbf{n} = \mathbf{C}^{-1} \mathbf{Dn} . \quad (1.9)$$

The rank of both matrices is related to the number of modes in the system, which is an overwhelming number. Obtaining an analytic solution to the equation is not

possible unless some simplification is used, as done in early studies [20]. Recently, several numerical approaches have been tried to obtain the exact solution through numerical inversion due to the tremendous improvements achieved in computer performance [21, 22]. Despite of these advances, the high complexity of the direct solution hides the physical insight. For that reason, more sophisticated simplified approaches, like the Kinetic Collective Model (KCM) described in next sections, can be really valuable.

### 1.2.1 Relaxation Time Approximation

To solve the problem due to the non-diagonal form of the collision term, the Relaxation Time Approximation (RTA) assumes that the rate at which a phonon  $\mathbf{q}$  relaxes does not depend on the non-equilibrium situation of the phonons colliding with it. In the case of the three phonon collisions this implies  $n_{\mathbf{q}'} = n_{\mathbf{q}'}^0$  and  $n_{\mathbf{q}''} = n_{\mathbf{q}''}^0$ , and only the phonon  $\mathbf{q}$  is displaced from equilibrium  $n_{\mathbf{q}} = n_{\mathbf{q}}^0 + \Delta n_{\mathbf{q}}$ . Under these considerations the BTE becomes diagonal and can be expressed as:

$$v_{\mathbf{q}} \nabla n_{\mathbf{q}}^0 = -\frac{n_{\mathbf{q}} - n_{\mathbf{q}}^0}{\tau_{\mathbf{q}}}, \quad (1.10)$$

where

$$\frac{1}{\tau_{\mathbf{q}}} = \Phi_{\mathbf{q}} \int \int P_{\mathbf{q},\mathbf{q}',\mathbf{q}''} \frac{d\mathbf{q}'d\mathbf{q}''}{(2\pi)^3}. \quad (1.11)$$

Eq. (1.10) states that when a phonon is excited, the distribution function relaxes to equilibrium as  $\Delta n_{\mathbf{q}}(t) = \Delta n_{\mathbf{q}}(t_0)e^{-t/\tau_{\mathbf{q}}}$  in a characteristic time  $\tau_{\mathbf{q}}$  independent of the rest of the distribution. This equation is diagonal in the  $\mathbf{q}$  space for the drift and collision operators. This makes the LBTE very easy to solve. The solution obtained is:

$$n_{\mathbf{q}} = n_{\mathbf{q}}^0 + \tau_{\mathbf{q}} v_{\mathbf{q}} \nabla n_{\mathbf{q}}^0. \quad (1.12)$$

By using the microscopic definition of the heat flux  $\mathbf{Q} = \langle \hbar\omega \mathbf{v}_{\mathbf{q}} \rangle$  and the Fourier law  $\mathbf{Q} = -\kappa \nabla T$ , the thermal conductivity can be expressed as a frequency integral over all the phonons:

$$\kappa^{i,j} = \int \hbar\omega \mathbf{v}_{\mathbf{q}}^i \mathbf{v}_{\mathbf{q}}^j \tau_{\mathbf{q}} \frac{\partial n_{\mathbf{q}}^0(\omega)}{\partial T} D(\omega) d\omega, \quad (1.13)$$

where  $T$  is the temperature and  $D(\omega)$  the density of states (DOS). Notice that  $\hbar\omega \partial n_{\mathbf{q}}^0(\omega) / \partial T$  represents the mode specific heat  $C_v$ .

A problem with the classical RTA is that it assumes that all collisions are able to relax the distribution function to equilibrium. This is not true, as conservation laws like those of energy and momentum are involved in the transition rates



between modes. Being more specific, a subgroup of three phonon collisions are known to conserve the crystal momentum of the distribution. These processes are called normal ( $N$ ) collisions. When only  $N$  collisions are considered, the distribution function should relax to a form keeping constant the total momentum of the distribution. Callaway already noticed that effect, and added an additional term to the thermal conductivity integral to remove the contribution of such processes [20, 23]. As will be discussed later, the large amount of experimental data obtained in recent years for different materials, shapes and heating conditions have made it necessary to improve this approach. In this sense, four main contributions have appeared: the iterative solution of phonon BTE, two direct solutions of the phonon LBTE and the KCM. The first three proposed solutions (known as full solutions) can provide exact solutions of LBTE for bulk samples from a kinetic theory viewpoint. The latter has been introduced from a hydrodynamic basis to account for the the shape and size effects that can not be studied in an easy way just from a kinetic theory.

The main difference between the KCM and the other mentioned current solutions is that the former imposes strictly the momentum conservation of  $N$  collisions and uses relaxation times generalized from the RTA maintaining the simplicity of such approximation. In this case, in contrast to the classical RTA, it is necessary to distinguish between momentum conserving and non-conserving collisions. In the other cases the collision operator is expressed in its full form and consequently the complexity increases. Equivalent results for the thermal conductivity are obtained in all the recent formulations.

## 1.2.2 Iterative solution of BTE (I-BTE)

An improvement of the RTA solution has been developed by Li *et al.* [24] by an iterative procedure. In this proposal, the collision term of the step  $i + 1$  is obtained from the distribution function of the step  $i$  in an iterative process

$$\left(\frac{\partial n_{\mathbf{q}}}{\partial t}\right)_{\text{scatt}}^{(i+1)} = \int \int [\Phi_{\mathbf{q}}^{(i)} - \Phi_{\mathbf{q}'}^{(i)} - \Phi_{\mathbf{q}''}^{(i)}] P_{\mathbf{q},\mathbf{q}',\mathbf{q}''} \frac{d\mathbf{q}'d\mathbf{q}''}{(2\pi)^3}. \quad (1.14)$$

The iterative BTE (I-BTE) starts from the RTA relaxation time as a zeroth-order solution ( $\Phi_{\mathbf{q}'}^{(0)} = \Phi_{\mathbf{q}''}^{(0)} = 0$  and  $\Phi_{\mathbf{q}}^{(0)} \neq 0$ ). The relaxation time in each step is  $\tau_{\mathbf{q}}^{(1)} = \tau_{\mathbf{q}}^{(0)}(1 + \Delta_{\mathbf{q}}^{(0)})$ , where  $\tau_{\mathbf{q}}^{(0)} = \tau_{RTA}$  includes terms of  $n_{\mathbf{q}}^0$ ,  $n_{\mathbf{q}'}^0$  and  $n_{\mathbf{q}''}^0$ , while  $\Delta_{\mathbf{q}}$  includes the ones corresponding to  $\Delta n_{\mathbf{q}}$ ,  $\Delta n_{\mathbf{q}'}$  and  $\Delta n_{\mathbf{q}''}$  from Eq. (1.6). Using Eq. (1.10) it is direct to obtain the non-equilibrium distribution function of the first iteration:

$$n_{\mathbf{q}}^{(1)} = n_{\mathbf{q}}^0 - v_{\mathbf{q}}\tau_{\mathbf{q}}^{(1)}\nabla n_{\mathbf{q}}^0. \quad (1.15)$$

In a second step a new relaxation time  $\tau_{\mathbf{q}}^{(2)} = \tau_{\mathbf{q}}^{(1)}(1 + \Delta_{\mathbf{q}}^{(1)})$  is calculated from the previous distribution function  $n_{\mathbf{q}}^{(1)}$  and the relaxation time  $\tau_{\mathbf{q}}^{(1)}$ . The iterative process is repeated until convergence is achieved  $\tau_{\mathbf{q}}^{(i)} - \tau_{\mathbf{q}}^{(i-1)} < \epsilon$ , with  $\epsilon$  a convergence threshold close to 0.

This method allows to account properly for the effect for  $N$  collisions, removing their contribution to the thermal resistance.

### 1.2.3 Direct solution of LBTE

Laurent Chaput [21] has solved in a direct procedure the LBTE (D-LBTE) for bulk systems in the frequency domain.

In first place, it is required to recover the term  $\frac{\partial n_{\mathbf{q}}}{\partial t}$  from Eq. (1.3), neglected in previous solutions

$$\left(\frac{dn_{\mathbf{q}}}{dt}\right)_{\text{scatt}} = \frac{\partial n_{\mathbf{q}}^1}{\partial t} + \mathbf{v}_{\mathbf{q}} \frac{\partial n_{\mathbf{q}}^0}{\partial \mathbf{r}}, \quad (1.16)$$

where  $n_{\mathbf{q}}^1$  is the first order deviation from equilibrium ( $n_{\mathbf{q}} \approx n_{\mathbf{q}}^0 + n_{\mathbf{q}}^1$ ). Notice that the drift operator is only applied on the equilibrium distribution function. To obtain a symmetric collision matrix, the scattering term is written as:

$$\left(\frac{\partial n_{\mathbf{q}}}{\partial t}\right)_{\text{scatt}} = - \sum_{\mathbf{q}'} \Omega'_{\mathbf{q},\mathbf{q}'} n_{\mathbf{q}'}^1 \frac{\sinh(x_{\mathbf{q}'}/2)}{\sinh(x_{\mathbf{q}}/2)}, \quad (1.17)$$

where  $x_{\mathbf{q}} \equiv \hbar\omega_{\mathbf{q}}/k_B T$ . Using the ansatz  $f_{\mathbf{q}} \equiv n_{\mathbf{q}}^1 \sinh(x_{\mathbf{q}}/2)$ , the LBTE in the Fourier space is:

$$-i\omega \mathbf{f}_{\mathbf{q}}(\omega) + \frac{x_{\mathbf{q}}}{4T \sinh(x_{\mathbf{q}}/2)} \mathbf{v}_{\mathbf{q}} = - \sum_{\mathbf{q}'} \Omega'_{\mathbf{q},\mathbf{q}'} \mathbf{f}_{\mathbf{q}'}(\omega). \quad (1.18)$$

At this point it is necessary to use crystal symmetries to reduce the calculation to the irreducible Brillouin zone (IBZ). From now on,  $\mathbf{k}$  will have the same role as  $\mathbf{q}$  but in the IBZ. Using the symmetry properties of  $\mathbf{v}_{\mathbf{q}}$ ,  $\Omega'_{\mathbf{q},\mathbf{q}'}$  and  $\mathbf{f}_{\mathbf{q}'}(\omega)$ , as well as rotations  $\mathbf{R}$  of the isogon point group of the crystal  $g$  and the multiplicity  $w_{\mathbf{k}}$  of each phonon  $\mathbf{k}$ , the LBTE is expressed as

$$\frac{x_{\mathbf{q}}}{4T \sinh(x_{\mathbf{q}}/2)} \sqrt{\frac{w_{\mathbf{k}}}{|g|}} v_{\mathbf{k}}^{\alpha} = -i \sum_{\beta \mathbf{k}'} (\tilde{\Omega}'_{\alpha \mathbf{k}, \beta \mathbf{q}'} - i\omega \delta_{\mathbf{k}, \mathbf{k}'} \mathbf{P}_{\mathbf{k}'}^{\alpha \beta}) \sqrt{\frac{w_{\mathbf{k}'}}{|g|}} f_{\mathbf{k}'}^{\beta}. \quad (1.19)$$

$|g|$  is the cardinal of the isogon point group,  $\mathbf{P}_{\mathbf{k}}^{\alpha \beta} = \frac{w_{\mathbf{k}}}{|g|} \sum_{\mathbf{R}} \mathbf{R}_{\alpha \beta} \delta_{\mathbf{k}, \mathbf{R}\mathbf{k}}$  and  $\tilde{\Omega}'_{\alpha \mathbf{k}, \beta \mathbf{q}'} = \sqrt{\frac{w_{\mathbf{k}} w_{\mathbf{k}'}}{|g|}} \sum_{\mathbf{R}'} \mathbf{R}'_{\alpha \beta} \Omega_{\mathbf{k}, \mathbf{R}'\mathbf{k}'}$ .  $\alpha$  and  $\beta$  denote Cartesian indices and the

delta function ensures energy and momentum conservation. From the definition of energy flux and the Fourier law it is obtained the thermal conductivity tensor in a compact matrix notation

$$\kappa^{\alpha\beta}(\omega) = \frac{2k_B T^2}{V} \langle f(\omega) | [\mathbf{I}(\alpha, \beta) + \mathbf{I}(\beta, \alpha)] \times (\tilde{\Omega} - i\omega\mathbf{P}) | f(\omega) \rangle, \quad (1.20)$$

where  $V$  is the volume of the IBZ and  $\mathbf{I}_{\gamma\mathbf{k},\gamma'\mathbf{k}'} = \delta_{\mathbf{k},\mathbf{k}'} \sum_{\mathbf{R}} \mathbf{R}_{\alpha\gamma} \mathbf{R}_{\beta\gamma'}$ . The commutation relation  $[\mathbf{I}_{\alpha\beta}, \tilde{\Omega} - i\omega\mathbf{P}] = 0$ , and the use of  $\mathbf{I}_{\alpha\beta} = \mathbf{I}_{\beta\alpha}^\dagger$  and  $\mathbf{I}_{\alpha\beta}(\tilde{\Omega} - i\omega\mathbf{P}) = (\mathbf{I}_{\beta,\alpha}(\tilde{\Omega} - \omega\mathbf{P}))^\dagger$  makes possible to diagonalize  $[\mathbf{I}_{\alpha\beta} + \mathbf{I}_{\beta\alpha}]|e_r\rangle = i_r(\alpha, \beta)|e_r\rangle$  and  $\tilde{\Omega}|e_r\rangle = \omega_r|e_r\rangle$ . Finally the dynamical thermal conductivity is reduced to

$$\kappa^{\alpha\beta}(\omega) = \int \frac{\rho_{\alpha\beta}(\omega')}{\omega' - i\omega} d\omega', \quad (1.21)$$

where  $\rho_{\alpha\beta}(\omega')$  is the spectral density defined from the eigenvectors  $i_r(\alpha, \beta)$  and the projection of the final distribution function on  $|e_r\rangle$  [25]. This expression allows to split the thermal conductivity into a real and an imaginary part, helpful to study frequency-dependent experiments. Moreover, it can be used for steady state calculations. For fast frequency variations, the use of the equilibrium distribution function in the drift term can lead to wrong results. A full complete treatment of the drift operator is required in such cases [15, 26].

As can be seen from Eq. (1.21), from this definition of thermal conductivity it is neither possible to define a carrier velocity nor a relaxation time. This is because in this solution the scattering matrix is not diagonalized.

## 1.2.4 Relaxon solution of the LBTE

The diagonalization of the full collision scattering operator, instead of neglecting non-diagonal terms like in RTA, allows obtaining eigenvectors that can be understood as collective phonon excitations, that are linear combination of phonons. These collective excitations are known as relaxons in the present approach. The relaxation time to the equilibrium function corresponds then to the inverse of the relaxon eigenvalues.

The direct digonalized solution of the LBTE (R-LBTE) developed by Andrea Cepellotti and Nicola Marzari [22] starts from the classical BTE in absence of external forces:

$$\begin{aligned} \frac{\partial n_{\mathbf{q}}^0}{\partial T} \left( \frac{\partial T(\mathbf{r}, t)}{\partial t} + \mathbf{v}_{\mathbf{q}} \nabla T(\mathbf{r}, t) \right) + \frac{\partial \Delta n_{\mathbf{q}}(\mathbf{r}, t)}{\partial t} + \mathbf{v}_{\mathbf{q}} \nabla (\Delta n_{\mathbf{q}}(\mathbf{r}, t)) \\ = -\frac{1}{V} \sum_{\mathbf{q}'} \Omega_{\mathbf{q}\mathbf{q}'} \Delta n_{\mathbf{q}'}(\mathbf{r}, t), \end{aligned} \quad (1.22)$$

where the changes

$$\tilde{\Omega}_{\mathbf{q}\mathbf{q}'} = \Omega_{\mathbf{q}\mathbf{q}'} \sqrt{\frac{n_{\mathbf{q}'}^0(n_{\mathbf{q}'}^0 + 1)}{n_{\mathbf{q}}^0(n_{\mathbf{q}}^0 + 1)}} \quad \text{and} \quad \Delta \tilde{n}_{\mathbf{q}} = \Delta n_{\mathbf{q}} (n_{\mathbf{q}}^0(n_{\mathbf{q}}^0 + 1))^{-1/2} \quad (1.23)$$

are required in order to obtain a diagonalizable real symmetric scattering matrix. In this case the eigenvectors (relaxons) are  $\theta_{\mathbf{q}}^{\alpha}$  and the real eigenvalues (relaxation times)  $1/\tau_{\mathbf{q}}^{\alpha}$ . The scalar product for this basis is  $\langle \alpha | \alpha' \rangle \equiv 1/V \sum_{\mathbf{q}} \theta_{\mathbf{q}}^{\alpha} \theta_{\mathbf{q}}^{\alpha'}$ . Then, the BTE can be written as:

$$\begin{aligned} \sqrt{\frac{C}{k_B T^2}} \left( \frac{\partial T(\mathbf{r}, t)}{\partial t} \langle 0 | \alpha \rangle + \nabla T(\mathbf{r}, t) \mathbf{V}_{0\alpha} \right) + \frac{\partial f_{\alpha}(\mathbf{r}, t)}{\partial t} \\ + \sum_{\alpha'} \mathbf{V}_{\alpha\alpha'} \nabla f_{\alpha'}(\mathbf{r}, t) = -\frac{f_{\alpha}(\mathbf{r}, t)}{\tau_{\alpha}}, \end{aligned} \quad (1.24)$$

where  $C$  is the specific heat at temperature  $T$  and  $\mathbf{V}_{\alpha\alpha'} = \langle \alpha | \mathbf{v}_{\mathbf{q}} | \alpha' \rangle$  is a coupled velocity for the perturbed distribution, except for the equilibrium term  $\mathbf{V}_{0\alpha}$  that defines the relaxon velocity.  $f_{\alpha}$  corresponds to the relaxon occupation number defined from  $\Delta \tilde{n}_{\mathbf{q}} = \sum_{\alpha} f_{\alpha} \theta_{\mathbf{q}}^{\alpha}$ . As the scattering operator only acts on the deviation from equilibrium, the  $n_{\mathbf{q}}^0$  distribution is not an eigenvector. For that the unitary vector  $\theta_{\mathbf{q}}^0 = \frac{\sqrt{n_{\mathbf{q}}^0(n_{\mathbf{q}}^0+1)} \hbar \omega_{\mathbf{q}}}{\sqrt{k_b T^2 C}}$  is introduced.

This procedure allows a relevant improvement from prior solutions of the BTE in computing thermal conductivity. In contrast, diagonalizing the scattering matrix renders the drift term very complicated and then second order expressions like second sound are difficult to be defined. To obtain a diagonal drift operator as well, it is necessary to set  $\nabla f_{\alpha} = 0$ , losing consequently part of information. This condition implies homogeneous perturbation, i.e., the solutions are obtained considering a constant homogeneous temperature gradient. In addition, it is considered steady state ( $\partial/\partial t = 0$ ) and small deviations from equilibrium. In that case, the obtained thermal conductivity is:

$$k^{ij} = C \sum_{\alpha} \mathbf{V}_{\alpha}^i \mathbf{V}_{\alpha}^j \tau_{\alpha}, \quad (1.25)$$

where the similarity with classical expressions is clear but instead of phonon velocities and relaxation times are those defined for relaxons.

## 1.2.5 Kinetic Collective Model

The lack of validity of the classical RTA approximation can be improved by the KCM, developed in recent years by C. de Tomás and F.X. Alvarez [1, 2]. The KCM is derived from the exact solution to the LBTE proposed by Guyer and Krumhansl [15], based on the splitting of the collision operator in  $N$  and resistive ( $R$ ) processes ( $C = N + R$ ) when calculating the scattering matrix.

In the R-LBTE approach, in order to obtain the distribution relaxation time the full collision matrix  $C$  is diagonalized. As  $N$  processes do not contribute directly to thermal resistance but redistribute momentum over all the phonon distribution, a suitable way to solve the LBTE in their presence is by using the basis that diagonalizes the  $N$  scattering collision operator. Contrary to  $R$  processes,  $N$  scattering can not relax the distribution functions to equilibrium. Following this reasoning, in KCM only the  $N$  operator is diagonalized and the LBTE is solved in the basis of such eigenvectors. This provides a set of equations that define a moment space related to different order perturbations of the phonon distribution function. In this framework, the momentum basis (eigenvectors) in the KCM is split into three elements:  $|\eta_0\rangle$ ,  $|\eta_1\rangle$ , and  $|\eta_2\rangle$  [15]:

$$|\eta_0\rangle = \mu x [2\sinh(x/2)]^{-1}, \text{ where } x \equiv \frac{\hbar\omega}{k_B T}, \text{ and} \quad (1.26)$$

$$|\eta_{1i}\rangle = \lambda_i q_i [2\sinh(x/2)]^{-1}, \quad (1.27)$$

where  $q_i$  is the component  $i$  of a reciprocal wave vector and  $|n_\mu\rangle$  are the eigenvectors.  $|\eta_0\rangle$  obtained from the phonon energy  $\hbar\omega$  represents the zero order moment (the energy  $\epsilon$  or local temperature).  $|\eta_1\rangle$  determined from the crystalline momentum  $\hbar q_i$  corresponds to the first order moment (i.e. heat flux  $\mathbf{Q}$ ). The second order moment (i.e. flux of the heat flux  $\mathbf{Q}^{(2)}$ ) and higher orders are gathered into  $|\eta_2\rangle$  [15].

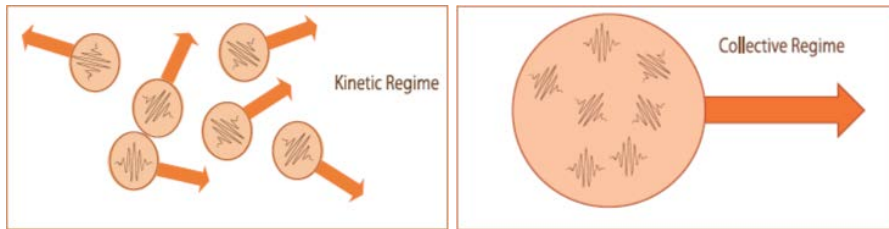


Figure 1.1: Sketch of the kinetic and collective transport regimes [1].

According to the KCM not all the energy is carried kinetically by independent collisions, but part of this energy is carried by collective modes, which have

their origin in the different effect of  $N$  collisions in front of the  $R$  ones. The collective behavior appears as a result of a coupling of modes generated through  $N$  processes. As a consequence, phonons of different modes perform as a whole  $R$  collisions. Therefore all modes share the same collision mean free time (MFT), the so-called collective MFT,  $\tau_c$ . These phenomena allow to split the thermal conductivity into a kinetic and a collective contribution weighed by a switching factor  $\Sigma \in [0, 1]$  measuring the relative importance of the  $N$  versus  $R$  scattering:

$$\kappa_T = \kappa_K + \kappa_C = \hat{\kappa}_K \cdot (1 - \Sigma) + \hat{\kappa}_C \cdot \Sigma, \quad (1.28)$$

where the effect of  $N$  processes is included in  $\Sigma$ , which determines the contribution of each transport regime, kinetic and collective. The hat  $\hat{\cdot}$  indicates the limit situation.

In addition, the diagonalization done in KCM allows solving the LBTE without complicating drastically the form of the drift operator, in contrast to previous solutions [21, 22, 24]. This will allow studying complex experiments from a hydrodynamic framework (see **Chapter 6**).

### Guyer and Krumhansl derivation

The derivation of KCM from Guyer and Krumhansl starts from the operator form of the BTE:

$$\mathbf{D}\mathbf{n}(\mathbf{q}, \mathbf{r}, t) = (\mathbf{N} + \mathbf{R})\mathbf{n}(\mathbf{q}, \mathbf{r}, t), \quad (1.29)$$

where  $\mathbf{n}$  corresponds to the phonon distribution function and  $\mathbf{D} = (\partial/\partial t) + \mathbf{v}\nabla_{\mathbf{r}}$  is the drift operator in absence of external forces. The previous equation can be solved to  $n^{th}$ -order in a suitable basis in the  $N$  process collision vector space for each moment representation of the distribution function. Guyer and Krumhansl show explicitly these basis related to the zero and first order moment (see Eqs. (1.26)-(1.27)), and perform the development of Eq. (1.29) in matrix form for isotropic dispersionless media. The BTE is symmetrized by using the change  $\mathbf{n}^* = \mathbf{n}2\sinh(x/2)$ . The total distribution function is then:

$$|\mathbf{n}^*\rangle = \sum_{\mu} \mathbf{a}_{\mu}(\mathbf{r}, t)|\eta_{\mu}\rangle, \quad (1.30)$$

where  $\mathbf{a}_i$  are the coefficients for each deviation. Using this basis, the BTE can be expressed as:

$$\left[ \begin{pmatrix} 0 & 0 & 0 \\ 0 & R_{11}^* & R_{12}^* \\ 0 & R_{21}^* & N_{22}^* + R_{22}^* \end{pmatrix} - \begin{pmatrix} D_{00} & D_{10} & 0 \\ D_{10} & D_{11} & D_{12} \\ 0 & D_{21} & D_{22} \end{pmatrix} \right] \cdot \begin{pmatrix} a_0 \\ \mathbf{a}_1 \\ \mathbf{a}_2 \end{pmatrix} = \begin{pmatrix} 0 \\ 0 \\ 0 \end{pmatrix}, \quad (1.31)$$

where  $\theta_{ij} = \langle i|\theta|j\rangle$ , being  $\theta$  any of the previous operators ( $\mathbf{D}$ ,  $\mathbf{R}$ ,  $\mathbf{N}$ ) and  $i, j$  the order of the distribution function. The first line of the equation defines the energy conservation

$$\frac{\partial a_0}{\partial t} + \mathbf{v}\nabla\mathbf{a}_1 = 0, \quad (1.32)$$

where  $\mathbf{v} = (v_x, v_y, v_z)$  is the phonon velocity vector. The second line defines the momentum conservation, which combined with the third line (higher order moment) can be expressed as:

$$D_{11}\mathbf{a}_1 + D_{10}a_0 = [R_{11}^* - (R_{12}^* - D_{12})(N_{22}^* + R_{22}^* - D_{22})^{-1}(R_{21}^* - D_{21})] \mathbf{a}_1. \quad (1.33)$$

The definition of the drift operator elements can be found elsewhere [15]. From this equation the quantity in brackets can be defined as the phonon momentum relaxation operator:

$$\tau = [R_{11}^* - (R_{12}^* - D_{12})(N_{22}^* + R_{22}^* - D_{22})^{-1}(R_{21}^* - D_{21})]^{-1}. \quad (1.34)$$

For simplicity steady state ( $D_{11} = D_{22} = \partial/\partial t \rightarrow 0$ ) and homogeneous medium ( $D_{12}$  and  $D_{22}$  vanish) is assumed, then:

$$\tau = \left[ R_{11}^* - \frac{R_{12}^*}{N_{22}^* + R_{22}^*} R_{21}^* \right]^{-1}. \quad (1.35)$$

Once defined the phonon relaxation time, the thermal conductivity can be expressed in its usual form:

$$\kappa^{ij} = \sum_{\mathbf{q}} C_{\mathbf{q}} v_{\mathbf{q}}^i v_{\mathbf{q}}^j \tau_{\mathbf{q}}. \quad (1.36)$$

The main complexity to compute the thermal conductivity from the exact solution of the BTE comes from the calculation of the terms  $R_{21}^*$ ,  $R_{22}^*$  and  $N_{22}^*$ . Knowing that  $R_{12}^* = R_{21}^*$  and studying the limit conditions when  $\mathbf{N}^* \rightarrow \infty$  and  $\mathbf{N}^* \rightarrow 0$  some approximations can be done [15]. The scattering terms can be then expressed as:

$$(R_{12}^*)^2 = R_{11}^* [R_{11}^* - (1/(\mathbf{R}^{*-1})_{11})] \quad \text{where} \quad (1.37)$$

$$(\mathbf{R}^{*-1})_{11} \rightarrow \langle 1|\tau_R(\mathbf{q})|1\rangle, \quad (1.38)$$

$$R_{11}^* \rightarrow \langle 1|\tau_R(\mathbf{q})^{-1}|1\rangle, \quad (1.39)$$

$$R_{22}^* \approx R_{11}^* \quad \text{and} \quad (1.40)$$

$$N_{22}^* \rightarrow (1/\tau_N) . \quad (1.41)$$

Notice that  $\tau_N$  is already an integrated value while  $\tau_R(\mathbf{q})$  is a wave vector dependent magnitude. In **Section 2.4** details of these calculations are provided. With these definitions, Eq. (1.35) can be expressed as:

$$\tau = \langle 1|\tau_R(\mathbf{q})|1\rangle \left[ \frac{\tau_N + \langle 1|\tau_R(\mathbf{q})^{-1}|1\rangle^{-1}}{\tau_N + \langle 1|\tau_R(\mathbf{q})|1\rangle} \right] . \quad (1.42)$$

At this point, the terms can be rearranged as:

$$\tau = \langle 1|\tau_R(\mathbf{q})|1\rangle \left( 1 - \frac{1}{1 + \frac{\tau_N}{\langle 1|\tau_R(\mathbf{q})|1\rangle}} \right) + \langle 1|\tau_R(\mathbf{q})^{-1}|1\rangle^{-1} \frac{1}{1 + \frac{\tau_N}{\langle 1|\tau_R(\mathbf{q})|1\rangle}} , \text{ where}$$

$$\frac{1}{1 + \frac{\tau_N}{\langle 1|\tau_R(\mathbf{q})|1\rangle}} = \Sigma , \quad \langle 1|\tau_R(\mathbf{q})|1\rangle = \tau_K \quad \text{and} \quad \langle 1|\tau_R(\mathbf{q})^{-1}|1\rangle^{-1} = \tau_C . \quad (1.43)$$

$\Sigma$  is the switching factor and  $\tau_K$  and  $\tau_C$  the kinetic and collective relaxation times respectively. Finally the thermal conductivity can be expressed in a simple form:

$$\kappa_T = \frac{1}{3} C_v c^2 [\tau_K(1 - \Sigma) + \tau_C \Sigma] = \hat{\kappa}_K \cdot (1 - \Sigma) + \hat{\kappa}_C \cdot \Sigma , \quad (1.44)$$

where  $c = |\mathbf{v}|$ .

The derivation of the model until Eq. (1.36) allows solving the LBTE exactly including all the terms of the perturbed distribution function. A simple calculation of the thermal conductivity can be done by some approximations (Eq. (1.40) and Eq. (1.41)) in the calculation of the scattering rates. Such approximation, reducing high order perturbation to first order, introduces an error that should be evaluated carefully, specially for complex experiments. On contrary this allows removing properly the contribution of  $N$  processes to thermal resistance and gives a clear picture of thermal transport. As  $N$  processes does not contribute to thermal resistance, in the ideal situation where only  $N$  processes are present, the thermal conductivity should be infinite [19]:

$$R \rightarrow 0; N \neq 0 \quad \text{then} \quad \kappa \rightarrow \infty . \quad (1.45)$$

This is obtained as the kinetic and collective thermal conductivity depend only on  $R$  processes, and consequently it is infinite when only  $N$  scattering exists.



### Maximization of the entropy derivation

The derivation of the KCM can be also done from the principle of maximization of entropy [1]. The microscopic entropy for a non-equilibrium distribution of phonons is:

$$\frac{S_{\mathbf{q}}}{k_B} = n_{\mathbf{q}} \ln n_{\mathbf{q}} - (n_{\mathbf{q}} - 1) \ln(n_{\mathbf{q}} - 1), \quad (1.46)$$

where  $S_{\mathbf{q}}$  is the entropy of the mode  $\mathbf{q}$ .

It is clear that momentum conserving processes do not contribute to thermal resistance, but contribute indirectly to the thermal conductivity in the way that such processes mix the different vibration modes affecting the drift-collision balance. Knowing this, when the  $N$  processes are negligible, this mixing is low and the entropy balance must be achieved individually, but in the other case, all modes are mixed and this balance must be fulfilled globally. The balance equations for the scattering and the drift operators can be expressed accordingly as:

$$\dot{S}_{\mathbf{q}}|_{\text{scatt}} = \frac{\Phi_{\mathbf{q}}}{T} \frac{\partial n_{\mathbf{q}}}{\partial t} \Big|_{\text{scatt}} \quad \text{and} \quad \dot{S}_{\mathbf{q}}|_{\text{drift}} = \frac{\mathbf{Q}_{\mathbf{q}}^2}{\kappa_{\mathbf{q}} T^2} \quad (1.47)$$

for the kinetic regime, and

$$\dot{S}_{\mathbf{q}}|_{\text{scatt}} = \int \frac{\Phi_{\mathbf{q}}}{T} \frac{\partial n_{\mathbf{q}}}{\partial t} \Big|_{\text{scatt}} d\mathbf{q} \quad \text{and} \quad \dot{S}_{\mathbf{q}}|_{\text{drift}} = \frac{\mathbf{Q}^2}{\kappa T^2} \quad (1.48)$$

in the collective regime, where in the latter the heat flux  $\mathbf{Q}$  and the thermal conductivity  $\kappa$  are already integrated magnitudes. From these expressions the thermal conductivity in each regime as a function of the phonon mode  $\mathbf{q}$  can be expressed as:

$$\kappa_{K,\mathbf{q}} = \frac{\mathbf{Q}_{\mathbf{q}}^2}{T \Phi_{\mathbf{q}} \frac{\partial n_{\mathbf{q}}}{\partial t} \Big|_{\text{scatt}}} \quad \text{and} \quad (1.49)$$

$$\kappa_C = \frac{\mathbf{Q}^2}{T^2 \int \frac{\Phi_{\mathbf{q}}}{T} \frac{\partial n_{\mathbf{q}}}{\partial t} \Big|_{\text{scatt}} d\mathbf{q}} \quad (1.50)$$

for the kinetic and collective regime respectively. Knowing that  $\mathbf{Q} = \int \mathbf{Q}_{\mathbf{q}} d\mathbf{q} = \int \hbar \omega_{\mathbf{q}} \mathbf{v}_{\mathbf{q}} n_{\mathbf{q}} d\mathbf{q}$ , where the distribution function is  $n_{\mathbf{q}} = n_{\mathbf{q}}^0 + \Phi_{\mathbf{q}} n_{\mathbf{q}}^0 (n_{\mathbf{q}}^0 + 1) / k_B T$ . If the deviation from equilibrium is  $\Phi_{\mathbf{q}} = c_{\mathbf{q}} \mathbf{q}$ , the thermal conductivity in each regime can be expressed as:

$$\kappa_K = \frac{1}{3} \int \hbar\omega\tau_{\mathbf{q}}c_{\mathbf{q}}^2 \frac{\partial n_{\mathbf{q}}^0}{\partial T} d\mathbf{q} \quad (1.51)$$

$$\kappa_C = \frac{1}{3} \frac{\left( \int c_{\mathbf{q}}q \frac{\partial n_{\mathbf{q}}^0}{\partial T} d\mathbf{q} \right)^2}{\int \frac{q^2}{\hbar\omega} \frac{1}{\tau_{\mathbf{q}}} \frac{\partial n_{\mathbf{q}}^0}{\partial T} d\mathbf{q}}, \quad (1.52)$$

where it can be observed that in a similar way as found in the derivation from Guyer and Krumhansl, the kinetic term has a direct integral of the relaxation time while in the collective term the inverse appears. Notice that in the integrals of Eq. (1.51) and Eq. (1.52) the variables  $c$  and  $q$  denote the modulus of  $\mathbf{v}$  and  $\mathbf{q}$ , and have been derived assuming isotropic media. In **Section 2.4** these expressions will be generalized for all systems.

It is important to notice that, although the KCM uses relaxation times obtained assuming  $n_{\mathbf{q}'} = n_{\mathbf{q}'}^0$  and  $n_{\mathbf{q}''} = n_{\mathbf{q}''}^0$  as done in the RTA, the splitting of  $N$  and  $R$  processes in the scattering operator and the projections to higher order perturbations ( $|n_{2i}\rangle$ ) captures properly the anharmonic effects that contribute to thermal transport.

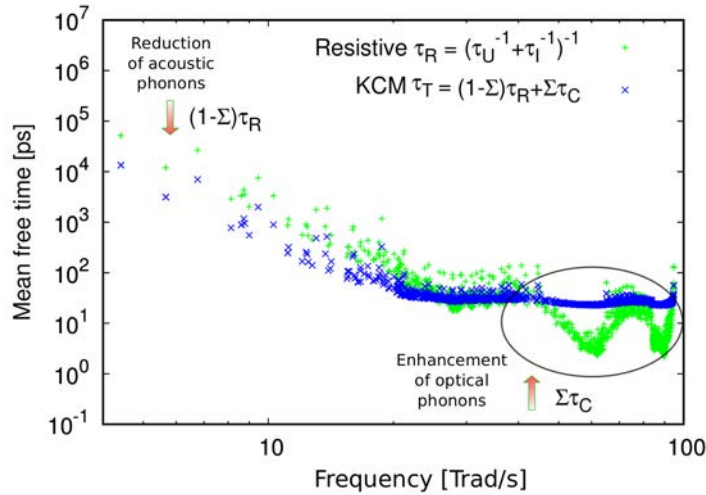


Figure 1.2: Resistive and total KCM relaxation times.

Fig. 1.2 shows the effect of  $N$  collisions in the resistive phonon distribution. It can be observed the effect of  $N$  scattering in the MFT through  $\Sigma$ ; reduces the contribution to the total thermal conductivity of low frequency phonons (acoustic), while increasing it for the optical ones [2]. The reduction of the contribution of the low energy phonons has been introduced extensively by including the  $N$

scattering as a resistive process, as done in the classical RTA. This widely known wrong assumption [20] can lead good results when collective effects are not important and high frequency phonons do not contribute significantly to thermal resistance, but can lead to physical misrepresentations. For that reason is more appropriate to use better approaches like full solutions or KCM, where the change in the relaxation times due to  $N$  scattering has a more suitable entropic interpretation.

### 1.3 Thermal transport beyond Fourier

It has been observed in recent experiments using fast or large gradient excitations at micro/nano scale that not all thermal transport can be explained by the Fourier law [4, 5, 6, 7, 8, 9, 10].

Diffusive transport is valid when the mean free path (MFP) is significantly shorter than the characteristic length of the sample. In this description it is assumed that phonons suffer enough scattering to be considered as moving in Brownian motion. When the sample under study has a size much smaller than the phonon MFP, phonons travel through the sample without suffering any scattering event. This process is known as ballistic transport and in such circumstances the measured thermal conductivity is smaller than the bulk one due to the reduced  $\tau_q$  (see Eqs. (1.51)-(1.52)), in contrast of what would be expected from electronic ballistic transport theory. Due to the large range of time and space scales that spans the relaxation of phonons there is a transition range between pure diffusive and ballistic transport where part of the phonons still suffer scattering while others remain traveling ballistically. These different transport regimes can be observed in Fig. 1.3.

From the kinetic point of view, phonon transport phenomena is based on considering that phonons are independent. From this point of view it is logical to think that non-local transport can be obtained by adding the different contribution of diffusive and ballistic particles depending on the sample scale. Despite of this, recent experiments performed in transient regimes by means of Time Domain Thermoreflectance (TDTR) have revealed that dynamics of energy transport in actual materials is much more complex than this. Conservation laws and thermodynamic constraints should be included in the picture. Their effect is to modify the relaxation processes of individual phonons in a way that they are no longer independent. In these circumstances it is expected that memory and non-local effects can be observed. Phonon hydrodynamics through the Kinetic Collective Model (KCM) [27] and superdiffusivity through Truncated Lévy Flights (TLF) [28] have been two models proposed to understand this transition.

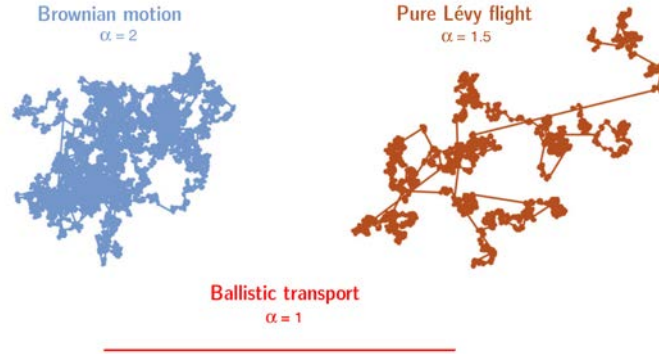


Figure 1.3: Sketch of Brownian motion, Lévy flight and ballistic transport [29].

### 1.3.1 Kinetic models and conservation laws

Solving the BTE in a non-homogeneous situation is a very difficult task. The problems of diagonalizing the collision term discussed in the previous sections are added to the problem that each point of the sample can have different temperature and heat flux. This makes that problem impossible to solve exactly and the use of approximate methods becomes necessary.

By using a kinetic model an approximate solution can be obtained by solving on a frequency basis the LBTE and then calculating the contribution of each mode. But to have a chance to solve it, a simplification of the collision term should be used. In the RTA approximation the LBTE takes the form

$$\frac{dn(\omega, x, t)}{dt} + v_\omega \cdot \nabla n(\omega, x, t) = -\frac{n(\omega, x, t) - n_0(\omega)}{\tau_\omega}. \quad (1.53)$$

The problem with Eq. (1.53) is that the relaxation times  $\tau_\omega$  used are obtained under the simplification approach of linealization and phenomenological diagonalization without taking the energy and momentum conservation laws under consideration. Letting the different modes evolve independently as the kinetic assumption states, these conservation laws are not guaranteed.

Additionally, the energy conservation is present in all type of collisions (impurities, boundaries, anharmonicities,...), and the momentum conservation is only present in the case of  $N$  collisions. When  $N$  collisions are relevant, both conservation laws should be imposed.<sup>1</sup>

<sup>1</sup>At this point we stress the use of the word relevant, and not dominant. With this we indicate that momentum conservation should be included whenever  $N$  collisions have an effect and not only when they dominate the transport.

In the work done by Collins *et al.* [30] Eq. (1.53) is combined with the conservation of energy

$$\int \int n_0 d\omega d\mu = \int \int n d\omega d\mu , \quad (1.54)$$

where  $\mu = \cos\theta$ . Eq. (1.54) states that the amount of energy stored in the non-equilibrium distribution function should be the same as that of the relaxed distribution.

Notice that Eq. (1.54) is a global constraint on the phonon individual transport. This means that each phonon is effectively influenced by the rest of the distribution function in a collective way. The inclusion of the energy conservation changes the contribution of the different modes in the conductivity that can be calculated as a suppression function acting on the bulk values.

The full solution of LBTE includes  $N$  scattering inside the relaxation times, but detailed calculations of their effects in terms of position and time are lost in current solutions based on direct diagonalization or iteration. In contrast, although by using the RTA the conservation laws are not satisfied, approximate results can be obtained. If energy and momentum conservation laws are imposed in a more rigorous way as done in the KCM formalism better results can be achieved.

The complexity of having a new equation for the momentum should be balanced by a different simplification. This is done by analyzing the possible forms of the distribution function. In a kinetic model, the distribution function can take an arbitrary complexity because the modes behave independently. In the KCM, the distribution function is a combination of only two different moments, the zero-order and the first-order moment. Moments of higher order than one are assumed to be non-observable because all the collisions (even  $N$  collisions) destroy them. This makes that the complexity of the LBTE can be extraordinarily reduced. The final combination makes the KCM a better approach in non-homogeneous situations.

When the LBTE is solved in the presence of boundaries, conservation laws also have an important role. When  $N$  collisions are important, the effect of the boundary on a specific mode is noticed on the rest of the modes. In kinetic models, the Fuchs-Sondheimer approach [31] has been widely used to include the effect of the boundaries [30]. But once again, this is done on an independent mode basis and the results can be significantly improved by KCM considering the momentum conservation in a rigorous way.

### 1.3.2 Memory and non-local effects

The inclusion of momentum conservation can be generalized to any order. The Extended Irreversible Thermodynamics (EIT) formalism [32] shows the path to this generalization of transport equations. In Fourier diffusive transport, the heat transport and the thermal energy are related by

$$\mathbf{Q}(\mathbf{r}, t) = -\kappa \nabla T . \quad (1.55)$$

When thermal transport is evaluated at times or sizes of the order of the MFT or MFP of the heat carriers, the previous relation is no longer valid. In such situations there appear non-local phenomena where the heat flux in one point at a certain time depends on the heat flux of its surroundings and at earlier times. These are known as spatial and temporal memory effects.

In last decades D. Jou *et al.* have developed a full framework to deal with thermal transport in the presence of non-local and memory effects viewpoint [16, 17, 33]. From the EIT the evolution equations of the heat transport can be expressed at different moment orders [16, 32, 34]:

$$\dot{e} = -\nabla \mathbf{Q}^{(1)} , \quad (1.56)$$

$$\tau \dot{\mathbf{Q}}^{(1)} + \mathbf{Q}^{(1)} = -\kappa \nabla T + \nabla \cdot \mathbf{Q}^{(2)} , \quad (1.57)$$

$$\tau_{(2)} \dot{\mathbf{Q}}^{(2)} + \mathbf{Q}^{(2)} = -\ell_{(2)}^2 \nabla \mathbf{Q}^{(1)} + \nabla \cdot \mathbf{Q}^{(3)} , \quad (1.58)$$

$$\tau_{(3)} \dot{\mathbf{Q}}^{(3)} + \mathbf{Q}^{(3)} = -\ell_{(3)}^2 \nabla \mathbf{Q}^{(2)} , \quad (1.59)$$

where  $e$  is the internal energy,  $\mathbf{Q}^{(1)} = \mathbf{Q}$  is heat flux,  $\mathbf{Q}^{(2)}$  the flux of the heat flux, and  $\mathbf{Q}^{(3)}$  represents a higher order flux. The parameters  $\ell_{(i)}$  and  $\tau_{(i)}$  correspond to different order characteristic lengths and relaxation times.

### 1.3.3 Phonon hydrodynamics

Reducing the second moment equation, Eq. (1.57), to the first moment equation, Eq. (1.58), for  $\dot{\mathbf{Q}}^{(2)} = 0$  and  $\mathbf{Q}^{(3)} = 0$  one obtains:

$$\tau \dot{\mathbf{Q}}^{(1)} + \mathbf{Q}^{(1)} = -\kappa \nabla T + \ell_{(2)}^2 (\nabla^2 \mathbf{Q}^{(1)} + 2\nabla \nabla \cdot \mathbf{Q}^{(1)}) . \quad (1.60)$$

This is a general hydrodynamic heat flux equation that includes memory (time derivative term) and non-local effects (laplacian term). This equation can be derived as well from the Guyer and Krumhansl solution of the BTE [15]. This is not strange as both formalisms are developed in the basis of moments.

Considering steady state  $\dot{\mathbf{Q}} = 0$ , strong geometric effects (spatial variations of  $\mathbf{Q}$  are higher than  $\mathbf{Q}$  itself)  $\mathbf{Q} \ll \ell^2 \nabla^2 \mathbf{Q}$ , and neglecting the term  $2\nabla \nabla \cdot \mathbf{Q}^{(1)}$ ,

Eq. (1.60) reduces to  $\nabla^2 \mathbf{Q} = \kappa_0 / \ell^2 \nabla T$ . The latter expression is analogous to Navier-Stokes equation doing the analogy  $\mathbf{Q} \Leftrightarrow \mathbf{v}$ ,  $T \Leftrightarrow p$  and  $\eta \Leftrightarrow \ell^2 / \kappa_0$ , where  $\mathbf{v}$  is the velocity,  $p$  the pressure and  $\eta$  the shear viscosity. This analogy is the responsible of the emergence of the so-called *phonon hydrodynamics*. For simplicity  $\ell_{(2)} = \ell$ . The solution of Eq. (1.60) under these circumstances for a cylindrical geometry leads to a parabolic profile for the cross section flux:

$$Q(r) = \frac{\kappa_0 \Delta T}{4\ell^2 L} (R^2 - r^2), \quad (1.61)$$

which integration with non-slip conditions ( $\mathbf{v} = 0$ , i.e. zero tangential flux on the wall) leads the Poiseuille-like equation for the heat flow:

$$Q^{(h)} = \frac{\kappa_0 \pi R^4 \Delta T}{8\ell^2 L}. \quad (1.62)$$

Eq. (1.62) allows defining an effective thermal conductivity as:

$$\kappa_{\text{eff}} = \frac{\kappa_0 R^2}{8\ell^2} = \frac{\kappa_0}{8\text{Kn}^2}, \quad (1.63)$$

where  $\text{Kn} = \ell/R$  is the Knudsen number.  $R$  and  $L$  are the radius and length of the sample. Notice that this expression has been derived in analogy to the flow in a pipe, then it is only valid for cylindrical geometries, i.e. wires. The dependence of  $\kappa_{\text{eff}} \propto R^2$  is a result of imposing non-slip condition at the walls. This is in contrast to experimental results where  $\kappa_{\text{eff}} \propto R$  for small samples, where  $R \ll \ell$ . This effect can be captured by including a slip boundary condition. A simple way to include a slip condition in the boundaries to account for roughness effects is by using a boundary condition like

$$Q_B = C\ell \left( \frac{\partial Q}{\partial r} \right)_{r=R}, \quad (1.64)$$

where  $C$  is a parameter that might depend on the geometry and the roughness (Maxwell boundary condition), related to the reflectivity and the diffusivity of the surface. Following the previous analogy with hydrodynamics, the effective thermal conductivity with slip boundary conduction leads to [17]:

$$\kappa_{\text{eff}} = \frac{\kappa_0}{8\text{Kn}^2} [1 + 4C\text{Kn}]. \quad (1.65)$$

The same derivation for a thin film gives:

$$\kappa_{\text{eff}} = \frac{\kappa_0}{12\text{Kn}^2} [1 + 6C\text{Kn}]. \quad (1.66)$$

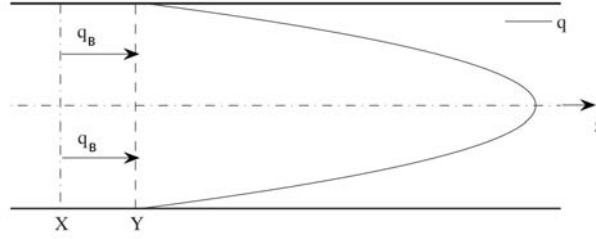


Figure 1.4: Heat flux profile with slip boundary condition [34].

It can be noticed that now, for small samples where  $R \ll \ell$ ,  $\text{Kn} \ll 1$ , Eq. (1.65) and Eq. (1.66) lead to a linear dependence of  $R$  on the thermal conductivity. When the size of the sample ( $L$ ) is smaller than the phonon characteristic length ( $\ell$ ), the effect of the boundary is not felt just in a small region close to the surface (Knudsen layer  $\sim \ell$ ), but it can have influence on the whole sample. In this situation, due to the linearity of the heat flux equations (Eq. (1.60) and Eq. (1.64)), it can be assumed that the local longitudinal heat flux is  $Q(r) = Q(r) + Q_B$ .

Fig. 1.4 shows how the addition of a slip boundary condition like Eq. (1.64) provides a non-zero flux on the walls in a certain  $X - Y$  region.

The previous developments open the door to a new way to study heat flux from a hydrodynamic framework from Eq. (1.60), and through the use of suitable boundary conditions  $Q_B$ .

### 1.3.4 Non-local effects in the KCM

The heat flux equations in the KCM leads to a generalization of Fourier's law including non-local terms. The KCM is derived up to 2nd-moment of the distribution function following the solution of the BTE proposed by Guyer and Krumhansl (Eq. (1.30)). This expansion allows, additionally, to fulfill the momentum conservation for  $N$  processes. Doing so, hydrodynamic effects appear due to the reduction of the 2nd-moment equation into the 1st order moment, leading consequently to a generalized set of equations suitable for heat transport calculations at the micro/nanoscale. These effects in the KCM framework can be reproduced in a kinetic-collective approach or full hydrodynamic model, as detailed in **Chapter 4**.

From Guyer and Krumhansl, heat transport equations for each transport regime, kinetic and collective, can be derived. To do that it is necessary to recover the terms  $D_{12} = D_{21}$  from the drift operator (see Eq. (1.30)) [15]. The derivation is done for an isotropic system. To study both regimes can be defined the lim-



iting cases  $\mathbf{R}^* \gg \mathbf{N}^*$  (kinetic regime) and  $\mathbf{N}^* \gg \mathbf{R}^*$  (collective regime). The momentum conservation equation in the kinetic case leads to:

$$\begin{aligned} \mathbf{a}_1 &= \langle 1 | \mathbf{R}^{*-1} | 1 \rangle D_{10} (1 + O(\mathbf{D}) + \dots) a_0 \rightarrow \\ \mathbf{Q} &= -\frac{1}{3} C_v c^2 \tau_K (1 + O(\mathbf{D}) + \dots) \nabla T . \end{aligned} \quad (1.67)$$

In the collective regime, where  $\mathbf{N}^* \gg \mathbf{R}^*$  :

$$\begin{aligned} R_{11}^* \mathbf{a}_1 &= D_{10} a_0 + (\mathbf{D} \mathbf{N}^{*-1} \mathbf{D}) \mathbf{a}_1 + \dots \rightarrow \\ \mathbf{Q} &= -\frac{1}{3} C_v c^2 \tau_C \nabla T + \tau_C \langle 1 | c \nabla \mathbf{N}^{*-1} c \nabla | 1 \rangle \mathbf{Q} + \dots . \end{aligned} \quad (1.68)$$

From the latter equations, the first order heat transport in each transport regime can be expressed as:

$$\mathbf{Q} = -\hat{\kappa}_K \nabla T , \quad (1.69)$$

that is the Fourier law, valid for the kinetic regime, where the boundary effects are simply included in  $\tau_K$  as a Matthiessen's rule, and

$$\tau \frac{d\mathbf{Q}}{dt} + \mathbf{Q} = -\hat{\kappa}_C \nabla T + \hat{\ell}_C^2 (\nabla^2 + 2\nabla \nabla \cdot) \mathbf{Q} \quad (1.70)$$

defines a hydrodynamic heat flux equation in the collective regime, where  $\hat{\ell}_C^2 = \langle c^2 \tau_N \rangle \langle \tau_C \rangle / 5$  in the isotropic case.

If higher orders are considered when  $\mathbf{R}^* \gg \mathbf{N}^*$ , momentum conservation can be expressed as:

$$\mathbf{Q} = -\frac{1}{3} C_v c^2 \tau_K \nabla T + \tau_K \langle 1 | c \nabla \mathbf{R}^{*-1} c \nabla | 1 \rangle \mathbf{Q} + \dots , \quad (1.71)$$

and therefore:

$$\mathbf{Q} = -\hat{\kappa}_K \nabla T + \hat{\ell}_K^2 (\nabla^2 + 2\nabla \nabla \cdot) \mathbf{Q} , \quad (1.72)$$

where  $\hat{\ell}_K^2 = \langle c^2 \tau_R \rangle \langle \tau_R \rangle / 5$  in the isotropic case. Eq. (1.72) for kinetic thermal transport can be obtained as well through gray medium models, where the crystal is idealized by a single phonon relaxation time and MFP.

A simple 1D analysis of a two phonon channel of the BTE leads to a heat transport solution that includes non-local effects [28, 29]. Here it is analyzed the single pulse response  $P(\xi, s)$  in the Fourier-Laplace domain of  $P(x, t)$ . Using as a starting premise a low frequency channel (1), that governs the thermal conductivity  $\kappa_0$ , and a high frequency one (2), which governs the heat capacity  $C_v$ , and considering large time scales compared to the phonon MFT  $|s| \tau_{1,2} \ll 1$ :

$$P(\xi, s) \simeq \left[ s + \frac{D_0 \xi^2}{1 + \xi^2 \Lambda_{(1)}^2} \right]^{-1}, \quad (1.73)$$

where  $\Lambda_{(1)}$  corresponds to the MFP of the low frequency phonon, and  $D_0$  is the thermal diffusivity. The inverse Fourier transformation of Eq. (1.73) imposing the initial condition  $P(\xi, t = 0) = 1$  leads to:

$$\left( 1 - \Lambda_{(1)}^2 \frac{\partial^2}{\partial x^2} \right) \frac{\partial P(x, t)}{\partial t} = -D_0 \frac{\partial^2 P(x, t)}{\partial x^2}. \quad (1.74)$$

Using the energy conservation relation  $\partial Q(x, t)/\partial x + \partial P(x, t)/\partial t = \delta(x)\delta(t)$ , and knowing that (from the starting premise)  $P \simeq C_{v,(2)}\Delta T$  and  $\kappa_0 \simeq C_{v,(2)}D_0$ :

$$Q(x, t) - \Lambda_{(1)}^2 \frac{\partial^2 Q(x, t)}{\partial x^2} = -\kappa_0 \frac{\partial \Delta T(x, t)}{\partial x}, \text{ for } t \gg \tau. \quad (1.75)$$

From this derivation it is clear the analogy between Eq. (1.72) and Eq. (1.75) obtained from the two different approaches.

### 1.3.5 Superdiffusive transport

Steady state thermal conductivity of several pure group IV semiconductors with weak  $N$  scattering processes can be explained properly from a pure diffusive kinetic model. In contrast, experimental transient measurements have shown that semiconductor alloys can exhibit a great frequency dependence when heated from an alternate current source with a modulated frequency [29]. Through this procedure phonons of different energy can be excited independently at time scales  $\tau_{\text{mod}}$  of the order of the phonon MFT and new phenomena can be studied. This kind of experiments has revealed that in alloys quasiballistic transport is present at certain time scales that can span several orders of magnitude. In addition, this superdiffusive regime can be also observed when the length scales of the sample are comparable to the phonon MFP. These phenomena can be studied by means TDTR imaging, which is able to capture the temporal and spatial response of energy impulses in the cross-plane direction of a sample.

The Maxwell-Cattaneo equation is usually used to describe ballistic to diffusive transition:

$$\tau \frac{\partial^2 T}{\partial t^2} + \frac{\partial T}{\partial t} = \chi \nabla^2 T, \quad (1.76)$$

which gives temperature  $T$  in terms of time  $t$ , where  $\tau$  is the MFT of phonons and  $\chi$  is the thermal diffusivity of the sample. In the diffusive regime  $\tau \frac{\partial^2 T}{\partial t^2} \ll \frac{\partial T}{\partial t}$  and the diffusion equation is recovered. When the inertial terms are important  $\tau \frac{\partial^2 T}{\partial t^2} \gg \frac{\partial T}{\partial t}$  and the wave equation is obtained. Eq. (1.76) assumes that the

transition from diffusive to ballistic transport occurs at the same time for all the phonons. This assumption is far from reality. The MFP or MFT spectral representations of thermal conductivity reveals that each phonon has its own MFP and MFT [3]. A correct treatment in this case would be to solve Eq. (1.76) for each mode, but the number of calculations will increase excessively. A more suitable way to study this transition is the TLF model.

### Ballistic transport

As it has been introduced, when phonons travel ballistically, there are no scattering events and thus these phonons do not contribute to thermal resistivity as expected from a diffusive framework. In this situation, the contribution to thermal conductivity of each ballistic phonon  $\kappa_{\mathbf{q}}(\Lambda_{\mathbf{q}}) = C_{v,\mathbf{q}}\Lambda_{\mathbf{q}}v_{\mathbf{q}}$  will be limited for the sample size, and then the contribution will be  $\kappa_{\mathbf{q}}(L_{\text{eff}}) = C_{v,\mathbf{q}}L_{\text{eff}}v_{\mathbf{q}}$ . As in ballistic transport  $L_{\text{eff}} < \Lambda_{\mathbf{q}}$ , the measured thermal conductivity will be smaller than the intrinsic one ( $\kappa_{\mathbf{q}}(L_{\text{eff}}) < \kappa_{\mathbf{q}}(\Lambda_{\mathbf{q}})$ ).

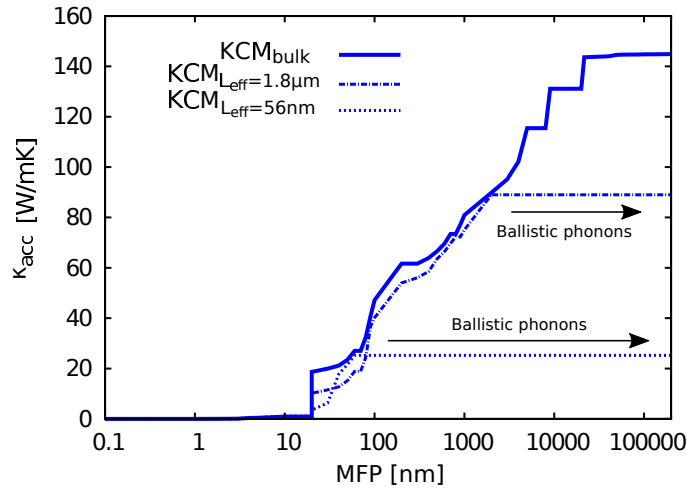


Figure 1.5: Accumulated thermal conductivity as a function of mean free path (MFP) for silicon samples with different size  $L_{\text{eff}}$ .

Fig. 1.5 shows the accumulated thermal conductivity for bulk silicon ( $L_{\text{eff}} = \infty$ ), 830 nm thin film and 56 nm nanowire in the KCM. As will be shown in **Section 2.3.4**, the effective length for a thin film is  $L_{\text{eff}} = 2.25h$ , then in this case  $L_{\text{eff}} = 1.8 \mu\text{m}$ . It can be observed that the phonons with a MFP larger than  $L_{\text{eff}}$  travel ballistically through the sample and do not contribute to thermal conductivity.

### The Truncated Lévy Flight model

The TLF is the generalization of the kinetic transport taking into account that energy carriers are not independent but related by the energy conservation. This, in combination with the large range of carriers MFP/MFT, defines the transition from a pure superdiffusive Lévy regime to a regular diffusion one. In TLF, the effect of different time scales is captured by quantifying the deviation from the diffusive behavior at short time scales using a fractal exponential ( $\alpha$ ) that captures the scaling of the mean-square displacement (MSD) of the thermal energy with time [11]. The diffusive to ballistic transition is described by using calculated parameters from the scaling law of the accumulated thermal conductivity in terms of MFP [28].

Anomalous behavior of the heat transport equation can be generalized in the fractional dimension defined by the TLF model [35]. The relation between heat flux and thermal energy including memory and non-local effects in 1D can be expressed with fractional integro-differentiation operators as:

$$\frac{\partial^\beta P(x, t)}{\partial t^\beta} = D_{\alpha\beta} \frac{\partial^\alpha P(x, t)}{\partial |x|^\alpha}, \quad (1.77)$$

where  $P(x, t)$  denotes the thermal energy density (single pulse response in the real space), which in a pure diffusive regime is  $P_0(x, t) = C_{v,0}T$ , being  $C_{v,0}$  the specific heat and  $T$  the temperature.  $\alpha$  and  $\beta$  are the fractal space and time dimensions of the superdiffusion transport regime respectively.

In alloys like SiGe or InGaAs it has been observed a reduction of the thermal conductivity up to a 50% in a frequency from 1-10 MHz [28]. This reduction is due to the presence of phonons with MFP larger than the thermal penetration length ( $d = \sqrt{\kappa/\pi C_v f}$ ) of the heat source. The superdiffusive Lévy regime defined in such situations can be expressed by a superlinear time evolution of the MSD  $\sigma(t) \sim t^\beta$  ( $1 < \beta < 2$ ) in a transport space with fractal dimension  $\alpha$  ( $1 < \alpha < 2$ ), where  $\beta = 3 - \alpha$ . The Brownian motion corresponds to a stochastic process with fractal dimension  $\alpha = 2$ , while the fractal dimension that governs the transport in a ballistic regime is  $\alpha = 1$ .

A direct way to interpret the  $\alpha$  and  $\beta$  parameters is through the accumulated thermal conductivity function. Its shape as a function of the MFP and MFT can be directly related to the fractal exponents knowing that  $\kappa(\Lambda, \tau) \sim (\Lambda, \tau)^\gamma$ , where  $\gamma = 2 - \alpha$ .

The TLF model is studied from the response  $P$  of a single pulse on a sample that obeys the BTE under RTA. This response analyzed in the Fourier-Laplace domain, with  $\xi$  and  $s$  being the spacial and temporal transformed variables, takes the form:

$$P(\xi, s) = \frac{\sum_{\mathbf{q}} C_{v,\mathbf{q}} \Psi_{\mathbf{q}}(\xi, s)}{\sum_{\mathbf{q}} \frac{C_{v,\mathbf{q}}}{\tau_{\mathbf{q}}} [1 - \Psi_{\mathbf{q}}(\xi, s)]}, \quad (1.78)$$

where

$$\Psi_{\mathbf{q}}(\xi, s) = \frac{1 + s\tau_{\mathbf{q}}}{(1 + s\tau_{\mathbf{q}})^2 + \xi^2 \Lambda_{\mathbf{q}}^2}. \quad (1.79)$$

The single pulse response can be understood in the Fourier-Laplace domain as  $P(\xi, s) = C\delta T(\xi, s)$ , where  $C$  is the total specific heat. From this, the MSD of the thermal energy is  $\sigma^2 = -\partial^2 P(\xi, s)/\partial \xi^2$  at  $\xi = 0$ . This magnitude provides the average spatial extent of the thermal field, equivalent to the thermal penetration length in a diffusive regime. When the temporal scale of the heating source is much faster than the phonon relaxation time ( $s \rightarrow \infty$ ) the MSD is  $\sigma^2(t) = \bar{v}^2 t^2$ , where  $\bar{v}$  is a mean phonon velocity. This limit represents the ballistic regime. On the other hand, when the temporal scales are slow compared with  $\tau$ , the phonons can scatter and a diffusive regime with  $\sigma^2(t) = 2Dt$  is recovered. Notice that in the diffusive regime the distribution tends to a Gaussian energy density with variance  $2Dt$ , while in the ballistic limit tends to a Lorentzian. The transition between both regimes is smooth for materials like silicon, while for alloys, where transport is dominated by independent collisions with alloying atoms, this transition have a definite slope that scales as  $\sigma^2 \sim t^\beta$ . The energy transport in such situation, known as Lévy stable process, is stochastically equivalent to a random walk with fractal dimension  $\alpha < 2$ . The pulse response in this intermediate region can be expressed as  $P(\xi, s) \simeq 1/(s + D_\alpha |\xi|^\alpha)$ , where  $D_\alpha$  is a fractional diffusivity. If this response is reexpressed as  $P(\xi, s) \simeq [s + \psi(\xi)]^{-1}$ , in the limit  $s \rightarrow 0$ :

$$\psi(\xi) = \xi^2 \frac{\sum_{\mathbf{q}} \frac{C_{v,\mathbf{q}} \Lambda_{\mathbf{q}}^2}{\tau_{\mathbf{q}} [1 + \xi^2 \Lambda_{\mathbf{q}}^2]}}{\sum_{\mathbf{q}} \frac{C_{v,\mathbf{q}}}{1 + \xi^2 \Lambda_{\mathbf{q}}^2}}, \quad (1.80)$$

where  $\psi(\xi)/\xi^2$  represents the spacial evolution of the fractal diffusivity  $D_\alpha$ . The thermal conductivity can be expressed equivalently as:

$$\kappa(\xi, s) = \sum_{\mathbf{q}} C_{v,\mathbf{q}} \frac{\sum_{\mathbf{q}} \frac{\kappa_{\mathbf{q}}}{1 + \xi^2 \Lambda_{\mathbf{q}}^2}}{\sum_{\mathbf{q}} \frac{C_{v,\mathbf{q}}}{1 + \xi^2 \Lambda_{\mathbf{q}}^2}}. \quad (1.81)$$

Fig. 1.6 represents the temporal evolution of the heat transport through the normalized MSD. A superdiffusive regime governed by a fractal exponent can be appreciated. In the time space, there is a transition from a ballistic regime at very small times ( $t < 10^{-12}$  s), where  $\sigma^2 \sim t^2$ , to a diffusive regime  $\sigma^2 \sim t$  for  $t > 10^{-8}$  s. In InGaAs and SiGe, this transition can be expressed by  $\sigma^2 \sim t^\beta$ ,

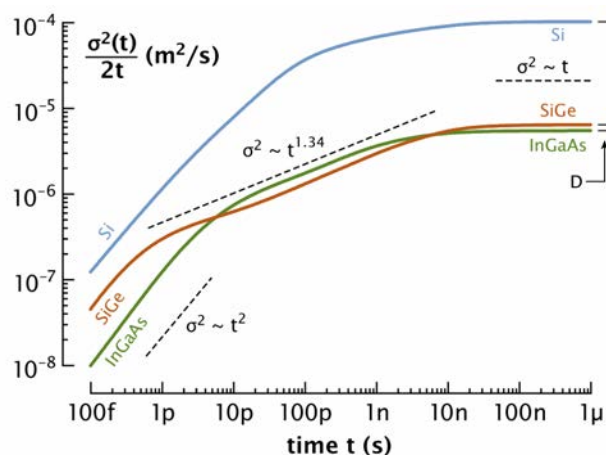


Figure 1.6: Renormalized mean squared displacement (MSD) obtained from the BTE for Si, SiGe and InGaAs [28].

while in Si there is a smooth transition. The lack of a definite slope for the case of silicon and the relation of the fractal exponents to the dominant scattering mechanism will be discussed in **Section 5.2** in the KCM framework. From a general point of view, it can be observed that in the diffusive limit  $\alpha \rightarrow 2$  and  $\beta \rightarrow 1$ , while in the ballistic limit  $\alpha \rightarrow 1$  and  $\beta \rightarrow 2$ .

In **Section 6.4** non-local effects will be analyzed, which in modified Fourier models as well as in the TLF are included as extra term that contributes as a thermal boundary resistivity (TBR) in the interface between the heating metal contact and the semiconductor sample  $r_{ms}$ .

## 1.4 Thermal boundary resistance

In a sample composed of two or more layers of different materials in contact there appears a mismatching between the different crystalline structures. This is a typical case in samples heated through a metallic contact. If heat flows through the interface, the incoming flux is reduced due to a resistance induced by the crystalline mismatch. This is known as Kapitza resistance or TBR. This effect has been widely studied in recent years from frequency dependent measurements of thermal conductivity [8, 11].

From an effective Fourier model it is required to change the value of  $r_{ms}$  for each pump modulation frequency in order to fit the experimental data of TDTR experiments [8]. On contrary, the TLF, which properly distinguishes interfacial dynamics from nearby quasiballistic heat flow suppression, is able to reproduce the experimental data with a single value of TBR [11].

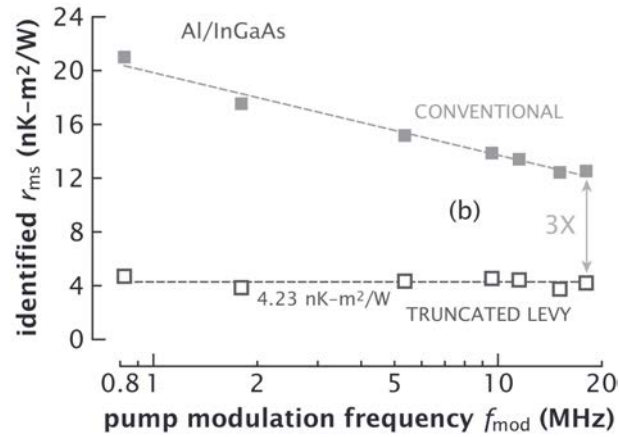


Figure 1.7: Frequency dependence of thermal boundary resistance (TBR)  $r_{\text{ms}}$  from TDTR experiments and comparison to a conventional (Fourier) and TLF model at room temperature [11].

In Fig. 1.7 the TBR from a conventional (Fourier) and TLF model is represented. It can be observed that for the Al/InGaAs interface, the  $r_{\text{ms}}$  value depends strongly on the modulation frequency when studied from a Fourier standpoint. This has been also reported for the Al/Si interface for instance [8]. In contrast, when using the TLF model, the TBR effects can be interpreted with a single value  $r_{\text{ms}} = 4.23 \text{ nK-m}^2/\text{W}$ .

As mentioned in the previous section, the effects of TBR will be discussed in **Section 6.4**.

## 1.5 Thermal measurements

All the theoretical models explained above to study thermal conductivity are developed in order to understand experimental evidence. For this suitable ways to determine experimentally the thermal conductivity and other thermal properties become also necessary. The easiest and oldest way to measure the thermal conductivity of a sample is to impose a constant heat flux, which will create a thermal gradient on the sample. Then measuring the variation of the temperature as a function of the heat flux and applying the Fourier law ( $\mathbf{Q} = -\kappa \nabla T$ ), the thermal conductivity can be obtained. This kind of measurement can be used in steady state and small temperature gradients, so thermal conductivity can be treated as a constant value. Actually, thermal conductivity varies with the temperature and can also vary with the frequency and orientation of the applied thermal gradient, so this expression is restricted to few situations. To account for different crystal orientations tensor expressions are required. In addition, thermal conductivity

measurement through this procedure introduces an error due to heat losses by blackbody radiation [36].

Recently, improved and more accurate measurement techniques have appeared, like the  $3\omega$  method [37] or time/frequency domain ultrafast spectroscopies [38]. In this group, TDTR have emerged as a powerful tool to measure the thermal conductivity as a function of time for samples in complex geometries.

### 1.5.1 $3\omega$ method

The  $3\omega$  method is a thermal conductivity measurement technique based on the measure of the third harmonic of an alternate voltage from an AC frequency signal  $\omega$  applied on a sample ( $I = I_0 \sin \omega t$ ). This electric current creates a temperature fluctuation on the sample that leads to a voltage fluctuation response. This response is directly related to thermal conductivity through [37]:

$$V_{3\omega} \approx \frac{\sqrt{2} I^3 R R' L}{\pi^4 \kappa S}, \quad (1.82)$$

where  $L$  and  $S$  are the length and the cross section of the sample, and the electrical resistance is given by  $R = R_0 + R'(T - T_0)$ .  $R'(T) = \partial R / \partial T$  and  $\kappa$  is the thermal conductivity of the sample.

This technique reduces the error produced by infrared radiation, specially for small samples below  $10^{-4}$  m [39]. Therefore  $3\omega$  method is a useful tool for thermal conductivity measurements of thin films and nanowires [37].

### 1.5.2 Time/frequency domain thermo-reflectance

TDTR has become one of the conventional techniques to characterize the thermal properties of thin film materials [38]. TDTR is a contactless optical pump-probe based on heating the sample using pulsed laser (pump signal) of frequency  $f_{\text{mod}}$  (typically  $f_{\text{mod}} \sim 10$  MHz). The beam heats a metal transducer deposited in the sample, and the diffusion of this heat along the sample is directly related to its thermal conductivity. The reflectivity of the sample is also affected by the temperature, then a delayed laser probe signal measures the change of thermorefectance, proportional to the transient thermal decay of the sample with picosecond resolution. By modulating the pump signal using electro-optic modulator (EOM), the thermal penetration depth  $d = \sqrt{D / (\pi f_{\text{mod}})}$  can be changed, where  $D$  is the thermal diffusivity. The signal is detected using a lock-in amplifier tuned to the modulation frequency. The characteristic times measured with this technique are given by  $\tau_{\text{mod}} = 1 / (2\pi f_{\text{mod}})$ . Notice that the expression for



the thermal penetration length is based on Fourier heat equation and it may need to be revisited in non-Fourier transport regime.

This technique is also specially useful to measure the frequency-dependent thermal conductivity observed in some materials [38] as well as transient transport regimes [28].

In frequency domain methods (FDTR), instead of measuring the response between temporal delayed pump and probe signals, the response of different modulated frequency signals is measured. This procedure avoids possible mechanical motion between pump and probe signals in TDTR.

### 1.5.3 Phonon measurements

The most general ways used to measure phonon information are by inelastic neutron scattering and by Raman spectrometry. The former enables to measure the phonon dispersion relations of semiconductor materials. The latter is used for the measurement of phonon linewidth of individual zone-center phonons.

When a beam of neutrons interacts with a crystal it suffers a scattering process. In an inelastic collision, the energy and the momentum of the beam will change, therefore analyzing the outgoing beam information about the process occurred can be obtained. From the difference of energy and momentum the dispersion relations ( $\omega(\mathbf{q})$ ) can be obtained along certain high symmetry directions [40].

In Raman scattering light is used instead of neutrons. The incident beam is inelastically scattered by a surface and changes its polarization due to the creation or annihilation of vibrational modes. The energy conservation of the light will provide information of the process occurred. If the frequency is reduced a phonon is created or excited (Stokes process); on contrary, if it increases, a phonon is annihilated or relaxed (anti-Stokes process). From the line width of the intensity peaks at each frequency, the phonon lifetime ( $\tau$ ) can be obtained as the inverse of the full width at half maximum (FWHM). A drawback of this method is that only phonons of similar wave vector to that of the incoming beam will interact.

Another method to measure phonon lifetimes is by successive light pulses. A principal beam is focused to the sample while a small part of it is split. The split part is delayed a certain amount of time and then refocused to the principal beam. Once the principal beam interacts with the sample it creates a phonon excitation. These excited phonons will decay in a characteristic time  $\tau$ . The delayed beam when interacts with the surface with active phonon modes will suffer backscattering depending on that population. Therefore the intensity of this backscattering can be related with the number of active modes and its decay time can be estimated [41].

## 1.6 Thermoelectric properties

The thermal conductivity of bulk materials is key for the study of thermoelectric materials. A dimensionless parameter  $ZT$  known as figure of merit gives the capacity of a material to work as thermoelectric:

$$ZT = \frac{\sigma S^2 T}{\kappa_e + \kappa_L}, \quad (1.83)$$

where  $\sigma$  is the electric conductivity,  $S$  the Seebeck coefficient,  $T$  the temperature, and  $\kappa_e$  and  $\kappa_L$  the electronic and lattice (phononic) thermal conductivity respectively. The product  $\sigma S^2$  is also defined as the power factor. From this equation it is clear that the lower the thermal conductivity the higher the efficiency.

In addition to a proper knowledge of thermal properties, to finally determine the goodness of a material as a thermoelectric, other properties need to be calculated, all of them related to electronic properties. Although this is not the main topic of this work, a brief summary is done to establish a complete picture.

### 1.6.1 Electronic properties

It is well known that the main contribution of the thermal conductivity comes from phonon interactions, but in semiconductors with high level of doping, small band gap or metals, electrons can also have a large, or even predominant, contribution to heat transport. When this occurs there is a clear split of the total thermal conductivity in two terms  $\kappa = \kappa_L + \kappa_e$ . As a good approach, the Widemann-Franz law provides an empirical expression of the electronic contribution to thermal conductivity  $\kappa_e$  from the value of the electronic conductivity  $\sigma$ :

$$\kappa_e = LT\sigma, \quad (1.84)$$

where  $L$  is the Lorentz number and  $T$  the temperature. In most cases as a first approximation of such contribution  $L = 2.44 \cdot 10^{-8} \text{W}\Omega/\text{K}^{-2}$  is treated as a constant. This value might depend on scattering mechanisms, then more accurate results will require a deeper study of  $L$  depending on the material and the temperature.

A more accurate calculation of the electronic contribution to thermal conductivity from the BTE for electrons can be done by using [42]:

$$\kappa_{e,\alpha\beta} = \kappa_{\alpha\beta}^0 - T v_{\alpha j} (\sigma_e^{-1})_{lj} v_{l\beta}, \quad (1.85)$$

where

$$\kappa_{\alpha\beta}^0 = \frac{1}{e_c^2 T V} \int \sigma_{e,\alpha\beta}(E_e) \cdot (E_e - \mu)^2 \left[ -\frac{\partial f_{\mu}^0(T, E_e)}{\partial E_e} \right] dE_e. \quad (1.86)$$

$\alpha$  and  $\beta$  are Cartesian coordinates for the tensorial magnitudes.  $f_\mu^0(T, E_e)$  is the Fermi-Dirac distribution function, and  $(\sigma_e^{-1})_{lj}v_{l\beta} = S_{j\beta}$  is the Seebeck coefficient, being

$$v_{\alpha\beta} = \frac{1}{e_c TV} \int \sigma_{e,\alpha\beta}(E_e) \cdot (E_e - \mu) \left[ -\frac{\partial f_\mu^0(T, E_e)}{\partial E_e} \right] dE_e. \quad (1.87)$$

$e_c$  is the electron charge,  $\mu$  the chemical potential,  $E_e$  the total energy of electron,  $V$  the volume, and  $\sigma_{e,\alpha\beta}$  the electrical conductivity:

$$\sigma_{e,\alpha\beta} = \frac{1}{V} \int \sigma_{e,\alpha\beta}(E_e) \left[ -\frac{\partial f_\mu^0(T, E_e)}{\partial E_e} \right] dE_e, \quad (1.88)$$

where

$$\sigma_{e,\alpha\beta}(E_e) = \frac{1}{N} \sum_{i,\mathbf{k}} e_c^2 \tau_{e,i,\mathbf{k}} u_\alpha(i, \mathbf{k}) u_\beta(i, \mathbf{k}) \frac{\delta(E_e - E_{e,i,\mathbf{k}})}{dE_e}. \quad (1.89)$$

The subindex  $i$  refers to a band index, while  $\mathbf{k}$  is the electron wave vector. The phonon relaxation time  $\tau_e$  can be calculated from its scattering matrix in a similar way as can be done for phonons (see **Section 2.3.5**). A full description can be found elsewhere [19].

All the previous set of equations (Eq. (1.84)-Eq. (1.89)), together with the lattice contribution to thermal conductivity, allow the calculation of the figure of merit  $ZT$  of a thermoelectric material.

## 1.7 Note on phonon drag

In some circumstances, when electron-phonon interaction is important, the lattice vibrations can contribute to the electron movement in the crystal, increasing then the electric conductivity and therefore the Seebeck effect and the thermoelectric performance. The quasiparticle associated to a electron-phonon interaction is known as polaron. Phonon drag can be understood as a thermal flux originated from the balance of momentum added by electron-phonon interactions and destroyed by phonon-phonon processes [43].

Recently some efforts have been done in order to quantify the phonon drag contribution to the Seebeck coefficient [43]. A way to evaluate this effect is by comparing thermal measurements of bulk and nanowires of a material. As phonon drag is quenched by boundary scattering, a comparison of such measurements will allow quantifying its effect in bulk samples.

In a general case, the Seebeck coefficient defined from the Mott relations, can be split into a diffusion and a phonon drag term,  $S = S_{\text{diff}} + S_{\text{p-d}}$ . Solving

the BTE for electrons including electron-phonon interactions it is possible to find approximate expressions for both contributions [43]:

$$eTS_{\text{diff}} = \frac{\int_0^\infty \frac{\partial f_{\mathbf{k}}^0}{\partial E} \tau_{\mathbf{k},e} v_{\mathbf{q},x}^2 D(E) (E - E_F) dE}{\int_0^\infty \frac{\partial f_{\mathbf{k}}^0}{\partial E} \tau_{\mathbf{k},e} v_{\mathbf{q},x}^2 D(E) dE} = \langle E - E_F \rangle, \quad (1.90)$$

where  $D(E)$  is the electronic density of states,  $v_{\mathbf{q},x}$  the electron velocity and  $E_F$  the Fermi energy level. In this case it is assumed that phonons are in equilibrium ( $n_{\mathbf{q}} = n_{\mathbf{q}}^0$ ), and only electrons are out of equilibrium ( $f_{\mathbf{k}} = f_{\mathbf{k}}^0 + \frac{\partial f_{\mathbf{k}}^0}{\partial E} \Phi_e$ ), where  $\Phi_e \propto \mathbf{k}$  measures the deviation from equilibrium. In real processes, the electrons can receive momentum and relax through phonon-phonon interactions. In these cases, the phonon distribution is also displaced from equilibrium a certain magnitude  $\Phi_{ph} \propto \mathbf{q}$ , then  $n_{\mathbf{q}} = n_{\mathbf{q}}^0 - \frac{\partial n_{\mathbf{q}}^0}{\partial \epsilon} \Phi_{ph}$ . The contribution of the terms regarding  $\Phi_{ph}$  will thus provide the magnitude of the phonon drag:

$$eTS_{\text{p-d}} = \frac{\frac{1}{2k^3} \int_0^\infty \tau_e v_x^2 \frac{\partial f_0}{\partial E} D(E) dE \cdot \int_0^{2kc} \frac{\Lambda_{ph} C_v(\omega)}{\Lambda_{e-p} f_0(\omega/2c)} d\omega}{\int_0^\infty \tau_e v_x^2 \frac{\partial f_0}{\partial E} D(E) dE}, \quad (1.91)$$

where  $c$  is the phonon velocity,  $C_v(\omega)$  the mode specific heat,  $k = |\mathbf{k}|$ , and  $\Lambda_{ph}$  and  $\Lambda_{e-p}$  are the phonon and polaron MFT respectively. In the derivation of Eq. (1.91) it has been assumed that  $\Phi_{ph} \neq f(f)$ . This assumption is valid for weak electron-phonon interaction. For strong interactions there will appear couplings between  $f$  and  $n$  that will no longer allow splitting  $S$  into their two contributions.

Eq. (1.91), even though is an approximation, suggests that longer phonon MFP and shorter polaron MFP will contribute to improve the Seebeck effect.



# Chapter 2

## First principles calculations

Since the development of quantum mechanics, big efforts have been done in order to implement such knowledge for computational modeling. This has allowed predicting experimental results with an incredible accuracy.

In this work, quantum mechanics will allow calculating the total energy of a system with a certain amount of atoms through the corresponding Hamiltonian, and afterwards a wide range of properties related to this total energy.

*First principles* calculations only require to define the atoms, specifically their type and position. In this work a full *ab initio* framework [44] is used to compute the total energy of different systems in order to study thermal transport.

Large amount of systems can be modeled using *ab initio* techniques, but not all have the same computational cost. The number of atoms and the expected spatial variation of the wave functions are the main parameters that determine the simulation time.

### 2.1 Total energy calculations

*Ab initio* calculations start by calculating the total energy of the system. For that purpose, the so-called many-body problem consists in obtaining the total energy and forces on each atom of a system with many interacting electrons. Therefore, in order to compute the total energy it will be necessary to solve the Schrödinger equation:

$$\mathcal{H}\psi = E\psi \quad , \quad (2.1)$$

that relates the Hamiltonian  $\mathcal{H}$  of the solid applied on its wave function to the total energy  $E$ .

The general expression for a Hamiltonian  $\mathcal{H}$  under a constant external potential  $\phi_0$  is:

$$\mathcal{H} = \phi_0 + \mathcal{T} + \mathcal{H}_2 + \mathcal{H}_3 + \dots \quad , \quad (2.2)$$

where  $\mathcal{T}$  is the kinetic energy and  $\mathcal{H}_2 + \mathcal{H}_3 + \dots$  are  $n$ -body crystal interaction potential terms.  $\mathcal{H} = \mathcal{T} + \mathcal{H}_2$  is defined as the harmonic Hamiltonian, where  $\mathcal{T} = K_e + K_n$  is the sum of the kinetic energy operator of the electrons and the nucleus, and  $\mathcal{H}_2 = U_{e-e} + U_{e-n} + U_{n-n}$  give the potential energy for electron-electron, electron-nucleus and nucleus-nucleus interaction.

The high number of variables force the use of some approximations and simplifications to solve Eq. (2.1) [44, 45].

### 2.1.1 Born-Oppenheimer approximation

The Born-Oppenheimer approximation allows separating the electronic and nuclear contribution in the many-body wave function due to the large difference in their respective masses. Moreover, the fact that the forces acting on the particles are the same makes possible to consider a gas of electrons in movement in a static configuration of cores. Then,  $K_n$  and  $U_{n-n}$  are taken as parametrized magnitudes and the Hamiltonian is reduced to the electron kinetic energy and the electron-electron and electron-ion interaction:

$$\mathcal{H} = \mathcal{T} + U_{e-e} + U_{e-n}, \text{ where } \mathcal{T} = -\frac{\hbar^2}{2m} \nabla^2. \quad (2.3)$$

### 2.1.2 Hartree-Fock approximation

Under the Born-Oppenheimer approximation, the interaction potential  $\mathcal{H}_2$  can be written as a summation over all the electrons of the solid:

$$\mathcal{H}_2 = \sum_i [U(\mathbf{r}_i) + W_i(\mathbf{r}_i)], \quad (2.4)$$

where  $U(\mathbf{r}_i)$  is the potential energy by the nuclei felt by an electron at  $\mathbf{r}_i$ , and  $W_i(\mathbf{r}_i)$  the interaction potential with the field created by the other electrons. When this electron-dependant potential is approximated by the potential from the whole electron cloud, including itself, it is known as the Hartree approximation:

$$\mathcal{H} = \sum_i \mathcal{H}_i = \sum_i \left[ -\frac{\hbar^2}{2m} \nabla^2 + U(\mathbf{r}_i) + W_H(\mathbf{r}_i) \right], \quad (2.5)$$

where

$$W_H(\mathbf{r}_i) = \int \frac{n(\mathbf{r}')}{|\mathbf{r}_i - \mathbf{r}'|} d^3\mathbf{r}' \quad (2.6)$$

and the solution can be written as a product of the mono-electronic wave functions  $\psi = \psi_1 \cdot \psi_2 \cdot \dots \cdot \psi_n$ , being  $\mathcal{H}_i \psi_i = E_i \psi_i$  the independent solutions that provides the total energy of the system as  $E = \sum_i E_i$ .

However, due to the fermionic nature of the electrons, the system must be anti-symmetric under the exchange of two electrons. Thus, requiring the solutions to be single Slater determinants, as opposed to simple wave function products, adds a non-local exchange term to the potential felt by electrons, accounting for the reduction of the energy of the electronic system caused by the anti-symmetry of the wave function  $E \rightarrow E - E_X$ . This is the Hartree-Fock approximation.

### 2.1.3 Density Functional Theory (DFT)

Hohenberg and Kohn [46] proved that there is a one-to-one correspondence between the external (i.e. non-purely electronic) potential acting on an electron gas and its ground state charge density. Moreover, they showed that the ground state charge density is the one that minimizes a universal (but unknown) energy functional depending only on the charge density, not the wave functions. Shortly after, Kohn and Sham [47] made the ansatz that the total energy of the gas of electrons can be calculated formally by an ancillary system of non-interacting electrons, related to the original many-body problem, moving in an effective non-local potential due to the other electrons.

The exchange-correlation energy  $E_{XC}$  is the contribution to the electronic energy of the system defined as the difference of many-body energy and the energy in the Hartree approximation:

$$E_{XC}(n) = \mathcal{T} - \mathcal{T}_i(n) + U_{e-e} - E_{Hartree}(n) , \quad (2.7)$$

where  $\mathcal{T}_i(n)$  is the kinetic energy of an independent electron and

$$E_{Hartree}(n) = \frac{1}{2} \int \int \frac{n(\mathbf{r})n(\mathbf{r}')}{|\mathbf{r} - \mathbf{r}'|} d^3\mathbf{r} d^3\mathbf{r}' \quad (2.8)$$

is the Hartree energy. Unfortunately, the exact form of  $E_{XC}(n)$  is not known.

The minimization of the total energy functional of the non-interacting problem, in terms of the constituent wave functions leads to an equivalent set of self-consistent one-electron equations known as Kohn Sham (KS) equations. The eigenvalues of these equations will lead to the total electronic energy of the system, and they are related to the spectrum of the true many-body system. The KS equations are:

$$\left[ \frac{-\hbar^2}{2m} \nabla^2 + U(\mathbf{r}) + W(\mathbf{r}) + V_{XC}(\mathbf{r}) \right] \psi_i(\mathbf{r}) = E_i \psi_i(\mathbf{r}) , \quad (2.9)$$



where  $V_{XC}$  corresponds to the exchange-correlation potential.

From a computational point of view, these set of equations must be solved self-consistently, iterating from a trial electronic density minimizing the total functional energy until convergence is achieved.

### Local Density Approximation and Generalized Gradient Approximation

Even the simplification reached using DFT, an approximate expression for the exchange-correlation energy for the one-electron set of equations is required. If the variation in the electronic density expected to be slow, the Local Density Approximation (LDA) can be used. LDA assumes that  $E_{XC}$  at the point  $\mathbf{r}$  is equal to the exchange-correlation energy per electron  $\epsilon_{XC}$  in a homogeneous electron gas with the same density of the electron gas at the point  $\mathbf{r}$ :

$$E_{XC}^{LDA}(n) = \int \epsilon_{XC}(n)n(\mathbf{r})d^3\mathbf{r}, \quad (2.10)$$

where  $n(\mathbf{r}) = \sum_i |\psi_i(\mathbf{r})|^2$  is the electronic density.

When LDA overestimates  $E_{XC}$ , the Generalized Gradient Approximation (GGA) provides a more accurate solution. This approximation expands the electronic density in terms of its magnitude and its gradient to correct for variations of the electronic density away from  $\mathbf{r}$ :

$$E_{XC}^{GGA}(n) = \int \epsilon_{XC}(n, \nabla n)n(\mathbf{r})d^3\mathbf{r}. \quad (2.11)$$

### Pseudopotential approximation

Most of the physical properties of solids are much more dependent on the valence electrons than on the core ones. The substitution of the full electron-ion potential by a weaker potential that deals only with the valence electrons, removing the core electrons and ionic potential, allows expanding the wave functions into a smaller set of plane waves that computationally greatly simplifies the solution of the Schrödinger equation. When using pseudopotentials, it is necessary to ensure the accuracy of the exchange correlation energy by having equal values of the integrals of the squared amplitudes of the pseudo and real wave functions outside the core. Such pseudopotentials are known as norm-conserving pseudopotentials.

To generate a pseudopotential it is necessary to perform all-electrons energy calculations for a single atom and then assure that a parametric form of the pseudopotential with suitable parameters provide the same wave functions beyond

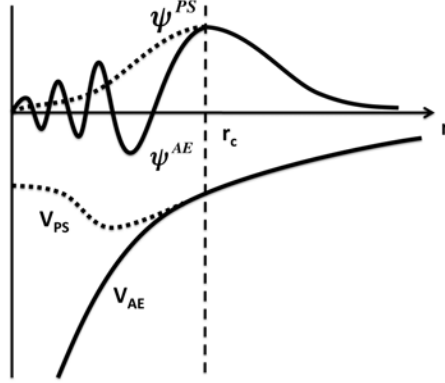


Figure 2.1: Sketch of a pseudopotential and all-electrons functions [44].

a cutoff radius  $r_c$  (typically 2-3 times the core radius), and the same eigenvalues as the all-electrons atom. In Fig. 2.1 the convergence of the pseudopotential function to the all-electron value beyond  $r_c$  is represented.

The generation of pseudopotentials must be made consistently with the XC functional that will be used. In the present work, pseudopotentials generated for use with the GGA as parametrized by Perdew, Burke and Ernzerhof (PBE) or for use with the LDA as parametrized by Perdew and Zunger will be employed.

#### 2.1.4 Periodic supercell and Bloch's theorem

Despite of the simplifications done to reduce the complexity of solving the total energy problem, it is necessary to face the problem of infinite number of non-interacting electrons in a static potential of an infinite number of ions. That means that is required to calculate infinite wave functions expanded on an infinite basis set. This problem can be solved by generating a periodic system that reproduces the original one using the Bloch's theorem. For simplification let us define the potential as  $V(\mathbf{r}) = U(\mathbf{r}) + W(\mathbf{r}) + V_{XC}(\mathbf{r})$ .

Fig. 2.2 represents a supercell created by repetition of a cubic cell by using translational symmetry. For an ideal crystal  $V(\mathbf{r})$  must have the periodicity of the Bravais lattice, then  $V(\mathbf{r}) = V(\mathbf{r} + \mathbf{R})$ ,  $\mathbf{R}$  being a real space lattice vector. This condition must be accomplished as well for the probability density of the stationary states:

$$|\psi_i(\mathbf{r} + \mathbf{R})|^2 = |\psi_i(\mathbf{r})|^2 . \quad (2.12)$$

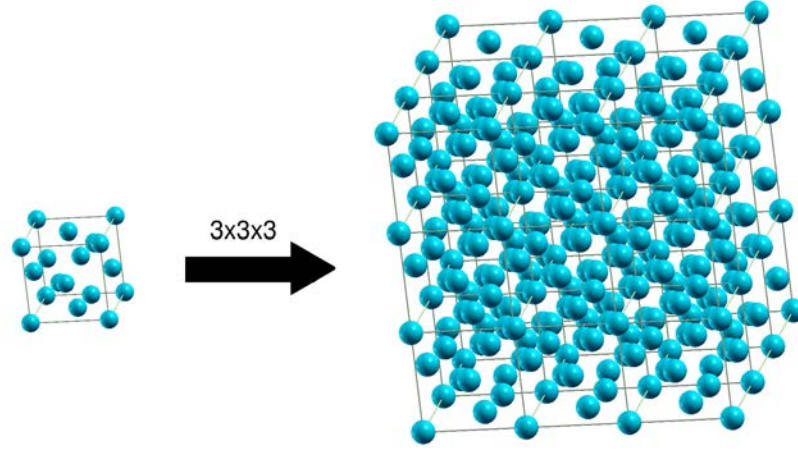


Figure 2.2: Cubic supercell created by a 3x3x3 repetition of a conventional diamond-like 8 atoms cell.

Then a general solution  $\psi_i(\mathbf{r}) = e^{i\mathbf{q}\mathbf{r}}u(\mathbf{r})$  leads to:

$$\psi_i(\mathbf{r} + \mathbf{R}) = e^{i\mathbf{q}\mathbf{R}}\psi_i(\mathbf{r}) , \quad (2.13)$$

known as Bloch's theorem, where  $\mathbf{q}$  is a reciprocal space vector.

From the previous concepts, the definition of  $\psi_{\mathbf{q}}(\mathbf{r})$  in the reciprocal space from the Fourier transform

$$\psi_{\mathbf{q}}(\mathbf{r}) = e^{i\mathbf{q}\mathbf{r}}u_{\mathbf{q}}(\mathbf{r}) = \sum_{\mathbf{G}} C(\mathbf{q} - \mathbf{G})e^{i(\mathbf{q}-\mathbf{G})\mathbf{r}} \quad (2.14)$$

allows expressing the Schrödinger equation as a simple linear system of equations:

$$\left[ \frac{\hbar^2|\mathbf{q} - \mathbf{G}|^2}{2m} - E_{\mathbf{q}} \right] C(\mathbf{q} - \mathbf{G}) + \sum_{\mathbf{G}''} V(\mathbf{G}'' - \mathbf{G})C(\mathbf{q} - \mathbf{G}'') , \quad (2.15)$$

where  $\mathbf{G}$  and  $\mathbf{G}''$  are reciprocal lattice vectors and the coefficients  $C$  are unknown values to be determined from the equations.

### 2.1.5 Perturbation theory

The solution of several real physical problems that require total energy calculations many times have to be treated inside perturbation theory. This requires introducing a perturbation term  $E(n, \lambda)$ , where  $n$  is the charge density and  $\lambda$  the

perturbation parameter. The perturbed energy can be expanded in series and the total energy can be found to the  $n$ -th order truncation of such perturbation:

$$E(n, \lambda) = E^0(n) + \frac{\partial E(n, \lambda)}{\partial \lambda} \lambda + \frac{1}{2!} \frac{\partial^2 E(n, \lambda)}{\partial \lambda^2} \lambda^2 + \frac{1}{3!} \frac{\partial^3 E(n, \lambda)}{\partial \lambda^3} \lambda^3 + \dots \quad (2.16)$$

Baroni, Giannozzi and Testa [48] used the perturbation theory in the DFT framework (Density Functional Perturbation Theory, DFPT), making it possible to compute anharmonic properties of semiconductors [49] from *ab initio* techniques.

## 2.2 Interatomic force constants

In order to calculate the total energy from the Hamiltonian Eq. (2.1), once all approximations are done, it is necessary to choose a pseudopotential able to reproduce the interaction terms defined above. The forces between atoms obtained provide the interatomic force constants (IFC), from which the terms of the crystal Hamiltonian can be rewritten:

$$\mathcal{H}_2 = \frac{1}{2!} \sum_{lk, \alpha} \sum_{l'k', \beta} \phi_{\alpha\beta}^{lk, l'k'} \mathbf{u}_{\alpha}^{lk} \mathbf{u}_{\beta}^{l'k'} \quad \text{and} \quad (2.17)$$

$$\mathcal{H}_3 = \frac{1}{3!} \sum_{lk, \alpha} \sum_{l'k', \beta} \sum_{l''k'', \gamma} \phi_{\alpha\beta\gamma}^{lk, l'k', l''k''} \mathbf{u}_{\alpha}^{lk} \mathbf{u}_{\beta}^{l'k'} \mathbf{u}_{\gamma}^{l''k''}, \quad (2.18)$$

where  $\phi_{\alpha\beta}$  corresponds to the harmonic force constants, and  $\phi_{\alpha\beta\gamma}$  to the anharmonic ones.  $\alpha$ ,  $\beta$  and  $\gamma$  are Cartesian indices to refer the direction of the displacement  $\mathbf{u}^{lk}$  (the perturbation) of the atom  $k$  in the unit cell  $l$ . Notice that all the magnitudes are defined in real space. In the same nomenclature, the kinetic energy term is expressed as:

$$\mathcal{T} = \frac{1}{2} \sum_{lk, \alpha} m_k [\dot{\mathbf{u}}_{\alpha}^{lk}]^2. \quad (2.19)$$

To obtain the total energy of the system from the IFC analytic methods are required.

For accurate calculations of the IFC a proper choice of the length of the atomic displacement is important. To calculate harmonic IFCs, the displacement should be small enough to avoid anharmonic contributions. In contrast, to account for the anharmonic effects these displacements have to be longer.

### 2.2.1 Harmonic force constants

The harmonic force constants correspond to the terms  $\phi_{\alpha\beta}(lk, l'k')$  defined in the total Hamiltonian of the system. These values can be obtained by doing displacements of two atoms (or one atom in two different directions) of the cell and calculating the total energy. The usual treatment of these magnitudes is to perform the calculations in the reciprocal space:

$$\phi_{\alpha\beta}^{k,k'}(\mathbf{q}, \mathbf{q}') = \sum_{l,l'} \phi_{\alpha\beta}^{lk,l'k'} e^{i\mathbf{q}\mathbf{R}^l} e^{i\mathbf{q}'\mathbf{R}^{l'}} , \quad (2.20)$$

where  $\mathbf{R}^l$  is the atomic position  $\mathbf{R}$  of the unit cell  $l$ . Then the harmonic force constants are calculated as:

$$\phi_{\alpha\beta}^{k,k'}(\mathbf{q}, \mathbf{q}') = \frac{\partial^2 E}{\partial u_{\alpha}^k(\mathbf{q}) \partial u_{\beta}^{k'}(\mathbf{q}')} , \quad (2.21)$$

where

$$u^k(\mathbf{q}) = \sum_l u^{lk} e^{i\mathbf{q}\mathbf{R}^l} \quad (2.22)$$

are the atomic displacements in the reciprocal space. Notice that now the atomic displacements are expressed in the reciprocal space as a Fourier transform of the displacement in the real space.

From the harmonic force constants the eigenvalue equation can be written, whose solution provides the phonon frequencies and eigenvectors, i.e. the dispersion relations (DR):

$$\sum_{\beta k'} \frac{1}{\sqrt{m_k m_{k'}}} D_{\alpha\beta}^{k,k'}(\mathbf{q}) e_{\beta}^{k'}(\mathbf{q}) = \omega^2 e_{\alpha}^k(\mathbf{q}) , \quad (2.23)$$

where  $m_k$  and  $m_{k'}$  are the masses of the displaced atoms,  $\omega$  the eigenvalue (i.e. the frequency),  $e(\mathbf{q})$  the eigenvectors, and  $D_{\alpha\beta}$  the dynamical matrix:

$$D_{\alpha\beta}^{k,k'}(\mathbf{q}) = \sum_{l'} \phi_{\alpha\beta}^{0k,l'k'} e^{i\mathbf{q}\mathbf{R}^{l'}} . \quad (2.24)$$

From the calculation point of view, to obtain the harmonic IFC it is enough to do one displacement for each of the different type of atom in the unit cell.

### 2.2.2 Anharmonic force constants

The anharmonic force constants are those of higher order interaction than the harmonic ones. Derivation of the expressions are given for third order anharmonic IFC. Extension to higher orders can be easily obtained from the presented

equations. The third-order derivatives of the total energy provide the third-order IFC from which phonon-phonon scattering rates can be obtained:

$$\phi_{\alpha\beta\gamma}^{k,k',k''}(\mathbf{q}, \mathbf{q}', \mathbf{q}'') = \frac{\partial^3 E}{\partial u_{\alpha}^k(\mathbf{q}) \partial u_{\beta}^{k'}(\mathbf{q}') \partial u_{\gamma}^{k''}(\mathbf{q}'')} . \quad (2.25)$$

In the last decade Esfarjani *et al.* [50] have developed the computational implementation of the calculation of harmonic and anharmonic IFC. To calculate anharmonic force constants in a supercell, the number of the interacting neighbors has to be limited, otherwise the number of calculations will be manually or computationally unachievable. Even doing this restriction, no less than interactions up to the third neighbor must to be considered if accurate anharmonic IFCs are desired. In this case the number of interactions still remain very high. Additional constrictions to reduce the number of calculations are based on the symmetry of the systems. Expressions of the constrictions are given for the IFC in the real space definition [51]. Higher order perturbation will require extra constrictions [50, 51]. These are important to capture anharmonicity at high temperature or low pressure systems.

#### a) Invariance under permutation of indices

From its definition, a force constant is a derivative of the total energy with respect to a perturbation (see Eq. (2.21) and Eq. (2.25)), then its value is independent on the order of differentiation:

$$\phi_{\alpha\beta}^{lk,lk'} = \phi_{\beta\alpha}^{l'k',lk} . \quad (2.26)$$

The same expression can be extended to higher orders.

#### b) Invariance under arbitrary translation of the system

The invariance of the force constants under an arbitrary translation of the system is known as acoustic sum rule (ASR). The ASR can be written mathematically as:

$$\sum_{l'k'} \phi_{\alpha\beta}^{0k,l'k'} = 0 \quad \forall (\alpha\beta, k) \quad \text{and} \quad (2.27)$$

$$\sum_{l''k''} \phi_{\alpha\beta\gamma}^{0k,l'k',l''k''} = 0 \quad \forall (\alpha\beta, k, k'') , \quad (2.28)$$

for the harmonic and anharmonic force constants respectively.

### c) Invariance under arbitrary rotation of the system

In analogy to the translation invariance, the IFC are invariant under an arbitrary rotation of the system.

$$\sum_{l'k'} \phi_{\alpha\beta\gamma}^{0k,l'k',l''k''} (r_{\delta}^{l''k''}) \epsilon^{\gamma\delta\nu} + \phi_{\gamma\beta}^{0k,l'k'} \epsilon^{\gamma\alpha\nu} + \phi_{\alpha\gamma}^{0k,l'k'} \epsilon^{\gamma\beta\nu} = 0 \quad \forall (\alpha\nu, l, kk') . \quad (2.29)$$

The latter equation is expressed using Einstein summation notation, where  $\epsilon^{\alpha\beta\gamma}$  is the antisymmetric Levy-Civita tensor. The term  $(r_{\delta}^{l''k''})$  corresponds to the component  $\delta$  of the vector from the origin to the atom  $k''$  in the unit cell  $l''$ .

### d) Other symmetries

Other symmetries depending on the crystal point/space group may help to reduce the number of force constants to be calculated, like lattice translation, rotation or mirror. For a certain mirror or rotation symmetry operation  $S$ :

$$\phi_{\alpha\beta}^{lk,l'k'} = \sum_{\alpha'\beta'} \phi_{\alpha'\beta'}^{lk,l'k'} S^{\alpha\alpha'} S^{\beta\beta'} \quad (2.30)$$

in the case of second order forces. For low symmetry crystals extra constraints on elastic constants can be used [52].

## 2.2.3 Calculation methods

There are two main methods to obtain the IFC, the  $2n+1$  theorem and finite differences method. Both of them make use of the invariance described above to compute only the minimal set of perturbations able to produce all the IFC for calculation of harmonic and anharmonic properties.

### a) Finite difference method

To obtain an approximate expression of the energy on the atoms once the system is perturbed under a displacement, a suitable treatment is to do a Taylor expansion of the energy respect to the displacement. When only one atom is displaced, in real space:

$$E(\delta u_{\alpha}^{lk}) \approx E(0) + \frac{\partial E}{\partial \delta u_{\alpha}^{lk}} \delta u_{\alpha}^{lk} + \frac{1}{2} \frac{\partial^2 E}{\partial^2 \delta u_{\alpha}^{lk}} (\delta u_{\alpha}^{lk})^2 , \quad (2.31)$$

where  $\delta u_\alpha^{lk}$  is a small displacement of the atom  $lk$  in the direction  $\alpha$  and  $E(0)$  the energy in the relaxed state. For two atoms displaced:

$$\begin{aligned} E(\delta u_\alpha^{lk}, \delta u_\beta^{l'k'}) &\approx E(0) + \frac{\partial E}{\partial \delta u_\alpha^{lk}} \delta u_\alpha^{lk} + \frac{\partial E}{\partial \delta u_\beta^{l'k'}} \delta u_\beta^{l'k'} \\ &+ \frac{1}{2} \frac{\partial^2 E}{\partial^2 \delta u_\alpha^{lk}} (\delta u_\alpha^{lk})^2 + \frac{1}{2} \frac{\partial^2 E}{\partial^2 \delta u_\beta^{l'k'}} (\delta u_\beta^{l'k'})^2 + \frac{\partial^2 E}{\partial \delta u_\alpha^{lk} \partial u_\beta^{l'k'}} \delta u_\alpha^{lk} \delta u_\beta^{l'k'}. \end{aligned} \quad (2.32)$$

To make use of the Taylor expressions of the energy, the harmonic force constants (Eq. (2.21)) can be rewritten in the real space as:

$$\phi_{\alpha\beta}^{lk,l'k'} = \frac{\partial}{\partial u_\alpha^{lk}} \frac{\partial E}{\partial u_\beta^{l'k'}} = \frac{\partial}{\partial u_\alpha^{lk}} \mathbf{F}_\beta^{l'k'}. \quad (2.33)$$

The previous expression represents a change in the force constant in the component  $\alpha$  of an atom  $lk$  when an atom  $l'k'$  is displaced a distance  $\delta u$  in the direction  $\beta$ . The simplest case to calculate the harmonic IFC is to consider  $lk = l'k'$  and  $\alpha = \beta$ , then rearranging terms from Eq. (2.31) and its opposite  $E(-\delta u_\alpha^{lk})$ :

$$\phi_{\alpha\beta}^{lk,l'k'} = \frac{\partial \mathbf{F}_\alpha^{lk}}{\partial u_\alpha^{lk}} \approx \frac{\mathbf{F}_\alpha^{lk} - \mathbf{F}_{-\alpha}^{lk}}{2\delta u_\alpha^{lk}}. \quad (2.34)$$

Eq. (2.34) is enough to compute the whole dynamical matrix. For the anharmonic IFC an analog treatment can be done:

$$\phi_{\alpha\beta\gamma}^{lk,l'k',l''k''} = \frac{\partial}{\partial u_\alpha^{lk}} \frac{\partial^2 E}{\partial u_\beta^{l'k'} \partial u_\gamma^{l''k''}}. \quad (2.35)$$

Then making use of Eq. (2.31) and Eq. (2.32) and its opposites  $E(-\delta u_\alpha^{lk})$  and  $E(-\delta u_\alpha^{lk}, -\delta u_\beta^{l'k'})$  with a little algebra:

$$\phi_{\alpha\beta\gamma}^{lk,l'k',l''k''} \approx \frac{\partial}{\partial u_\alpha^{lk}} \frac{E_{\beta\gamma}^{l'k',l''k''} + E_{-\beta-\gamma}^{l'k',l''k''} - E_\beta^{lk} - E_{-\beta}^{lk} - E_\gamma^{l''k''} - E_{-\gamma}^{l''k''} + 2E(0)}{2\delta u_\beta^{l'k'} \delta u_\gamma^{l''k''}}, \quad (2.36)$$

where the terms  $\partial E_{\beta\gamma}^{l'k',l''k''} / \partial u_\alpha^{lk} = F_{\beta\gamma}^{l'k',l''k''}(\alpha, lk)$  refers to the force that feels the component  $\alpha$  of the atom  $lk$  when the atom  $l'k'$  is displaced  $\delta u$  in the direction  $\beta$  ( $\delta u_\beta^{l'k'}$ ) and the atom  $l''k''$  is displaced in the direction  $\gamma$  ( $\delta u_\gamma^{l''k''}$ ).

The total energy calculations involved in the previous equations can be done in the DFT framework.



### b) 2n+1 theorem

The use of DFT together with perturbation theory leads to the density functional perturbation theory (DFPT), able to compute harmonic and anharmonic couplings [53]. The 2n+1 theorem of DFPT establishes the relationship of the (2n+1)-order energy derivatives to the first  $n$ -th order eigenfunctions of a system. Then, to obtain at least 3rd order energy derivatives to compute anharmonic effects (Eq. (2.31)) just the first derivatives of the charge density are required, which can be expressed as well using the perturbation theory as:

$$n(\mathbf{r}, \lambda) = n^0(\mathbf{r}) + \frac{\partial n(\mathbf{r})}{\partial \lambda} \lambda + \frac{1}{2!} \frac{\partial^2 n(\mathbf{r})}{\partial \lambda^2} \lambda^2 + \frac{1}{3!} \frac{\partial^3 n(\mathbf{r})}{\partial \lambda^3} \lambda^3 + \dots \quad (2.37)$$

Treating the atomic displacements as a perturbation of the system  $\lambda$ , the linear response  $\partial n(\mathbf{r})/\partial \lambda$  will provide the third derivatives of the energy. To do that it is necessary to do self-consistent calculations as a function of the atomic displacements. Phonon energies are also obtained with this methodology.

In some special cases like for calculation of phonon dispersion of metallic or magnetic systems, or when using ultrasoft pseudopotentials, the use of direct methods becomes more suitable.

## 2.3 Phonon scattering mechanisms

When a perturbation in energy (or temperature) or in crystal momentum is induced in a crystal, the phonon population becomes displaced from the equilibrium one. Due to the interaction of phonons with boundaries, impurities and other phonons, such population relaxes to the equilibrium one in a characteristic time, known as the phonon lifetime.

The phonon scattering processes govern the dynamics of a crystal. Independent phonon oscillations correspond to harmonic vibrations of the lattice that provide the dispersion relations. Regarding anharmonic vibrations, 3-phonon scattering mechanisms have been proved to be enough to compute the thermal conductivity of pure bulk semiconductors. When impurities and/or boundaries are present in the sample extra scattering mechanisms need to be included in the calculations.

### 2.3.1 Fermi Golden Rule

To find the probability of a transition from an initial state  $E_i$  to a final state  $E_f$  it is necessary to use Fermi's Golden Rule (FGR):

$$\Gamma = \frac{2\pi}{\hbar} \sum_f |\langle i|\mathcal{H}|f\rangle|^2 \delta(E_i - E_f) , \quad (2.38)$$

where the Hamiltonian  $\mathcal{H}$  can be as generic as desired. The delta function  $\delta(E_i - E_f)$  corresponds to the conservation of the energy between the initial and final state. For anharmonic processes  $\mathcal{H}^{anharmonic} = \mathcal{H}_3$ , defined in **Section 2.1**.

### 2.3.2 3-phonon scattering rates

When a system is perturbed from its equilibrium the atomic positions starts to vibrate and there appear linear combinations of vibration modes. Some of these vibrations can interact with a probability that depends on the well known FGR. All of these interactions between phonons must conserve the energy between the initial and final states, but the crystalline momentum  $\hbar\mathbf{q}$  can be conserved or not. When in a collision the momentum is conserved is defined a normal ( $N$ ) process, otherwise is called umklapp ( $U$ ) process<sup>1</sup>. Moreover two other kinds of processes can occur, one phonon interacting with another to produce a final single phonon (type 1) or one phonon that splits into two phonons (type 2).

The quantum of energy for a phonon is defined as  $E = \hbar\omega$ , then the conservation of energy:

$$\omega_{\mathbf{q}} = \omega_{\mathbf{q}'} + \omega_{\mathbf{q}''} \quad \text{or} \quad \omega_{\mathbf{q}} + \omega_{\mathbf{q}'} = \omega_{\mathbf{q}''} . \quad (2.39)$$

The conservation of momentum for  $N$  processes is:

$$\mathbf{q} = \mathbf{q}' + \mathbf{q}'' \quad \text{or} \quad \mathbf{q} + \mathbf{q}' = \mathbf{q}'' , \quad (2.40)$$

while for  $U$  processes:

$$\mathbf{q} = \mathbf{q}' + \mathbf{q}'' + \mathbf{G} \quad \text{or} \quad \mathbf{q} + \mathbf{q}' = \mathbf{q}'' + \mathbf{G} , \quad (2.41)$$

where  $\mathbf{G}$  is a reciprocal lattice vector.

From Fig. 2.3, when  $\mathbf{q}''_0$  is inside the first Brillouin Zone (1BZ)  $\mathbf{G} = 0$  and a  $N$  process ( $\mathbf{q}''_0 = \mathbf{q}''$ ) occurs. On the contrary, when  $\mathbf{q}''_0$  is outside the 1BZ, the process is re-expressed in a 1BZ equivalent  $\mathbf{q}$ -vector  $\mathbf{q}''$  and becomes an  $U$  process.

To define properly the  $N$  and  $U$  processes it is important to have the 1BZ zone centered at  $\mathbf{q} = (0, 0, 0)$ , the so-called  $\Gamma$  point. With these premises, it is

<sup>1</sup>Strictly speaking, umklapp collisions also conserve crystalline momentum, but a non-zero vector of the reciprocal lattice must be used to bring back the final momentum to the first Brillouin zone.

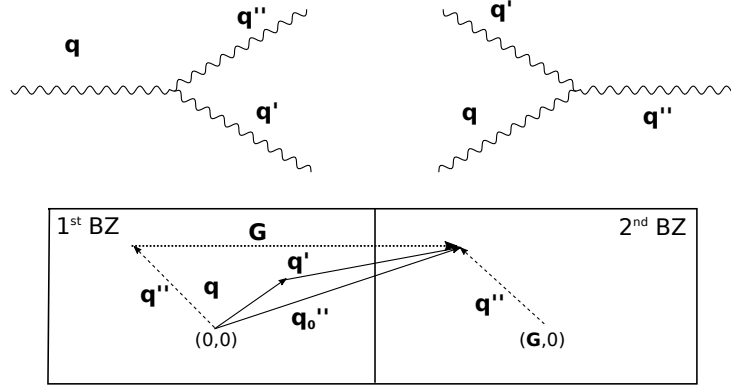


Figure 2.3: Top: Feynman diagram of type 1 and type 2 processes. Bottom: Sketch of phonon-phonon scattering processes.

considered that  $N$  and  $U$  processes are only properly defined in the 1BZ of the primitive cell centered at  $\Gamma$ , otherwise the splitting  $N-U$  can be different.

For simplicity of notation let's use the sub/super index  $q$  to indicate the dependence of a magnitude on a phonon mode and capital  $\mathbf{q}$  to denote the phonon wave vector. The goal of calculating the scattering rates is to obtain the relaxation time of each process as:

$$\tau_{\mathbf{q}} = \frac{1}{2\Gamma_{\mathbf{q}}}, \quad (2.42)$$

where here  $\Gamma_{\mathbf{q}}$  represents the scattering rate, and can be split into two types of processes:

$$\Gamma_{\mathbf{q}} = \Omega_{\mathbf{q}}^{q'q''} + \Omega_{\mathbf{q}q'}^{q''}. \quad (2.43)$$

The first term corresponds to type 1 processes and the second to type 2.  $\Omega$  is the transition rate of each process, which is defined in terms of the scattering matrix:

$$\Omega_{\mathbf{q}}^{q'q''} = \frac{\pi}{2\hbar^2 N_{\mathbf{q}}} \sum_{\mathbf{q}'\mathbf{q}''} |V_{\mathbf{q}}^{q'q''}|^2 (1 + n_{\mathbf{q}'} + n_{\mathbf{q}''}) \delta(\omega_{\mathbf{q}} - \omega_{\mathbf{q}'} - \omega_{\mathbf{q}''}) \quad (2.44)$$

$$\Omega_{\mathbf{q}q'}^{q''} = \frac{\pi}{\hbar^2 N_{\mathbf{q}}} \sum_{\mathbf{q}'\mathbf{q}''} |V_{\mathbf{q}q'}^{q''}|^2 (n_{\mathbf{q}'} - n_{\mathbf{q}''}) \delta(\omega_{\mathbf{q}} + \omega_{\mathbf{q}'} - \omega_{\mathbf{q}''}). \quad (2.45)$$

$V_{\mathbf{q}q'}^{q''}$  is the 3-phonon transition matrix,  $n$  the Bose-Einstein distribution function for each mode and  $\delta(\omega)$  is a Dirac delta.  $N_{\mathbf{q}}$  refers to the number of  $\mathbf{q}$ -points considered in the mesh sampling over the Brillouin zone. The factor 1/2 in Eq. (2.44) is introduced to avoid counting twice the same process  $\mathbf{q} = \mathbf{q}' + \mathbf{q}'' = \mathbf{q}'' + \mathbf{q}'$ . Notice that the selection of the  $\mathbf{q}$ -points will determine if the process

is  $N$  or  $U$ . One can determine  $N$  or  $U$  scattering rate by doing the summation over all the  $\mathbf{q}, \mathbf{q}', \mathbf{q}''$  that fulfill the condition that  $\mathbf{G} = 0$  ( $N$ ) or  $\mathbf{G} \neq 0$  ( $U$ ) (see Eq. (2.40) and Eq. (2.41)).

At this point, the calculation of the scattering matrix in the reciprocal space can be expressed in terms of anharmonic IFC described in previous sections:

$$V(\mathbf{q}\mathbf{q}'\mathbf{q}'') = \left(\frac{\hbar}{2}\right)^{3/2} \sum_k \sum_{l'k'} \sum_{l''k''} \sum_{\alpha\beta\gamma} \phi_{\alpha\beta\gamma}^{0k,lk',lk''} e^{i\mathbf{q}'\mathbf{R}_{l'}} e^{i\mathbf{q}''\mathbf{R}_{l''}} \cdot \frac{e_{\alpha}^{\mathbf{q}} e_{\beta}^{\mathbf{q}'} e_{\gamma}^{\mathbf{q}''}}{\sqrt{m_k m_{k'} m_{k''} \omega_{\mathbf{q}} \omega_{\mathbf{q}'} \omega_{\mathbf{q}''}}}, \quad (2.46)$$

where  $e$  and  $\omega$  are the eigenvectors and the eigenvalues for each mode obtained from the solution of the dynamical matrix and  $m_k$  the mass of the atom in the position  $k$ . The term of the Fourier transform  $e^{i\mathbf{q}\mathbf{R}_l}$  for the basis atom has been omitted as  $R = 0$ . In the latter expression, the summation in  $k$  goes over all the atoms of the primitive cell, and  $k'$  and  $k''$  over all the number of selected neighboring cells  $l', l''$ .

From symmetry conditions one can see that  $|V_{\mathbf{q}}^{\mathbf{q}'\mathbf{q}''}| = |V_{\mathbf{q}'}^{\mathbf{q}\mathbf{q}''}| = |V(\mathbf{q}\mathbf{q}'\mathbf{q}'')|$  then:

$$\Gamma_{\mathbf{q}} = \frac{\pi}{2\hbar^2 N_{\mathbf{q}}} \sum_{\mathbf{q}'\mathbf{q}''} |V(\mathbf{q}\mathbf{q}'\mathbf{q}'')|^2 [(1 + n_{\mathbf{q}'} + n_{\mathbf{q}''})\delta(\omega_{\mathbf{q}} - \omega_{\mathbf{q}'} - \omega_{\mathbf{q}''}) + 2(n_{\mathbf{q}'} - n_{\mathbf{q}''})\delta(\omega_{\mathbf{q}} + \omega_{\mathbf{q}'} - \omega_{\mathbf{q}''})]. \quad (2.47)$$

From a computational point of view, the conservation of energy determined by the delta function can be expressed as a Gaussian or Lorentzian function, where a smearing parameter  $\epsilon$  must be included in order to determine the restriction of the condition. This parameter should be modified with the mesh sampling, the finer the mesh, the smaller the smearing:

$$\delta_{Gaussian}(x) = \frac{e^{-(\frac{x}{\epsilon})^2}}{\epsilon\sqrt{\pi}}, \quad \delta_{Lorentzian}(x) = \frac{1}{\pi} \frac{\frac{\epsilon}{2}}{x^2 + (\frac{\epsilon}{2})^2}. \quad (2.48)$$

Instead of using a Gaussian or Lorentzian approaches, the relaxation time can be also determined from the imaginary part of the phonon propagator self-energy  $\Sigma(\mathbf{q})$  of 3-phonon scattering process [54, 55]:

$$\Sigma(\mathbf{q}) = \frac{1}{2\hbar^2 N_{\mathbf{q}}} \sum_{\mathbf{q}'\mathbf{q}''} |V(\mathbf{q}\mathbf{q}'\mathbf{q}'')|^2 \cdot \left[ \frac{1 + n_{\mathbf{q}'} + n_{\mathbf{q}''}}{\omega_c - \omega_{\mathbf{q}'} - \omega_{\mathbf{q}''}} + \frac{2(n_{\mathbf{q}'} - n_{\mathbf{q}''})}{\omega_c + \omega_{\mathbf{q}'} - \omega_{\mathbf{q}''}} \right], \quad (2.49)$$

where  $\omega_c = \omega_{\mathbf{q}} - i\epsilon$ , being  $\epsilon$  a smearing factor depending on the  $\mathbf{q}$ -point mesh, as found for in the Gaussian or Lorentzian cases. Then, as  $\Sigma(\mathbf{q}) = \Sigma'(\mathbf{q}) - i\Sigma''(\mathbf{q})$ ,  $\tau_{\mathbf{q}} = 1/2\Sigma''(\mathbf{q})$ . Notice that  $\Sigma''(\mathbf{q}) = \Gamma_{\mathbf{q}}$ .

Another way to compute the 3-phonon scattering rates is by means the improved tetrahedron method. In this method the Brillouin zone is sampled by tetrahedrons and linear interpolation is done to compute the phonon eigenvalues [56]. The main advantage of this method is that it is not required to define an smearing value, as done in the Gaussian and Lorentzian functions.

As pointed out, the number of selected neighbors is important to capture the anharmonicity of the crystal, but is not the only important parameter. As a good approximation to reproduce for instance the thermal conductivity of semiconductors it is valid to use the Bose-Einstein equilibrium distribution function to compute the transition scattering matrix. In recent experiments [4, 5, 6, 7, 8, 9, 10] where ultrafast heating or huge temperature gradients are employed this approximation is no longer valid as the deviation from equilibrium is important.

An analogous derivation can be done to compute the electron relaxation time  $\tau_e$  required for the calculation of the electrical conductivity  $\sigma_e$  and the electrical thermal conductivity  $\kappa_e$ . In analogy with phonons, while the process  $\mathbf{q} \rightarrow \mathbf{q}'\mathbf{q}''$  is expressed as  $n(1+n')(1+n'')$ , for electrons the process  $\mathbf{k} \rightarrow \mathbf{k}'\mathbf{k}''$  is expressed as  $f(1-f')(1-f'')$ , where  $f$  is the electron occupation number. In equilibrium,  $f_0$  is the Fermi-Dirac distribution function.

### 2.3.3 Mass variation scattering

In real crystals there exists a certain number of imperfections that can scatter phonons. Boundaries, grain boundaries and dislocations are some of them, but the most relevant mechanisms for highly crystalline solids are the ones due to mass variations. Its origin relies basically in impurities, different isotopic concentrations and different atomic species like in the case of alloys. This scattering rate can be also derived from the FGR. To do that it is necessary to know the expression of the perturbed Hamiltonian due to mass variations. An expression given by Klemens [57, 58] and Tamura [59] is:

$$\mathcal{H} = \frac{1}{2}\delta M \left( \frac{d\mathbf{r}}{dt} \right)^2, \quad (2.50)$$

where  $\mathbf{r}$  is the atomic position. If the interaction is elastic, then the energy and the crystalline momentum are conserved. Moreover, if cubic symmetry is considered, then from the FGR [59]

$$\Gamma_{\mathbf{q}}^I = \frac{\pi}{4N_{\mathbf{q}}}\omega_{\mathbf{q}}^2 \sum_{\mathbf{q}'} \delta(\omega_{\mathbf{q}} - \omega_{\mathbf{q}'}) \sum_s \gamma(s) |e^*(s, \mathbf{q}')e(s, \mathbf{q})|^2, \quad (2.51)$$

where

$$\gamma(s) = \sum_i f_i(s) \left(1 - \frac{m_i(s)}{M_s}\right)^2 \quad (2.52)$$

is the mass fluctuation factor.  $f_i$  is the fraction of the  $i$ th isotope with mass  $m_i$  and  $M_s = \sum_i f_i m_i(s)$  the averaged mass.

Notice that Eq. (2.51) does not have any spatial dependence, then after a little algebra the mass variation impurity scattering can be expressed in terms of the density of states  $D_\omega$  in a very simple way [60]:

$$\tau_I^{-1} = \frac{\pi}{6} \gamma(s) D(\omega) \omega^2 . \quad (2.53)$$

Notice that all these magnitudes are calculated and no free parameters are used.

The alloy relaxation time needs a more detailed discussion. In single species crystals the mass defect term describes the variability in isotopic abundance but in alloys it should also account for the variability in the force and lattice constants [57]. In this case it is necessary to redefine the fluctuation factor:

$$\gamma(s) = \frac{1}{12} \gamma_M^2 + \left( \frac{1}{\sqrt{6}} \gamma_{c^2} - \sqrt{\frac{2}{3}} Q G \gamma_R \right)^2 , \quad (2.54)$$

where

$$\gamma_\alpha = \sum_i x_i \left( \frac{\alpha_i - \bar{\alpha}_x}{\bar{\alpha}_x} \right)^2 \quad (2.55)$$

is the coefficient of variance of mass ( $M$ ), squared velocity ( $c^2$ ) or impurity radius ( $R$ ), being  $\alpha_i$  the value for the isotope/species  $i$  and  $\bar{\alpha}_x$  the averaged value over all the atoms.  $Q$  is a factor that depends on the type of the impurity (for substitution  $Q = 4.2$  [57]) and  $G$  is the Grüneisen parameter. This parameter relates the change in the phonon frequency with the volume of the crystal, and can be obtained from *first principles* as:

$$G_{\mathbf{q}} = -\frac{1}{6\omega_{\mathbf{q}}} \sum_k \sum_{l'k'} \sum_{l''k''} \sum_{\alpha\beta\gamma} \phi_{\alpha\beta\gamma}^{0k,lk',lk''} \cdot \frac{e_{\alpha}^{\mathbf{q}*} e_{\beta}^{\mathbf{q}'}}{\sqrt{m_k m_{k'}}} e^{i\mathbf{q}'\mathbf{R}_{l'}} \gamma_{\delta}^{l''k''} . \quad (2.56)$$

As done by Capinski *et al.* [60], in Eq. (2.53), instead of the Debye approximation, the density of states (DOS) obtained from the full dispersion relations (DR) at stoichiometry  $x$ ,  $D(\omega)$  is used. As expected, the second and third terms reduce to zero for pure silicon or germanium and the isotopic mass defect corresponding to the first term is the only one remaining.

### 2.3.4 Boundary scattering

A widely extended way to account for the individual collisions of phonons with the boundaries in a certain geometry is to use Casimir's expression [61]  $\tau_b(\omega) = L_{\text{eff}}/v(\omega)$ . This expression acts as a limiter for phonons with a mean free path (MFP)  $v\tau$  longer than  $L_{\text{eff}}$ . Different simple geometries can be studied with this expression using that  $L_{\text{eff}}$  is the diameter for wires,  $1.12l$  for rods (i.e. rectangular cross section beams), where  $l = \sqrt{l_1 \cdot l_2}$ , and  $2.25h$  for thin films, where  $h$  is the film thickness [1].

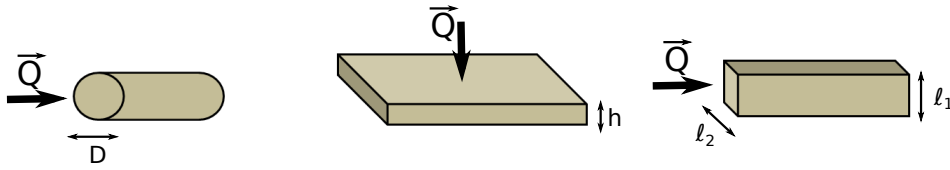


Figure 2.4: Sketch of typical sample geometries. From left to right: wire, film and rod.

In kinetic models the way to include Casimir's expression for boundary effects is to add it through the Mathiessen rule  $\tau_K = (1/\tau_{\text{int}} + 1/\tau_B)^{-1}$ , where  $\tau_{\text{int}}$  correspond to the intrinsic relaxation times (umklapp and impurity). Boundary effects become more important as the temperature decreases. At low temperatures the umklapp scattering decreases drastically, as atomic movements are decreased, and then its relaxation time becomes huge. In contrast, Casimir's expressions is independent of temperature. At these temperatures low energy phonons dominate the thermal conductivity.

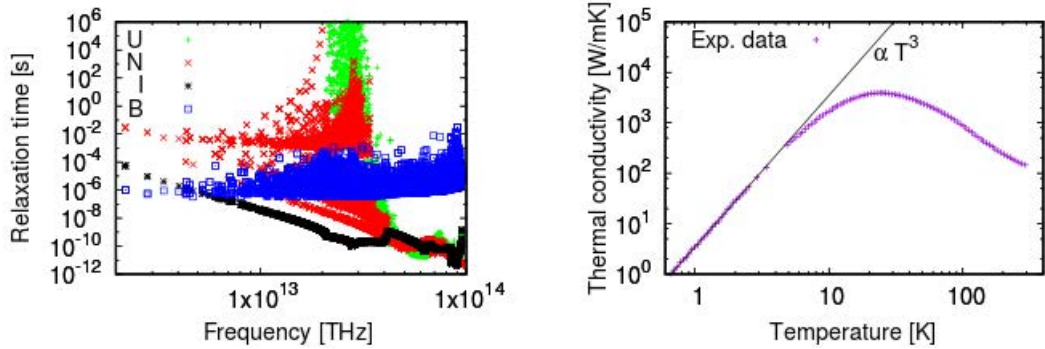


Figure 2.5: Left: Umklapp (U), normal (N), impurity (I) and boundary (B) relaxation times for silicon at  $T = 3$  K and  $L_{\text{eff}} = 2.8$  mm. Right: Silicon experimental thermal conductivity [62].

Fig. 2.5 shows all the relaxation times involved in thermal transport at  $T = 3$  K and the experimental thermal conductivity of silicon. As can be observed in

Fig. 2.5 left, at low temperatures it is clear that the boundary scattering relaxes much faster than the other mechanisms. Fig. 2.5 right shows the temperature dependence of the thermal conductivity and the specific trend at low temperatures. In the KCM framework, at low temperatures  $\Sigma \rightarrow 0$  and therefore the total thermal conductivity tends to the kinetic one ( $\kappa_T \rightarrow \kappa_K$ ). As  $\kappa_K = C_v v_x^2 \tau$ , and the dominant mechanism is the boundary  $\tau \rightarrow \tau_B = L_{\text{eff}}/v_x$ , thus  $\kappa_T = C_v v_x L_{\text{eff}}$ . The phonon velocity and the effective length are temperature independent, then  $\kappa_T$  only depends on temperature through the specific heat. It is well known that at low temperatures  $C_v \propto T^3$ , then  $\kappa_T \propto T^3$ .

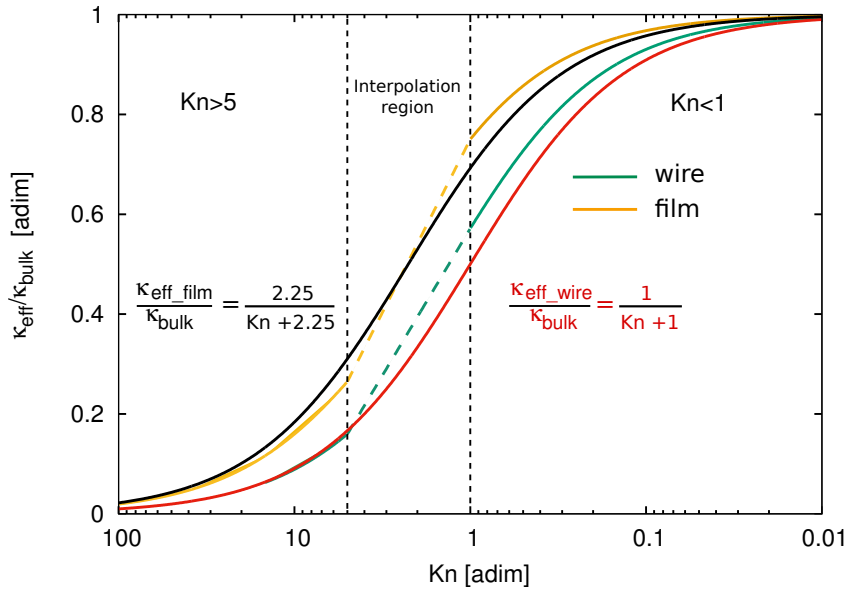


Figure 2.6: Normalized effective thermal conductivity as a function of the Knudsen number. Dashed lines represent logarithmic interpolation for  $1 > \text{Kn} > 5$ . Analogy with Casimir's expressions are written for comparison.

The geometry effects have been also studied in terms of the dimensionless Knudsen number ( $\text{Kn} = \Lambda/L$ ), where  $\Lambda_i$  is the intrinsic phonon MFP and  $L$  the length of the sample. Two expressions are given by Zang [63] to express the effective thermal conductivity for wires and thin films for small and high Knudsen values. In this case,  $L$  refers directly to the diameter for wires and to the thickness for films, without any proportionality constant.

For high Knudsen  $\text{Kn} > 5$ :

$$\frac{\kappa_{\text{eff}}}{\kappa_{\text{bulk}}} = \frac{2\text{Kn} - 1}{\text{Kn}^2 + 2\text{Kn} - 1} \quad \text{for films ,} \quad (2.57)$$

$$\frac{\kappa_{\text{eff}}}{\kappa_{\text{bulk}}} = \frac{4\text{Kn} - 1}{4\text{Kn}^2 + 4\text{Kn} - 1} \quad \text{for wires .} \quad (2.58)$$



For small Knudsen  $\text{Kn} < 1$  it is possible to use the same expression for wires and films:

$$\frac{\kappa_{\text{eff}}}{\kappa_{\text{bulk}}} = \frac{m}{m+1} \quad \text{for } \text{Kn} < 1, \quad (2.59)$$

where  $m = 3$  for films and  $m = 4/3$  for wires.

Fig. 2.6 shows Zang's expressions in comparison with Casimir's expression rewritten in terms of  $\kappa_{\text{eff}}/\kappa_{\text{bulk}}$  for wires and films. Notice that as Zang's expressions are only defined for  $\text{Kn} > 5$  and  $\text{Kn} < 1$ , therefore interpolation is required in between. Even the trend for films and wires is similar in both derivations, small differences can be appreciated in the region from  $\text{Kn} = 0.1$  to  $\text{Kn} = 10$ .

In **Chapter 4** boundary effects are studied from a kinetic-collective approach and from a full hydrodynamic framework.

### 2.3.5 Electron-phonon scattering

Dealing with highly doped semiconductors having a carrier concentration above  $10^{17} \text{ cm}^{-3}$  or metals, the electron-phonon interaction can be a source of scattering events that contribute to the reduction of the thermal conductivity [64]. In a vibrating lattice, atoms are displaced from its equilibrium position, and then the effective electrostatic potential that an electron feels is altered [19].

An analog treatment to the one found for 3-phonon scattering can be done considering the Fermi-Dirac distribution function for electrons. In this case the conservation of energy and momentum is also applicable:

$$\Gamma_{\mathbf{q}\lambda} = \frac{\pi}{\hbar} \sum_{mn, \mathbf{k}} |g_{mn}^{\lambda}(\mathbf{q}, \mathbf{k})|^2 \cdot [f_{n\mathbf{k}}(1 - f_{m\mathbf{k}+\mathbf{q}})n_{\mathbf{q}\lambda}\delta(\epsilon_{m\mathbf{k}+\mathbf{q}} - \epsilon_{n\mathbf{k}} - \hbar\omega_{\mathbf{q}\lambda}) - f_{n\mathbf{k}}(1 - f_{m\mathbf{k}-\mathbf{q}})(n_{\mathbf{q}\lambda} + 1)\delta(\epsilon_{m\mathbf{k}-\mathbf{q}} - \epsilon_{n\mathbf{k}} + \hbar\omega_{\mathbf{q}\lambda})], \quad (2.60)$$

where  $f, \mathbf{k}$  and  $n, \mathbf{q}$  are the electron and phonon distribution functions and wave vectors respectively,  $\epsilon$  the electron energy, and  $g_{mn}^{\lambda}$  the transition matrix. Details of the matrix elements can be found elsewhere [19, 64]. This contribution can be added to the phonon-phonon scattering rate in order to compute the total thermal conductivity. In the case of electron-phonon collisions, the momentum conservation also allows distinguishing between  $N$  and  $U$  processes [19]  $\mathbf{q} + \mathbf{k} = \mathbf{k}' + \mathbf{G}$  or  $\mathbf{q} = \mathbf{k} + \mathbf{k}' + \mathbf{G}$ , for  $\mathbf{G} = 0$  or  $\mathbf{G} \neq 0$ , again restricting the definition to the 1BZ of the primitive cell centered at  $\Gamma$ .

A simplified way to compute the contribution of phonon-electron interaction without the need of calculating all the collision matrix is using [42]:

$$\kappa_{e-p} = \frac{27LT I_4^2}{\rho_e (T_D/T)^6 \pi^2 z_e^2}, \quad (2.61)$$

where  $L$  is the Lorentz number,  $\rho_e$  the electrical resistivity,  $T_D$  the Debye temperature,  $z_e$  the number of free electrons per atom and

$$I_n = \int_0^{T_D/T} \frac{x^n e^x}{(e^x - 1)^2} dx, \text{ with } x \equiv \frac{\hbar\omega}{k_B T}. \quad (2.62)$$

Notice that Eq. (2.61) does not allow distinguishing between normal and umklapp processes, in contrast to Eq. (2.60).

As it has been shown in **Section 1.7**, the electron-phonon interaction has a contribution to the Seebeck coefficient ( $S$ ). Therefore improvement of this term will lead to an increase of the figure of merit ( $ZT$ ). A subject of future study could be to observe if a collective transport regime emerged from dominant  $N$  electron-phonon interaction can be relevant to improve  $S$  and consequently the thermoelectric performance.

## 2.4 *Ab initio* KCM expressions

In a general situation the thermal conductivity is a complex calculation including different order relaxation times. The Kinetic Collective Model (KCM) offers a way to calculate the total thermal conductivity by imposing momentum conservation in the normal scattering term of the collision matrix. This allows splitting the total thermal conductivity into a kinetic and a collective contribution:

$$\kappa_T(T) = \hat{\kappa}_K(T) \cdot (1 - \Sigma) + \hat{\kappa}_C(T) \cdot \Sigma = \kappa_K(T) + \kappa_C(T), \quad (2.63)$$

where the hat  $\hat{\phantom{x}}$  indicates the maximum possible contribution of each regime and:

$$\Sigma(T) = \frac{\Gamma_N(T)}{\Gamma_N(T) + \Gamma_R(T)}, \quad (2.64)$$

where  $\Gamma_N(T)$  and  $\Gamma_R(T)$  are averaged  $N$  and resistive ( $R$ ) scattering rates. The kinetic and collective terms have two main differences. The first is the way to calculate the total mean free time of the participating scattering mechanisms, and the second is the form to include boundary effects in the calculations. In this section will be considered the first aspect. The inclusion of boundary effects will be treated in **Chapter 4**. Here, the KCM transport equations, as derived from Guyer and Krumhansl [15] and extended to anisotropic systems (see **Appendix A**) together with the maximization of entropy derivation [1], are presented.

The expressions for the calculations of the thermal conductivity can be calculated as a summation over all the modes  $\mathbf{q}$  in the first Brillouin zone or by doing a frequency integral accounting for the density of states  $D(\omega)$  of each mode <sup>2</sup>:

<sup>2</sup>This assumption is only valid for isotropic systems.

$$\frac{1}{N_{\mathbf{q}}V_0} \sum_{\mathbf{q}} \rightarrow \int_0^{\omega_{max}} D(\omega) d\omega, \quad (2.65)$$

where  $N_{\mathbf{q}}$  is the number of  $\mathbf{q}$ -points in the mesh sampling and  $V_0$  the volume of the unit cell. This procedure (when applicable) will reduce the computational time by binning the modes in a  $d\omega$  fraction with its respective weight determined by the DOS.

For the sake of simplicity, the different projections of the phonon distribution function in the momentum space found in the KCM equations in terms of  $C_{\mathbf{q},i}$  are defined as:

$$C_{\mathbf{q},i} = \left(\frac{\mathbf{q}}{\omega}\right)^i C_{\mathbf{q}}, \text{ for } i = 0, 1, \quad (2.66)$$

and

$$C_{\mathbf{q},i} = \left(\frac{\mathbf{q} \otimes \mathbf{q}}{\omega^2}\right) C_{\mathbf{q}}, \text{ for } i = 2. \quad (2.67)$$

These terms appears as a generalization of the Debye dispersionless approximation used in the original derivation of Guyer and Krumhansl [15] (see **Appendix A**). Notice that Eq. (2.67) for  $i = 0$  is the mode specific heat  $C_{\mathbf{q}}$ .

Using the summation over  $\mathbf{q}$ , the kinetic contribution is defined as:

$$\hat{\kappa}_K(T) = \frac{1}{N_{\mathbf{q}}V_0} \sum_{\mathbf{q}} C_{\mathbf{q},0} \mathbf{v}_{\mathbf{q}} \otimes \mathbf{v}_{\mathbf{q}} \tau_{\mathbf{q},R}, \quad (2.68)$$

where

$$\tau_{\mathbf{q},R}^{-1} = 2\Gamma_{\mathbf{q},R} = 2(\Gamma_{\mathbf{q},I} + \Gamma_{\mathbf{q},U}) \quad (2.69)$$

is the total resistive relaxation time of the mode  $\mathbf{q}$ , calculated through the addition of the impurity  $\tau_I$  and umklapp  $\tau_U$  scattering rates times, intrinsic of each material. The considered intrinsic processes are those that do not depend on geometry nor external effects. From the definition of the kinetic thermal conductivity, the kinetic mean free time (MFT) can be directly expressed as:

$$\hat{\tau}_R(T) = \frac{\hat{\kappa}_K(T)}{\sum_{\mathbf{q}} C_{\mathbf{q},0} \mathbf{v}_{\mathbf{q}} \otimes \mathbf{v}_{\mathbf{q}}} = \frac{\sum_{\mathbf{q}} C_{\mathbf{q},0} \mathbf{v}_{\mathbf{q}} \otimes \mathbf{v}_{\mathbf{q}} \tau_{\mathbf{q},R}}{\sum_{\mathbf{q}} C_{\mathbf{q},0} \mathbf{v}_{\mathbf{q}} \otimes \mathbf{v}_{\mathbf{q}}}. \quad (2.70)$$

The other contribution to the total thermal conductivity  $\kappa_T$ , the collective contribution, is calculated as:

$$\hat{\kappa}_C(T) = \frac{1}{NV_0} \frac{\sum_{\mathbf{q}} C_{\mathbf{q},1} \mathbf{v}_{\mathbf{q}} \otimes \sum_{\mathbf{q}} C_{\mathbf{q},1} \mathbf{v}_{\mathbf{q}}}{\sum_{\mathbf{q}} C_{\mathbf{q},2} \tau_{\mathbf{q},R}^{-1}}, \quad (2.71)$$

where the collective MFT is an average over the whole distribution:

$$\tau_C(T) = \frac{\sum_{\mathbf{q}} C_{\mathbf{q},2}}{\sum_{\mathbf{q}} \tau_{\mathbf{q},R}^{-1} C_{\mathbf{q},2}}. \quad (2.72)$$

The  $N$  scattering involved in the calculation of the switching factor  $\Sigma$  defined in Eq. (2.64) is:

$$\Gamma_N(T)^{-1} = \frac{\sum_{\mathbf{q}} \Gamma_{\mathbf{q},N}^{-1} C_{\mathbf{q},0}}{\sum_{\mathbf{q}} C_{\mathbf{q},0}}, \quad (2.73)$$

and the resistive scattering rate is nothing but  $\Gamma_R(T) = (2\hat{\tau}_R(T))^{-1}$ .

From the previous expressions, the total relaxation time per mode in the KCM is defined as:

$$\tau_T(\mathbf{q}, T) = \hat{\tau}_{\mathbf{q},K} \cdot (1 - \Sigma) + \hat{\tau}_C(T) \cdot \Sigma = \tau_{\mathbf{q},K} + \tau_C(T). \quad (2.74)$$

Notice that the collective MFT is already an integrated value that is constant for all the modes. This contribution is the responsible of the enhancement of the optical modes [2], as shown in Fig. 1.2. In analogy, the total temperature dependent MFT will be:

$$\tau_T(T) = \hat{\tau}_K(T) \cdot (1 - \Sigma) + \hat{\tau}_C(T) \cdot \Sigma = \tau_K(T) + \tau_C(T). \quad (2.75)$$

These MFT in the KCM framework correspond to the so-called collectons. Similar to relaxons, the collectons are a linear combination of phonons.

### 2.4.1 Note on Matthiessen's rule

It has been reported in recent works that Matthiessen's rule approximation may fail in some materials [22, 65, 66, 67], specially at low temperatures [22]. The total thermal conductivity computed from individual relaxation times will overestimate the real thermal conductivity computed from a full collision matrix including all the scattering mechanisms:

$$\frac{1}{\kappa_T} \leq \frac{1}{\kappa_1} + \frac{1}{\kappa_2}. \quad (2.76)$$

As pointed out by Cepellotti *et al.*, the major failure of this approximation comes from the splitting of  $N$  and  $U$  processes and adding the thermal conductivity obtained from their individual contributions.<sup>3</sup> In the KCM,  $N$  processes do not contribute to the thermal conductivity, but they play an important role through the switching factor. Therefore this failure is not present in the KCM.

<sup>3</sup>We want to remark that  $N$  processes alone must not contribute to the thermal resistance as are momentum conserving collisions.

## 2.5 Calculation methodologies

The study of material properties through *ab initio* calculations can be performed by lattice and molecular dynamics. In lattice dynamics simulations, the Newton's movement equations are solved analytically assuming harmonic vibrations and fixed positions. In this kind of simulations, thus, crystalline materials with high symmetry are required in order to allow the use of periodic conditions to solve the equations. To account for atomic interactions a potential obtained under perturbation theory is required, which should include anharmonic terms to compute temperature effects.

Lattice dynamics simulations based on the solution of the BTE have achieved in the last decade great importance as can be computed in a full *first principles* framework, thus avoiding fitting parameters. Good agreement between experimental data and *ab initio* calculations has been achieved [3, 24, 68, 69].

Molecular dynamics is a calculation approach used to study material properties by numerically integrating the classical Newton equations. This approach consists in a simulation of an atomic system that uses analytical potentials (like Lennard-Jones or Stillinger-Weber) to account for the interaction between atoms, allowing the study of time-dependent phenomena like first order phase transitions, or the efficient computation of thermodynamic quantities.

The equilibrium structure is determined by an initial random guess of the velocity of the particles and averaging over long time intervals at a fixed temperature and pressure. To control these two latter parameters, a Nose-Hoover thermostat and a Berendsen barostat can be used, respectively [42]. Then from the force acting on each atom, the acceleration is determined and the velocity is estimated at each time step. From these parameters it is possible to calculate the heat flux at each time and position using:

$$\mathbf{Q} = \frac{d}{dt} \sum_{i=1}^N \mathbf{r}_i E_i, \quad (2.77)$$

where  $\mathbf{r}_i$  is the atomic position and  $E_i$  its respective energy excluding the site energy. The thermal conductivity can be computed using the Green-Kubo relations:

$$\kappa = \frac{1}{k_B T^2 V} \int_0^\infty \langle \mathbf{Q}(t + \tau) \mathbf{Q}(t) \rangle d\tau, \quad (2.78)$$

where the thermal conductivity  $\kappa$  is related to the heat flux autocorrelation function  $\langle \mathbf{Q}(t + \tau) \mathbf{Q}(t) \rangle$ .  $V$  and  $T$  are the volume and temperature of the calculation respectively. Another way to compute the thermal conductivity is by determin-

ing the heat flux under an external temperature gradient and using the Fourier law (non-equilibrium molecular dynamics (NEMD)).

## 2.6 System modeling

As explained in previous sections, a wrong choice of the potential or number of atoms could lead to a very time expensive or high computational cost calculation. The use of pseudopotentials in the framework of the total energy pseudopotential method does not require such amount of information (i.e. memory) as the real potential of each atom.

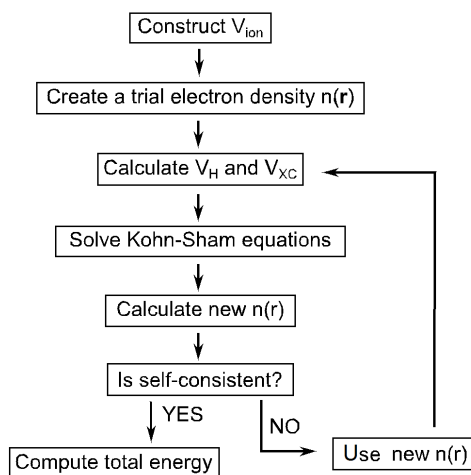


Figure 2.7: Work flow of *ab initio* calculations [44].

The previous scheme shows the standard calculation procedure for total energy calculations, where  $V_{ion}$  is the ionic potential obtained by summing the product of the structure factor  $S(G)$  and the pseudopotential over all species of atoms.

Starting from a trial function of the electronic density, expressions for  $V_H$  and  $V_{XC}$  are constructed. From these potentials the Kohn-Sham equations are solved and the eigenstates of the system are obtained. These eigenstates generate a new electronic density, which normally differs from the trial one. If both are the same, the solution is self-consistent and the total energy is computed. On the contrary, from the new electronic density new  $V_H$  and  $V_{XC}$  are calculated and the process is repeated until the starting electric density is the same as the final one up to some predetermined tolerance.

In order to obtain accurate results able to obtain the correct properties of a crystal, some convergence tests, not just self-consistency, have to be done.

### Equilibrium lattice constant

To find the equilibrium lattice constant that minimizes the energy of the system it is necessary to perform several total energy calculations varying the lattice constant until find the one that leads to the minimum total energy for the system. This parameter will correspond to the minimum of the curve in an energy-lattice constant plot.

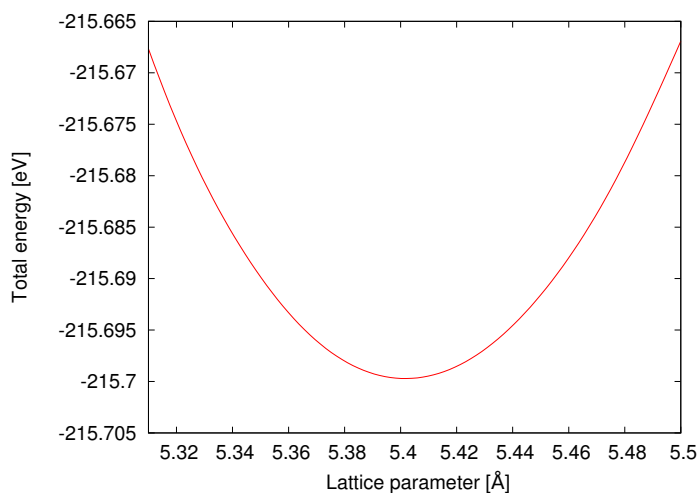


Figure 2.8: Total energy *versus* lattice constant for a 2-atoms silicon primitive cell.

### Convergence criteria

The electronic states and the total energy of the system are calculated in a special set of  $\mathbf{q}$  points in the Brillouin Zone using a homogeneous Monkhorst-Pack grid. Good performance is obtained for insulators and semiconductors with broad grids, while for semi-metals and metals a denser grid is required in order to define the Fermi surface more accurately. For self-consistent calculations, the total energy should converge as the density of the grid increases.

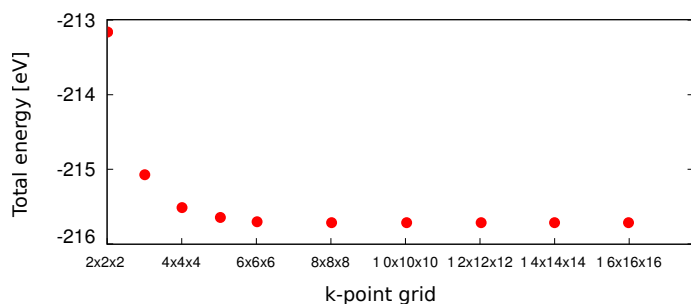


Figure 2.9: Total energy *versus*  $\mathbf{q}$ -point grid sampling for a 2-atoms silicon primitive cell.

### Kinetic energy cutoff

In theory, the electronic wave functions must be expanded in an infinite plane-wave basis set, but computationally this is impossible. Taking into account that the plane waves coefficients in Bloch's theorem for the lower kinetic energy states are the important ones, the basis set can be truncated to a certain energy value. The total energy of the system should converge as the cutoff energy is increased.

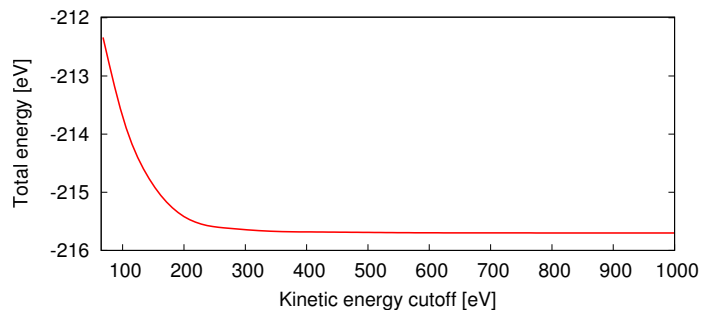


Figure 2.10: Total energy *versus* kinetic energy cutoff for a 2-atoms silicon primitive cell.

### 2.6.1 Alloy simulation

Some important properties of materials can be found not in pure materials but in alloys. In the case of two well known thermoelectric materials like Si and Ge, an important reduction of thermal conductivity is found in the alloy  $\text{Si}_{1-x}\text{Ge}_x$  for germanium concentrations higher than  $x = 0.05$ . The computational simulation of alloys is done mainly by two procedures, the Virtual Crystal Approximation (VCA) and the random distribution of impurities.



### a) Virtual crystal approximation

The VCA is employed when the total energy pseudopotential calculations framework is used. This technique uses a mixture of the pseudopotential of the two compounds that forms the alloy in the desired composition [70]. Once the new pseudopotential is obtained the calculation is done in the same way as described in **Section 2.1**.

### b) Random distribution of impurities

Alloy can be also simulated by generating supercells with random substitutions of a certain number of impurities to the desired alloy composition. Calculations for a fixed number of impurities need to be done with different distributions and average the results in order to improve the procedure. A big enough supercell is required for these simulations to avoid the interaction of defects with the ones of the neighboring supercell. A convergence test can be done increasing the supercell size maintaining the impurity ratio until the total energy converges.

The simulation of defects (vacancies) in a cell can be done in the same way as the random distribution of impurities but instead of substituting the atom, removing it.

This kind of alloy simulations are more suitable for molecular dynamics simulations where large systems can be implemented. This way the distribution of alloying atoms or defects can be more arbitrary and does not require to run as much different simulations and averaging.

A comparison of the phonon scattering rates, relaxation times and the density of states using both techniques can be obtained elsewhere [71].

An improvement of this technique are the special quasirandom structures (SQS's) [72]. In this case, it is demonstrated that for a finite number of periodic cells, there exist specific configurations that improve the results instead of completely random configurations. The selection criteria has a physical meaning, for example using that generally distant atoms contribute less to the total energy than the closer ones.

Another technique used for the simulation of alloys is the so-called cluster expansion [73], which allows rapid evaluation of different configurations in order to obtain averaged properties.

## 2.7 Computational methods

In this section the general workflow used for the KCM *ab initio* calculations of thermal properties is detailed.

The *ab initio* methods allow calculating the harmonic properties of the crystal, such as the dispersion relations and density of states, as well as anharmonic properties from the interatomic force constants. All these calculations can be done with available software such as QUANTUM ESPRESSO [49] or VASP package [74, 75, 76, 77].

The first step is to describe the crystal under study. In this case, parameters such as an initial guess of lattice constant based on the experimental value, cell structure and atomic masses need to be specified. In a second step, it is necessary to choose a suitable pseudopotential and run convergence tests to find the lattice parameter that minimizes the total energy of the system. Once this parameter is obtained the supercell can be created. The size of the supercell will be determined by the total number of atoms. As explained, in *ab initio* lattice dynamics simulations the time and memory of the simulation is determined by the number and type of atoms. A reasonable supercell will have around 100-200 atoms. Tests on computational time and memory use can be done in order to determine the most suitable supercell.

A second step is to determine the harmonic properties of the crystal. This will allow knowing the phonon band structure.


Once the harmonic information of the crystal is known, in order to study thermal transport it is necessary to obtain anharmonic IFC from small atomic displacements. To determine the number of displacements and the atoms involved it is necessary to establish a cutoff radius. This value will determine the number of neighbors involved in the calculation. This procedure can be done directly by open source codes such as ALAMODE [78] or Phono3py [79]. Depending on the desired cutoff radius, the number of interactions will be determined and reduced according to the crystal symmetries (see **Section 2.2**). For each of these displacements will be required to find the total energy of the system in order to obtain the IFC. It is recommended to use a supercell at least twice the size of the cutoff radius [50].

The last step prior to compute the thermal properties of the system is to determine the 3-phonon interaction scattering rates according to Eq. (2.43). ALAMODE and Phono3py can calculate directly the scattering matrix in order to obtain the phonon relaxation times. For the calculation of the thermal properties, ALAMODE has already as an output the thermal conductivity under the Relaxation Time Approximation (RTA). In the case of Phono3py in addition to RTA, the direct solution of the BTE (D-LBTE) is also available.

In the KCM, the computation of thermal properties requires the splitting of  $N$  and  $U$  processes. This has been manually implemented in both ALAMODE and Phono3py codes to test the model. Recently Phono3py has included the option of this splitting in the source code. The *ab initio* KCM equations (**Section 2.4**) have been implemented in an open source code and uploaded to be used as a

post-processing tool of Phono3py outputs in order to calculate the thermal conductivity and hydrodynamic parameters.

```
$ python KCM.py --pa="0 1/2 1/2 1/2 0 1/2 1/2 1/2 0" POSCAR kappa-m202020.hdf5
```



KINETIC COLLECTIVE MODEL Version 1.0

-----

Running calculation of thermal conductivity on a 20x20x20 mesh

Temp[k]	Kappa[W/mK]	NL-length[nm]	K_kin[W/mK]	K_col[W/mK]	Sigma[adin]
200.0	249.911	332.358	241.257	8.655	0.513
300.0	138.636	162.718	133.562	5.074	0.523

-----

Calculation done

-----> Writting output files

|  
v  
Done

Figure 2.11: KCM thermal transport program example [80].

In Fig. 2.11 an example of the output of the KCM script developed to compute thermal properties of semiconductors from *first principles* is shown [80]. From this program it can be obtained the thermal conductivity for bulk materials as for reduced size samples using the kinetic-collective boundary approach (see **Chapter 4**). In addition the accumulated thermal conductivity as a function of the frequency and mean free path (MFP) can be obtained, as well as temperature dependent relaxation times and non-local length to be used in a full hydrodynamic model.

### 2.7.1 Calculation tips

In the calculations of IFCs using the direct method in a supercell it is preferable to use a cubic supercell. This will simplify the identification of the crystal symmetries. In addition, a cubic supercell is more suitable for an isotropic choice of neighboring atoms in the calculation of anharmonic IFC.

In the calculation of the thermal conductivity in the KCM it is required to split  $N$  and  $U$  processes. As defined above, the differentiation of this processes is related to the 1BZ. Therefore depending on the choice of the cell used in for

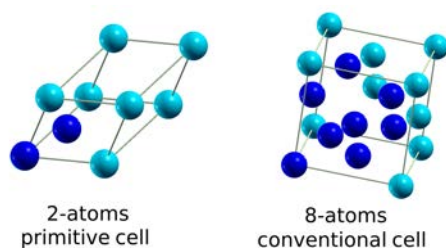


Figure 2.12: Primitive and conventional representation of the diamond-like cell for silicon. The dark blue atoms represent the atoms of the basis.

the sampling of the reciprocal space this splitting can be slightly different. Even though in the general definition of  $N$  and  $U$  processes it is not taken into account, the proper way to define them is in the 1BZ of the primitive cell, otherwise the choice of  $N$  and  $U$  processes will be arbitrary.

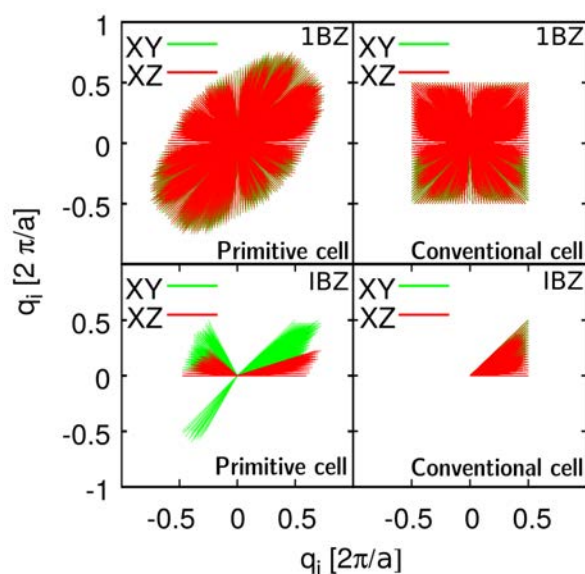


Figure 2.13: First Brillouin zone (1BZ) and irreducible Brillouin zone (IBZ) for the cubic conventional 8-atom cell (right) and for the primitive 2-atom cell (left) of the FCC structure. Green and red lines denote the projection of  $\mathbf{q}$  on the XY and XZ planes respectively.

In Fig. 2.12 the primitive cell and a conventional cell for silicon are represented in order to observe the different shape in each case. In Fig. 2.13 is represented the sampling of the reciprocal space in the primitive and conventional cells shown in Fig. 2.12. As expected, the reciprocal space of the rhombic primitive cell has a different shape as the one for the cubic conventional one.

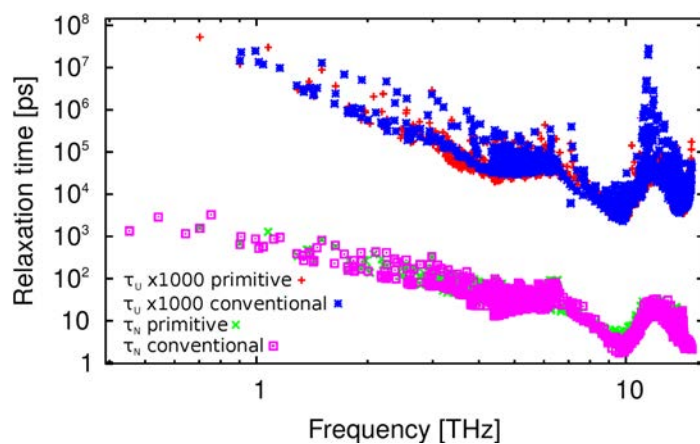


Figure 2.14: Normal and umklapp relaxation times calculated from a 2-atoms FCC primitive cell and 8-atoms conventional cell for silicon. The umklapp relaxation time is multiplied by x1000 to easier differentiation.

The  $N$  and  $U$  relaxation times as a function of frequency are represented in Fig. 2.14. As can be observed, even though the shape is quite similar in both cases, small differences can be appreciated. For simple structures this might not have a relevant effect in the calculation of thermal conductivity, but in complex cells the difference could be higher. Therefore it is always recommended to deal with primitive cell when using KCM to have well defined  $N$  and  $U$  processes.

# Chapter 3

## Thermal transport of bulk semiconductors in the KCM

In **Chapter 1** the Kinetic Collective Model (KCM), a framework that allow describing the phonon heat transport in solids including non-local and memory effects, has been presented. It has been shown how to obtain the relaxation times that determine the propagation of the different phonons on a sample as correction from the values obtained from the Relaxation Time Approximation (RTA).

In **Chapter 2** a set of equations and techniques allowing to calculate the magnitudes involved in the transport properties from *ab initio* have been described. In a first stage, it was explained how to obtain from the harmonic interactions of the lattice the phonon dispersion relations (DR) and mode velocities. On a second step, anharmonic effects allow calculating the phonon relaxation times for the different phonon collisions.

In this chapter, *ab initio* techniques are used in the KCM to describe the thermal conductivity avoiding any fitting parameter.

First, thermal conductivity of several well known diamond-like bulk semiconductors as Si, Ge, C (diamond) and GaAs are calculated in a wide range of sizes and temperatures, showing good agreement with experimental data without the use of any fitting parameter. The study is extended to other structures different from classical diamond-like crystals, like lead telluride (PbTe) or more complex materials such as  $\alpha$ -quartz ( $\text{SiO}_2$ ) or bismuth telluride ( $\text{Bi}_2\text{Te}_3$ ).

On a second part the KCM is applied to study the thermal conductivity of  $\text{Si}_{1-x}\text{Ge}_x$  and  $\text{In}_x\text{Ga}_{1-x}\text{As}$  alloys. The calculated thermal conductivities match well with the experimental data at different alloy concentrations. The model shows that impurity concentrations as little as 0.4% effectively suppress the collective contribution to the thermal conductivity in  $\text{Si}_{1-x}\text{Ge}_x$ , while in  $\text{In}_x\text{Ga}_{1-x}\text{As}$ , non-negligible collective contribution (15%) is present at all alloy concentrations. The study shows the significance of proper inclusion of  $N$  processes even

in alloys for accurate modeling of the thermal transport.

Finally graphene has been also calculated in the KCM to study a sample material where collective regime is dominant. The correct prediction of kinetic alloys and collective graphene shows the strength of the KCM.

The results are compared with conventional pure kinetic models and is shown that the split of the thermal conductivity in a kinetic and collective contribution allows to understand some discrepancies with experimental data of those models.

### 3.1 Dispersion relations and density of states

To obtain the DR of the studied materials, information about the unit cell and atomic masses is required. In the present case, for Si, Ge, C, a FCC bravais lattice with 2 atoms in the basis is defined, known as diamond structure. In this case the basis consists on one atom in the position (0,0,0) and the other at (1/4, 1/4, 1/4). For GaAs, Ga is in (0,0,0) while As in (1/4, 1/4, 1/4). In the case of the alloys, the virtual  $\text{Si}_{1-x}\text{Ge}_x$  atom behaves in the same way of Si for instance, but with the mass of the defined stoichiometry  $x$ . On the other side,  $\text{In}_x\text{Ga}_{1-x}\text{As}$  behaves like GaAs, where the place of Ga is occupied by a virtual atom  $\text{In}_x\text{Ga}_{1-x}$ . PbTe has a NaCl structure, that is a FCC with 2 atoms in the basis, one at (0,0,0) and the other at (0, 1/2, 0). In the case of more complex structures,  $\alpha$ -quartz has an hexagonal cell with 9 atoms and  $\text{Bi}_2\text{Te}_3$  an hexagonal cell with 15 atoms. The different studied structures can be observed in Fig. 3.1.

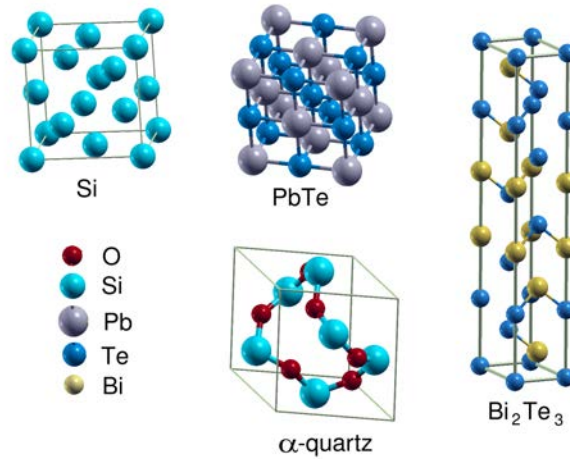


Figure 3.1: Crystal structures of the different studied materials obtained with XCrySDen [81].

All the *ab initio* magnitudes required for the calculations of DR and density

of states (DOS) detailed in **Section 2.2** are calculated from *first principles* using the QUANTUM ESPRESSO package [49] and VASP package [74, 75, 76, 77].

For Si, Ge, C, GaAs and the alloys QUANTUM ESPRESSO has been used, which implements Density Functional Theory (DFT) [46, 47] under the Local Density Approximation (LDA) in the parametrization of Perdew and Zunger [82]. Core electrons were accounted for with norm-conserving pseudopotentials of the Von Barth-Car type [83]. Plane waves were cut off at an energy of 60 Hartree. Born effective charges, which account for the electrons shared in the covalent bond in polar materials, and dielectric tensor were employed for GaAs to account for its polar behavior. The calculations have been carried on a  $3 \times 3 \times 3$  supercell with 216 atoms generated from the conventional 8-atoms cell. The harmonic and anharmonic interatomic force constants (IFC) have been calculated in a  $4 \times 4 \times 4$   $\mathbf{q}$ -point grid.

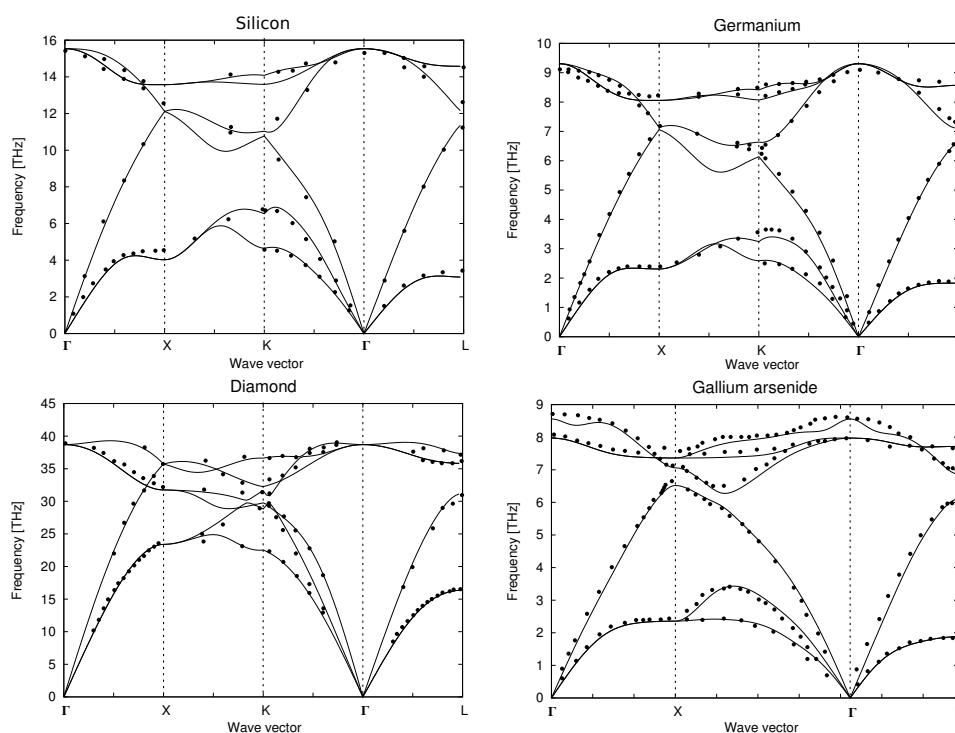


Figure 3.2: Dispersion relations of silicon, germanium, diamond and gallium arsenide along high symmetry directions. Dots represent experimental data from [40, 84, 85].

Fig. 3.2 shows the DR of the studied pure semiconductors. As one can observe, the DR for silicon and germanium are quite similar despite differences in the maximum frequency value. For diamond, the optical branches achieve fre-



quencies as high as 40 THz due to the small mass of the atoms. The lighter the atom, the higher the maximum frequency.

The DR of gallium arsenide have one important difference compared to the above materials. At the gamma point ( $\Gamma$ ) there is a splitting of the optical branches that is not observable in the other studied materials. The origin of such behavior is the effect of the Born charges appeared as a consequence of its polar nature.

From the DR it is possible to calculate the DOS for each material through a binning of the frequencies of each branch in a frequency region  $d\omega$ . Fig. 3.3 shows the DOS obtained from the DR shown in Fig. 3.2. Direct correlation can be observed from the shape of the DR and DOS. The zones in the DR where there is more concentration of occupied bands corresponds to the higher concentration of states in the DOS.

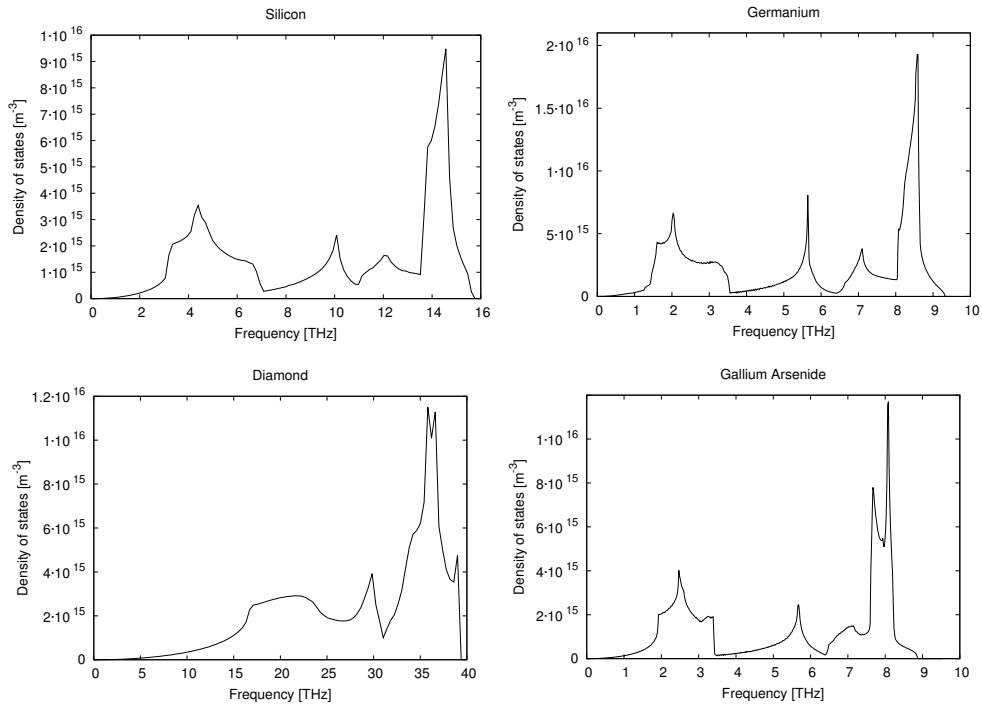


Figure 3.3: Density of states of silicon, germanium, diamond and gallium arsenide.

For the calculation of  $\text{Si}_{1-x}\text{Ge}_x$  and  $\text{In}_x\text{Ga}_{1-x}\text{As}$  alloys the Virtual Crystal Approximation (VCA) described in **Section 2.6.1** has been used. At each composition  $x$ , the lattice parameter was adjusted until the pressure was less than 0.1 kbar. Solution of the ensuing dynamical matrix provides the DR and transport parameters. In this case the DR will have a similar shape as found in the

previous cases, as the crystal cell is the same. While  $\text{Si}_{1-x}\text{Ge}_x$  will have DR similar to those of Si and Ge,  $\text{In}_x\text{Ga}_{1-x}\text{As}$  will have the shape of GaAs, again with the splitting of the optical branches at the  $\Gamma$  point due to its polar behavior.

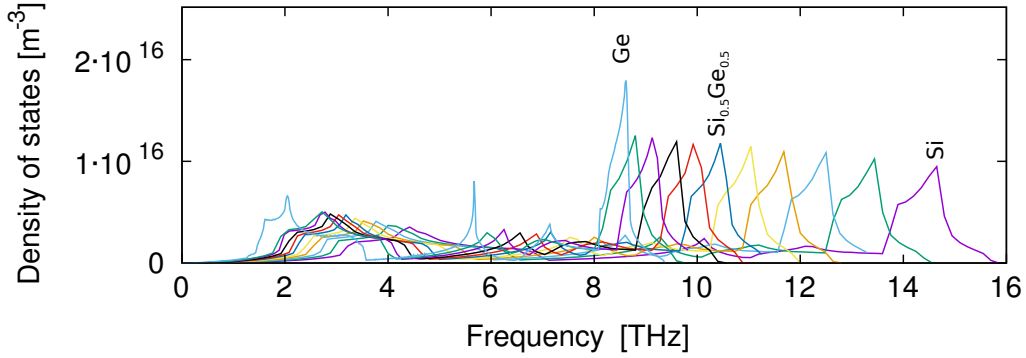


Figure 3.4: Density of states for different  $\text{Si}_{1-x}\text{Ge}_x$  alloys ranging from silicon to germanium with increments of  $x=0.1$  in the germanium concentration.

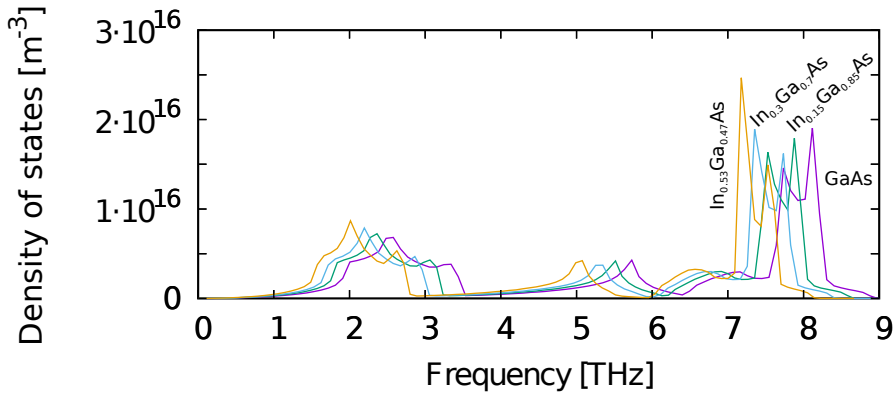


Figure 3.5: Density of states for different  $\text{In}_x\text{Ga}_{1-x}\text{As}$  alloy concentration.

Fig. 3.4 and Fig. 3.5 show the DOS for the  $\text{Si}_{1-x}\text{Ge}_x$  and  $\text{In}_x\text{Ga}_{1-x}\text{As}$  alloys for different alloy concentrations  $x$ . It can be observed how the DOS of each stoichiometry has a similar shape but the maximum achievable frequency is reduced as the total mass is increased.

In the case of PbTe and more complex materials as  $\alpha$ -quartz and  $\text{Bi}_2\text{Te}_3$  the calculations have been done using VASP under the LDA. LDA pseudopotentials in the parametrization of Perdew and Zunger are used [86]. Plane waves are

cut off at 300 eV. For the simulations of PbTe is used a  $4 \times 4 \times 4$  cubic cell, for  $\alpha$ -quartz a  $6 \times 6 \times 3$  supercell with 972 atoms, and for  $\text{Bi}_2\text{Te}_3$  a  $3 \times 3 \times 1$  supercell of 135 atoms. For the computation of DR, DOS and IFC has been used a  $4 \times 4 \times 4$   $\mathbf{q}$ -point grid in the first case, a  $4 \times 4 \times 2$  for  $\alpha$ -quartz and  $3 \times 3 \times 1$  for  $\text{Bi}_2\text{Te}_3$ .

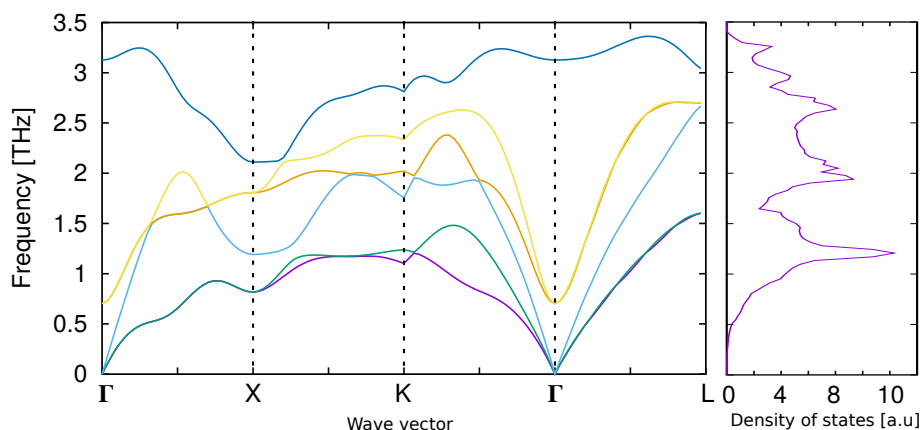


Figure 3.6: Dispersion relations along high symmetry directions and density of states of PbTe.

Fig. 3.6 shows the DR and DOS of PbTe. It can be observed that, although is a FCC structure with 2 atoms in the basis as in the previous studied cases, the shape of both representations is quite different. This is caused by the different basis of each crystal structure. In Fig. 3.7 the same plot is done for  $\alpha$ -quartz. In this case, the primitive cell has 9 atoms, therefore will appear 27 phonon bands. An appreciable feature of this material is the appearance of a gap larger than 5 THz.

In  $\text{Bi}_2\text{Te}_3$  the shape of the DR and DOS is used a hexagonal conventional cell of 15 atoms instead of the trigonal one of 5 atoms. This is more suitable for the generation of a symmetric supercell for next anharmonic ICF calculations.

The used cell will provide 45 phonon branches. In this case, as well as in  $\alpha$ -quartz, the high mass of the atoms are responsible for the low energy phonons, in the opposite way as pointed out for diamond in Fig. 3.3.

## 3.2 Scattering rates and mean free times

To compute the thermal conductivity, in addition to the DR and DOS, which provide the phonon velocities and number of phonon modes, it is necessary to obtain the phonon collision relaxation times. Such relaxation times are obtained from the phonon scattering rates through the collision matrix.

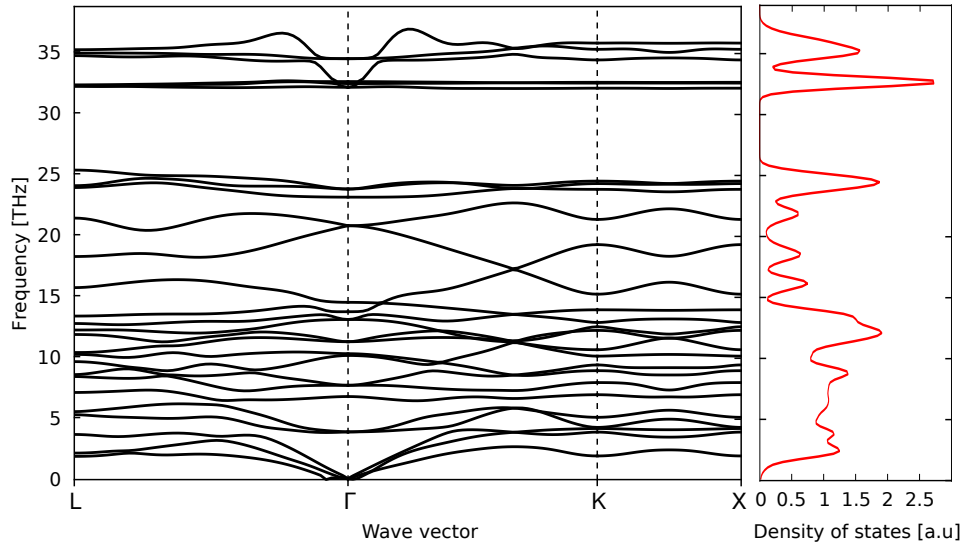


Figure 3.7: Dispersion relations along high symmetry directions and density of states of  $\alpha$ -quartz.

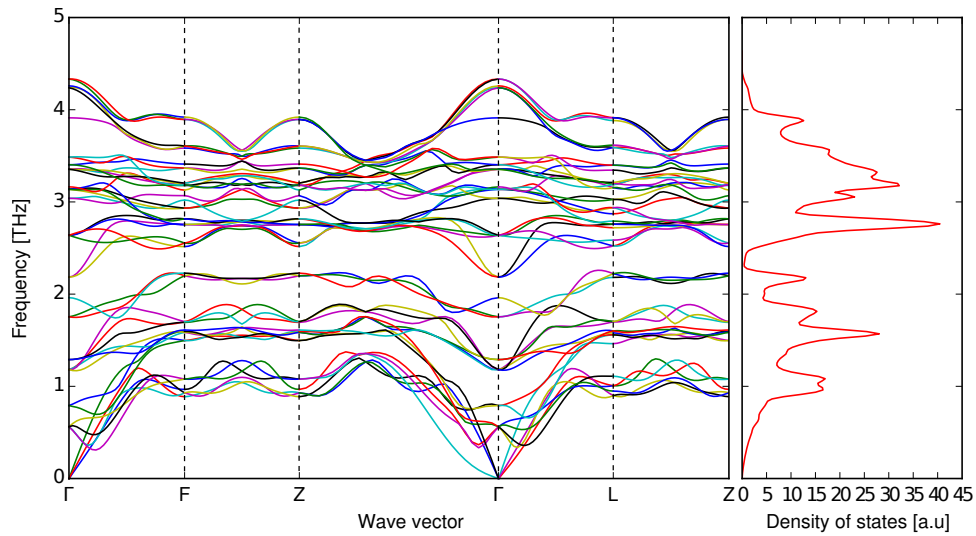


Figure 3.8: Dispersion relations along high symmetry directions and density of states of  $\text{Bi}_2\text{Te}_3$ .

In the KCM, the phonon relaxation times are obtained by a combination of two contributions, the kinetic and the collective relaxation times. These are two different averages of the resistive scattering mechanisms present in the sample.

The linear combination is calculated through the switching factor  $\Sigma$ , including normal ( $N$ ) scattering as defined in **Section 2.4** Eqs. (2.74)-(2.75).

The originality of KCM approach is that the relaxation times are based on the RTA but splitting  $N$  and umklapp ( $U$ ) processes. From this, the KCM can be understood as a generalization of the RTA. In addition, this generalization allows including the effect of the conservation laws on the thermal transport. The connection of conservation laws with the changes in the relaxation times allows a deeper understanding of the underlying physics despite of the simplicity of the approach.

The calculation of the relaxation times requires to obtain a set of anharmonic IFC to generate the collision matrix (see **Section 2.3**). This step requires a large number of calculations. For cubic cells it is possible to use the same supercell as used in the calculation of the DR. Calculations of the interactions up to 3rd neighbors have been performed to compute second and third order force constants.  $N$  and  $U$  phonon relaxation times are obtained through the anharmonic IFC. A  $40 \times 40 \times 40$   $\mathbf{q}$ -point grid is used for phonon Brillouin zone sampling in such calculations, while a  $160 \times 160 \times 160$  mesh is used for a finer DOS calculations. For this purpose the open code package ALAMODE [78] is used, where splitting of  $N$  and  $U$  events has been manually implemented in the code. Extrapolation of the latter values has been done for low frequencies in the DOS mesh sampling.

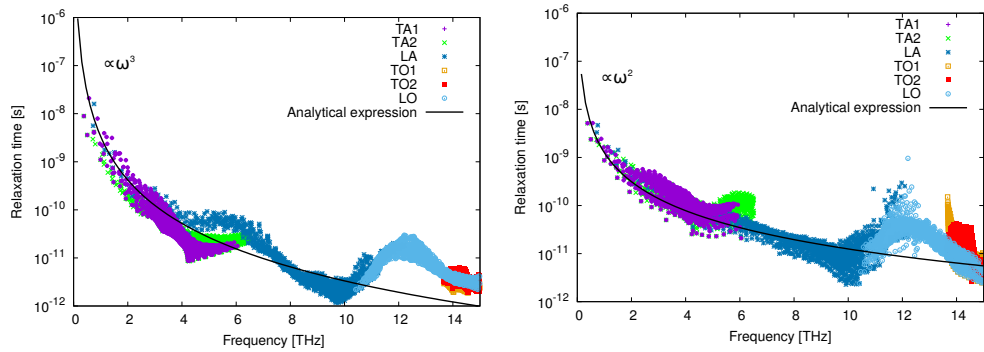


Figure 3.9: Umklapp (left) and normal (right) silicon relaxation times calculated from *first principles* in a  $40 \times 40 \times 40$   $\mathbf{q}$ -point grid at 300 K. Solid lines represent analytical expressions.

From Fig. 3.9 the relaxation times of each of the acoustic and optical branches of silicon can be observed. It is interesting to compare the *ab initio* results with analytical expressions  $\tau = A \cdot \omega^n$ . This kind of analytical expressions were used previously of the implementation of the *first principles* calculations in an achievable computational time [1, 27]. Nowadays analytical expressions for the

relaxation times can be used as a good approximation for fast calculations or even to obtain results at very low frequencies, where the required computational resources are still very high, as shown in **Section 5.3**.

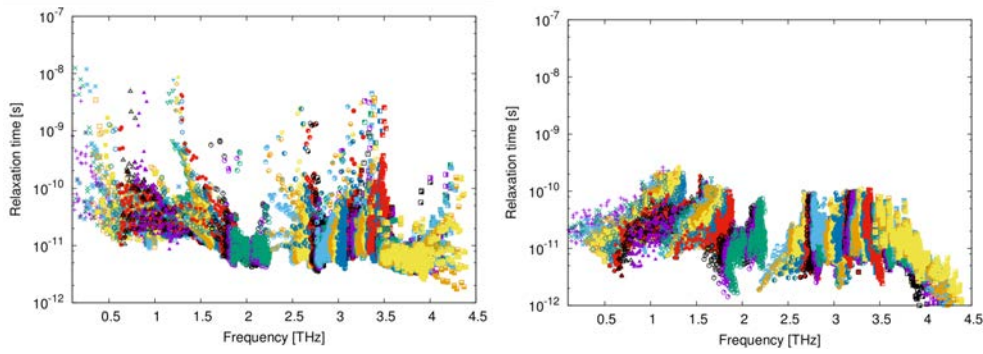


Figure 3.10: Umklapp (left) and normal (right) bismuth telluride relaxation times calculated from *first principles* in a  $24 \times 24 \times 8$   $\mathbf{q}$ -point grid at 300K. Indexation has been omitted to avoid mix-up. Colors are considered to show the trend of the different branches.

For  $\text{Bi}_2\text{Te}_3$  and  $\alpha$ -quartz the  $N$  and  $U$  three phonon scattering relaxation times are calculated using Phono3py [79] in a  $24 \times 24 \times 8$  and  $20 \times 20 \times 20$   $\mathbf{q}$ -point grid sampling respectively.

For diamond-like semiconductors the trend of the  $N$  and  $U$  relaxation times are very similar as they are strongly dependent of cell structure. For more complex materials like  $\text{Bi}_2\text{Te}_3$  the frequency behavior can be significantly different. In Fig 3.10 are represented the  $N$  and  $U$  relaxation times for  $\text{Bi}_2\text{Te}_3$ . As it can be observed, there is a huge dispersion in the relaxation time of each branch in terms of frequency. This behavior makes it complicated to define an analytic expression able to fit the data as has been found for the previous semiconductors. Despite of this drawback, approximate calculations in terms of frequency can be done by averaging the relaxation time in a fraction  $d\omega$ . More accurate results can be obtained through a full  $\mathbf{q}$ -mode calculation, but from a computational point of view access to low frequency phonons is still complicated.

Finally, in addition to the  $N$  and  $U$  relaxation times, for real bulk materials its is also necessary the relaxation time corresponding to the impurity/mass defect scattering events. Using Eq. (2.51) or Eq. (2.53) from **Section 2.3** in a  $\mathbf{q}$  or  $\omega$ -mode respectively the isotope scattering can be directly calculated. Fig. 3.11 shows the impurity relaxation time for the studied pure samples corresponding to natural isotopic concentration. As can be observed, at low frequencies the trend is  $\tau_I \propto \omega^{-4}$ . From Tamura's expression Eq. (2.53) there is a dependence  $\tau_I^{-1} \propto D(\omega)\omega^2$ , where  $D(\omega)$  is the DOS. At low frequencies  $D(\omega) \propto \omega^2$ , therefore it

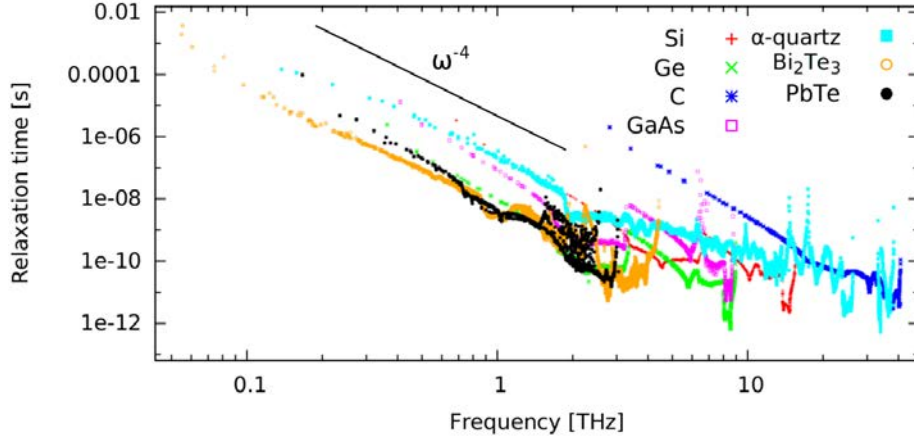


Figure 3.11: Impurity relaxation time for Si, Ge, C, Ge, PbTe,  $\alpha$ -quartz and  $\text{Bi}_2\text{Te}_3$  as a function of frequency in a  $20 \times 20 \times 20$   $\mathbf{q}$ -point grid.

is clear that  $\tau_I \propto \omega^{-4}$ . In **Section 5.2** the influence of this scattering event in the transient response of thermal conductivity of alloys is discussed.

### 3.3 Kinetic slowdown

In the RTA  $N$  processes are treated equivalent to  $R$  ones. Therefore, the total relaxation time obtained under this approximation can be expressed as:

$$\tau_{RTA}(\omega) = \frac{1}{\frac{1}{\tau_R(\omega)} + \frac{1}{\tau_N(\omega)}}. \quad (3.1)$$

As in most cases  $\tau_N < \tau_R$  (specially at low frequencies),  $\tau_N$  dominates, and the obtained relaxation time is lower than considering only resistive collisions. A reduction of the resistive effects is necessary but not sufficient to obtain the thermal conductivity. The KCM may have an explanation of why the thermal conductivity in the classical RTA seems to indicate that  $N$  scattering is acting as a resistive collision. Having a look at the KCM expression, the total relaxation time is expressed as  $\tau_{KCM}(T) = \hat{\tau}_K(T) \cdot (1 - \Sigma) + \hat{\tau}_C(T) \cdot \Sigma$ , where  $\hat{\tau}_K(T) \cdot (1 - \Sigma) = \tau_K(T)$  and  $\hat{\tau}_C(T) \cdot \Sigma = \tau_C(T)$  are the kinetic and collective contributions to the total relaxation time. The hat  $\hat{\cdot}$  denotes the limiting cases. Developing the kinetic contribution term:

$$\tau_K = \hat{\tau}_K(T) \cdot (1 - \Sigma) = \hat{\tau}_K(T) \cdot \left(1 - \frac{1}{1 + \frac{\tau_N(T)}{\hat{\tau}_K(T)}}\right) = \frac{1}{\frac{1}{\hat{\tau}_K(T)} + \frac{1}{\tau_N(T)}}, \quad (3.2)$$

where  $\hat{\tau}_K(T) = \tau_R(T)$ . Notice the similarities between the kinetic relaxation time  $\tau_K$  and  $\tau_{RTA}$ . The main difference is that in one case it is an integrated value depending only on the temperature, while in the other it is a frequency dependent magnitude. From this, it can be observed that in the KCM the factor that produces the reduction of the contribution of resistive terms is  $(1 - \Sigma)$ . This effect is the so-called kinetic slowdown, which can be observable in the relaxation times (see Fig. 1.2) but also directly in the thermal conductivity (see Fig. 3.16). This reduction of the mean free time (MFT) is a consequence of the appearance of a collective regime. In addition, from  $\tau_{KCM}(T)$  it can be observed that the total relaxation time requires an extra contribution  $\tau_C(T)$ . In systems where  $\tau_N > \tau_R$ ,  $\Sigma \rightarrow 0$  and  $\tau_{RTA} \approx \tau_{KCM} = \hat{\tau}_K$  provides a good approximation. On the contrary, when  $\tau_N \ll \tau_R$ , the contribution of  $\tau_C$  is relevant and the RTA underestimates the thermal conductivity [3].

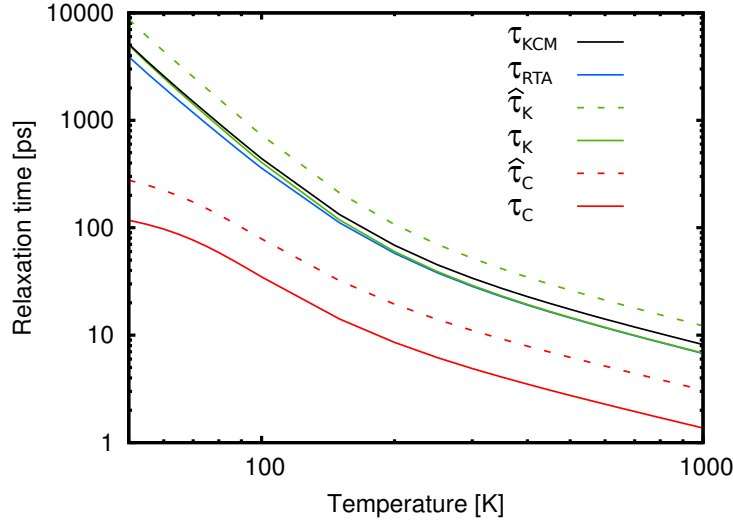


Figure 3.12: Temperature dependent relaxation times for bulk silicon.

The effect of  $N$  processes on the relaxation times in the RTA and KCM for bulk silicon is represented in Fig. 3.12. It can be observed that for temperatures above 150 K,  $\tau_{RTA}$  is equivalent to  $\tau_K$ , while at lower temperatures they are slightly different. This is not strange as, although the expressions are quite similar, in one case the addition of  $N$  and  $R$  processes is done prior to integration and in the other case afterwards. As, at low temperatures, thermal transport is dominated by low frequency phonons (where  $N$  scattering dominates), the failure of the RTA is higher in this region. At 300 K, for instance, the kinetic slowdown induced by  $(1 - \Sigma)$  in the KCM gives a value very close to the one obtained under the RTA. In this case, it can be also noticed that the non-negligible collective



contribution  $\tau_C(T)$  makes the total relaxation time in the KCM slightly higher than in the RTA. This difference will be more remarkable in materials where  $N$  processes are more dominant, like diamond.

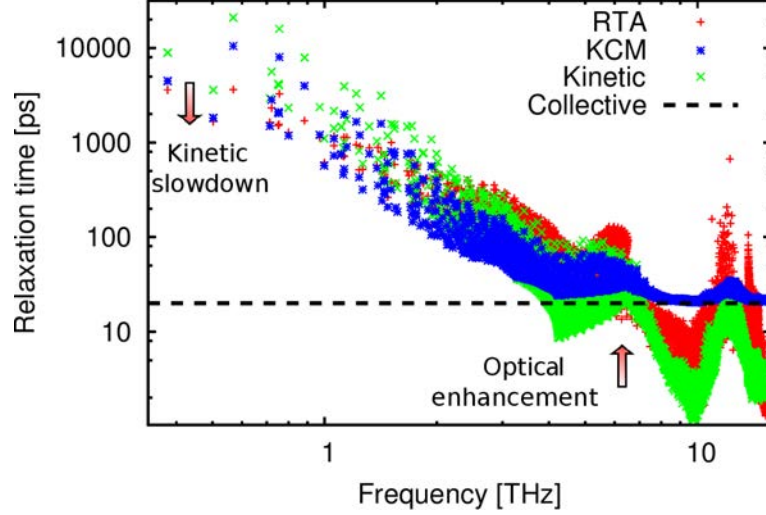


Figure 3.13: Frequency dependent relaxation times for bulk silicon. Comparison of RTA, KCM, kinetic (resistive) and collective relaxation times from Alamode.

In the frequency domain, the kinetic slowdown is represented in Fig. 3.13. Here the kinetic (resistive, i.e. umklapp and impurity/mass defect) and collective relaxation times, which give the total KCM relaxation time ( $\tau(\omega) = \hat{\tau}_K(\omega) \cdot (1 - \Sigma) + \hat{\tau}_C(T) \cdot \Sigma$ ) are compared to RTA. Notice that the collective relaxation time is also resistive but frequency independent (see **Section 2.4**). From this figure the effect of  $\Sigma$  in reducing the contribution of the low frequency resistive phonons is clear. In addition, it is observable that the RTA in this region provides similar relaxation times. What the RTA is not able to reproduce properly is the enhancement of optical phonons. This effect is caused by the collective contribution  $\hat{\tau}_C \cdot \Sigma$ . As in the high frequency region  $\tau_C > \tau_K$ , the total relaxation time is dominated by the collective term. This contribution makes the RTA underestimate the thermal conductivity of silicon by  $\sim 20$  W/mK [3]. In addition, this is the reason why in Fig. 3.12  $\tau_{RTA} < \tau_{KCM}$ .

As have been shown, the incorrect inclusion of the  $N$  processes as resistive in the RTA gives a reduction of the thermal conductivity that must be interpreted correctly based in the KCM formalism. Otherwise wrong results will be obtained in cases where  $N$  scattering is dominant. Also, the use of the  $\Sigma$  factor allows quantifying exactly the reduction of the thermal conductivity due to  $N$  effects. This information is completely lost using RTA or with full solutions, as

in the latter case only a single value of relaxation time or thermal conductivity is obtained, in contrast to the KCM.

## 3.4 Thermal conductivity of bulk materials

The thermal conductivity of bulk materials have been calculated using the KCM *ab initio* relaxation times shown in **Section 3.2** and the thermal transport equations from **Section 2.4**.

The model has been tested successfully using integrations with averaged frequency and  $\mathbf{q}$  dependent expressions. While for the latter case it is necessary to increase the grid point sampling until achieve convergence, the former allows easy extrapolation to low frequencies with suitable expressions (see **Section 5.3**).

### 3.4.1 Group IV and III-V semiconductors

Table 3.1 shows the values of the parameters concerning the calculations of thermal conductivity.

Material	Lattice parameter [Å]	$\gamma$ [adim]
Silicon	5.401	$20.01 \cdot 10^{-5}$
Germanium	5.775	$58.7 \cdot 10^{-5}$
Diamond	3.573	$7.54 \cdot 10^{-4}$
Gallium Arsenide	5.547	$\gamma_{Ga} = 0, \gamma_{As} = 1.97 \cdot 10^{-4}$

Table 3.1: Values of lattice parameter, mass defect term  $\gamma$  for natural bulk group IV and III-V semiconductors.

The calculated thermal conductivities of KCM compared to experimental measurements for bulk Si, Ge, diamond and GaAs samples in a range of temperatures are plotted in Fig. 3.14. Good agreement is obtained between predictions and experimental data without any adjustable parameter. Similar results for bulk samples have been reported using the iterative solution of the BTE [90]. As discussed in **Section 3.3**, in samples where  $N$  scattering is important, like diamond or graphene, RTA underestimates the thermal conductivity [24], as the collective contribution is neglected in this approach. Notice that the experimental data have a finite size of the order of  $\sim 10^{-3}$  m, therefore boundary effects can be noticed at low temperatures.

The dependence of  $\Sigma$  on temperature and size could be key to interpret experiments at different temperatures and sizes [6, 91]. Indeed, the collective con-

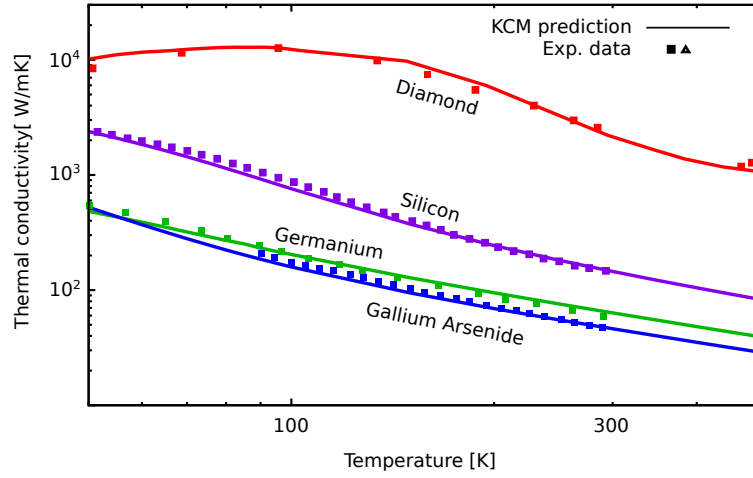


Figure 3.14: Thermal conductivity of bulk silicon, germanium, diamond and gallium arsenide in terms of temperature [62, 87, 88, 89].

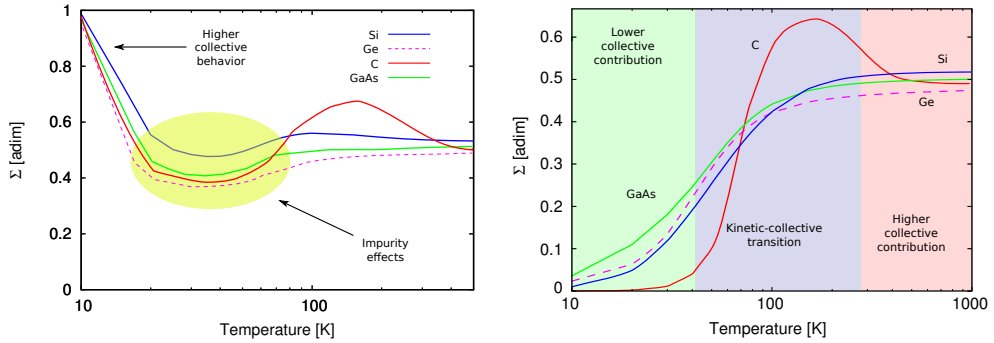


Figure 3.15: Switching factor  $\Sigma$  for Si, Ge, GaAs and C in terms of temperature. Left: bulk. Right:  $L_{\text{eff}} = 2.8$  mm.

tribution, which is the contribution to heat transport due to momentum conservation, is probably responsible for the hydrodynamic behavior proposed recently to describe thermal conduction in recent works [13, 14]. Then, hydrodynamic effects are expected to be relevant for finite values of  $\Sigma$ .

Fig. 3.15 shows the switching factor for the presented group IV and III-V semiconductors as a function of temperature. In the left plot is represented the  $\Sigma_{\text{bulk}}$ , where no boundary effects are included, which represents the intrinsic collective behavior. If boundary scattering does not limit the thermal transport, at low temperatures the thermal conductivity tends to infinite, as  $N$  scattering dominates. This dominance of  $N$  effects at low temperatures is also reflected in  $\Sigma_{\text{bulk}}$ . From this representation it can be observed that when no boundaries are

considered the collective behavior becomes more important as the temperature decreases. This increase is due to the fact that at low temperatures, although anharmonicities decrease, the  $N$  scattering is dominant in front of  $U$  processes. In recent theoretical works it has been reported the appearance of a hydrodynamic behavior at low temperatures in 2D materials like graphene [13, 14], in agreement with the behavior predicted by  $\Sigma_{\text{bulk}}$ . It is expected that when materials intrinsically exhibit collective behavior, as found in silicon or diamond, hydrodynamic heat flux equations can be used with suitable boundary conditions to compute the thermal conductivity as a function of temperature and size [15].

The  $\Sigma_{\text{bulk}}$  representation allows in addition to observe that the range where the impurity scattering has more impact on the thermal transport is around 20-100 K for the presented samples. It is also interesting to see the high value of  $\Sigma_{\text{bulk}}$  for diamond in the range of 70-300 K due to the dominance of  $N$  processes.

In real samples, even though are named bulk, boundary effects are present, and can be noticed at low temperatures. Boundary scattering is resistive, and its inclusion on the total resistive relaxation time will change the value of  $\Sigma$ . In Fig. 3.15 right it can be observed that for finite sizes near to bulk values ( $L_{\text{eff}} = 2.8$  mm) the collective contribution to thermal conductivity goes to zero as the temperature decreases due to boundary effects. As boundary scattering is independent of the temperature, at low temperatures it will dominate the thermal transport. At intermediate temperatures, around 100 K the samples exhibit a transition from a kinetic ( $\Sigma = 0$ ) to a collective ( $\Sigma = 1$ ) transport regime, where boundary effects begin to lose importance in front of impurity and 3-phonon scattering. When the temperature is increased  $\Sigma$  tends to saturate to a fixed value. In this region the collective contribution to thermal conductivity has its maximum value. In the next chapter it will be described in detail the effects of the boundaries on the collective regime through the  $\Sigma$  factor.

From Fig. 3.15 it can be observed that the reduction of the kinetic contribution (kinetic slowdown) at 300 K is around 50% for the presented materials ( $\Sigma \sim 0.5$ ). Despite of this significant value of  $\Sigma$ , the collective contribution to thermal conductivity is less than 10% for Si, Ge and GaAs. In contrast, in diamond such contribution is up to 16% of the total thermal conductivity. This means, that the effect of  $N$  processes in this material has a higher impact, not just by reducing the kinetic contribution but leading a significant collective one. Even though in Si, Ge and GaAs the collective contribution to thermal conductivity is not as important as in C, the high  $\Sigma$  indicates that hydrodynamic effects are expected to be observed at reduced scales.

The kinetic and collective contributions to thermal conductivity of  $L_{\text{eff}} = 1$  mm diamond as a function of temperature are represented in Fig. 3.16. It can be observed, that skipping the low temperature range where due to the finite size the boundary dominates, there is an important collective contribution to thermal

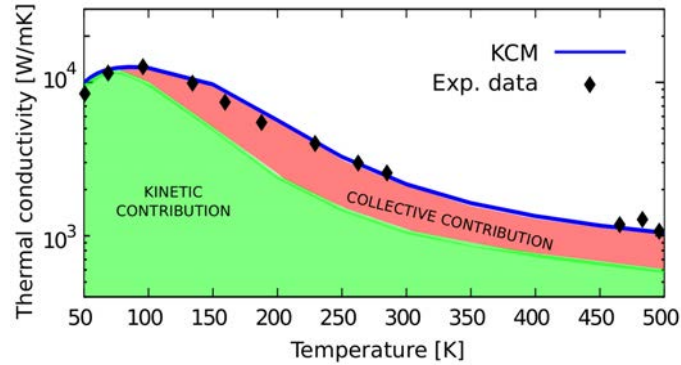


Figure 3.16: Kinetic and collective contributions to thermal conductivity of  $L_{\text{eff}} = 1$  mm diamond in terms of temperature. Experimental data from [88].

conductivity in the whole range, being  $\sim 400$  W/mK at 300 K.

### 3.4.2 Other pure structures

Regarding bulk materials, other structures as PbTe with different basis of that diamond-like materials,  $\alpha$ -quartz and  $\text{Bi}_2\text{Te}_3$  has been also studied in the *ab initio* KCM framework.

#### Bismuth telluride

The low thermal conductivity of  $\text{Bi}_2\text{Te}_3$  has made of this material a valuable thermoelectric, having a figure of merit around  $ZT \sim 1$  in its bulk form and achieving values up to 1.4 at reduced dimensions [92]. Recently it has been reported that *first principles* calculations of high anharmonic crystals may require to consider the temperature dependence of the Born-Oppenheimer potential energy surface [92]. Despite of this, LDA pseudopotentials at  $T = 0$  K have demonstrated also to provide good results [86]. Table 3.2 shows the parameters used for the *ab initio* calculations.

For the calculation of the thermal conductivity of bismuth telluride, due to its anisotropy, the thermal conductivity tensor will not be diagonal and with the same values for each component, as found in Si or Ge for instance. In this case it is not possible to do the classical simplification of  $\mathbf{v}_{\mathbf{q}} \otimes \mathbf{v}_{\mathbf{q}} \rightarrow 1/3c^2$ . It will be necessary to compute the whole tensor to determine the thermal conductivity of each component.

The thermal conductivity  $\kappa_{XX}$  of  $\text{Bi}_2\text{Te}_3$  is represented in Fig. 3.17. Good agreement between experimental data and the KCM prediction is obtained. As can be observed, the collective regime has only a small contribution at low

Material	Lattice parameter [Å]	$\gamma$ [adim]
Bismuth telluride	$a_1=(4.35, 0, 0)$ $a_2=(-2.18, 3.77, 0)$ $a_3=(0, 0, 29.86)$	$\gamma_{Bi} = 0, \gamma_{Te} = 2.84 \cdot 10^{-4}$

Table 3.2: Values of lattice parameter and mass defect term  $\gamma$  for natural bismuth telluride. The lattice vectors correspond to the conventional hexagonal cell.

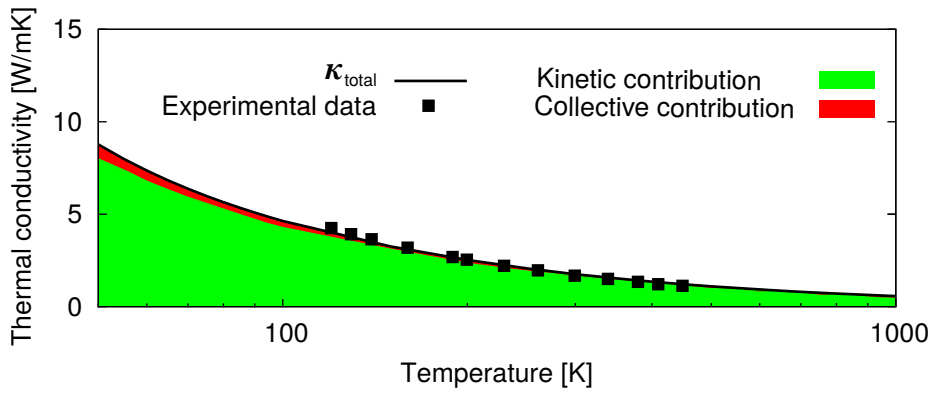


Figure 3.17: Thermal conductivity of bulk bismuth telluride. Solid black line represents the total thermal conductivity. The filled green line accounts for the kinetic contribution and the filled red zone for the collective contribution. Experimental data from [93].

temperatures, being less than 10% at 300 K. In contrast, the kinetic slowdown caused by the effect of  $N$  processes reduces the kinetic contribution up to a 53% ( $\Sigma = 0.53$ ).

The low thermal conductivity of bulk  $\text{Bi}_2\text{Te}_3$  has its origin on the high  $U$  scattering rates at low frequencies. As the  $U$  scattering rate increases the relaxation time decreases. Therefore, as  $\kappa \propto \tau_U$ , the thermal conductivity will be small. Comparing Fig. 3.9 and Fig. 3.10, it can be observed how in silicon the  $U$  relaxation time increases as  $\tau_U \propto \omega^3$  at low frequencies, while for  $\text{Bi}_2\text{Te}_3$  the exponent is clearly smaller than 2. This explains the huge difference of thermal conductivity between both materials.

### Lead telluride and $\alpha$ -quartz

Another test of the model has been done to calculate the thermal conductivity of PbTe and  $\alpha$ -quartz. In the case of  $\alpha$ -quartz, due to its high asymmetry, the

thermal transport will strongly depend on the crystal direction. Although the available experimental data for the  $YY$  and  $ZZ$  components is quite old [94], a broad comparison can be done with the KCM prediction. The values used for the *ab initio* simulations are shown in Table 3.3.

Material	Lattice parameter	$\gamma$
	[Å]	
Lead telluride	6.57	$\gamma_{Pb} = 1.94 \cdot 10^{-5}, \gamma_{Te} = 2.84 \cdot 10^{-4}$
$\alpha$ -quartz	$a_1=(4.87, 0, 0)$ $a_2=(-2.43, 4.22, 0)$ $a_3=(0, 0, 5.37)$	$\gamma_{Si} = 2.01 \cdot 10^{-4}, \gamma_O = 3.36 \cdot 10^{-5}$

Table 3.3: Values of lattice parameters and impurity terms  $\gamma$  for natural PbTe and  $\alpha$ -quartz. The lattice vectors corresponds to the NaClc and hexagonal cell respectively.

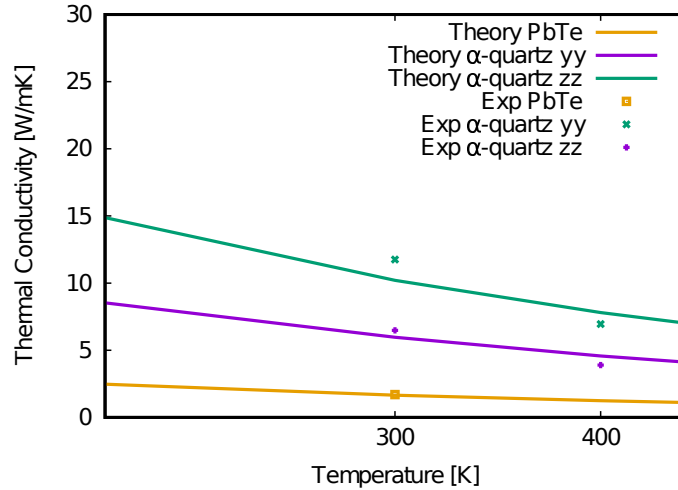


Figure 3.18: Thermal conductivity of PbTe and  $\alpha$ -quartz predicted by KCM. Experimental data from [94] and [95] for  $\alpha$ -quartz and PbTe respectively.

In Fig. 3.18 the KCM prediction of thermal conductivity in terms of temperature for PbTe and  $\alpha$ -quartz is represented. Good agreement with the experimental data in both cases can be observed. The small disagreement found in  $\alpha$ -quartz can have several explanations. As the crystal structure has very low symmetry, this can affect to the *first principles* calculations. A deeper study of convergence of all the parameters used for the calculations, as well as larger supercell is required in order to achieve better results. More recent experimental data will also help to compare with the theoretical predictions. The low thermal conductivity

of this materials can be attributed to the flatness of the phonon bands, which lead to small phonon velocities.

In the case of PbTe,  $\alpha$ -quartz<sub>YY</sub> and  $\alpha$ -quartz<sub>ZZ</sub> the kinetic slowdown is 50%, 48% and 55% respectively. Despite of the high  $\Sigma$ , the collective contribution to thermal conductivity in both materials is  $\sim 1\%$ ,  $\sim 6\%$  and  $\sim 0.4\%$  respectively.

### 3.4.3 Alloy thermal conductivity

Pure semiconductors can have significant collective effects while alloys, due to the high impurity scattering, are mainly kinetic. In the KCM, the splitting of the thermal conductivity in two contributions is able to describe properly the transition from a pure material to an alloy, in contrast to pure kinetic approaches.

The calculations for alloy samples require the use of mixed pseudopotentials using the VCA and the special treatment of the alloy scattering term described in **Section 2.6.1**.

The DR, DOS, IFC and different scattering terms have been computed for different alloy concentrations  $x$ . For  $\text{Si}_{1-x}\text{Ge}_x$ , such calculations have been carried in the VCA for  $x = 0.0025, 0.004, 0.01, 0.04, 0.1, 0.2, 0.4, 0.5, 0.82$  and for  $\text{In}_x\text{Ga}_{1-x}\text{As}$  at  $x = 0.01, 0.15, 0.3, 0.53$  compositions. Interpolation has been used in the latter case for smaller and intermediate concentrations.

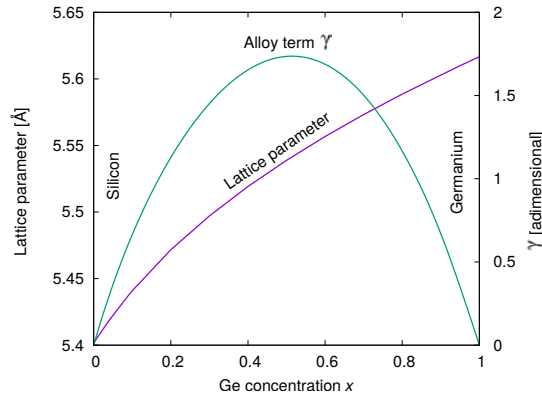


Figure 3.19: Lattice parameter and alloy term  $\Gamma$  for  $\text{Si}_{1-x}\text{Ge}_x$  alloy as a function of germanium concentration  $x$ .

In Fig. 3.19 the lattice parameter and the alloy term  $\gamma$  for  $\text{Si}_{1-x}\text{Ge}_x$  in terms of the Ge concentration  $x$  is represented. As can be observed, as the Ge con-



centration increases, both the lattice parameter and the alloy term increases as well. As it is expected, the lattice parameter continue increasing until achieve the value of pure germanium. In contrast, the alloy term increases until an alloy concentration of  $\sim 50\%$  and then starts to decrease, defining an inverse parabolic shape.

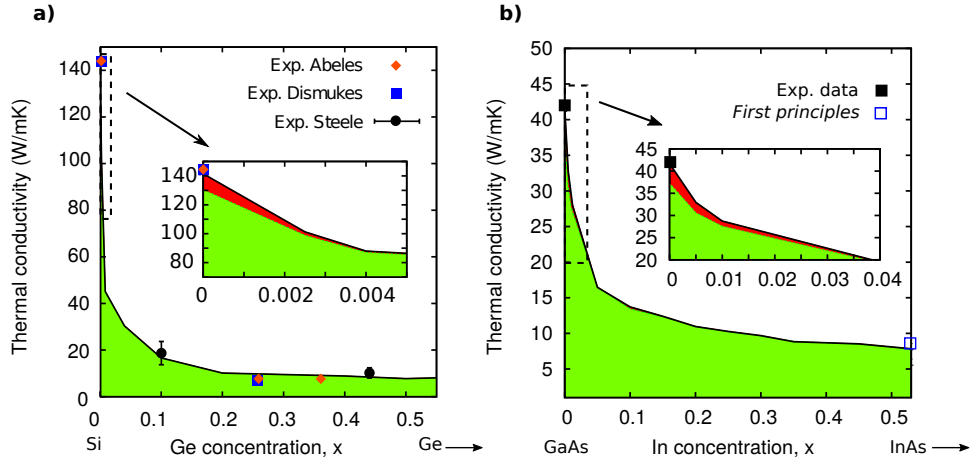


Figure 3.20: Thermal conductivity of  $L_{\text{eff}} = 7\text{mm}$  rods in terms of alloy concentration  $x$  at 300 K for **a)**  $\text{Si}_{1-x}\text{Ge}_x$  and **b)**  $\text{In}_x\text{Ga}_{1-x}\text{As}$ . Green and red filled zones denote the kinetic and collective contributions to the thermal conductivity respectively. The black solid line is the total thermal conductivity. Insets represent magnifications at low impurity concentrations. Experimental data for  $\text{Si}_{1-x}\text{Ge}_x$  are from [96, 97, 98]. GaAs experimental data are taken from [89] and the *first principles* model from [28].

Fig. 3.20 shows the KCM prediction of the thermal conductivity for  $\text{Si}_{1-x}\text{Ge}_x$  and  $\text{In}_x\text{Ga}_{1-x}\text{As}$  rods at 300 K. One observes that theoretical predictions (black lines) agree with experimental data for  $\text{Si}_{1-x}\text{Ge}_x$ . For  $\text{In}_x\text{Ga}_{1-x}\text{As}$  some inconsistencies between old published bulk experimental data [96, 99] can be noticed, reporting values smaller than 5 W/mK, and recent 1.6  $\mu\text{m}$  thin films measurements of 5.5 W/mK for  $\text{In}_{0.53}\text{Ga}_{0.47}\text{As}$  at 300 K [100]. The recent data suggests that bulk values are expected to be higher than 5.5 W/mK. Note that collective thermal transport (red region) is only important for very pure materials close to  $x = 0$ , being mostly destroyed with impurity fractions as low as 0.4% and 4% for  $\text{Si}_{1-x}\text{Ge}_x$  and  $\text{In}_x\text{Ga}_{1-x}\text{As}$  respectively.

From the insets it can be appreciated that although the kinetic contribution can describe most of the concentration range, it is not able to explain the conductivity near the pure region  $x \sim 0$ , where the collective term contributes almost up to a 10% of the thermal conductivity [71]. It is the correct treatment of  $N$  processes, as done by KCM or iterative and full solution methods, that provides good predictions at all concentrations. These results show that a proper

description of the collective contribution is necessary to understand the large drop in thermal conductivity at small impurity concentrations. In the case of  $\text{In}_x\text{Ga}_{1-x}\text{As}$ , it is visible that the reduction of the collective contribution when the alloy concentration is increased is not that sharp as found in  $\text{Si}_{1-x}\text{Ge}_x$ . This is a consequence of the difference of the strength of the alloy scattering in each sample: the isotopic mass variation term in  $\text{Si}_{1-x}\text{Ge}_x$  alloys is several times larger than in  $\text{In}_x\text{Ga}_{1-x}\text{As}$  alloys (see **Section 5.1**).

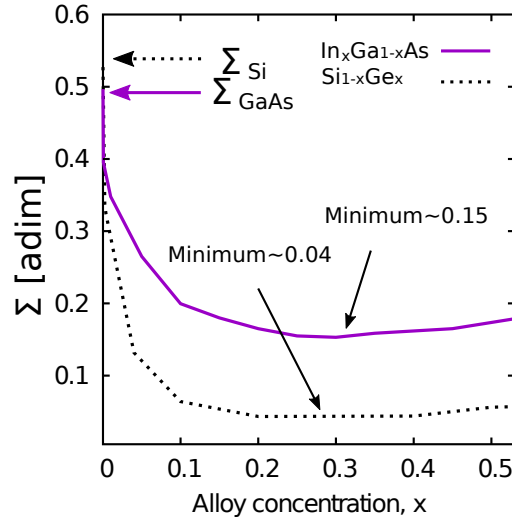


Figure 3.21: Switching factor  $\Sigma$  corresponding to Fig. 3.20a) and b) showing the transition to a kinetic-dominant regime as impurity increases.

A magnitude that quantifies differences between  $\text{Si}_{1-x}\text{Ge}_x$  and  $\text{In}_x\text{Ga}_{1-x}\text{As}$  is the  $\Sigma$  factor, represented in Fig. 3.21. For pure materials like Si and GaAs values of  $\Sigma_{\text{Si}} \sim 0.52$  and  $\Sigma_{\text{GaAs}} \sim 0.49$  at 300 K are obtained. When the alloy concentration is increased this value decreases fast below 0.1 for  $\text{Si}_{1-x}\text{Ge}_x$ , with a minimum of  $\sim 0.04$  around  $\text{Si}_{0.7}\text{Ge}_{0.3}$ . In contrast, in the case of  $\text{In}_x\text{Ga}_{1-x}\text{As}$  the reduction of  $\Sigma$  is smoother, decreasing from  $0.49 \rightarrow 0.15$  for In concentrations going from  $x = 0 \rightarrow x = 0.3$ . Since the larger the value of  $\Sigma$  the larger the collective contribution, the sharper change of  $\Sigma$  in  $\text{Si}_{1-x}\text{Ge}_x$  alloys as impurity increases translates into a sharper drop in conductivity, as displayed in Fig. 3.20.

A second issue to be pointed out, is that as a consequence of  $N$  scattering, do not only appear a collective contribution to thermal conductivity but also causes the slowdown of kinetic modes (kinetic slowdown). The pure kinetic term  $\hat{k}_k$  is thus reduced by a factor  $(1 - \Sigma)$ . Since the minimum values of  $\Sigma$  displayed in Fig. 3.21 are 0.04 for  $\text{Si}_{1-x}\text{Ge}_x$  and 0.15 for  $\text{In}_x\text{Ga}_{1-x}\text{As}$ , this correction amounts at least a 4% and a 15%, respectively. In general, according

to these calculations, it will be more important in  $\text{In}_x\text{Ga}_{1-x}\text{As}$  than in  $\text{Si}_{1-x}\text{Ge}_x$ .

It is important to notice, that although full solutions can provide the exact value of thermal conductivity, as KCM, the contribution of  $N$  effects can not be directly quantified. In contrast, the splitting of the thermal conductivity in a kinetic and a collective contribution in the KCM allows quantifying easily such contribution.

### 3.5 Graphene

In the study of bulk samples, the KCM has been applied in graphene, a trending topic 2D material, although intrinsically it is a zero bandgap semiconductor. Moreover, even though is a 2D material, the calculation of the thermal conductivity do not require to apply any boundary condition.

Material	Lattice parameter $\cdot a[\text{\AA}]$	$\gamma$ [adim]
Graphene	$a_1=(1, 0, 0)$ $a_2=(0.5, \sin(2\pi/3), 0)$ $a_3=(5, 0, 0)$	$7.39 \cdot 10^{-5}$

Table 3.4: Values of lattice parameter and mass defect term  $\gamma$  for natural graphene. The lattice vectors correspond to the primitive cell with lattice parameter  $a = 2.4678 \text{ \AA}$ .

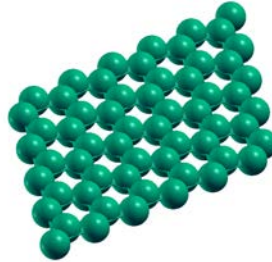


Figure 3.22: Crystal structure of graphene obtained with XCrySDen [81].

Table 3.4 and Fig. 3.22 show the crystal parameters and structure of graphene respectively used for the *first principles* calculations. As done with the other materials, first of all is required to calculate the DR, DOS and IFC. From Table 3.4 can be observed that despite of being a 2D material it is specified a  $z$  component. That is because the available *ab initio* softwares requires this parameter in order to create a supercell. In these calculations a  $6 \times 6 \times 1$  supercell with 72 atoms

has been used. Notice that the distance  $z(a_3)$  must be larger than the other two dimensions in order to avoid interaction of the atoms from the upper sheet when calculating IFC. The harmonic and anharmonic IFC have been computed in a  $3 \times 3 \times 1$   $\mathbf{q}$ -point mesh sampling.

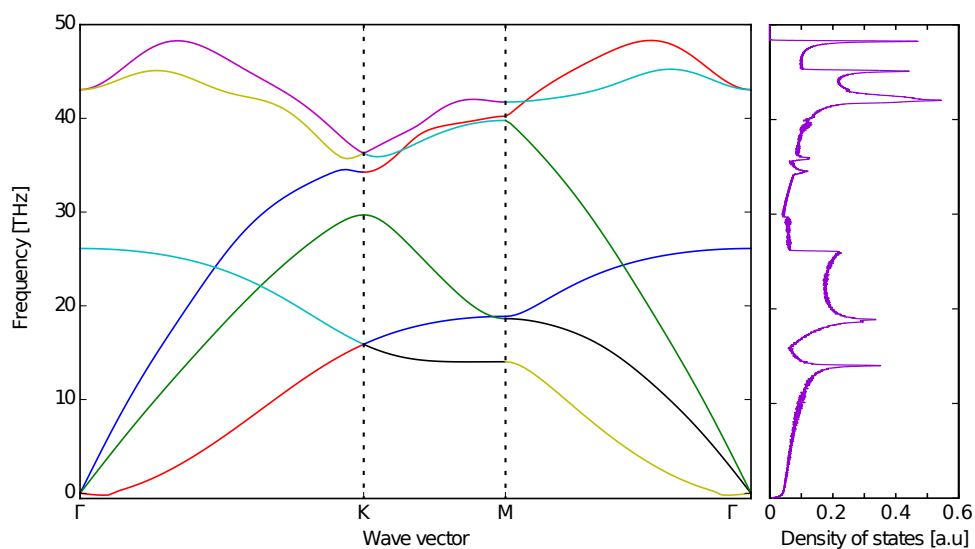


Figure 3.23: Dispersion relations and normalized density of states of graphene monolayer.

Fig. 3.23 shows the DR and DOS of graphene. As the primitive cell has 2 atoms in its basis, the DR representation shows 6 phonon bands.

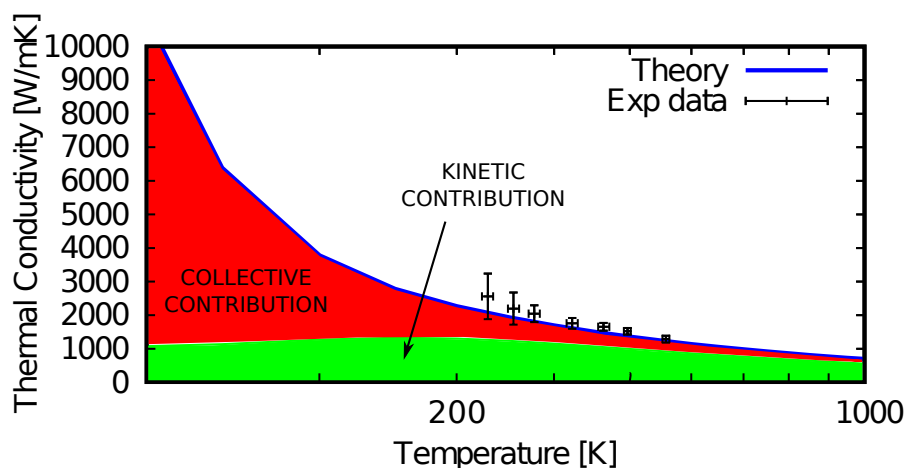


Figure 3.24: Thermal conductivity of graphene monolayer in terms of temperature. Experimental data are taken from [101].

The *ab initio* calculation of the thermal conductivity of graphene requires to scale the output value to the real volume. As it can be observed in Eq. (2.68) and Eq. (2.71), the thermal conductivity is normalized by the volume. As in the cell generation it is used a large  $z$  component to avoid undesired interactions, the larger the parameter the smaller the thermal conductivity. To obtain the final value of lattice thermal conductivity it is necessary to rescale this value to the interlayer distance of the bulk material, graphite in this case.

The thermal conductivity of a graphene monolayer with natural isotopic impurity concentration is shown in Fig. 3.24. The electronic contribution of intrinsic graphene has been measured to be around  $\kappa_e \sim 10$  W/mK at 300 K [102]. This value has been removed as a constant contribution at all temperatures to compare to the KCM prediction. For high doped graphene such contribution can achieve values of  $\kappa_e \sim 300$  W/mK at 300 K [103]. It can be observed that KCM provides a close prediction to experimental data within the error bars. A proper inclusion of the temperature dependent electronic contribution will help to improve the predictions. In this figure it is clear that in the thermal transport of graphene the collective regime plays an important role. At 300 K the contribution of the collective regime to the thermal conductivity is of 42%, and increases as the temperature goes down. This is due to the dominance of  $N$  scattering in front of the resistive mechanisms, having  $\Sigma \sim 0.7$  at 300 K. In agreement with KCM, the importance of collective effects on graphene has been recently proposed in several works to understand its thermal transport [14, 13].

Despite of the high importance of graphene for several electronic applications, its performance as a thermoelectric material is poor as intrinsically has no gap and high thermal conductivity. Other monolayer materials like phosphorene can be more suitable for this purpose [104].

From the present results obtained for graphene, it is clear that collective effects are important in order to understand its thermal transport. Therefore, a model able to quantify exactly the contribution of this collective effects, as done by KCM, is appropriate to study this kind of materials.

### 3.6 Thermal conductivity in other models

The solution of thermal conductivity provided by the *ab initio* KCM has been compared with other models presented in **Section 1.2**.

In Fig. 3.25 the predictions of the thermal conductivity as a function of temperature of the different presented models for natural bulk silicon and diamond are represented. As can be observed all the recent solutions provide good approximation to experimental data. It can be observed that the RTA slightly un-

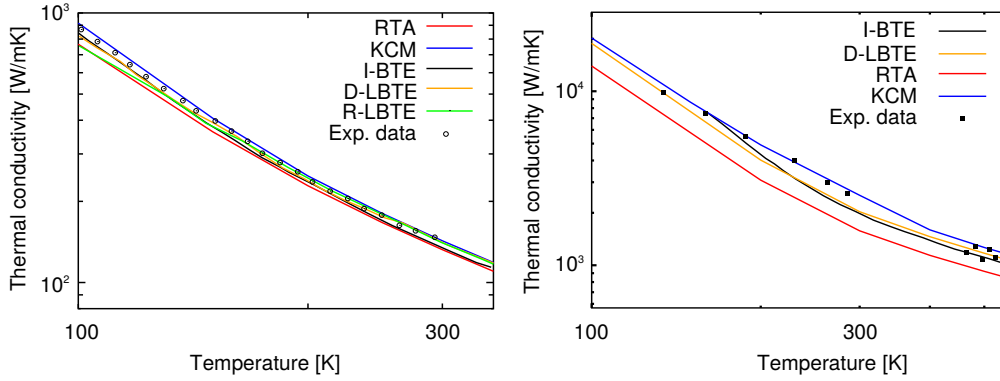


Figure 3.25: Left: Thermal conductivity of natural bulk silicon as a function of temperature for RTA, I-BTE [68], D-LBTE [21], R-LBTE [22] and KCM. Right: Thermal conductivity of natural bulk natural diamond as a function of temperature for RTA, I-BTE [68], D-LBTE and KCM using  $\mathbf{q}$ -mode integration.

derestimates the experimental value of the thermal conductivity in the whole temperature range for silicon, while for diamond underestimates up to 27%.

Differences between KCM and other models can be due to the expansion of the non-equilibrium distribution function. In general approaches it is used that the non-equilibrium distribution function is expanded to the first order in energy  $n = n_{eq} + n_1(\epsilon)$  (0th-moment of the distribution) or first order in momentum  $n = n_{eq} + n_1(\mathbf{q})$  (1st-moment of the distribution). This procedure accounts for the conservation of energy of the whole distribution but the momentum conservation is not globally imposed. The action of  $N$  scattering in the distribution can not be properly accounted because this scattering mechanism can not relax the 1st-moment (heat flux) and the 2nd-moment (flux of the heat flux) is directly affected. In contrast, the KCM, regarding the approximation done to calculate the relaxation times, is derived up to  $n$ th-moment of the distribution function. This expansion allows in addition to fulfill the momentum conservation globally. Doing so, hydrodynamic effects appear due to the reduction of the 2nd-moment equation to the 1st-moment, leading consequently to a generalized set of equations for the micro/nanoscale heat transport.

From a computational point of view, the energy and momentum conservation can also affect the solutions obtained by I-BTE, D-LBTE and R-LBTE. In first place, the energy conservation is imposed mathematically by a delta function. As explained in **Section 2.3**, this delta function is computed by a Gaussian or Lorentzian function or in a tetrahedron method, therefore, the energy conservation is never exactly fulfilled, even though the weight can be very small. In addition, having a phonon distribution function  $n \simeq n_0 + \Phi \cdot n_0(n_0 + 1)/k_B T$ , the scattering matrix element derived by Ziman [19] in Eq. (2.44) for the process

$$\mathbf{C} = \begin{pmatrix} \boxed{0} & 0 & 0 \\ 0 & \boxed{0} & 0 \\ 0 & 0 & N_{22} \end{pmatrix} + \begin{pmatrix} \boxed{0} & 0 & 0 \\ 0 & R_{11} & R_{12} \\ 0 & R_{21} & R_{22} \end{pmatrix}$$

Figure 3.26: Collision operator split in normal and resistive processes. Each line of the matrix corresponds to a different moment of the distribution function.

of annihilation of one phonon can be expressed as:

$$\Gamma_i \propto (\Phi_{i,1} - \Phi_{i,2} - \Phi_{i,3}), \quad (3.3)$$

where  $i$  refers to energy or momentum for instance. In the case of the energy,  $\Phi_i \propto \epsilon$  and for the momentum conservation  $\Phi_i \propto \mathbf{q}$ . Therefore for  $N$  processes  $\Gamma_i \equiv 0$  for the energy and momentum. The fact that this is not exactly fulfilled due to computational restrictions can have consequences in the calculation of any parameter derived from the scattering matrix, like the thermal conductivity.

In the KCM the energy and momentum conservation is always fulfilled because, as this is a known premise, it is directly imposed in the scattering matrix. In Fig. 3.26 the scattering matrix solved in the KCM is represented. As can be observed, the scattering matrix is split in two terms, referring to  $N$  and resistive ( $R$ , umklapp and impurity/mass defect) processes. The first element of the diagonal (red square) of each matrix corresponds to the energy conservation, and the second one (blue square) to the momentum conservation. As can be observed inside squares, the energy conservation is directly imposed in both terms. In addition, it can be noticed that the momentum conservation for  $N$  processes (blue square) is also imposed, as expected.

In the precise case of dealing with the full scattering matrix, when  $N$  collisions are dominant, the null value in the matrix element can carry problems on the diagonalization. In such cases this matrix element will fluctuate around the zero and the diagonal matrix is not invertible. Computationally this will create a divergence on the solution.

In Fig. 3.27 the solution of the D-LBTE from 20-1000 K compared with KCM solutions including spurious terms is represented. The series of KCM simulations for different values  $f \cdot \Gamma_N$ , where  $f = 1, 10^{-1}, 10^{-2}, 10^{-3}, -10^{-1}, -10^{-2}, -10^{-3}$  represents the effect of include a value  $f \cdot \Gamma_N$  where must be a zero according to Fig. 3.26. As it can be observed above 150 K this spurious terms do not have any effect on the thermal conductivity, but at lower temperatures, where  $N$  processes become more important, create divergences on the solution

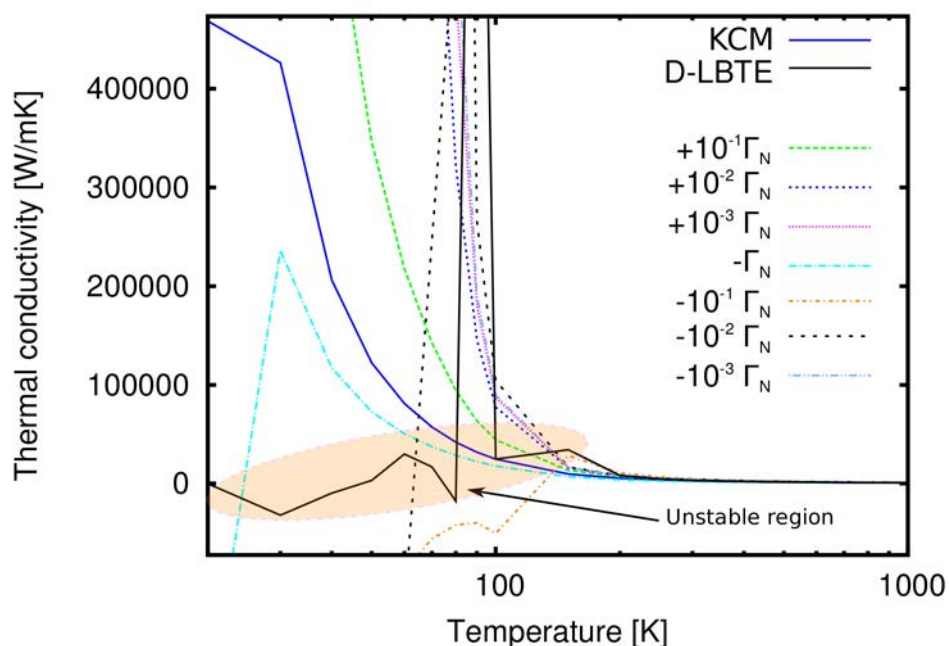


Figure 3.27: Thermal conductivity of natural bulk natural diamond as a function of temperature for D-LBTE obtained from Phono3py [79], KCM and altered solutions.

of the thermal conductivity. This kind of divergences are also observable in the D-LBTE solution (unstable region).

Regarding iterative methods to solve the BTE, it has been demonstrated that a wrong choice of the initial guess for the relaxation times can lead to divergences [22]. This can happen when the initial guess is very far from the real value. As the starting point is the classical RTA relaxation time, in materials where  $N$  is important, this value is far from the real one. This can happen in materials like diamond or graphene for instance. In such situations a more suitable starting point could be the KCM relaxation times, which are quite close to the real value and can provide fast convergence.





# Chapter 4

## Low dimension thermal conductivity in the KCM

When studying thermal transport, low dimension systems are of great importance. Once the size of a sample is reduced, thermal properties are different from those expected for bulk materials. In the case of thermal conductivity, boundary effects at reduced sizes induce a reduction of the thermal transport.

The most common way to introduce boundary effects has been to limit the contribution of phonons through Casimir's model [61]. In recent years the evolution of the technology has allowed to synthesize samples of small size up to few nanometers, where the boundary effects in thermal transport need a more complex treatment.

The KCM gives a new approach to the problem of boundary effects with respect to the viewpoint of pure kinetic models, where only individual boundary scattering processes can be accounted. Although the latter models with adjustable parameters can provide good fits to experimental data at the nanoscale, the relaxation times used at small scales still need to be modified with respect to the ones used in bulk [105].

From the general Guyer and Krumhansl kinetic-collective boundary approach in the KCM, a kinetic treatment of the boundary effects through the Matthiessen's rule of the Casimir's term in the kinetic regime is used. In contrast, for the collective regime contribution, the use of a form factor  $F$  gives a Poiseuille-like profile to the heat flux. Using this model, good predictions for small samples can be achieved.

Additionally, a full KCM hydrodynamic model is used to study thermal transport at the nanoscale. This approach shows that a hydrodynamic model with suitable boundary conditions can also provide remarkable agreement with the experimental data at low dimension scales.

## 4.1 Kinetic-collective boundary approach

In **Chapter 3** boundary effects have been neglected. To include size effects in the classical KCM formulation it is required to treat the kinetic and collective regime independently. In the kinetic term, boundary effects are included, as usual, through the Matthiessen's rule using Casimir's expression  $\tau_B = L_{\text{eff}}/v$  [61], where  $L_{\text{eff}}$  is the characteristic size of the sample and  $v$  the phonon velocity. In the collective contribution phonons behave like a whole defining a hydrodynamic flow, therefore boundary conditions should be equivalent to the ones felt in a system like the flow in a pipe. Boundary effects in the collective regime are determined by a form factor  $F(L_{\text{eff}})$  obtained by solving a hydrodynamic heat flux equation with non-slip boundary conditions ( $\mathbf{Q}_B(R) = 0$ ) [33]. This form factor, which depends on the effective length of the sample is expressed as:

$$F(L_{\text{eff}}) = \frac{1}{2\pi^2} \frac{L_{\text{eff}}^2}{\ell^2} \left( \sqrt{1 + 4\pi^2 \frac{\ell^2}{L_{\text{eff}}^2}} - 1 \right), \quad (4.1)$$

where  $L_{\text{eff}} = d_{\text{wire}}$  is the diameter in the case of wires,  $L_{\text{eff}} = 2.25h$  for thin films, with  $h$  the film thickness, and  $L_{\text{eff}} = 1.12\sqrt{A}$  for square rods of cross section  $A$ . In this case  $\ell$  denotes the phonon mean free path (MFP) in the collective regime limit  $\tau_N \ll \tau_R$ , which can be expressed as  $\ell^2 = \langle v^2 \tau_N \rangle \langle \tau_C \rangle$  [15]. Notice that the factor 1/5 in the collective characteristic length appears only in the isotropic dispersionless approximation [15].

Using the previous boundary condition in the collective regime (Eq. (4.1)), the collective contribution to thermal conductivity will be  $\kappa_C = \hat{\kappa}_C \cdot \Sigma \cdot F$ . From this derivation one can do calculations of thermal conductivity for bulk and simple geometries like wires, films and rods using:

$$\kappa_T = \kappa_K^B \cdot (1 - \Sigma) + \kappa_C \cdot \Sigma \cdot F. \quad (4.2)$$

From Fig. 4.1 it can be observed that the kinetic boundary effects reproduce a homogeneous flow where the heat flux is the same in the whole cross section of the sample. In contrast, in the collective regime the hydrodynamic boundary condition reproduces the parabolic profile observed in a Poiseuille flow. As explained, while boundary scattering  $\tau_B$  is included through the Matthiessen's rule in the kinetic contribution, the form factor  $F(L_{\text{eff}})$  describes size effects in the collective term. Thus, in the calculation of  $\tau_c$  only umklapp ( $U$ ) and impurity scattering processes are considered. In bulk materials  $\tau_B \rightarrow \infty$  and,  $F(L_{\text{eff}}) = 1$ , then the thermal conductivity only depends on intrinsic scattering events.

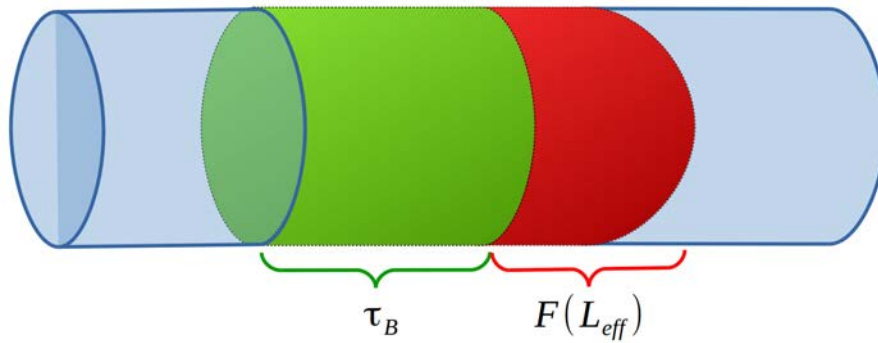


Figure 4.1: Heat transport profile sketch to identify the contribution of kinetic and hydrodynamic boundary effects.

#### 4.1.1 Group IV and III-V semiconductors

The thermal conductivity of several bulk semiconductor materials has been studied in **Chapter 3**. In the present section the thermal conductivity of silicon nanowires and films is studied using the kinetic-collective boundary approach for reduced size samples.

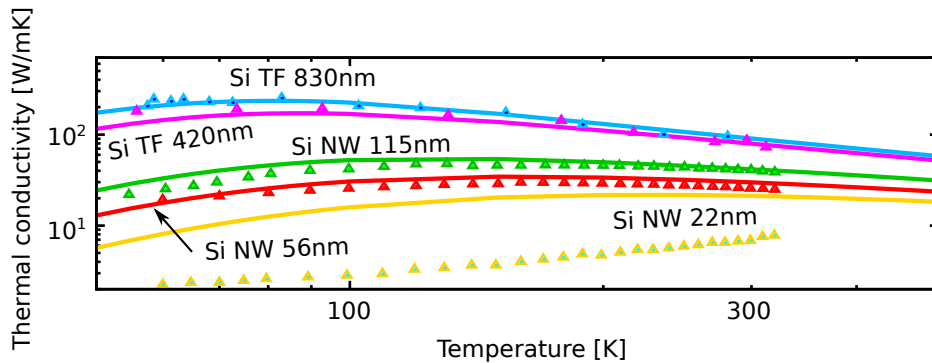


Figure 4.2: Thermal conductivity of silicon thin films and nanowires in terms of temperature [106, 107].

Fig. 4.2 shows the KCM predictions of the thermal conductivity for silicon nanowires and films. Good predictions are obtained for both type of samples at sizes bigger than  $L_{eff}=50$  nm. The strong reduction observed in the experimental data of the 22 nm NW could be associated to an enhancement of the boundary effects due to the high roughness of the surface. This effect is not captured in the simple specular and diffuse scattering model used in the present approach. While in the case of thin films, good predictions have been obtained in previous works as a function of size [108], the KCM is pioneer on predictions

of silicon nanowires as a function of temperature and size using a parameter-free approach. Some normal( $N$ )-as-resistive based descriptions like classical RTA have also provided good fits to data at the nanoscale by including a form factor and by using different isotopic scattering relaxation times from the bulk ones [105, 109]. In contrast, in KCM the use of a diffuse-specular scattering and hydrodynamic model in the kinetic and collective terms, respectively, allows to make nanoscale predictions without modifying bulk parameters. In this case, the form factor  $F$  is derived ensuring the conservation of energy and momentum of the whole phonon distribution [26, 33], in contrast to form factors derived from  $N$ -as-resistive standpoints.

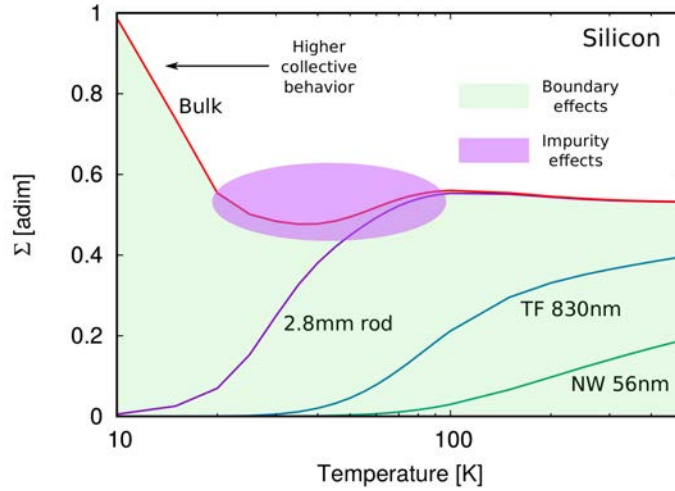


Figure 4.3: Switching factor  $\Sigma$  for bulk silicon, 2.8 mm rod, 830 nm film and 56 nm wire as a function of temperature. The purple region indicates the effect of the impurity scattering.

The value of  $\Sigma$ , as defined in Eq. (2.64), for bulk silicon, 2.8 mm rod, 830 nm thin film and 56 nm nanowire in terms of temperature is represented in Fig. 4.3. The dependence of  $\Sigma$  on size and temperature can be directly obtained by examining how resistive ( $R$ ) and  $N$  processes change as those parameters are modified. Since the boundary scattering  $\tau_B$  has been introduced in the resistive term  $\tau_R^B$ , as size is reduced, the rate of boundary collisions increases (and so the  $R$  collision rates), meanwhile  $N$  scattering rates do not change. As a result, as size is reduced  $R$  collisions become dominant and the parameter  $\Sigma$  tends to zero. The observed reduction of  $\Sigma$  as the temperature decreases has the same origin: at low temperatures, anharmonicities become less important in front of boundary and impurity scattering rates, which are temperature independent, and this reduces the collective contribution. At high temperatures,  $\Sigma$  increases in all cases tending to a constant value. The bulk value  $\Sigma_{\text{bulk}}$ , which represents the intrinsic

collective behavior, has been also included in Fig. 4.3 for comparison. It can be observed that at low temperatures, if boundary scattering did not limit heat transport, thermal transport would be dominated by the collective regime due to the dominance of  $N$  processes in front of the  $R$  ones.

#### 4.1.2 Bismuth telluride

A set of different wire diameter  $\text{Bi}_2\text{Te}_3$  nanowires has been studied in the KCM framework. Bulk  $\text{Bi}_2\text{Te}_3$  has already a very low thermal conductivity, therefore it is expected a higher reduction when the diameter is decreased. For that propose Muñoz *et al.* [110] have synthesized well oriented nanowires along a specific low conductivity direction  $[1\ 1\ 0]$ , with perfect stoichiometry, high density, and high crystal quality.

For the calculation of the thermal conductivity along a certain direction it is necessary to project the phonon velocity towards the desired orientation. In the case of hexagonal  $\text{Bi}_2\text{Te}_3$  cell, the direction  $[1\ 1\ 0]$  corresponds to the normalized vector  $\mathbf{v}=(\sin(2\pi/3), 0.5, 0)$ .

Wire diameter [nm]	Total thermal conductivity [W/mK]	Lattice thermal conductivity [W/mK]
$300 \pm 75$	$1.78 \pm 0.46$	$1.72 \pm 0.48$
$52 \pm 5$	$0.72 \pm 0.37$	$0.53 \pm 0.4$
$45 \pm 4$	$0.58 \pm 0.47$	$0.36 \pm 0.51$
$25 \pm 4$	$0.52 \pm 0.35$	$0.18 \pm 0.38$

Table 4.1: Experimental total and lattice thermal conductivity for bismuth telluride nanowires at 300 K [110].

The experimental thermal conductivity of  $\text{Bi}_2\text{Te}_3$  nanowires is shown in Table 4.1. The total thermal conductivity corresponds to the direct experimental measurement. To determine the lattice thermal conductivity, the electronic contribution has been removed using Wiedemann-Franz law with a constant Lorentz number of  $L = 2.44 \cdot 10^{-8} \text{ W}\Omega/\text{K}^2$ . The electrical conductivity of the samples, necessary to determine the electronic contribution, is of the order of  $\kappa_e \sim 10^4 \text{ S/m}$  at 300 K [111].

Fig. 4.4 shows the experimental and predicted by KCM thermal conductivity for a set of nanowires ranging from 300 nm to 25 nm. A  $4 \mu\text{m}$  thick film is used as reference. The predicted values agree with the experimental data within the error bars. It can be observed that as the wire diameter is reduced the thermal conductivity decreases significantly until  $0.18 \pm 0.38 \text{ W/mK}$  for the  $25 \pm 4 \text{ nm}$  wire.

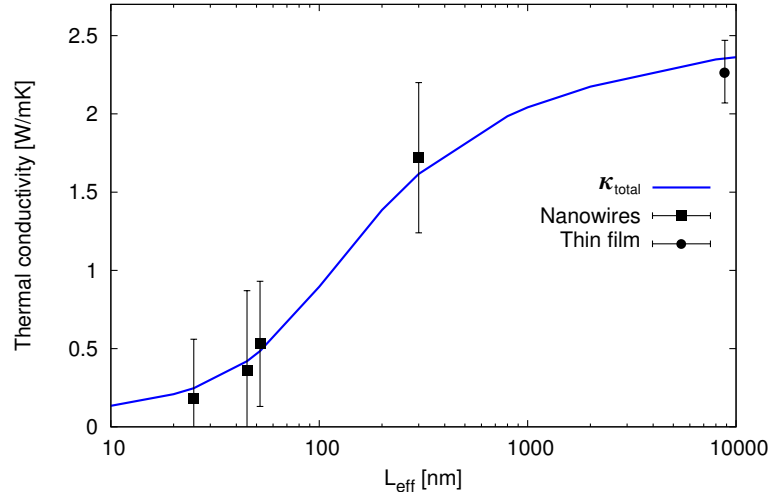


Figure 4.4: Thermal conductivity at 300K of  $\text{Bi}_2\text{Te}_3$  nanowires and a thin film  $[110]$  oriented.  $L_{\text{eff}}$  corresponds to the diameter for the wires and  $2.25h$  for the film. Experimental data are taken from [110].

For the present samples, the grain size was estimated to be  $\sim 10\mu\text{m}$  [110]. Since boundary scattering limit the phonons with MFP larger than the wire diameter ( $D \ll 10\mu\text{m}$ ), the estimated grain size does not affect the thermal conductivity.

Comparing the micro/nano  $\text{Bi}_2\text{Te}_3$  samples and bulk, one can realize that it is necessary to have very small crystalline samples in order to have a thermal conductivity smaller than the bulk one.

### 4.1.3 SiGe alloys

In addition to silicon nanowires,  $\text{Si}_{1-x}\text{Ge}_x$  nanowires have been also studied in the KCM in the kinetic-collective boundary approach.  $\text{Si}_{1-x}\text{Ge}_x$  alloys are of great interest for thermoelectric applications, as in their bulk form they already have a very low thermal conductivity. Therefore it is expected to find an even better performance in reduced samples.

The results from Fig. 4.5 show that the kinetic-collective approach of boundary effects is not enough to predict the whole trend of the thermal conductivity in terms of temperature, even though at room temperature good agreement is obtained. As can be observed, the general trend defined by the present approach tends to flatten the temperature profile from quite low temperatures, while experimental data features a slower increase with a different slope. Therefore it seems that the kinetic-collective approach as defined in the present case is not enough to

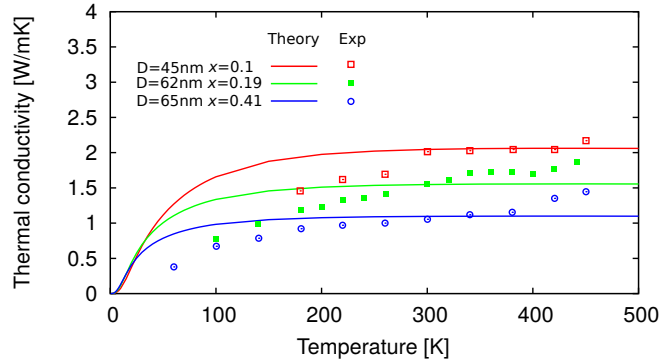


Figure 4.5: Thermal conductivity in terms of temperature for  $\text{Si}_{1-x}\text{Ge}_x$  at different alloy concentration  $x$ . Experimental data are taken from [112].

describe the temperature profile of thermal conductivity for these highly kinetic samples.

## 4.2 Hydrodynamic KCM approach

In recent years hydrodynamic heat transport has emerged as a promising approach in order to predict the thermal conductivity of semiconductors at small scales [16, 17, 34, 113]. Phonon hydrodynamics, introduced in **Section 1.3**, allows to explore the study of thermal transport of reduced size systems like nanowires or thin films. This approach may help to study some micro/nano samples where other models fail.

In **Section 2.3** boundary effects have been introduced from a kinetic point of view. In the previous section, the KCM has dealt with kinetic boundary effects in the kinetic regime and with hydrodynamic derived conditions in the collective one. In this section, a full hydrodynamic equation, able to describe mixed kinetic and collective regimes, is used to predict the thermal conductivity of nanowires. This allows to use suitable boundary conditions to have into account the geometry of each sample under study. In small samples, where their characteristic size is of the same order or smaller than the characteristic phonon MFP, the effect of roughness has been demonstrated also to have an important impact on the thermal conductivity [105]. In these cases, expressions including geometric parameters accounting for surface roughness are required.



### 4.2.1 KCM heat flux equations

Despite of the richness of works that have proposed generalizations of the Fourier law, up to now none of these models allows reproducing the experimental results at all scales and different geometries. The lack of a model tested in a sufficiently wide range of experimental situations supposes, on one hand, a theoretical challenge to physicists. On the other hand it is an important drawback to engineers, who need valid equations to determine the behavior of their designs prior to fabrication.

Here a generalized equation that is able to reproduce several of the discrepancies from the Fourier law observed in different experiments up to now [4, 5, 6, 7, 8, 9, 10] is proposed:

$$\tau \frac{d\mathbf{Q}}{dt} + \mathbf{Q} = -\kappa \nabla T + \ell^2 (\nabla^2 \mathbf{Q} + 2\nabla \nabla \cdot \mathbf{Q}), \quad (4.3)$$

where  $\tau$ ,  $\kappa$  and  $\ell$  are bulk (i.e. without considering any boundary effect) total relaxation time, thermal conductivity and non-local length respectively. This is the so-called hydrodynamic KCM equation. The value of  $\ell$  determines the non-local range in phonon transport and is related to the viscosity (i.e. friction) that the phonon distribution notices.

The main advantage that the hydrodynamic KCM offers in front of kinetic models is that starting from the hydrodynamic equation (Eq. (4.3)) avoids to solve directly the LBTE for phonons, which is quite complicated for complex geometries such as multilayer or 3D structures, for instance. To do these calculations in KCM for any geometry it is necessary to define the parameters in the hydrodynamic equation that merges both limits, kinetic and collective. The derivation of Eq. (1.60) done by Guyer and Krumhansl is done studying the limiting case where  $N$  processes dominate,  $\tau_N \ll \tau_R$ . In this limit, corresponding to the collective regime (i.e.  $\Sigma = 1$ ), the non-local length is  $\hat{\ell}_C^2 = \langle v^2 \tau_N \rangle \langle \tau_C \rangle$ . The hat  $\hat{\phantom{x}}$  only indicates that it is a limit situation. To have a global hydrodynamic equation, the kinetic limit  $\tau_N \gg \tau_R$  (i.e.  $\Sigma = 0$ ) has been studied in the KCM framework. In this case the non-local length tends to  $\hat{\ell}_K^2 = \langle v^2 \tau_R \rangle \langle \tau_R \rangle$ . From the KCM equations, where the thermal conductivity is calculated as an interpolation through  $\Sigma$  between the kinetic and the collective limits (see Eq. (1.28)), the non-local length can be generalized as:

$$\ell^2 = \hat{\ell}_K^2 \cdot (1 - \Sigma) + \hat{\ell}_C^2 \cdot \Sigma = \ell_K^2 + \ell_C^2. \quad (4.4)$$

The generalized non-local length together with the total thermal conductivity and relaxation time expressed as  $\tau = (1 - \Sigma) \cdot \tau_K + \Sigma \cdot \tau_C$ , define all the parameters of hydrodynamic KCM equation. This equation, together with

suitable boundary conditions, can be solved by finite elements to study thermal properties in complex geometries. Calculating the temperature dependence of  $\tau$ ,  $\kappa$  and  $\ell$  from *first principles* complex experimental setups can be predicted, where boundary effects need to be introduced as boundary conditions. Further extensions of Eq. (4.3) can be done by considering a dependence of the thermal conductivity on the temperature gradient as  $\kappa(\nabla T)$  or considering the effect of Lévy flights.

### 4.2.2 Effective thermal conductivity

In the present work, in collaboration with CRM, the KCM hydrodynamic equation Eq. (4.3) has been solved analytically by splitting the radial and axial components of the flux in a cylindrical geometry [114]. Doing so, a generic expression of the effective thermal conductivity (ETC) is obtained:

$$\frac{\kappa_{eff}}{\kappa_0} = \left( 1 - \frac{2 \text{Kn} I_1(\text{Kn}^{-1})}{I_0(\text{Kn}^{-1}) + C I_1(\text{Kn}^{-1})} \right), \quad (4.5)$$

where  $I_\nu$  represents the modified Bessel function of first kind. In this case  $\text{Kn} = \ell/R$ , where  $\ell$  is the non-local length and  $R$  is the wire radius. The parameter  $C$  that determines the specular and diffuse scattering will be related to the geometry of the roughness, represented on Fig. 4.6.

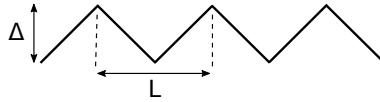


Figure 4.6: Sketch of roughness parameters.

### General hydrodynamic boundary conditions

In order to solve analytically the KCM hydrodynamic equation, Eq. (4.3), some boundary conditions are necessary. As stated, the generic solution of the effective thermal conductivity has been done by spitting the heat flux in radial ( $v$ ) and axial ( $w$ ) components  $\mathbf{Q}(v, w)$ . The most general boundary conditions that can be applied are:

$$v|_{r=0} = 0, \quad v|_{r=R} = 0, \quad (4.6)$$

$$\frac{\partial w}{\partial r}|_{r=0} = 0, \quad w|_{r=R} = -\text{Kn} C \frac{\partial w}{\partial r}|_{r=R}, \quad (4.7)$$

where  $C \neq 0$  is a slip boundary parameter depending on the roughness of the surface. A general value used for the slip condition is  $C = 1$ . To capture the variation of the slip condition in temperature, it can be generalized. When  $C = 0$  the flux at the boundary is zero but for  $C > 0$  the flow is not completely removed at the boundary. For very rough surfaces, the specularity is very low, this means that the flux at the boundary tends to zero, and in that case  $C \rightarrow 0$ . On the contrary, when the specularity increases, the flux does not notice the boundary and  $C \rightarrow \infty$ . The  $C$  value can thus be determined by the comparison between the wavelength of the phonons and the average height of the roughness. At high temperatures the wavelength of the phonons is small and consequently the specularity is reduced, while at low temperatures the averaged wavelength increases and the phonons notice more specular boundary effect. To avoid the use of  $C$  as a fitting parameter, it is calculated from the microscopic information. As the interaction of the carriers with the boundary depends on the specularity of the surface, the slip parameter  $C$  will depend on these collisions. To model this behavior the slip coefficient can be expressed as [17]:

$$C(T) = \frac{1 + p(T)}{1 - p(T)}, \quad (4.8)$$

where  $p(T)$  is the specularity defined from the ratio of the roughness height  $\Delta$  (see Fig. 4.6) and the mean wavelength of the phonon distribution at each temperature,  $\lambda(T)$  [19]:

$$p(T) = e^{-\pi \left( \frac{4\pi\Delta}{\lambda(T)} \right)^2}. \quad (4.9)$$

The mean wavelength of the phonon distribution can be calculated from the mean wave vector  $\mathbf{q}(T)$  as  $\lambda(T) = 2\pi/\mathbf{q}(T)$ , where:

$$\mathbf{q}(T) = \frac{\sum_{\mathbf{q}} C_{\mathbf{q}} \mathbf{q}_{\mathbf{q}}}{\sum_{\mathbf{q}} C_{\mathbf{q}}}, \quad (4.10)$$

being  $C_{\mathbf{q}}$  the mode specific heat and  $\mathbf{q}_{\mathbf{q}}$  the wave vector.

Under the previous conditions, if the surface is purely diffuse,  $p = 0$  and  $C = 1$ . On contrary, when the surface is purely specular  $p = 1$  and  $C \rightarrow \infty$ . Thus,  $C \in [1, \infty)$  determines the behavior of the surface. Notice that in none of the two limits a zero flow at the boundary ( $C = 0$ ) is obtained. The heat flow at the boundary is an average between those phonons moving towards the surface and those leaving it. The boundary condition only acts on those leaving, making impossible to completely destroy the incoming flow. To get values lower than  $C = 1$  it is required to include backscattering. In this situation, if phonons leaving the surface backward generate a flux in the opposite direction of those going forward, the average flux will be destroyed. A generalization of Eq. (1.64) in this case could be [34]:

$$Q_B = C\ell \left( \frac{\partial Q}{\partial r} \right)_{r=R} - \alpha\ell^2 \left( \frac{\partial^2 Q}{\partial r^2} \right)_{r=R}, \quad (4.11)$$

where  $\alpha$  measures the intensity of the backscattering and will depend on the roughness. This phenomena appears only in the presence of very large roughness and will not be considered in this work.

### 4.2.3 Hydrodynamic thermal transport in nanowires

The hydrodynamic KCM equation (Eq. 4.3) has been applied to study the thermal transport of several nanowire samples. In this case it has been used to predict the thermal conductivity of silicon nanowires. The solution can be obtained equivalently from the ETC solution or by direct computation in a finite elements software using the general boundary conditions defined in Eq. (4.6) and Eq. (4.7), with  $C$  as defined in Eq. (4.8). To obtain this parameter, a small roughness has been considered,  $\Delta=0.4 \text{ \AA}$ . On one side, the hydrodynamic model has been applied to silicon nanowires, where already the kinetic-collective boundary approach has shown good performance. On the other side, as  $\text{Si}_{1-x}\text{Ge}_x$  alloys are not so well predicted by the latter approach, it has been tested on the hydrodynamic model in order to improve the prediction.

The time derivative term accounting for memory effects has been neglected, as the present study only considers steady state.

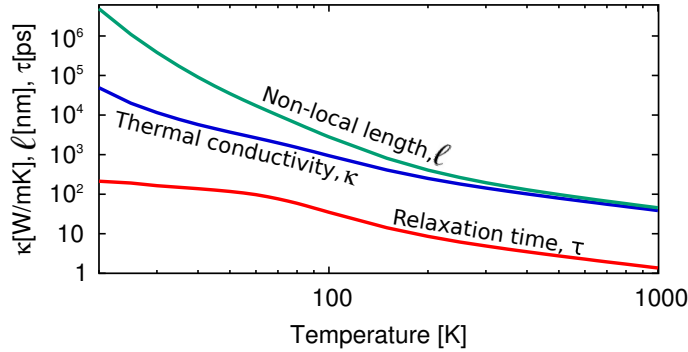


Figure 4.7: Thermal conductivity, non-local length and relaxation time of bulk silicon as a function of temperature.

The hydrodynamic KCM only requires intrinsic (i.e. bulk) properties to be used. In the case of silicon, the bulk thermal conductivity, non-local length and total relaxation time as a function of temperature are represented in Fig. 4.7.

Full hydrodynamic KCM predictions for silicon nanowires of 115 nm, 56 nm and 37 nm are represented in Fig. 4.8. The upper red line represents the intrinsic

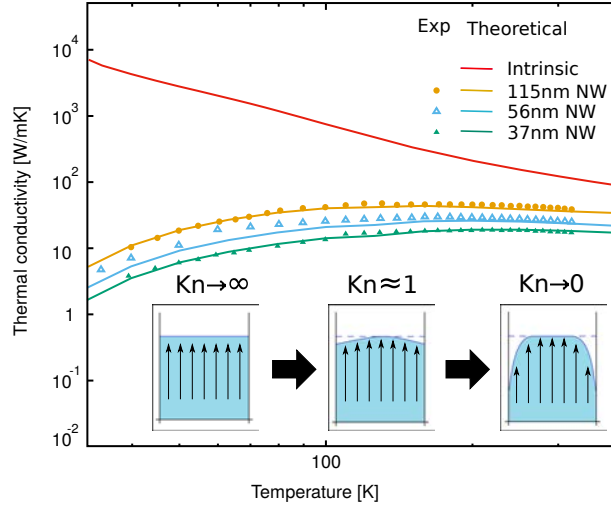


Figure 4.8: Thermal conductivity of silicon nanowires as a function of temperature with full hydrodynamic KCM. Sketch of three hydrodynamic regions is overhead. Experimental data from [107].

insic thermal conductivity, which is used as an input. From this value, applying boundary conditions the thermal conductivity of the wires is calculated. Good agreement with the experimental data for the three samples in the whole temperature range can be observed. In the case of the 56 nm wire, the small underprediction below 100 K could be caused by a wrong assumption of the impurity scattering, as natural isotope concentration has been assumed in all cases.

In the hydrodynamic KCM approach, the characteristics of the hydrodynamic regime are determined by the value of the non-local length  $\ell$ , through the Knudsen number ( $Kn = \ell/L$ ). When  $Kn \rightarrow 0$ , the hydrodynamic behavior is not important and the Fourier law is recovered. On the contrary, when the  $Kn \rightarrow \infty$ , the hydrodynamic behavior is important and Eq. (4.3) including non-local effects is needed.

In Fig. 4.9 different heat flux profiles are represented as a function of the slip condition for a cylindrical geometry. As can be observed, when  $Kn \rightarrow \infty$  the profile flattens and can be interpreted as a Fourier model. This effect is similar to the trend of  $\Sigma$  at low temperatures in the KCM when boundary effects are included:  $\Sigma \rightarrow 0$ . In this situation a pure kinetic framework can be used. Notice that both Fourier and Guyer-Krumhansl equations are continuous equations. This leads to believe that an effective Fourier law can be used to interpret the hydrodynamic equation in certain limits.

In the case of  $Si_{1-x}Ge_x$  alloys, the kinetic-collective approach of boundary effects is not enough to reproduce the whole temperature trend (see Fig. 4.5). To improve this, the full hydrodynamic KCM approach has been used to predict the

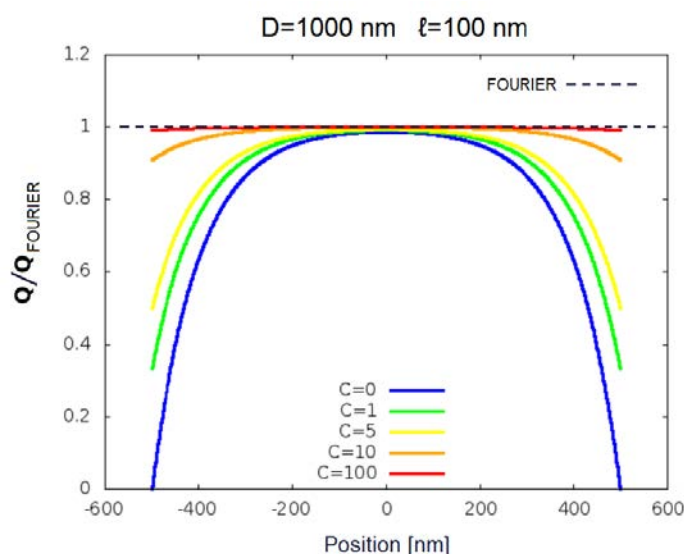


Figure 4.9: Effective heat flux profile for different values of slip condition in a wire.

temperature profile of the presented  $\text{Si}_{1-x}\text{Ge}_x$  alloys.

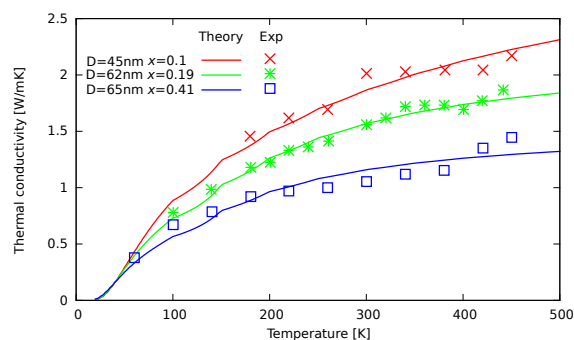


Figure 4.10: Thermal conductivity of  $\text{Si}_{1-x}\text{Ge}_x$  nanowires as a function of temperature for different diameters and concentrations  $x$ . Experimental data are taken from [112].

In the case of silicon nanowires, as indicated previously the bulk thermal conductivity was used as an input. This means that there is no *a priori* limitation of phonon transport. This premise was not enough to reproduce the experimental data for  $\text{Si}_{1-x}\text{Ge}_x$  alloys. Doing that, the temperature profile was the same as found in the kinetic-collective approach (see Fig. 4.5). To fully reproduce the temperature trend in this case the thermal conductivity in the input file needed to be limited by the length of the wire. Phonons with MFP longer than the length of the sample are removed.

Fig. 4.10 shows the thermal conductivity as a function of temperature for  $x = 0.1$ ,  $x = 0.19$ , and  $x = 0.41$   $\text{Si}_{1-x}\text{Ge}_x$  wires of different diameter. It can be observed that the finite elements solution is able to reproduce the experimental data in the whole temperature range.

The good agreement between the experimental data and the KCM hydrodynamic approach shows that the hydrodynamic heat flux can be a useful framework to model the thermal transport at the nanoscale. To improve the model, the limitation of the thermal conductivity due to the wire length found in  $\text{Si}_{1-x}\text{Ge}_x$  alloys should be included as a boundary condition to solve the hydrodynamic equation. This effect might be due to Lévy Flights or other not considered non-local effects that should be studied in future work.

### 4.3 Boundary effects in other models

In addition to the treatment of boundary effects done by KCM, both in the kinetic-collective approach and in the hydrodynamic approach, other models have also proposed ways to deal with the boundary effects beyond Casimir's expression.

The iterative solution of the Boltzmann Transport Equation (I-BTE), introduced in **Section 1.2**, can also include size effects for the case of nanowires (NW) through an exponential suppression function based on Fuchs-Sondheimer works [31], aiming reproducing a Poiseuille profile, as done in the KCM. In this case, the relaxation time for the iteration ( $i$ ) considering pure diffuse scattering can be expressed as:

$$\tau_{\mathbf{q}}^{(i)} = \tau_{\mathbf{q}}^{(i-1)} (1 + \Delta_{\mathbf{q}}^{(0)}) \left( \frac{1}{S_c} \int_{S_c} (1 - e^{-|\mathbf{r}-\mathbf{r}_b|/\tau^{(i-1)}v_{\mathbf{q}}}) d\mathbf{S} \right), \quad (4.12)$$

where  $\mathbf{r}$  and  $\mathbf{r}_b$  denote the cartesian coordinate in the wire and the border respectively, and  $S_c$  the cross section of the NW. While the BTE can be solved exactly iteratively for bulk materials, the inclusion of boundary effects makes it necessary to approximate the relaxation times by its averaged values  $\bar{\tau}_{\mathbf{q}}$  and  $\bar{\Delta}_{\mathbf{q}}$  over the cross section of the wire.

Cepellotti *et al.* recently have done as well a hydrodynamic boundary approach to their relaxon solution of the LBTE (R-LBTE) [115]. In this case, in order to obtain a suitable expression for the heat transport it is required to obtain a linear combination of relaxons, with occupation numbers  $d_i$  and solve the LBTE. The solution for a cylindrical geometry leads to:

$$d_i = d_i^{\infty} (1 - e^{-(y \pm W/2)/\lambda_i^{(y)}}), \quad (4.13)$$

where  $d_i$  in the boundaries are considered null.  $W$  represents the wire diameter,  $d_i^\infty$  the bulk occupation numbers and  $\lambda_i^{(y)}$  are the eigenvalues of the friction length matrix  $\Lambda_{\alpha\beta}^{(y)}$  that account for boundary effects. It can be noticed the analogy of the friction length with the non-local length used in the KCM and in turn its analogy with the viscosity of a fluid.

Similarities between the latter equation and the solution obtained from I-BTE in Eq. (4.12) can be observed. In both cases there is an exponential reduction depending on the distance towards boundaries.

In the case of the R-LBTE solution including boundary effects it is required to obtain a linear combination of relaxons (that already are a linear combination of phonons) in order to find a basis to solve the problem.

A third way to introduce boundary effects in kinetic models is through a phonon suppression function  $S$  that removes the contribution of MFP ( $\Lambda$ ) larger than the characteristic size ( $L$ ) of the sample [116]:

$$\kappa_{\text{eff}} = \sum_{\mathbf{q}} S \left( \frac{\Lambda_{\mathbf{q}}}{L} \right) \kappa_{\mathbf{q}}(\Lambda). \quad (4.14)$$

The shape of the suppression function is dependent of the geometry of the system, which can be obtained analytically for simple geometries. For complex geometries a hydrodynamic-based approach with general boundary conditions would be more suitable (see **Chapter 6**).

The success of KCM on solving the thermal transport of nanowires (see **Section 4.2**) shows that simply using the moment basis of two well known tangible magnitudes as temperature  $T$  and heat flux  $\mathbf{Q}$  (see **Section 1.2.5**) is enough to solve the thermal transport at reduced scales.

Fig. 4.11 presents a comparison of KCM and I-BTE [24] calculations of the thermal conductivity from bulk to 22 nm wires at 300 K. KCM provides good predictions without any fitting parameter for wires as small as 56 nm. The overprediction of the smallest wires, as seen in Fig. 4.2, could be associated to an increased roughness effect [105, 117]. This behavior has also been observed for thin films at similar scales [108]. The green zone in Fig. 4.11 displays the kinetic contribution to thermal conductivity, namely  $\kappa_K$ . The difference between the black line and the green zone is the collective contribution (red zone),  $\kappa_C$ . While the agreement to the experimental data using only kinetic transport is good for the smallest diameters (where the red zone vanishes), for bigger sizes a collective contribution appears. This explains the convergence of  $\kappa_T$  to  $\kappa_K$  for small samples displayed in Fig. 4.11.

The boundary effects as included in the I-BTE and R-LBTE frameworks can be used to compute the thermal conductivity in wires as a function of its diameter. The shape reproduced by their equations will reproduce a curved heat



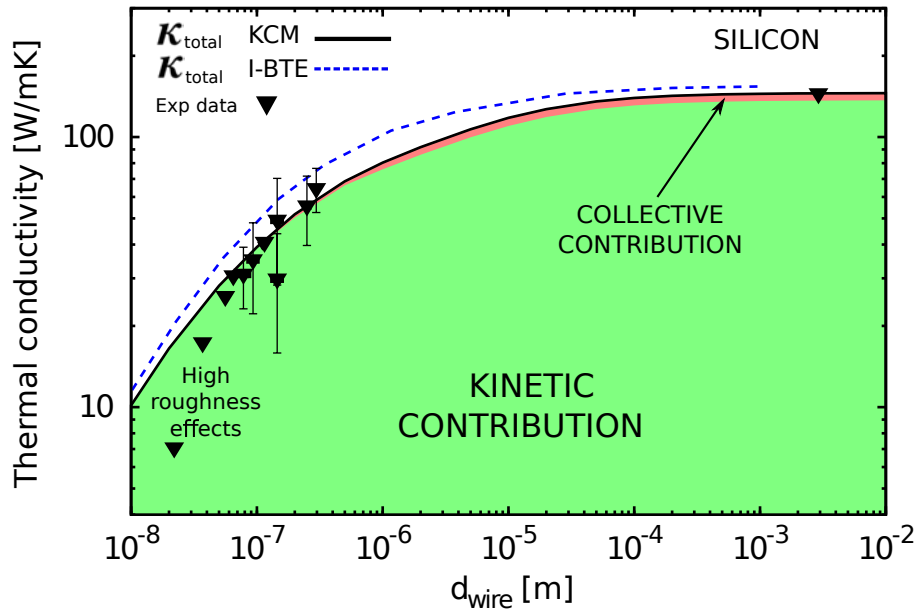


Figure 4.11: Theoretical predictions and experimental data for thermal conductivity of silicon wires at  $T=300$  K as a function of the wire diameter. Kinetic (green), collective (red) and total thermal conductivity (black solid line) predicted by KCM and iterative BTE predictions from [24] (blue dashed line). Experimental data (symbols) are taken from [62, 107].

flux profile similar to the one found in the KCM approach based in a hydrodynamic formulation. The main drawback of these analytic equations is that are still limited to very simple geometries like wires or thin films. In contrast, a full hydrodynamic model will allow the study of thermal transport of more complex geometries from finite elements simulations, as shown in **Chapter 6**.

# Chapter 5

## Phonon spectrum and transient regimes in the KCM

The goal of reduce the device sizes and obtain faster performance has caused that recent experiments are moving the focus to measurements at short length and time scales [4, 5, 6, 7, 8, 9, 10]. This makes it necessary to have a model which is able to work in the transient regime between diffusive and ballistic heat transport. Such models would depend strongly on the phonon mean free paths (MFP) and mean free times (MFT). For that reason, models able to provide a deeper insight on the different transport phenomena would become a suitable tool for such experiments. Works along this line have demonstrated that pure kinetic models are not enough to understand thermal conductivity at short length and time scales [8, 10]. A collective or hydrodynamic flow has been used to explain the origin of the non-monotonous dependence of the thermal boundary resistance as a function of the size of the heating source arising from ultrafast laser heating experiments [10]. Also theoretically, collective transport has been successfully used to understand *first principles* results on graphene thermal transport [14, 13], where normal ( $N$ ) scattering plays an important role. All seems to point out that models including collective effects will be necessary in next years in order to analyze these new experiments.

These results open the door to discuss how the precise combination of kinetic and collective contributions to heat transport could provide a useful framework to interpret recent complex experiments displaying non-Fourier behavior.

### 5.1 Phonon spectrum

In the last years, several works have pointed out the importance of long MFP (i.e. low frequency) phonons in thermal conductivity. It is widely accepted that

these phonons have a very important contribution to heat transport, but current Density Functional Theory (DFT) calculations seem to provide larger contributions by long MFP phonons than the experimental observations [118, 119]. The origin of this effect is the finite  $\mathbf{q}$ -point mesh sampling of the Brillouin zone achievable computationally. To be able to predict correctly the thermal conductivity from such *ab initio* calculations, Akhiezer damping has been proposed. This macroscopic relaxation mechanism has been phenomenologically used to reduce the *first principles* obtained MFT as an extra scattering mechanism in the Matthiessen's rule [119]. In the KCM framework alternative explanations to account for the reduction in the contribution of low frequency phonons to thermal conductivity are proposed based on the effects of the collective regime and on the calculation of low energy relaxation times.

To give a detailed overview of the phonon spectrum in the KCM framework, four different types of samples will be studied. In first place, the most commonly studied semiconductor, silicon; second, two typical thermoelectric alloys,  $\text{Si}_{1-x}\text{Ge}_x$  and  $\text{In}_x\text{Ga}_{1-x}\text{As}$ ; third, low thermal conductivity compounds,  $\text{Bi}_2\text{Te}_3$ ,  $\text{PbTe}$  and  $\alpha$ -quartz, and finally graphene.

### 5.1.1 KCM phonon spectrum of Si

As explained in Section 2.4, a suitable way to run fast thermal transport calculations is by binning the  $\mathbf{q}$ -mode values in  $\omega$  dependent parameters with a weight determined by the density of states (DOS).

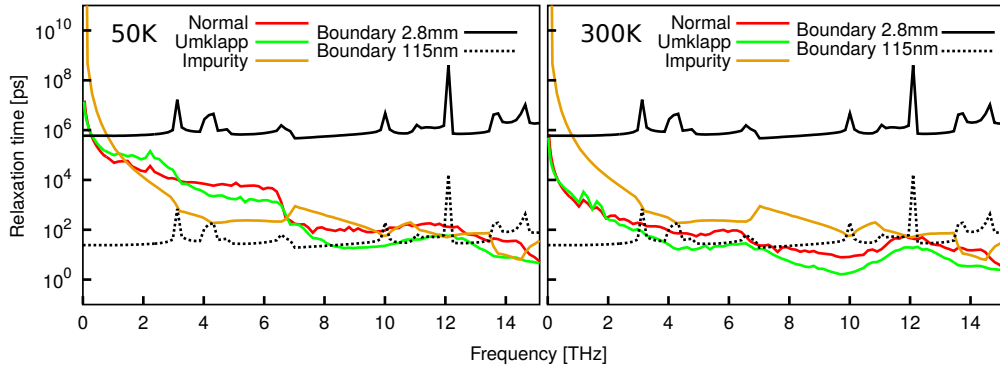


Figure 5.1: Normal, umklapp, impurity and boundary relaxation times for  $L_{\text{eff}} = 2.8 \text{ mm}$  and  $L_{\text{eff}} = 115 \text{ nm}$  silicon at 50 K and 300 K in terms of frequency.

Fig 5.1 shows the averaged frequency dependent relaxation times for  $L_{\text{eff}} = 2.8 \text{ mm}$  and  $L_{\text{eff}} = 115 \text{ nm}$  silicon at 50 K and 300 K. Notice that the reduction of the parameters to an averaged frequency dependent magnitude still maintains the

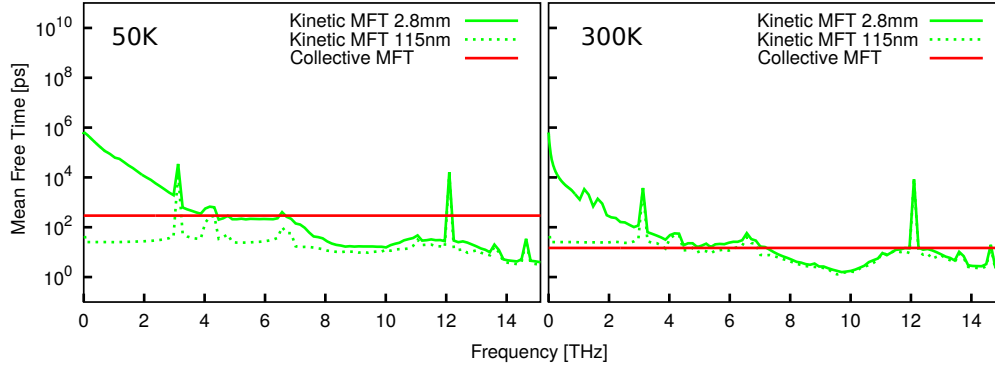


Figure 5.2: Kinetic and collective mean free times (MFT) for  $L_{\text{eff}} = 2.8$  mm and  $L_{\text{eff}} = 115$  nm silicon at 50 K and 300 K in terms of temperature

same trend observed in the direct calculation (Fig. 3.9). From this figure it can be observed that as the temperature is increased the  $N$  and umklapp ( $U$ ) relaxation times are reduced, i.e., the distribution relaxes faster to equilibrium. In addition, it is evidenced that the boundary and impurity/mass defect relaxation times are temperature independent. The boundary effects accounted from Casimir's expression depend on the frequency through the velocity, while the impurity/mass defect scattering does so through the DOS. From the individual relaxation times, a MFT can be defined as the time between collisions in a transport phenomena. In the KCM two transport regimes are defined, kinetic and collective. In the kinetic regime all phonons interact individually and therefore all processes can be arranged in a frequency dependent MFT through the Matthiessen's rule. In contrast, in the collective regime, the effect of  $N$  processes acts like a glue between phonons and a single frequency-independent MFT is defined for all of them. In Fig 5.2, the MFT of both transport regimes for  $L_{\text{eff}} = 2.8$  mm and  $L_{\text{eff}} = 115$  nm silicon at 50 K and 300 K is represented. For big size samples the boundary effects in the kinetic regime are only visible at very low frequencies, while in nano/micro samples this effect flattens the MFT curve even at intermediate frequencies. The completely straight line of the collective regime (red line) highlights its frequency independent behavior. In addition, there are no differences between small and thick samples in this regime, as boundary effects do not affect to the relaxation time but the collective thermal conductivity as an external form factor  $F$  (see Eq. (4.2)).

Fig. 5.3 top displays the kinetic and collective thermal conductivity accumulation function (TCSD) predicted by KCM for bulk silicon in terms of frequency at 300 K, where one observes that both contributions span the whole range of the spectra. While at low frequencies the kinetic regime dominates, the collective contribution becomes more important at high frequencies. From the ther-

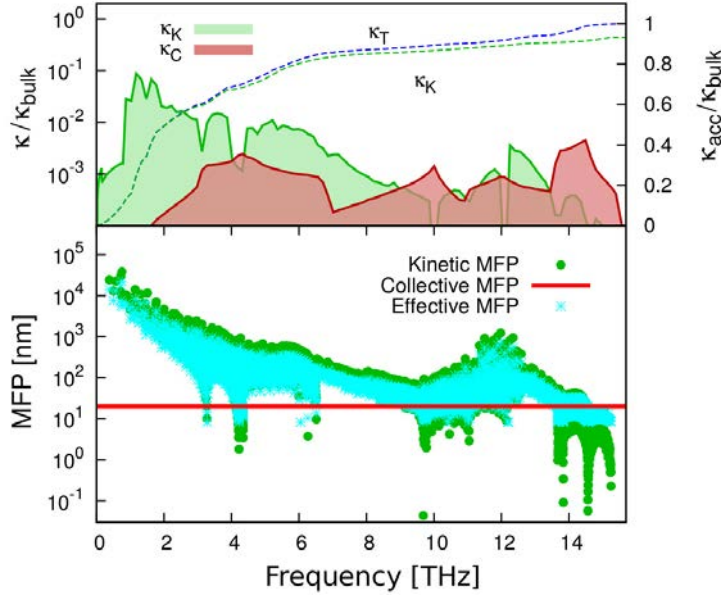


Figure 5.3: Top: Thermal conductivity spectral distribution (TCSD) in terms of frequency for bulk silicon at  $T=300\text{K}$ . Filled curves are the kinetic and collective contributions to TCSD. Blue line represents the total thermal conductivity accumulation function (TCAF), that is, the integral of TCSD. The green line represents the kinetic thermal conductivity, thus the difference between both is the collective contribution. Bottom: Mode kinetic and collective MFP in terms of frequency.

mal conductivity accumulation function (TCAF) it can be observed that phonons with frequency lower than 2 THz contribute to 40% of the thermal conductivity. On the other side, phonons with frequency higher than 6 THz contribute up to a 20%. A direct correspondence with the MFP spectral distribution (Fig. 5.3 bottom) can be done through this representation. Fig. 5.3 bottom shows the MFP in terms of frequency for the kinetic and collective terms. From the KCM,  $\Lambda_K(\omega, T) = v\tau_K$  is the kinetic MFP, and  $\Lambda_C(T) = \bar{v}\tau_C$  is the collective MFP, where

$$\bar{v} = \frac{\sum_{\mathbf{q}} v_{\mathbf{q}} C_{\mathbf{q}}}{\sum_{\mathbf{q}} C_{\mathbf{q}}} \quad (5.1)$$

is the mean phonon velocity (independent of  $\omega$ ).  $v_{\mathbf{q}}$  and  $C_{\mathbf{q}}$  are the phonon mode velocity and specific heat respectively. It is important to notice that while the kinetic MFP is different for all the modes, the collective MFP is the same for all of them. An effective MFP (blue asterisk) has been included to show the effect of the collective phonons from a pure kinetic point of view, where  $\Lambda_{\text{eff}}(\omega, T) = \Lambda_K(\omega) \cdot (1 - \Sigma) + \Lambda_C(T) \cdot \Sigma$ . From this representation it can be appreciated a reduction of the MFP of long MFP phonons at low frequencies and an increase for the smaller ones at high frequencies [2]. This effect caused by the

collective regime is a consequence of the energy and momentum conservation of the whole distribution introduced through  $\Sigma$  [26].

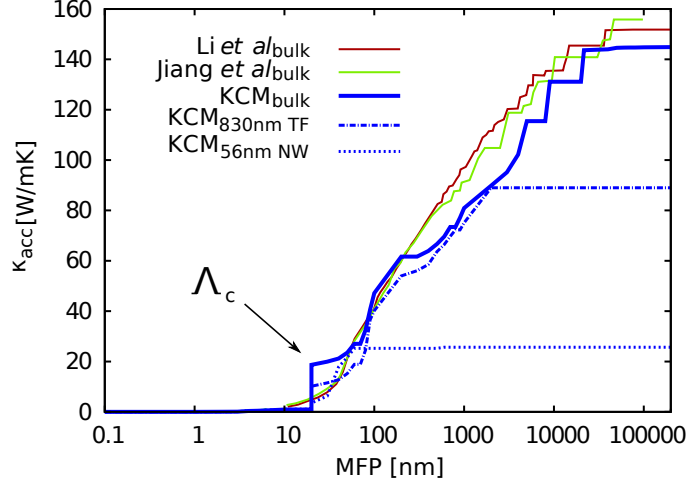


Figure 5.4: Thermal conductivity accumulation function (TCAF) in terms of MFP for bulk silicon at  $T=300$  K in the KCM compared to that of Li *et al.* [24] and Jiang *et al.* [119]. KCM predictions for 830 nm film and 56 nm wire are also included.

In Fig. 5.4 the accumulated thermal conductivity in terms of MFP for bulk silicon at 300 K is represented to show the differences between KCM and current kinetic models. It can be observed that, in contrast to the other presented models, in the KCM the larger MFP phonon that contributes to  $\kappa$  is  $\Lambda_K \sim 20 \mu\text{m}$ , in agreement with experimental observations [119]. This is due to the fact that for low frequency phonons, the use of Han's expressions [120] provides a  $\tau_U^{-1} \propto \omega^2$  dependence for the  $U$  processes instead of the widely used approximation  $\tau_U^{-1} \propto \omega^3$ . Note that the use of an analytical expression allows avoiding the over/underestimations provided by the limited grid in DFT calculations at these frequency ranges [118].

A characteristic feature of the KCM accumulation function is the appearance of a step at the collective MFP,  $\Lambda_C$ . From Fig. 5.4 it can be seen that while the kinetic contribution spans all the distribution, the collective one occurs only at a fixed MFP,  $\Lambda_C \sim 20$  nm for natural silicon at 300 K. The height of this step is proportional to the value of  $\Sigma$  and, as the switching factor depends on the size of the sample, it will be different for each  $L_{\text{eff}}$ , according to Fig. 4.3. Comparing the curves for different sizes (56 nm nanowire, 830 nm thin film and bulk) in Fig. 5.4 it can be concluded that the TSDF of a sample can not be obtained by just removing from the bulk curve the contribution of phonons with MFP larger than its characteristic length  $L_{\text{eff}}$  [108].

The position of the step at  $\Lambda_C$  in the TCAF can be related to a characteristic non-local scale  $\ell$  (see Eq. (4.2.1)) that is associated with hydrodynamic effects like Poiseuille flow or second sound. A direct detection of this step would be difficult for small samples because at these scales  $\Sigma$  is small. The calculated non-local scale for silicon at 300 K is  $\ell \sim 190$  nm. Recent experiments carried on bulk silicon by Hoogetboom-Pot *et al.* [10] show that collective effects appear when characteristic scales of the order of  $10^2$  nm are considered in the experiment. Although this scale is in agreement with the obtained non-local length  $\ell$ , deeper study is required to understand properly the origin of this non-local effect. It is important to remark that the consequences of collective effects on the measured thermal conductivity will depend on each experimental setup. This experiment is discussed in detail in **Section 6.1**.

The phonon spectrum of the other studied group IV and III-V semiconductors present the same general features as shown for silicon. In the case of diamond for example, as the collective contribution to thermal conductivity is higher, the height of the step corresponding to this contribution in the accumulation function in terms of MFP will be larger.

### 5.1.2 KCM phonon spectrum of $\text{Si}_{1-x}\text{Ge}_x$ and $\text{In}_x\text{Ga}_{1-x}\text{As}$

In order to observe differences between pure semiconductors and alloys, the kinetic and collective contributions to thermal conductivity in terms of frequency for  $L_{\text{eff}} = 7$  mm  $\text{Si}_{1-x}\text{Ge}_x$  and  $\text{In}_x\text{Ga}_{1-x}\text{As}$  at 300 K are presented in Fig. 5.5.

Fig. 5.5 displays the TCAF for the two presented alloys at  $x = 0.01$ , showing a significant slowing down of the kinetic transport. This reduction of the kinetic heat transport due to  $N$  collisions is obtained in the classical RTA approach through the inclusion of  $N$  scattering as a resistive mechanism in the Matthiessen's rule. The present model thus helps to understand why, when  $\Sigma$  is small, the RTA is expected to work. Notice that KCM offers a more general framework for accounting the effects of  $N$  scattering, namely, the reduction of kinetic transport (kinetic slowdown), and the existence of a collective heat transport.

In Fig. 5.6 the phonon spectral distribution of the thermal conductivity at two common alloy concentrations  $\text{Si}_{0.82}\text{Ge}_{0.18}$  (top) and  $\text{In}_{0.53}\text{Ga}_{0.47}\text{As}$  (bottom), at 300 K and  $L_{\text{eff}} = 7$  mm is shown. The green region represents the kinetic and the red one the collective contribution to thermal conductivity respectively. The general trend of the spectral distribution is the same as found in silicon but having a smaller contribution of the collective regime in the whole frequency range. In contrast, the accumulation function is remarkably different. While in silicon the contribution of modes below 2 THz had a contribution of 40% to the total thermal conductivity, for the two presented alloys this contribution is up to 90%.

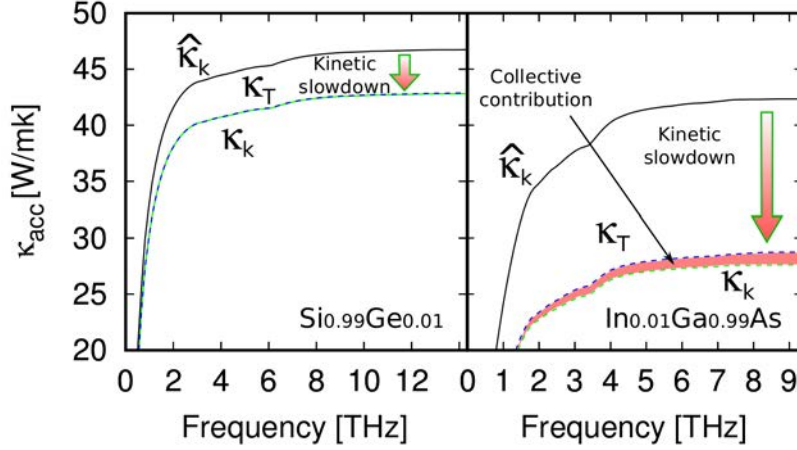


Figure 5.5: Thermal conductivity accumulation function (TCAF) for  $\text{Si}_{0.99}\text{Ge}_{0.01}$  (left) and  $\text{In}_{0.01}\text{Ga}_{0.99}\text{As}$  (right) for  $L_{\text{eff}} = 7$  mm rods at  $T=300$  K. Blue dashed line represents the total TCAF. The kinetic contribution to the thermal conductivity  $\kappa_K$  (green dashed line) is reduced the factor  $(1-\Sigma)$  as compared to the pure kinetic conductivity  $\hat{\kappa}_K$  (black line). The red region denotes the collective contribution. Even though the collective term  $\kappa_C$  may be small for 1% alloy samples, the kinetic transport is significantly slowed down due to normal processes.

In addition, the contribution of phonons with a frequency higher than 6 THz is almost negligible in both alloys. The insets in Fig. 5.6, representing a magnification of the high frequency region, show that only in the case of  $\text{In}_{0.53}\text{Ga}_{0.47}\text{As}$  appears a small (but insignificant) collective contribution to the thermal conductivity at high frequencies.

From a microscopic point of view, collective and kinetic contributions should have very different transient behavior. This can be shown by noticing that while each mode has a different MFP in the kinetic regime, the collective MFP is the same for all of them. Fig. 5.7 shows the MFP accumulation function for  $\text{Si}_{0.82}\text{Ge}_{0.18}$ ,  $\text{In}_{0.53}\text{Ga}_{0.47}\text{As}$  and natural Si at 300 K with  $L_{\text{eff}} = 7$  mm. It can be observed that for  $\text{Si}_{0.82}\text{Ge}_{0.18}$  (dashed light green) the main contribution to  $\kappa_T$  comes from large MFP phonons, with an important contribution of those bigger than  $100 \mu\text{m}$ . On the other hand, for silicon all the contribution to  $\kappa_T$  comes from phonons with MFP smaller than  $\sim 20 \mu\text{m}$ , larger phonons does not affect. In the case of  $\text{In}_{0.53}\text{Ga}_{0.47}\text{As}$  it is found an intermediate behavior. A jump in the cumulative thermal conductivity due to collective effects can be seen clearly for silicon at the MFP of  $\sim 20$  nm. In contrast, the contribution of the collective phonons to thermal conductivity in the alloys is almost negligible. Accordingly, a definite slope can be observed in the TCAF. Notice that this does not mean that  $N$  scattering is not important, as kinetic slowdown is still present.



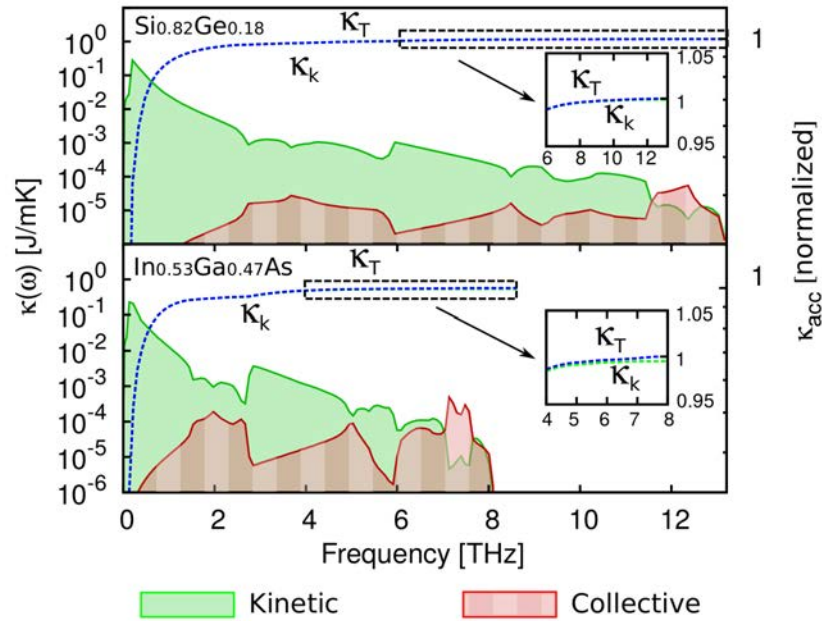


Figure 5.6: Thermal conductivity spectral distribution (TCS) and thermal conductivity accumulation function (TCAF) in terms of frequency for  $\text{Si}_{0.82}\text{Ge}_{0.18}$  (top) and  $\text{In}_{0.53}\text{Ga}_{0.47}\text{As}$  (bottom) for  $L_{\text{eff}} = 7$  mm rods at  $T=300$  K. Filled curves are the kinetic and collective contributions to TCS. Inset: High frequency magnification of TCAF.

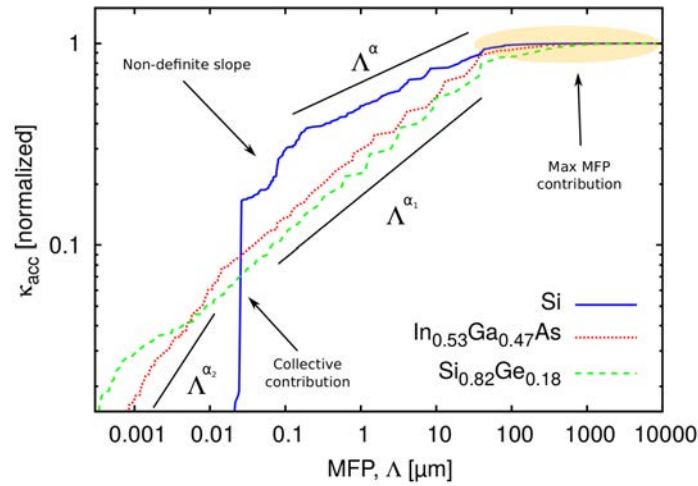


Figure 5.7: Thermal conductivity accumulation function (TCAF) for natural Si and  $\text{Si}_{0.82}\text{Ge}_{0.18}$  at 300 K and  $L_{\text{eff}} = 7$  mm.

Present results from Fig. 5.6 and Fig. 5.7 agree with recent works pointing

on the direction that long MFP phonons are important to predict the thermal conductivity in alloy samples [28, 29, 121]. In kinetic transport regimes, as found in alloys and in the kinetic contribution of pure samples, the phonon distribution spans all the MFP range. On the contrary, the collective contribution found in pure samples, appearing as a result of the momentum conservation of  $N$  processes, contributes as a single step. From the phonon contribution to thermal transport at each frequency and/or MFP useful information of the experimental observations of transient phenomena can be obtained.

As shown in previous articles, silicon has an important collective behavior [1, 2, 3]. The non-negligible collective contribution to  $\kappa_T$  in a single MFP found in silicon [3] could be a reason behind the non-definite slope in the total thermal conductivity contribution. Fig. 5.7 shows how the addition of the collective term to  $\kappa_K$  in silicon causes the appearance of a non-definite slope in  $\kappa_T$ . If the MFP information is obtained by the reconstruction through a kinetic model this behavior can not be appreciated. Information of the thermal conductivity in terms of frequency and MFP for kinetic and collective regimes separately is key to understand the behavior of an specific sample.

### 5.1.3 KCM phonon spectrum in low $\kappa$ compounds

The KCM has been used to study the thermal conductivity of low thermal conductivity compounds as  $\text{Bi}_2\text{Te}_3$ ,  $\text{PbTe}$  and  $\alpha$ -quartz, showing good agreement to experimental data (see **Section 3.4**). Now, the phonon spectrum is studied to get more information about the different contributions to thermal conductivity.

In the case of  $\text{Bi}_2\text{Te}_3$ , Fig. 5.8 shows the TCAF and the TCSD for a 4  $\mu\text{m}$  film and two wires of 300 nm and 25 nm at 300 K. It can be observed that the size reduction has a deep effect on the contribution of low frequency phonons to the thermal conductivity. In addition, a strong decrease of the high frequency phonon contribution can be noticed in the case of the 25 nm NW. The TCAF representation shows that phonons with frequencies lower than  $10^{12}$  rad/s have a small contribution to thermal conductivity for the presented samples. The major contribution in all cases comes from phonons with frequencies of  $6 \cdot 10^{12}$  rad/s and forward.

The decrease of the thermal conductivity contribution at low frequencies from Fig. 5.8 can be attributed to a reduction of the MFP of the acoustic phonons due to boundary scattering effects. This effect becomes more important for the smallest samples as the surface to volume rate is increased. Notice that even at diameters as small as 25 nm the suppression of low frequency modes is not complete. This indicates that boundary scattering does not block totally the thermal conductivity even at these extremely reduced sizes. In addition it can be observed that the main contribution to thermal conductivity comes from phonons

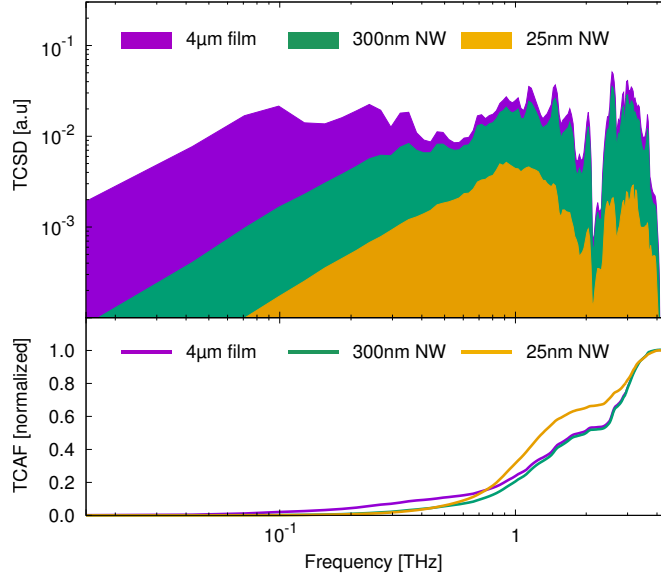


Figure 5.8: Spectral and accumulated thermal conductivity for a  $4 \mu\text{m}$  film, 300 nm and 25 nm wires of  $\text{Bi}_2\text{Te}_3$  at 300 K. Top: Spectral thermal conductivity as a function of frequency. Bottom: Accumulated thermal conductivity as a function of frequency.

with a frequency higher than  $10^{13}$  rad/s. Therefore there is a significant contribution of optical modes.

According to the mode velocity obtained from the dispersion relations (DR) and Fig. 5.8, the higher contribution to thermal conductivity comes from phonons with MFP smaller than 1.5 nm. It is interesting to notice that for silicon, in contrast, more than 50% of the contribution is due to phonons with MFP smaller than  $1 \mu\text{m}$ .

In Fig. 5.9 the  $N$  and  $U$  relaxation times (top) and TCAF (bottom) for PbTe in terms of frequency are represented. As can be observed, the  $U$  relaxation time follows the trend  $\tau_U \sim \omega^{-3}$  predicted by Herring [122], while for  $\tau_N \sim \omega^{-1.5}$ , slightly lower than the expected  $\tau_N \sim \omega^{-2}$  for diamond-like materials. This might be caused by the different atomic basis of the FCC structure. In the TCAF representation a smooth increase of the thermal conductivity from 0.2 THz can be observed. As pointed out in **Section 3.4**, in PbTe the collective contribution to thermal conductivity is  $\kappa_C \sim 1\%$ , therefore it is not observable. The significant effect represented in this figure is the kinetic slowdown. As  $\Sigma_{\text{PbTe}}(300 \text{ K})=0.5$ , the kinetic contribution  $\hat{\kappa}_K$  is significantly reduced (50%).

In the case of  $\alpha$ -quartz, Fig. 5.10 shows the  $N$  and  $U$  relaxation times (top) and TCAF (bottom) in terms of frequency. From the relaxation time it can be observed that there is an important dispersion of values due to the high number of

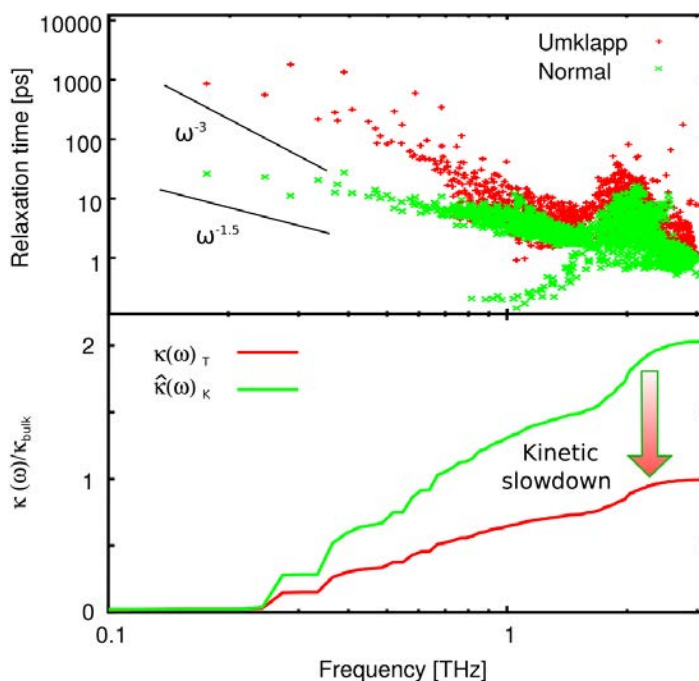


Figure 5.9: Top: *First principles* normal and umklapp relaxation times for PbTe as a function of frequency. Bottom: Thermal conductivity accumulation function (TCAF) in terms of frequency.

phonon branches, 27 in this case. From the TCAF important differences between  $\kappa(\omega)_{YY}$  and  $\kappa(\omega)_{ZZ}$  can be observed. While  $\kappa(\omega)_{YY}$  shows a smooth increase of the thermal conductivity from 0.2 THz, similar to that found in PbTe (Fig. 5.9 top), in  $\kappa(\omega)_{ZZ}$  there is a huge contribution of low frequency phonons. It can be observed that phonons with less than 1 THz provide more than 95% of the total thermal conductivity. This is caused by the different phonon mode velocity in each direction. In addition, while for  $\alpha$ -quartz $_{ZZ}$  the collective contribution is negligible (0.4%), in  $\alpha$ -quartz $_{YY}$  a collective contribution of 6% due to high frequency phonons is observable.

#### 5.1.4 KCM phonon spectrum of graphene

In addition to the studied 3D samples, here the phonon spectrum and the thermal conductivity accumulation functions for graphene are presented.

Fig. 5.11 shows the *first principles* relaxation times for graphene. The red line corresponds to the impurity scattering with natural isotope concentration, and the green and blue ones the  $N$  and  $U$  relaxation times respectively. The visible splitting of the scattering mechanisms corresponds to different vibrational

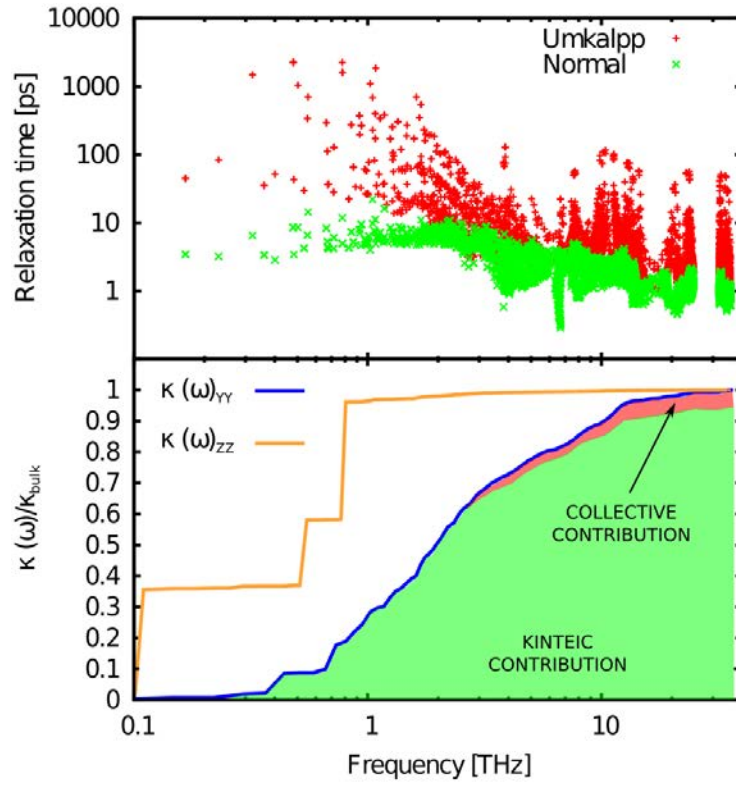


Figure 5.10: Top: *First principles* normal and umklapp relaxation times for  $\alpha$ -quartz as a function of frequency. Bottom: Thermal conductivity accumulation function (TCAF) in terms of frequency for  $\alpha$ -quartz $_{\gamma\gamma}$  and  $\alpha$ -quartz $_{zz}$ .

modes. From this representation it is clear that the  $N$  scattering dominates at medium and low frequencies. While at high frequencies all the scattering mechanisms have a relaxation time of the same order, at medium and low frequencies the differences between the  $N$  scattering and the other mechanisms is more than one order of magnitude. This dominance of  $N$  processes indicates that there will be a high importance of collective effects, and therefore phonon hydrodynamics will dominate the transport, as reported in recent works [13, 14].

The TCAF for graphene is represented in Fig. 5.12. Here the contributions of the kinetic and collective regime to thermal conductivity are represented. It can be observed that the kinetic modes have a contribution of almost 60% at low frequencies. In contrast, the collective modes contribute up to a 40% from frequencies higher than 1 THz. The visible step at low frequencies of the accumulation function is due to the limited grid sampling.

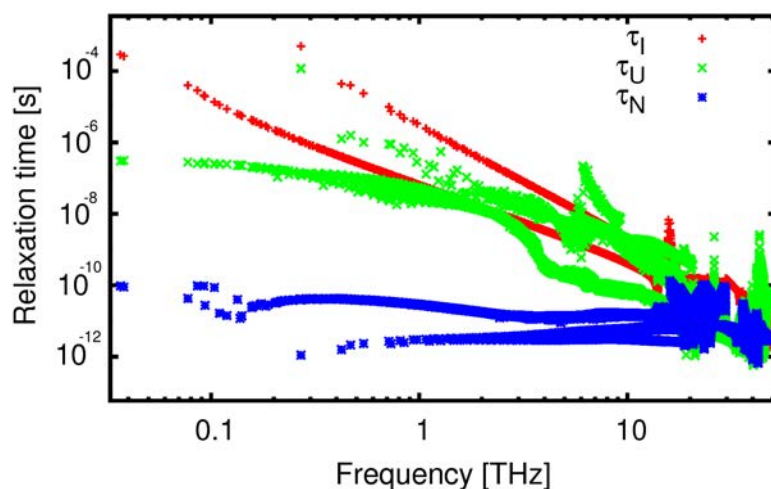


Figure 5.11: Phonon relaxation times for graphene.  $\tau_I$  corresponds to the impurity relaxation time of natural isotopic concentration, and  $\tau_U$  and  $\tau_N$  to the umklapp and normal relaxation times obtained from *first principles* respectively.

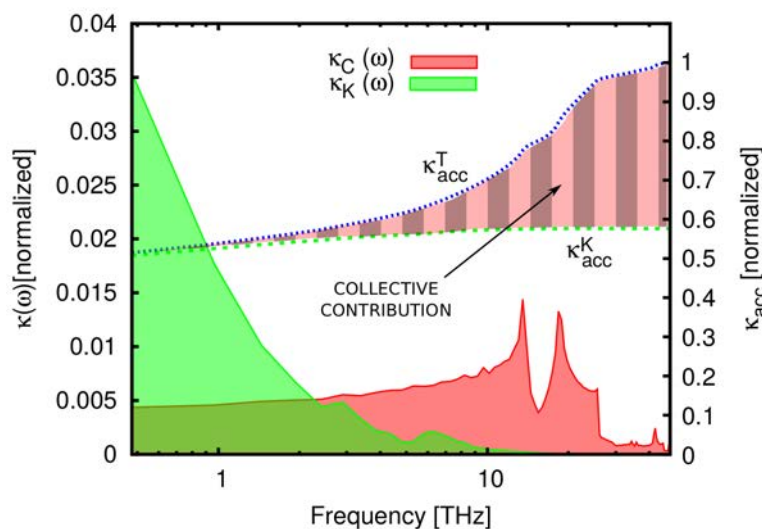


Figure 5.12: Spectral and accumulated thermal conductivity of natural graphene as a function of frequency.

## 5.2 Transient regimes

The diffusive transport in the KCM deals with the heat transport from the point of view of the dominance of resistive scattering processes over the non-resistive ones. On the contrary, the ballistic transport is based on the differentiation of boundary scattering versus the other scattering processes. Since the KCM has

been applied successfully in the diffusive regime, a next step is to see how the kinetic and collective regime can give new insight in transient regimes from diffusive to ballistic transport.

At short time scales, transient regimes measured by means Time Domain Thermo Reflectance (TDTR) have revealed that dynamics of energy transport in actual materials is more complex than a broad distinction between ballistic and diffusive regimes. Phonon MFP can span several orders of magnitude and the transition from ballistic to diffusive is not at the same time or length scale for each mode. This means that for a specific time scale, part of the phonons can be ballistic while other should remain diffusive. This behavior leads to the appearance of a superdiffusive regime, explained accurately by Truncated Lévy Flights (TLF) for highly kinetic samples [28] (see **Section 1.3**). In materials where collective transport is important, like silicon, the diffusive-ballistic transition behaves in a different way due to the emergence of a collective regime. A careful study of MFP and frequency dependence of thermal conductivity is needed in order to understand such phenomena.

The phonon spectral distribution of the thermal conductivity in the KCM combined with the TLF formalism [28, 29] seems a suitable framework to deal with the transition from diffusive to ballistic thermal transport in pure and alloy semiconductors. This transition from short to long time scales can be described by the Maxwell-Cattaneo equation [123]  $\tau \partial^2 T / \partial t^2 + \partial T / \partial t = \chi \nabla^2 T$ , where  $\tau$  is the mean characteristic time of phonon distribution and  $\chi$  is the thermal diffusivity of the sample. Despite of this clear distinction, dynamics of energy transport in actual semiconductors is more complex. The Maxwell-Cattaneo equation is valid only when a single characteristic time  $\tau$  can be defined from the phonon distribution. This is only possible in the collective regime, as all the modes share the same MFT. However, in the kinetic-dominated regime this is not possible as the MFT of the different phonons can span several orders of magnitude. Therefore the diffusive to ballistic transition has a different time scale for each phonon mode.

As seen in Fig. 5.7 for alloys, all the modes span all the phonon distribution. Therefore in high kinetic samples like alloys, the relaxation times of each mode are different and the transition from ballistic to diffusive is at different times  $\tau(\omega)$ . As each phonon has its own MFP, the Maxwell-Cattaneo equation, which assumes that the transition from diffusive to ballistic occurs at the same time for all the phonons, can not be applied. A correct treatment in this case would be to solve the Maxwell-Cattaneo equation for each mode, but the number of calculations will increase drastically.

In Fig. 5.13 the effect of Lévy Flights in the spatial domain has been reproduced in order to study the impact of collective transport. The kinetic expression of TLF has been introduced in **Section 1.3.5** Eq. (1.81). From the Laplace trans-

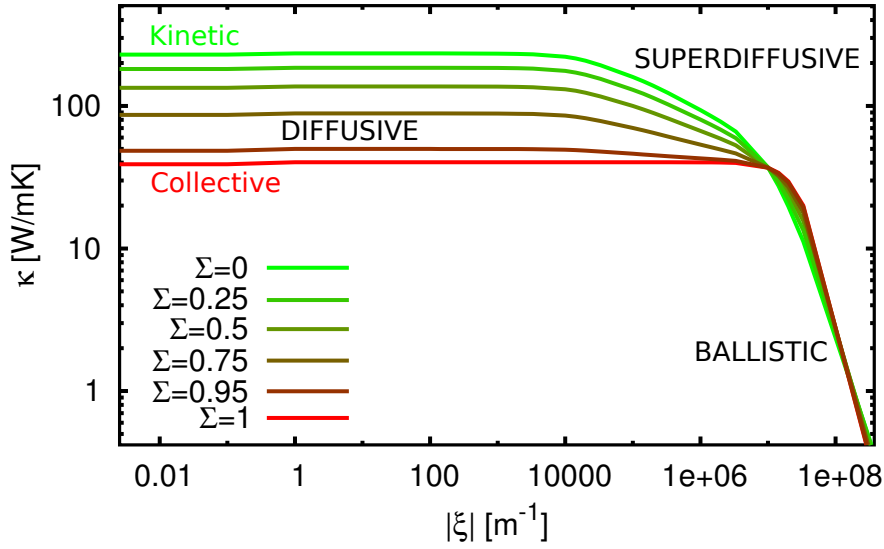


Figure 5.13: Fractal thermal conductivity reproduced in the KCM framework for silicon at 300 K.

formed of the steady state hydrodynamic KCM equation in the collective regime, neglecting the term  $2\nabla\nabla\cdot\mathbf{Q}$ , the collective thermal conductivity is expressed as:

$$\kappa(\xi, T) = \frac{\kappa(T)}{1 + \xi^2 \Lambda_C(T)^2}. \quad (5.2)$$

As it can be observed, in the kinetic regime, where  $\Sigma = 0$  and the TLF model is completely valid, there is a transition from diffusive to ballistic transport through a superdiffusive (or quasiballistic) regime. In the collective regime, where  $\Sigma = 1$ , the transition from diffusive to ballistic is very sharp, that means that there is a single spatial scale that governs this transition. In intermediate regimes, where  $\Sigma \in (0, 1)$ , there is a transition from the TLF limit to the collective limit. When  $\Sigma$  increases the superdiffusive region tends to flatten until is completely destroyed in the ideal collective transport.

The spatial evolution of the thermal diffusivity for  $\text{In}_{0.53}\text{Ga}_{0.47}\text{As}$  and  $\text{Si}_{0.82}\text{Ge}_{0.18}$  [28, 29] is represented in Fig. 5.14. In the case of alloys the transition to diffusive to ballistic transport regime is clearly governed by a superdiffusive region with a fractal exponent. It can be observed that the region with a superdiffusive behavior with fractional exponent spans 4 orders of magnitude in time for  $\text{Si}_{0.82}\text{Ge}_{0.18}$  while 3 orders for  $\text{In}_{0.53}\text{Ga}_{0.47}\text{As}$ . In Si the transition from pure ballistic to diffusive regime seems to be smoother, as has been observed in Fig. 5.13.

In previous works [28, 29], the transient diffusive-ballistic behavior related to the cumulative thermal conductivity slope by fractal superdiffusive expo-



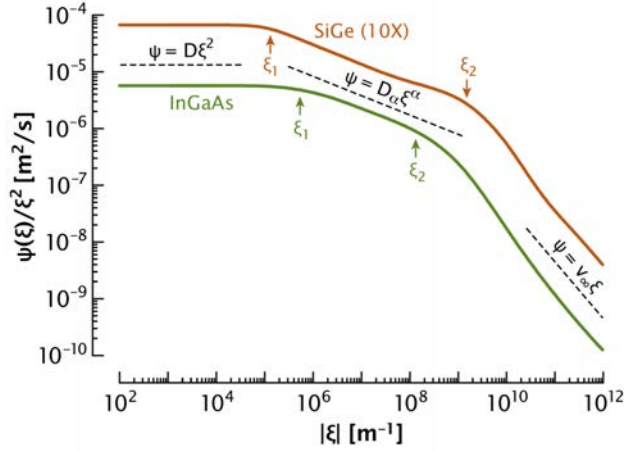


Figure 5.14: Fractal diffusivity defined from  $\psi(\xi)/\xi^2$  for  $\text{In}_{0.53}\text{Ga}_{0.47}\text{As}$  and  $\text{Si}_{0.82}\text{Ge}_{0.18}$ .  $\text{Si}_{0.82}\text{Ge}_{0.18}$  curve is upscaled to ease the visualization [28]. Three scaling regions with different exponents may be identified.

nents in the TLF model appears to behave different in Si and  $\text{Si}_{1-x}\text{Ge}_x$  alloys. In Fig. 5.14 the emergence of a superdiffusive regime with exponent 1.34 for  $\text{Si}_{1-x}\text{Ge}_x$  alloy can be observed, while in Fig. 5.13 for silicon ( $\Sigma \sim 0.5$ ), where collective phonons are not negligible, there is a smoother transition from ballistic to diffusive regimes. This behavior may be explained in terms of the different weight of the collective contribution  $\Sigma$  shown in Fig. 3.21. As detailed in Fig. 5.13, the fractal behavior is a kinetic phenomenon and, as the collective contribution increases, the temporal window where this behavior can be probed shrinks.

The origin of the different slopes pointed out previously in Fig. 5.7 and Fig. 5.14 can be observed in Fig. 5.15. As noticed by Vermeersch *et al.* [28], the slope of the accumulation function can be related to the exponent of the dominant scattering mechanism. To see this relation, Fig. 5.15 shows the  $U$  and impurity/alloy relaxation times for Si,  $\text{In}_{0.53}\text{Ga}_{0.47}\text{As}$ , and  $\text{Si}_{0.82}\text{Ge}_{0.18}$ . It can be observed that  $U$  scattering is dominant for silicon, which has a trend that goes from  $\tau \propto \omega^{-3}$  to  $\tau \propto \omega^{-2}$ , according to the *first principles* calculations and in agreement with Han's expressions [124]. For  $\text{Si}_{0.82}\text{Ge}_{0.18}$  and  $\text{In}_{0.53}\text{Ga}_{0.47}\text{As}$  the dominant scattering is the alloy term with  $\tau \propto \omega^{-4}$ , although is stronger in  $\text{Si}_{0.82}\text{Ge}_{0.18}$ . This shows why both have also the same exponent in the accumulation function but with different extents of the superdiffusive region.

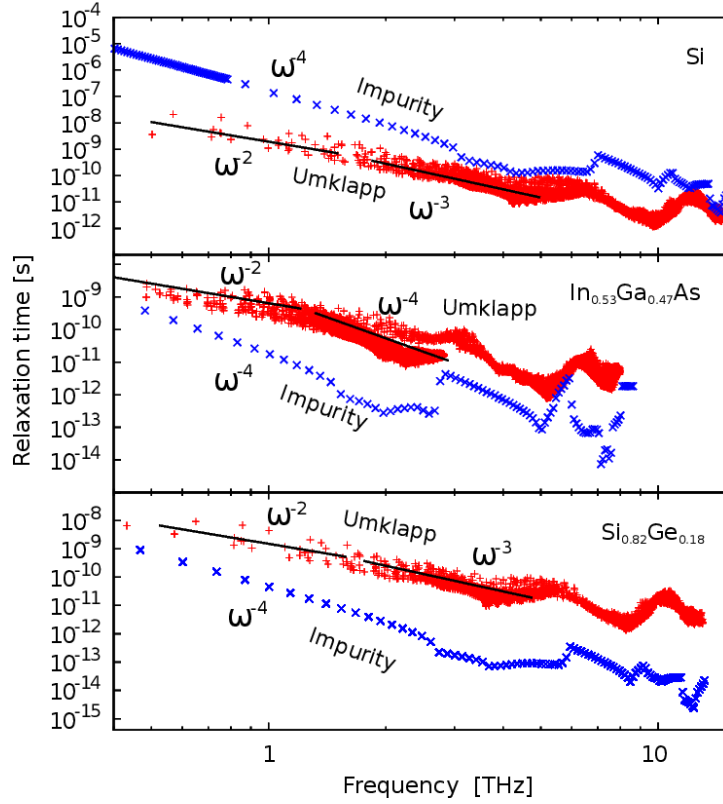


Figure 5.15: Umklapp and impurity/alloy *first principles* relaxation times for Si,  $\text{In}_{0.53}\text{Ga}_{0.47}\text{As}$  and  $\text{Si}_{0.82}\text{Ge}_{0.18}$  at 300 K.

### 5.3 The role of low energy phonons

It has been already pointed out and observed from various representations of the thermal conductivity as a function of frequency that low frequency phonons can have relevant consequences on the calculations of thermal conductivity, especially in alloys.

The low energy phonon calculations regarding thermal conductivity involve harmonic and anharmonic terms. From an *ab initio* framework, while the harmonic terms can be calculated without further complications for fine  $\mathbf{q}$ -point mesh sampling, the anharmonic ones require higher computational resources. The goodness of such calculations are determined by the interatomic force constants (IFC) computed from *first principles*. In order to obtain proper IFC, the modeling of the system and the convergence of the different involved parameters should be tested accurately (see **Section 2.2** and **Section 2.5**).

In the calculation of the 3-phonon scattering rates, the access to low en-

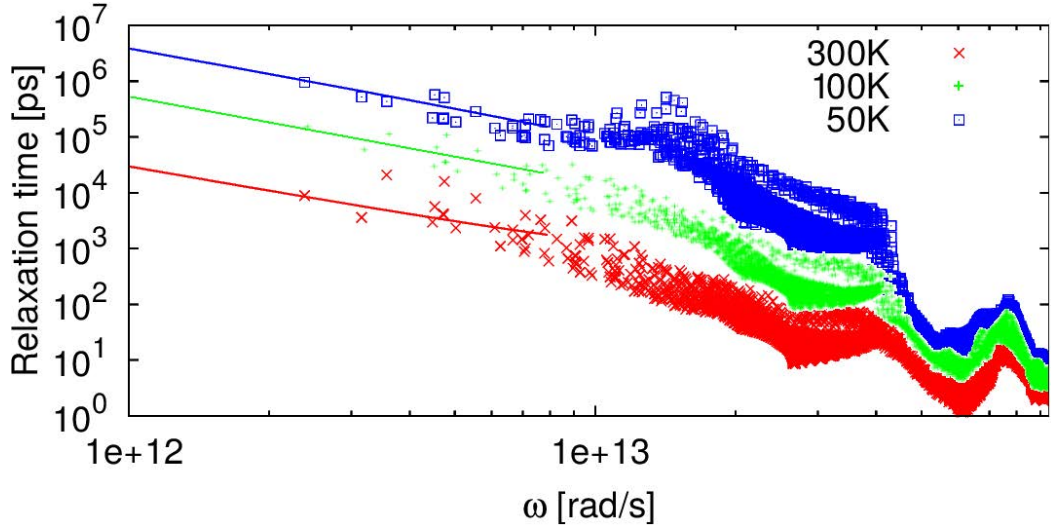


Figure 5.16: Umklapp relaxation times at 300 K, 100 K and 50 K for natural silicon. Symbols represent the *ab initio* values and lines Han's expressions

ergy phonons depends on the  $\mathbf{q}$ -point mesh sampling. The finer the mesh, the lower the available energy phonons. This makes very complex the access to anharmonic information of very low frequency phonons from a computational viewpoint. If the thermal conductivity is computed directly in a  $\mathbf{q}$ -mode summation with a coarse mesh sampling, the information of low energy phonons is neglected and could lead to wrong results. In such situations, Akheizer damping has been introduced as an extra relaxation time in order to avoid this effect [119]. As explained in previous chapters, it is possible to average the  $\mathbf{q}$ -mode information in order to deal with frequency integrals. In this case, extrapolations for  $N$  and  $U$  relaxation times at low energy phonons have been deduced analytically [120, 122, 124]. These expressions make it easy to obtain such parameters even for extremely low frequencies, preventing thus to lose the information from these phonons. Doing so, it is not required to introduce any extra relaxation time in order to predict the experimental data.

For  $N$  processes at low frequency Herring [122] demonstrated that the  $N$  relaxation times have a  $\tau_N \propto \omega^2 T^3$  frequency and temperature dependence for diamond-like structures. In the case of  $U$  processes, such dependence is more complex. Han and Klemens [120, 124] deduced an expression to determine the relaxation time for different transition processes at low frequencies:  $T + L \rightarrow L$  and  $T + T \rightarrow L$ , where  $L$  and  $T$  indicate longitudinal and transverse branches respectively. In the case diamond-like semiconductors the most common process is  $T + L \rightarrow L$ , being the relaxation time expressed in the continuum approxima-

tion as:

$$\tau_{U,i}^{-1} = \frac{\gamma^2 \hbar}{3\pi^2 \rho v_T^2} \frac{\omega_i(\omega_L - \omega_i)\omega_L}{\sqrt{2\omega_i\omega_L - \omega_i^2}} Gr_c^2 \left( \frac{1}{e^{\hbar(\omega_L - \omega_i)/k_B T} - 1} - \frac{1}{e^{\hbar\omega_L/k_B T} - 1} \right), \quad (5.3)$$

where here  $\gamma$  is the Grüneisen parameter,  $\rho$  the material density and the subscripts  $L$  and  $T$  refer to longitudinal and transverse modes.  $r_c$  is the radius of the 1BZ expressed as:

$$r_c = R \left( \frac{G}{2} - \frac{\omega_i}{c} \right) / \left( \frac{G}{2} \right), \quad (5.4)$$

where  $G = |\mathbf{G}| = 4\pi/a$  and  $R = \pi/(\sqrt{2}a)$  for the  $[1\ 0\ 0]$  direction in a cubic cell, being  $a$  the lattice parameter and  $c$  the sound velocity of the phonon  $i$ .

Fig. 5.16 represents the *ab initio*  $U$  relaxation times and Han's expression for silicon at 300 K, 100 K and 50 K using the density of silicon and its averaged  $\gamma$  calculated from *first principles* in a 40x40x40  $\mathbf{q}$ -point grid. As can be observed, Han's expression for  $T + L \rightarrow L$  processes reproduces properly the *ab initio* calculated relaxation times at intermediate-low frequency region and provides a good extrapolation at low frequencies.

## 5.4 Relaxation times from the full scattering matrix

The linearized Boltzmann Transport Equation (LBTE) can be solved in different ways, as has been introduced in **Section 1.2**. Depending on how it is solved, the total relaxation time of distribution function of the heat carrier can be different.

Fig. 5.17 compares the total relaxation time of the carrier distribution for silicon and diamond in the Relaxation Time Approximation (RTA), the relaxation solution of the LBTE (R-LBTE) and KCM models obtained from *first principles* calculations on Phono3py package [79]. Notice that in this figure carrier relaxation times are compared, not just phonon relaxation times. In the case of the R-LBTE the heat carriers have been defined as relaxons [22]. In analogy, in the KCM the heat carriers are called collectons. From this figure it can be observed that in both KCM and R-LBTE the relaxation times of the carriers at high frequencies are higher than the phonon relaxation times in RTA. In the KCM this effect is attributed to collective regime, which leads to an enhancement of the optical phonons [2] as shown in Fig. 1.2. In addition, it can be observed that the relaxation times obtained in KCM (collectons) and R-LBTE (relaxons) reproduce a similar trend. This suggests that as well as in KCM, the full solution

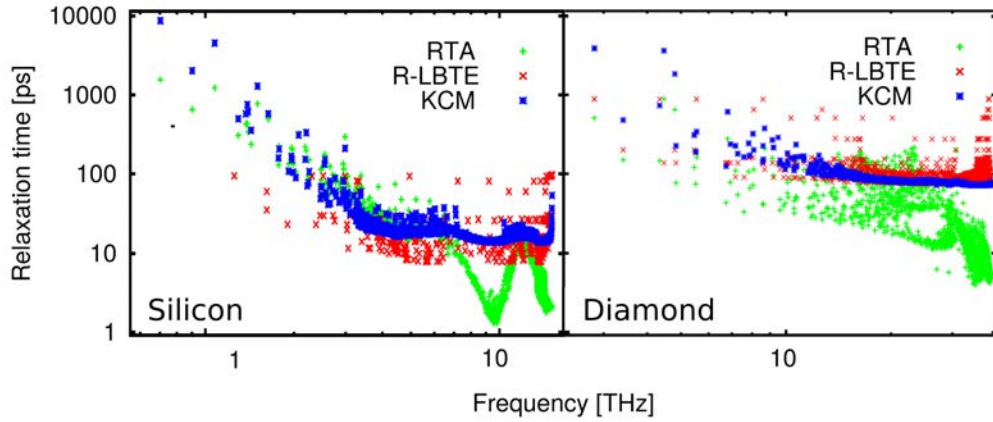


Figure 5.17: *First principles* total relaxation times for silicon (left) and diamond (right) under the Relaxation Time Approximation (RTA), relaxon solution of LBTE (R-LBTE) and KCM models from Phono3py.

of the collision matrix also captures the effect of the collective regime. This is expected as both models are solutions of the same phonon LBTE. Finally, comparing the relaxation times for silicon and diamond, it can be observed that the light atomic mass of the carbon atoms leads to a weak phonon interaction, visible as a higher relaxation time.

In previous sections of this chapter it has been shown that high frequency phonons do not have a remarkable contribution to the thermal conductivity in most cases, except for diamond or graphene. Therefore direct consequences of the enhancement of the optical phonons by the collective regime can not be analyzed, in general, from the thermal conductivity of bulk materials. The enhancement of optical phonons depends on the collective relaxation time  $\tau_C$  as well as on the  $\Sigma$  factor. Those are parameters that are only defined in the KCM framework. Therefore, even though the relaxation time of the distribution function in other models can be similar, those parameters can not be obtained and the origin of the mentioned enhancement is hidden. As will be explained in **Chapter 6**, complex experiments can be reproduced by the KCM hydrodynamic model. In this case, non-local parameters that are directly related to the collective regime are required (see Eq. (4.2.1)).

## Chapter 6

# Geometric effects in complex experiments

The use of complex geometries and heating conditions in recent experiments have shown that Fourier law is not able to reproduce all the obtained results [4, 5, 6, 7, 8, 9, 10]. In this line, the KCM equations for the heat flux including memory and non-local effects have been proposed as an explanation for the observed behavior. This chapter includes a novel work that combines experimental and theoretical research performed in collaboration with the Birck Nanotechnology Center (West Lafayette, USA), where steady state and transient heat transport have been studied on silicon and  $\text{In}_{0.53}\text{Ga}_{0.47}\text{As}$  samples. In addition, the KCM provides new explanations for two recent published experiments that exhibit non-Fourier effects in 1- and 2-dimension systems.

In materials where normal ( $N$ ) scattering is important, such as Si, Ge, GaAs or diamond, the KCM has been used to calculate the thermal conductivity of bulk and in simple geometries like nanowires and thin films, from nanometer to micron scales showing good agreement with experimental data [3]. In these simple geometries, non-locality can be analytically integrated and included into a form factor  $F$  that modulates the collective contribution to thermal conductivity depending on the sample size [3, 33]. In addition, the analytic solution of the hydrodynamic KCM equation and the solution by finite elements have shown good results in such systems (see **Section 4.2**).

In the present chapter more general geometries in situations where an analytic solution is not available are studied. In these cases, it is required to use the hydrodynamic heat flux equation presented in **Section 4.2**:

$$\tau \frac{d\mathbf{Q}}{dt} + \mathbf{Q} = -\kappa \nabla T + \ell^2 (\nabla^2 + 2\nabla \nabla \cdot) \mathbf{Q} . \quad (6.1)$$

The first terms on the left and the right sides of Eq. (6.1) define the clas-

sical Fourier law. The second term on left hand side includes thermal inertia effects and is necessary when the time variations are of the order of the heat carrier mean free time (MFT). In most semiconductors, this time is of the order of picoseconds, much smaller than the characteristic time of many pump-probe experiments, which detect temperature changes in 100's of picoseconds to nanosecond range. The second term on the right side includes non-local effects and it depends on the non-local length  $\ell$ , which is of the order of hundreds of nanometers for many semiconductors, as  $v \sim 10^3$  m/s and  $\tau \sim 10^{-12}$  s. As it will be shown, this term can dominate the observed non-Fourier behavior. This term is analogous to the viscous term in the Navier-Stokes equations of fluid mechanics, and it reflects the partial conservation of crystalline momentum in  $N$  collisions. Notice that this term is not necessarily along the direction of the temperature gradient and, as a result, the heat flux generated by Eq. (6.1) can not be parallel to the temperature gradient, a behavior that can not be described by an effective Fourier law. Obviously, Eq. (6.1) can not reproduce all the complexities of the phonon spectrum and interactions, such as the Lévy flights [29], but, as shown in this chapter, it can explain the main deviations from the Fourier law observed in experiments.

## 6.1 1D heat propagation

The simplicity of 1D geometries allows comparing the hydrodynamic KCM results with both experimental data and BTE solutions, where models can sometimes be simplified and analytically solved. The hydrodynamic heat transport can be also studied from a 1D spatially sinusoidal temperature pattern created on a silicon membrane and left to return to equilibrium [4]. Johnson *et al.* obtain the effective thermal conductivity in this setup by measuring the decay time of the patterned heat, known as transient thermal grating (TTG). By combining Fourier law using an effective thermal conductivity with the energy conservation the expected decay rate can be obtained:

$$\gamma = \frac{\kappa_{\text{eff}} \zeta^2}{C}, \quad (6.2)$$

where  $\zeta = 2\pi/L$  is the inverse scale length,  $L$  being the grating period and  $C$  the specific heat. Standard Fourier theory predicts a constant thermal conductivity and consequently a quadratic rise in the decay rate as a function of the inverse length scale. Experimental data do not follow this prediction, showing a decrease of the apparent effective conductivity with increasing values of  $\zeta$ . One should note that since a patterned heat source is created in the volume of the membrane,

this does not introduce an additional boundary in the system. Thus the use of a boundary relaxation time is not justified to fit the results.

In this specific configuration a solution of Eq. (6.1) in 1D can be easily obtained in the transformed Fourier space. The spatial derivatives of the heat flux in that equation give a contribution equal to  $3\ell^2\zeta^2$  in the left hand side. The decay rate is then:

$$\gamma = \frac{\kappa\zeta^2 c\ell}{1 + 3\ell^2\zeta^2}. \quad (6.3)$$

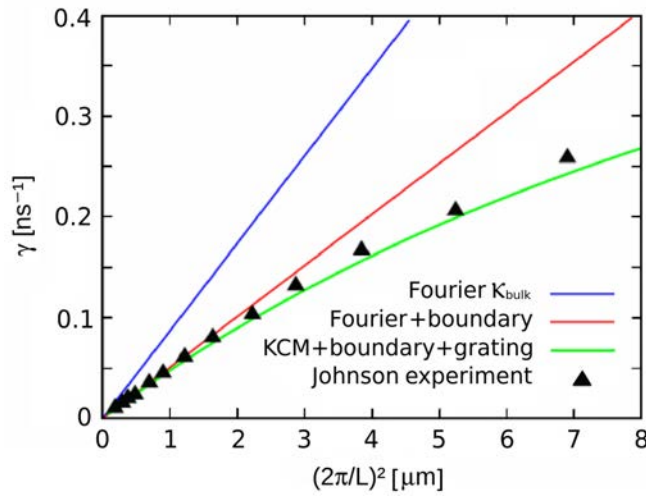


Figure 6.1: Effective decay rate as a function of the inverse grating length scale: experiments (symbols), Fourier predictions with the bulk heat conductivity (blue line), the effective thin film conductivity (red line) and hydrodynamic KCM predictions, Eq. (6.1) (green line).

The obtained 1D solution can not be applied to Johnson's [4] experiment for a membrane of small thickness  $h$  much larger than  $\ell$ . In this case the transverse coordinate must be taken into account in Eq. (6.1), and therefore the solution deviates from the one-dimensional form. It can be shown (see **Appendix B**) that, for the small values of  $\ell\zeta$  that are relevant in the experiment, the effect of the transverse profile is to substitute the bulk conductivity  $\kappa$  by the effective in-plane conductivity of the membrane,  $\kappa_{\text{eff}}(h)$ , and the parameter  $\ell^2$  by an effective value reduced in the same proportion,  $\ell_{\text{eff}}^2 = \ell^2 \kappa_{\text{eff}}/\kappa$ . In Fig. 6.1, the experimental results and the prediction of Eq. (6.2) are plotted using the bulk value of the thermal conductivity and the KCM prediction given by Eq. (6.1). The non-local length calculated from *first principles* is  $\ell = 190$  nm.

Using the Boltzmann Transport Equation (BTE), a similar expression has been obtained in which the reduction of the thermal conductivity is a conse-



quence of phonon suppression function eliminating phonons from the distribution when their mean free path (MFP) was approximately larger than the grating period [4]. In the case of Eq. (6.1), this factor has a hydrodynamic interpretation, that is to say, it is not based on individual phonons but it describes the collective heat flow.

In higher spatial dimensions, Eq. (6.1) is quite useful as compared to the direct solution of BTE since the vector nature of the heat flow is directly taken into account. In 2D and 3D, BTE can only be solved in very simplified geometries extracting a limited amount of information. Iterative solutions in general configurations are computationally prohibitive as solutions may not be local in space. KCM offers the possibility to solve Eq. (6.1) combined with the energy conservation law by using a finite element approach. This avoids analytic matrix inversion and integration, in contrast to kinetic approaches of BTE. It is necessary to complement the second-order differential equation with appropriate boundary conditions to fix the heat flux at the boundaries. Slip boundary conditions have been used in this approach (see **Appendix C**).

The same grating experiment has been analyzed also by Zeng *et al.* for two set of silicon membranes of 390 nm thick [116]. In this work, different models are used in order to interpret the results. On one side a spectral Monte Carlo (MC) simulation with boundary scattering and on the other a gray MC and effective MFP model based on phonon suppression functions.

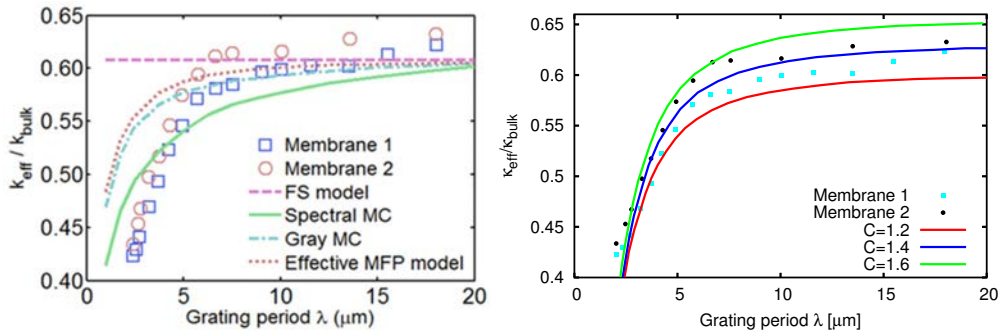


Figure 6.2: Thermal grating simulations from different models. Left: Fuchs-Sondheimer (FS), spectral monte carlo (MC), gray MC and effective mean free path (MFP) model [116]. Right: Hydrodynamic KCM with different slip boundary conditions and non-local length  $\ell = 190$  nm.

In Fig. 6.2 is represented the experimental data of thermal grating on silicon membranes and the different models used to analyze them. In the left plot the different models used by Zeng *et al.* are shown. In addition, the Fuchs-Sondheimer (FS) calculation, which neglects the effect of grating, shows the limit situation [31]. In the right plot are represented the predictions of the hydrodynamic KCM model for different slip boundary conditions and a non-local

length of  $\ell = 190$  nm. In comparison it can be appreciated that KCM performs better than the other models, as the tail for small grating periods is perfectly predicted for any slip condition. The drop of the tail depends only on the non-local length  $\ell$ . Regarding the exact value of the slip condition, as it has been mentioned in **Section 4.2**, it depends on the characteristics of the roughness of the sample, therefore a deeper study is required in order to obtain the exact value.

The better performance of the KCM can be understood from the non-equilibrium framework. Kinetic models, as the ones represented in Fig. 6.2 left, are solved from individual phonon relaxation times  $\tau(\omega, T)$  calculated from standard non-equilibrium distribution functions where the perturbation only depends on a temperature gradient  $A(\nabla T)$  (see **Section 1.1.1**). In the present experimental setup it is clear that also exists a heat flux gradient, therefore  $A(\nabla T, \nabla \cdot \mathbf{Q})$ , then the relaxation times calculated from the first approach alone are no longer valid. In the KCM, in contrary, is used a hydrodynamic equation with an integrated relaxation time  $\tau(T)$  for each temperature. Although this relaxation time is calculated from a perturbation  $A(\nabla T)$ , the hydrodynamic equation is derived from higher order perturbations (see **Section 1.3.3**) regarding variations of the heat flux  $\mathbf{Q}$ . This makes the hydrodynamic KCM approach more suitable for these kind of experiments.

As mentioned by Zeng *et al.*, the effective models derived in their work are specific for the studied geometry (a membrane) and can not be applied in other systems. The hydrodynamic KCM equation, as include generic boundary conditions, can be applied to any geometry when solved by finite elements.

## 6.2 2D heat propagation

As the second test of validity, Eq. (6.1) is used to describe a phenomenon that has been observed by using several heating lines in a patterned configuration [10]. These arrays are nickel heating lines of width  $L$  grown on a silicon substrate separated periodically a distance  $4L$ .

A laser generates a short heating pulse on the lines and their thermal decay is measured using pump-probe techniques. The authors find a maximum in the effective thermal boundary resistance (TBR) as  $L$  is reduced; that is, as the lines become closer to each other, the effective TBR increases up to a point around 300 nm, below which it decreases. Then, for the closest lines, the substrate seems to evacuate energy better than for lines slightly farther apart. This was interpreted so that, when the nanoscale heat sources are close enough, collective effects among phonons from the different heater lines increase dissipation efficiency. By using the finite element solution of Eq. (6.1) (without any TBR), predictions of the hydrodynamic model for an isolated heater line and for the

periodic array of lines are obtained. Interestingly, the KCM predicts an effect equivalent to the one attributed to an effective thermal resistivity in the interface between the heater and the sample, i.e. the TBR. This effective thermal resistivity is obtained as the best fit of a TBR to match the KCM decay curve when using a Fourier law for the substrate. Fig. 6.3 shows that, by using a non-local length  $\ell = 190$  nm the hydrodynamic model is able to predict the experimental data for line widths larger than 300 nm. The advantage of the hydrodynamic model with a fixed  $\ell$  is that it avoids the need to fit by hand the effective resistivity for each sample. Also, the fact that the value for the non-local length for this experiment is the same the one used to describe the previous experiment on silicon from **Section 6.1** supports the consistency of the model.

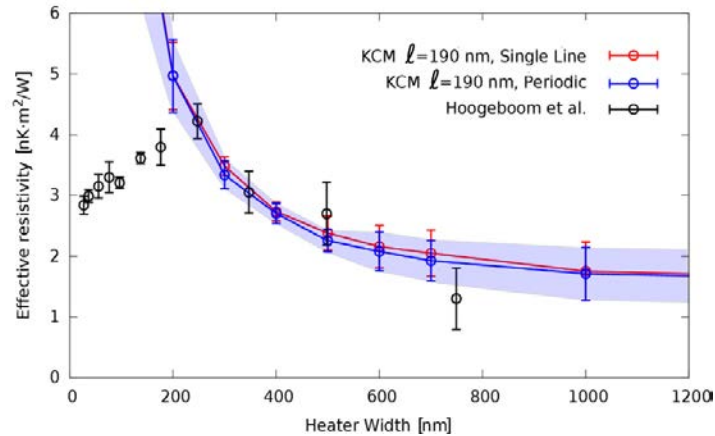


Figure 6.3: Effective thermal resistivity as a function of the heater width  $L$  with periodicity  $4L$  on top of silicon. Black dots denote the effective resistivity needed by a Fourier law to fit the experimental data [10]. Red and blue dots correspond to the values of the effective resistivity in a Fourier model needed to reproduce the KCM decay curves for a single line and a periodic array of lines, respectively. The blue zone corresponds to the error in the KCM with periodic configuration.

When the heating line width decreases below a value around 300 nm the KCM model fails, as it provides a monotonic increase of the effective resistivity. This behavior is not amended by considering an array of heater lines instead of a single line, since the model predictions are the same in both cases (no cooperative behavior among lines is predicted by the KCM model). However, the KCM can give some insight on the decay of the effective thermal resistivity at small sizes observed in the experiment. The origin of this behavior may be related to some experimental observations found in the next experiment on silicon and will be discussed in **Section 6.3**.

### 6.3 Steady state and transient heat transport

This study consists in an experiment in which metal lines are deposited on a semiconductor substrate and they are heated using an electrical current. By using gold heater lines of different widths fabricated using electron beam lithography, features smaller than the phonon characteristic MFP are obtained. This study has been performed with different size heating lines on top of silicon and  $\text{In}_{0.53}\text{Ga}_{0.47}\text{As}$ .

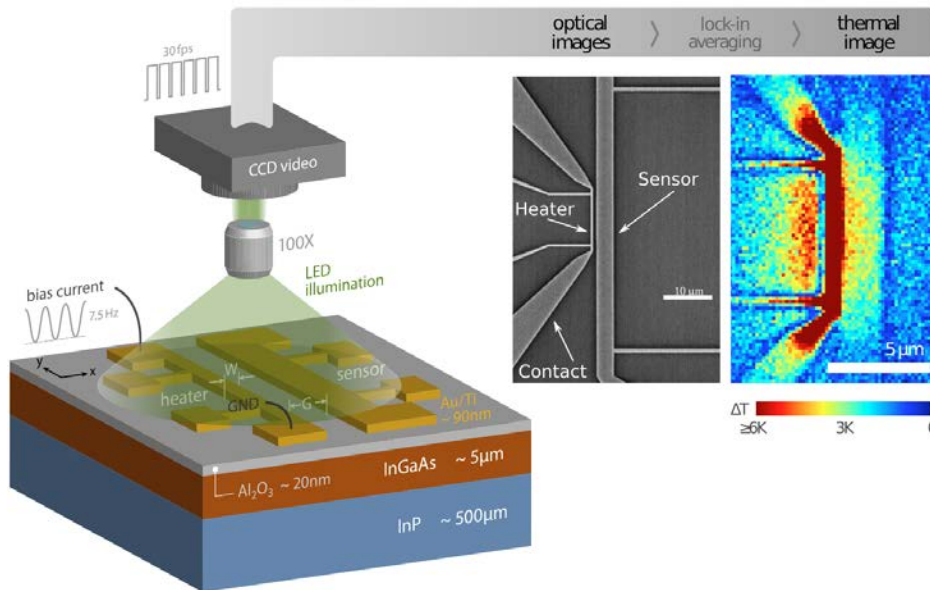


Figure 6.4: Experimental setup of TDTR imaging [125].

In Fig. 6.4 the experimental setup used for thermal imaging of silicon and  $\text{In}_{0.53}\text{Ga}_{0.47}\text{As}$  is represented. The figure reproduces the exact configuration for  $\text{In}_{0.53}\text{Ga}_{0.47}\text{As}$ , where an InP layer is also observable. In the case of silicon, the configuration is just formed by a single layer of silicon of  $500\ \mu\text{m}$ . On the top of the sample, a 20 nm insulating layer of  $\text{Al}_2\text{O}_3$  is deposited. Samples are heated through the metal heating lines by Joule effect applying an alternating current. This heating lines, of 90 nm thickness, are deposited on the top of  $\text{Al}_2\text{O}_3$  through a small 5 nm layer of Ti for adhesion proposes. The amount of heat deposited on the line is determined by a two contact voltage measurement and the temperature rise can be independently measured using the resistance of the metal lines or through the temperature field on the substrate using Time Domain Thermoreflectance (TDTR) (more details about the experimental setup are provided in Ref. [125]). The silicon samples do not have the sensor golden

line, therefore in the  $\text{In}_{0.53}\text{Ga}_{0.47}\text{As}$  case a step in the temperature profile near to the heating line, not appearing in the silicon samples, will be appreciated.

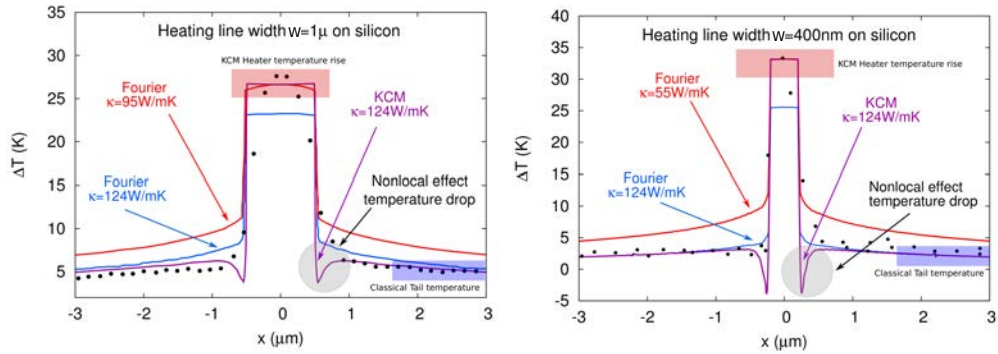


Figure 6.5: Temperature profile of TDTR measurement on silicon with a 1  $\mu\text{m}$  (left) and 400 nm gold heating line (right).

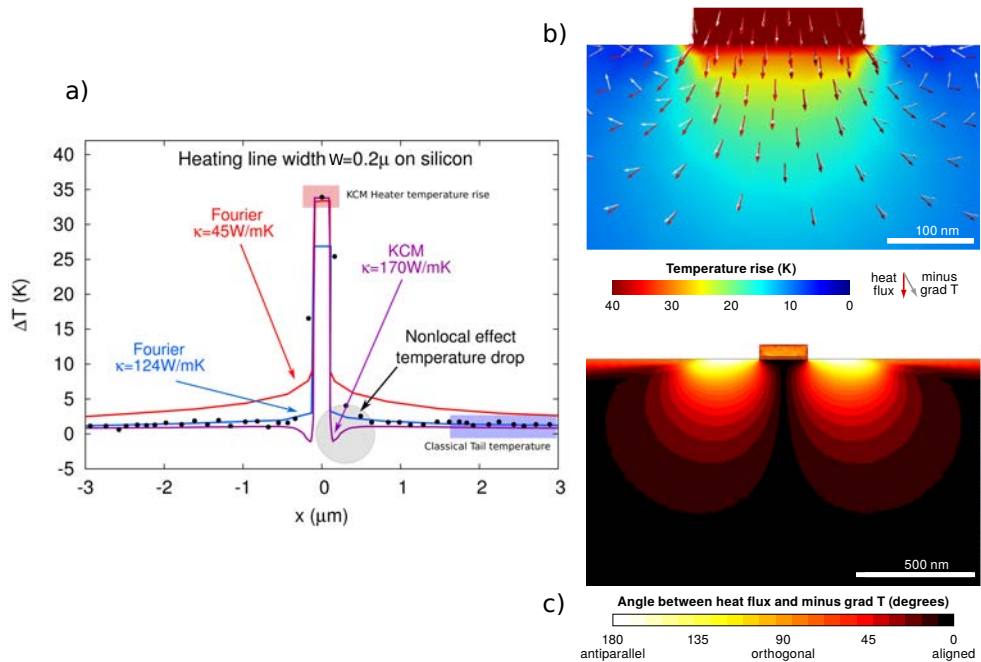


Figure 6.6: a) Temperature profile of TDTR measurement on silicon with a 200 nm gold heating line. b) 2D temperature profile for the 200 nm line based on KCM, and superposed heat flux vector  $\mathbf{Q}$  (red arrows) with the minus temperature gradient  $-\nabla T$  (grey arrows). c) Color representation of the angle between  $\mathbf{Q}$  and  $-\nabla T$ .

Eq. (6.1) combined with the energy balance equation can be solved through finite elements for this specific geometry to give the temperature profiles measured by TDTR. In Fig. 6.5 and Fig. 6.6, the KCM steady state solution for the cross section temperature profile on and around the metal lines on top of silicon is compared with experimental data. Notice that the nominal (i.e. bulk) value of thermal conductivity for silicon is 124 W/m·K. This indicates a small impurity content in the sample, which will have an impact on the calculation of the non-local parameters. The agreement of the hydrodynamic KCM model with experiments is remarkable. It can be observed that for 1  $\mu\text{m}$  and 400 nm width lines the hydrodynamic model is able to predict the temperature profile in the whole spatial range by using the bulk thermal conductivity and a non-local parameter of  $\ell = 293$  nm. Notice that this parameter does not correspond to the one used in pure silicon samples. For the 200 nm heating line, the KCM using bulk properties overestimates the heater temperature. In order to fit all the temperature profile is necessary to use a thermal conductivity value of  $\kappa = 170$  W/mK, larger than the reported bulk values. This can be caused by the leak of inclusion of superdiffusive effects in the model or other effects related to a possible dependence of the thermal conductivity on the temperature gradient ( $\kappa(\nabla T)$ ). It is interesting to compare the KCM solution to that obtained from an effective Fourier approach. It can be seen that if one uses Fourier's law to interpret the data it is not possible to completely explain the full temperature distribution. Using the nominal conductivity, the tail of the profile can be predicted but the heater temperature is underestimated. On the other hand, if a lower effective thermal conductivity (adjusted) is used to reproduce the increase in the heater temperature, the tail is over-predicted. These theoretical predictions are in agreement with previous works [8] where a non-isotropic thermal conductivity for in-plane and out of plane directions are used in order to describe the observed thermal profiles in similar setups. However, required anisotropy of thermal conductivity is unphysical for diamond-like crystals, whereas KCM can predict the data assuming an isotropic thermal conductivity [125].

The observed lower temperatures near the heat source, as compared to Fourier prediction, can be explained based on the properties of the non-local term in Eq. (6.1). The hydrodynamic behavior of the heat flux can be observed in the details in Fig. 6.6b and Fig. 6.6c. Using the vector identity  $\nabla^2 \mathbf{Q} = \nabla(\nabla \mathbf{Q}) - \nabla \times (\nabla \times \mathbf{Q})$  in a steady situation ( $\nabla \mathbf{Q} = 0$ ) one can see that the heat flux is, in general, not parallel to the temperature gradient  $\mathbf{Q} = -\ell(\nabla \times \boldsymbol{\omega}) - \kappa \nabla T$ , where  $\boldsymbol{\omega} = \nabla \times \mathbf{Q}$  is the vorticity of the heat flux. Near the edge of the heater the incoming heat flux, which initially has only  $y$  component  $Q_y$ , changes along the  $x$  direction when it enters into the substrate generating a vorticity  $\omega_z = \partial Q_y / \partial x$ . This vorticity is confined to a layer of the order of  $\ell$  near the interface, and will give a rotational contribution to the heat flux  $Q_x^r = -\ell \partial \omega_z / \partial y$ . This contribution

to the heat flux is opposite to the conduction term  $Q_x^c = -\kappa\partial T/\partial x$ , producing an effective reduction of local temperature. Such information is lost if one reduces the description from 2D to 1D imposing a cylindrical symmetry, in which case an increase in the thermal boundary resistance needs to be introduced [5, 8]. This effect has been discarded experimentally to be due to diffraction by doing thermoreflectance imaging measurements with different wavelengths.

A recent work on electric transport in graphene has reported a similar response of the electric resistivity attributed to electron viscosity phenomena [126].

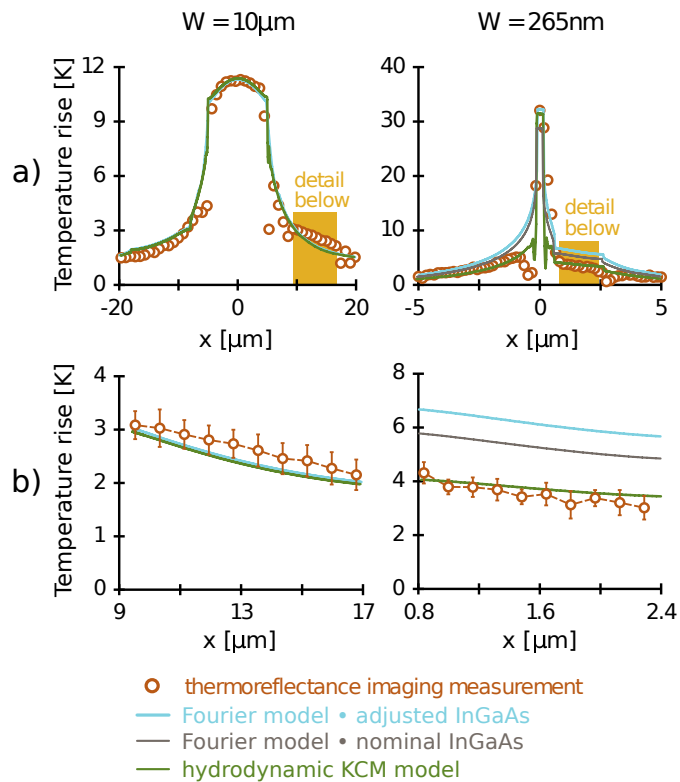


Figure 6.7: TDTR imaging for a  $10\ \mu\text{m}$  and  $2\ \mu\text{m}$  heating lines on  $\text{In}_{0.53}\text{Ga}_{0.47}\text{As}$  [125]. a) Full cross section. b) Magnification of the zone close to the heater.

In comparison with the experiment analyzed in **Section 6.2**, KCM properly describes the stationary temperature profiles for heater lines larger than 400 nm. However, for the 200 nm width line (Fig. 6.6a) it was necessary to increase the bulk thermal conductivity as  $\kappa_{\text{eff}} = 1.4\kappa$  in order to fit the temperature profile. Therefore, in the setup of **Section 6.2**, for heating lines smaller than 300 nm it can be expected the need to increase the thermal conductivity in order to fit the data. Pure KCM model is able to describe both experiments at line widths larger

than 300 nm and requires modification of the thermal conductivity at smaller sizes. Actually using the same factor  $\kappa_{\text{eff}} = 1.4\kappa$ , the value obtained for the effective resistivity ( $3.5 \pm 0.4 \text{ nKm}^2/\text{W}$ ) predicts the experimental data ( $3.8 \pm 0.3 \text{ nKm}^2/\text{W}$ ) within the error bars. The substrate seems to evacuate heat faster than expected from the current formulation of the model.

Going back to the 3D setup, similar results to those found for silicon are also observable in Fig. 6.7 for  $\text{In}_{0.53}\text{Ga}_{0.47}\text{As}$ . Now, the experimental configuration corresponds exactly to Fig. 6.4. As has been observed for silicon, TDTR shows enhanced heat transport adjacent to junctions at distances of the order of its non-local length  $\ell \sim 120 \text{ nm}$ . Again, the Fourier model, even adjusting the thermal conductivity is not able to reproduce the whole trend. From the magnification of the zone close to the heater, it can be appreciated that both nominal and adjusted Fourier overpredict the thermal conductivity, while the hydrodynamic model provides good agreement in all the cross section. In agreement with the observations for silicon, the heat flow around large heating lines ( $W > 1 \mu\text{m}$ ) is well predicted by nominal Fourier. On contrary, the reduced size devices are better predicted by the KCM hydrodynamic model.

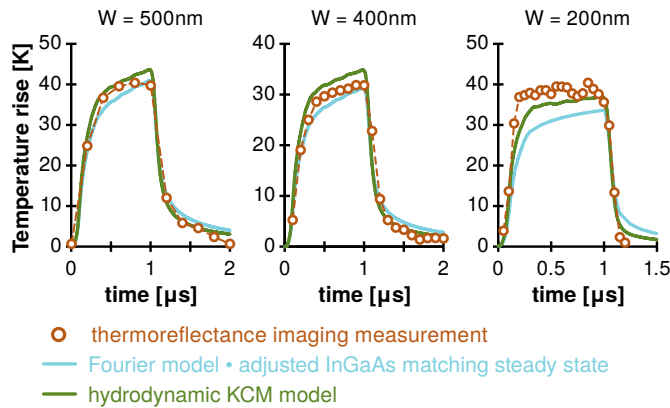


Figure 6.8: Temporal response of different width heating lines on  $\text{In}_{0.53}\text{Ga}_{0.47}\text{As}$  [125]. Dots represent experimental data and lines finite elements simulations.

Fig. 6.8 shows the transient response for 500 nm, 400 nm and 200 nm heating lines on  $\text{In}_{0.53}\text{Ga}_{0.47}\text{As}$ . Experimental data (dots) are compared with Fourier theory with adjusted thermal conductivity and the KCM hydrodynamic model. It can be observed that the rise in temperature is well predicted in both models for the two bigger devices. On the other hand, for the smallest device the modified Fourier underpredicts considerably the temperature rise. In addition it can be observed a faster cooling than the predicted by the Fourier theory in all cases. In



this sense, the hydrodynamic model provides a better agreement for all devices, even though small discrepancies still exist, especially for the smallest device.

## 6.4 Effective modeling of KCM

In this chapter the hydrodynamic KCM has been applied to explain different experiments on thermal transport. Here, the effect of the hydrodynamic heat transport governed by the term  $\ell^2 \nabla \mathbf{Q}$  is studied from the point of view of an effective thermal conductivity and compared with the effects of TBR and anisotropy.

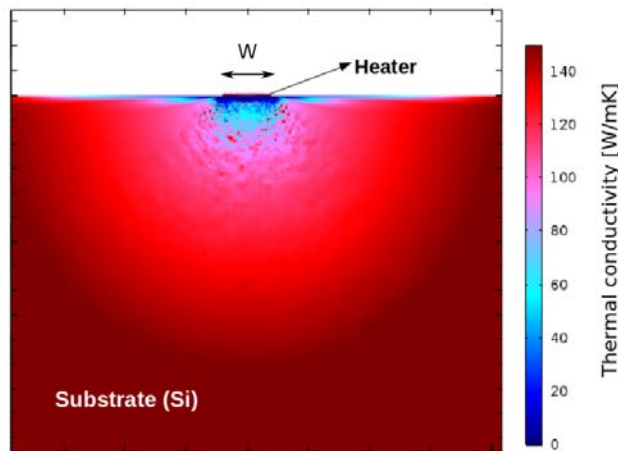


Figure 6.9: Effective thermal conductivity obtained from a Fourier representation of the KCM solution.

In Fig. 6.9 the effective thermal conductivity obtained for the experiment on silicon detailed in the **Section 6.3** is presented. To obtain an effective thermal conductivity value from the KCM solution, it is assumed the Fourier law, and therefore from the obtained flux  $\mathbf{Q}$  and the temperature gradient  $\nabla T$  in each point the effective thermal conductivity is obtained as  $\kappa_{\text{eff}} = -|\mathbf{Q}|/|\nabla T$ . As it can be observed, close to the heater the effect of the viscosity term is to reduce the effective thermal conductivity. Far to the heater, the effect of this term disappears and the bulk thermal conductivity is recovered. The observed reduction of the thermal conductivity near to the heater can be assimilated to a TBR. For this propose a simulation of the same setup in  $\text{In}_{0.53}\text{Ga}_{0.47}\text{As}$  using a Fourier model and including an extra layer between the heater and the substrate has been done. In this case, the thermal conductivity of the layer and its thickness  $H$  will determine the value of its resistivity as  $r_{ms} = H/\kappa_L$ .

Fig. 6.10 shows the solution obtained by the KCM and the effective Fourier including an adjusted TBR. It can be observed that the inclusion of a TBR can

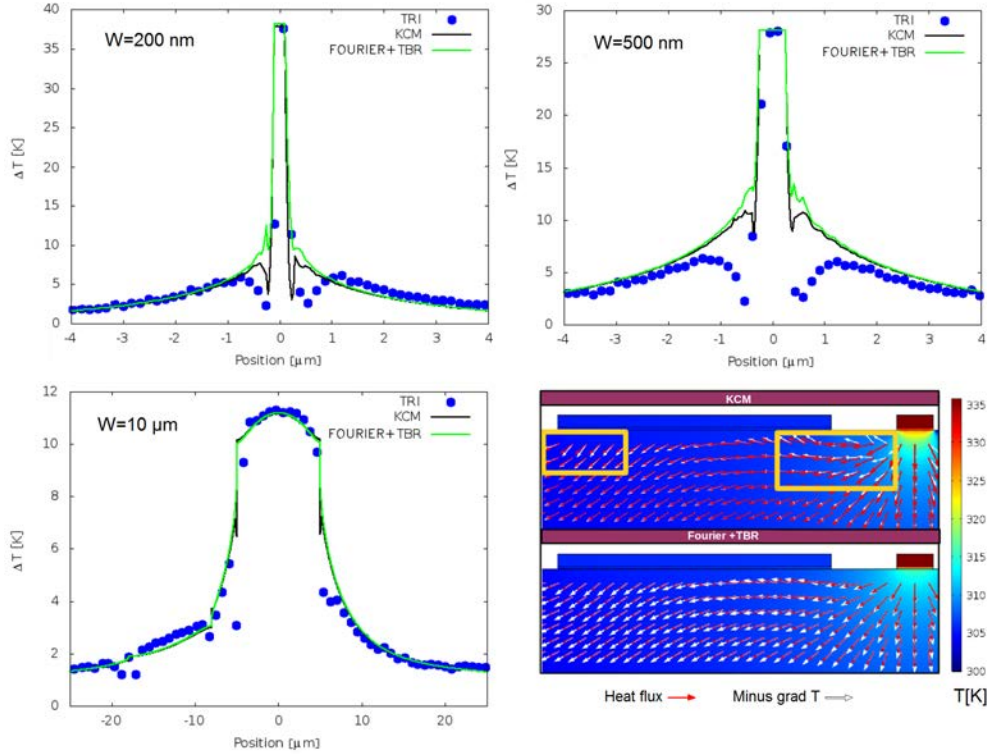


Figure 6.10: Temperature profile on  $\text{In}_{0.53}\text{Ga}_{0.47}\text{As}$  for  $W=200$  nm,  $W=400$  nm and  $W=10$   $\mu\text{m}$ . Bottom right: 2D temperature profile with KCM and Fourier+TBR superposed with heat flux vector  $\mathbf{Q}$  (red arrows) and minus temperature gradient  $-\nabla T$  (white arrows).

Width	200 nm	500 nm	10 $\mu\text{m}$
	KCM / Fourier		KCM / Fourier
$\kappa_{\text{eff}}$ [W/mK]	8.1 / 8.1	6.1 / 6.1	5.3 / 5.3
TBR [ $\text{nKm}^2/\text{W}$ ]	0 / 35.8	0 / 33.7	0 / 9.2

Table 6.1: Values of effective thermal conductivity and TBR for different width heating lines on  $\text{In}_{0.53}\text{Ga}_{0.47}\text{As}$ .

reproduce the same trend found by the KCM and in agreement with the experimental data. Table 6.1 contains the values used to reproduce these data. As it can be observed, both models need to adjust the thermal conductivity for small heater widths. On the other hand, while in the KCM a constant value of  $\ell = 150$  nm is used for all the samples, the TBR in the Fourier model needs to be adjusted for each sample. In addition, the values required for the TBR are very large compared to the reported AMM/DMM values [11, 29]. In the 2D temperature profile

it can be observed that, while in the KCM the heat flux and minus gradient of  $T$  are not always parallel, in the Fourier model have always the same direction.

Finally, due to recent attempts to explain Fourier failures from an anisotropic point of view in isotropic systems [8], an anisotropic Fourier model has been used to reproduce the  $\text{In}_{0.53}\text{Ga}_{0.47}\text{As}$  experimental data. In this case, different in plane and out of plane thermal conductivity values have been adjusted in order to obtain the best fit.

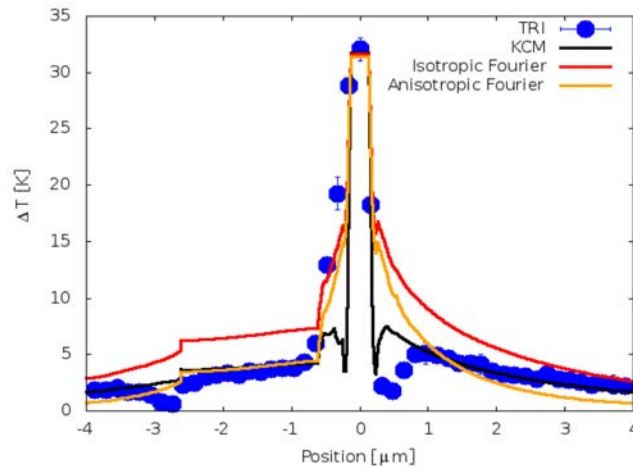


Figure 6.11: Best anisotropic fit to experimental  $\text{In}_{0.53}\text{Ga}_{0.47}\text{As}$  temperature profile with  $W=500$  nm.

The anisotropic Fourier model that fit the temperature on the center of the heater and on the top of the sensor is represented in Fig. 6.11. The values used are  $\kappa_{\text{InGaAs},IP} = 1.1$  W/mK and  $\kappa_{\text{InGaAs},OP} = 11.7$  W/mK. As it can be observed, even though the temperature at the heater and the sensor are correct, the trend of the temperature profile far from the center does not correctly reproduce the experimental data. It is not strange that an anisotropic model fails to predict experiments in isotropic crystals such as  $\text{In}_{0.53}\text{Ga}_{0.47}\text{As}$  or silicon.

# Chapter 7

## Conclusions

A novel contribution of this work has been to develop the equations of Guyer and Krumhansl (GK) in a *first principles* framework considering the maximization of the entropy to obtain a fully predictive model to compute the thermal conductivity of semiconductors. These equations have been combined with Extended Irreversible Thermodynamics (EIT) to obtain a hydrodynamic equation to describe the heat flux beyond the Fourier law including non-local and memory effects able to reproduce recent experiments under ultra-fast heating or high temperature gradients. All these set of equations to describe the thermal conductivity and heat flux is what conforms the Kinetic Collective Model (KCM) framework.

The collective behavior has been introduced as a fundamental piece to understand the thermal conductivity when normal ( $N$ ) scattering plays an important role. This new transport mechanism is combined with the kinetic transport in the KCM, providing a way to calculate the thermal conductivity without treating normal scattering as a resistive mechanism, in contrast to N-as-resistive approaches like in the classical Relaxation Time Approximation (RTA).

The importance of collective behavior in a specific sample is determined by the parameter  $\Sigma$ , calculated from the ratio of normal to resistive scattering rates. As boundary scattering is included in the resistive term, when size is reduced  $\Sigma \rightarrow 0$ , and also vanishes at low temperatures. In bulk samples, where boundaries are not considered, the collective behavior is relevant at all temperatures, becoming more important as temperature decreases. Since the collective regime is expected to be the responsible for the appearance of hydrodynamic effects, for finite values of  $\Sigma$  hydrodynamic equations can be used to study heat transport.

By using *first principles* calculations, KCM has provided good agreement with experimental data for a large number of samples without free parameters. They include several bulk materials and micro/nano silicon films and wires in a wide range of temperatures. While thermal conductivity of some samples can

be predicted by RTA, KCM additionally provides good predictions for bulk diamond and silicon nanowires thanks to the correct treatment of normal processes and the form factor used in the collective regime to account for boundary effects.

Regarding bulk samples, the role of normal scattering in heat transport of alloys has been also analyzed. Thermal conductivity values derived from the KCM for  $\text{Si}_{1-x}\text{Ge}_x$  and  $\text{In}_x\text{Ga}_{1-x}\text{As}$  alloys show good agreement with experimental data and previous calculations. Without introducing any fitting parameters, the proper combination of kinetic and collective transport can accurately predict thermal conductivity at low alloy concentrations. Impurity concentrations as little as 0.4% almost eliminate the collective contribution in  $\text{Si}_{1-x}\text{Ge}_x$ , while in  $\text{In}_x\text{Ga}_{1-x}\text{As}$ , the collective contribution is strongly reduced, but not completely removed, at 4% concentrations. This insight could be useful when addressing phenomena such as phonon drag or dopant effects in semiconductor thermoelectrics. Moreover, while the impact of collective transport on steady-state thermal conductivity of bulk alloys is negligible at most concentrations, the role of normal scattering is always important by slowing down the kinetic transport, thus reducing thermal conductivity by 4-15% at room temperature. The latter effect can have a big impact on the analysis of ultrafast thermal transport at small length scales. The slowing down of the kinetic modes have been reported to be also relevant in all the studied samples for finite values of  $\Sigma$ , reducing the kinetic contribution up to 50% in most cases.

On the study of low dimension samples two approaches have been used. On one side, the GK kinetic-collective approach has been applied successfully to several silicon and  $\text{Bi}_2\text{Te}_3$  samples. In this approach, phonons larger than the sample characteristic size are limited in the kinetic regime while a hydrodynamic form factor accounts for the boundaries in the collective one. A full hydrodynamic approach derived from GK and EIT have also shown good performance on silicon and has improved the prediction for  $\text{Si}_{1-x}\text{Ge}_x$  nanowires of different impurity concentrations.

From the phonon spectral analysis the contribution to the thermal conductivity of each heat carrier in terms of frequency and mean free path (MFP) has been obtained. While high frequency carriers have a significant contribution for pure materials, low frequency ones are the responsible of heat transport in alloys.

The role of low energy phonons has been demonstrated to be important in order to compute the thermal conductivity and to analyze the thermal conductivity accumulation function in terms of MFP. KCM supplies an explanation for the reduction of the contribution of long MFP phonons based on the effect of the collective regime and the calculation of low frequency relaxation times. In addition, in the KCM accumulation function the emergence of a collective characteristic length provides information of the scales where deviations from Fourier can be relevant, which is not visible from classical representations. Moreover, the de-

---

pendence of  $\Sigma$  on the characteristic size  $L_{\text{eff}}$  changes the shape of this function, and therefore override the general belief that the thermal conductivity for a certain size  $L_{\text{eff}}$  can be obtained by removing the contribution from phonons with MFP greater than it.

The spectral MFP information has allowed to study the transient response between diffusive and ballistic regimes. It is shown that the collective regime, where phonons share the same MFP, narrows the spatial window of superdiffusive heat transport. In addition, the slope of the accumulation function has been correlated to the dominant scattering mechanism.

The study of complex experimental setups has evidenced that the hydrodynamic KCM thermal transport equation can explain the observed deviations from Fourier law in nanoscale devices with several geometries. The model using intrinsic material properties is able to describe the different studied experiments up to scales larger than 200 nm. The hydrodynamic transport includes a non-local term  $\ell$  resembling viscous friction in fluids, thus increasing the resistance of heat to flow as size becomes smaller. It has been shown that this increased resistance produces the same effect as an increase of thermal boundary resistance (TBR) as size is reduced. Then, experiments which have been interpreted by considering a size-dependent TBR may be reinterpreted as a hydrodynamic effect. The hydrodynamic view has the advantage of predicting the thermal response using a single non-local length,  $\ell$ , instead of fitting the TBR for each experiment.

In summary, the collective regime defined in KCM introduces relevant information on phonon transport that could be useful to describe experiments where non-Fourier behavior has been reported, as in high temperature gradients or ultra-fast experiments using pump-probe and/or thermoreflectance setups. The hydrodynamic KCM has been applied successfully to general 3D geometries, where BTE approaches are hard to implement. Its implementation via a finite elements method could be directly combined with current tools used in nanoelectronics device modeling and optimization. In addition, this new model could lead to a better understanding of the heat transport from microscopic to macroscopic scales and help to a deeper study of the microscopic interpretation of the TBR.



# Appendix A

## Generalization of the KCM equations

In certain systems where differences between normal and umklapp processes are relevant or the symmetries of the crystal are complex, the Debye approximation used in the first formulation of the model—where homogeneity and isotropy are assumed [15]—is no longer valid. Some discrepancies to experimental data can appear in such situations.

In order to improve the solution, some terms need to be reformulated. In the first case, the normalization constant  $\lambda$  from  $\langle 1|1\rangle$ , previously defined as  $\lambda^2 = 3k_B\hbar^2c^2/C_v$ , takes the form:

$$\lambda_{ij}^2 = \frac{\hbar^2 k_B}{\sum_{\mathbf{q}} \left( \frac{q_i \otimes q_j}{\omega_{\mathbf{q}}^2} \right) x_{\mathbf{q}}^2 \frac{e_{\mathbf{q}}^x}{(e^x - 1)^2}}, \quad (\text{A.1})$$

where  $x_{\mathbf{q}} = \hbar\omega_{\mathbf{q}}/k_B T$ . Notice that the denominator represents the mode specific heat corrected by a term  $(q_i \otimes q_j/\omega_{\mathbf{q}}^2)$ .





## Appendix B

# Hydrodynamic heat flow in two dimensions

A major difference between the Fourier law and the hydrodynamic heat flux equation, Eq. (6.1), is that the heat flux provided by the latter is not, in general, parallel to the temperature gradient. In addition, it may contain a non vanishing vorticity. This behavior can not be seen in purely one-dimensional systems, but it can already be observed in two-dimensional ones. Here a general solution for the heat flux given by Eq. (6.1) is provided, making explicit this behavior. This solution also yields a general expression for the decay time in grating experiments.

In two dimensions, thermal magnitudes are functions of the  $x, y$  coordinates only. The heat flux has two components,  $\mathbf{Q} = (Q_x, Q_y)$ , which are the solution of Eq. (6.1):

$$\left[ \begin{pmatrix} 1 & 0 \\ 0 & 1 \end{pmatrix} - \ell^2 \begin{pmatrix} 3\partial_x^2 + \partial_y^2 & 2\partial_x\partial_y \\ 2\partial_y\partial_x & \partial_x^2 + 3\partial_y^2 \end{pmatrix} \right] \begin{pmatrix} Q_x \\ Q_y \end{pmatrix} = - \begin{pmatrix} \kappa & 0 \\ 0 & \kappa \end{pmatrix} \begin{pmatrix} \partial_x T \\ \partial_y T \end{pmatrix}, \quad (\text{B.1})$$

where the time derivative and  $2\nabla\nabla \cdot \mathbf{Q}$  have been neglected. Separable solutions in which the dependence on the spatial coordinates are of the form:

$$T, \mathbf{Q} \propto e^{i(m_x x + m_y y)}, \quad (\text{B.2})$$

with  $\mathbf{m} = (m_x, m_y)$  a possibly complex wave vector. Substituting Eq. (B.2) into Eq. (B.1) gives:

$$\left[ \begin{pmatrix} 1 & 0 \\ 0 & 1 \end{pmatrix} - \ell^2 \begin{pmatrix} 3m_x^2 + m_y^2 & 2m_x m_y \\ 2m_y m_x & m_x^2 + 3m_y^2 \end{pmatrix} \right] \begin{pmatrix} Q_x \\ Q_y \end{pmatrix} = -i\kappa T \begin{pmatrix} m_x \\ m_y \end{pmatrix}. \quad (\text{B.3})$$

The matrix on the left hand side of this equation has two eigenvalues,  $\mu^\alpha$  and  $\mu^\beta$ . From one side,  $\mu^\alpha = 1 + 3m^2\ell^2$  has eigenvectors parallel to  $\mathbf{m}$ , and can be expressed as  $\mathbf{Q}^\alpha = i\mathbf{m}\Phi = \nabla\Phi$ , where  $\Phi$  is a scalar function with potential heat flux, and therefore non-rotational, and  $m = |\mathbf{m}|$ . From the other side,  $\mu^\beta = 1 + m^2\ell^2$  has eigenvectors normal to  $\mathbf{m}$ , and can be expressed as  $\mathbf{Q}^\beta = i\mathbf{z} \times \mathbf{m}\psi = \mathbf{z} \times \nabla\psi$ .  $\mathbf{z}$  is the unit vector normal to the  $xy$  plane, and the scalar  $\psi$  is analogous to the stream function in fluid mechanics. This heat flux has non-vanishing curl  $\nabla \times \mathbf{Q}^\beta = \mathbf{z}\nabla^2\psi = -\mathbf{z}m^2\psi$ . Then it is qualitatively different from the heat flux in Fourier theory.

It can be observed that the right hand side of Eq. (B.3) is an  $\alpha$  eigenvector. Then, expressing the total heat flux  $\mathbf{Q}$  as a combination of the two eigenvectors,  $\mathbf{Q} = \mathbf{Q}^\alpha + \mathbf{q}^\beta = i\mathbf{m}\Phi + i\mathbf{z} \times \mathbf{k}\psi$ , two equations can be obtained from Eq. (B.3):

$$(1 - 3m^2\ell^2)\mathbf{Q}^\alpha = -\kappa iT\mathbf{m} \text{ and} \quad (\text{B.4})$$

$$(1 - m^2\ell^2)\mathbf{Q}^\beta = 0. \quad (\text{B.5})$$

Since both equations are uncoupled they can be solved independently. From Eq. (B.4) the potential  $\Phi$  is obtained:

$$\Phi = -\frac{\kappa T}{1 + 3m^2\ell^2}. \quad (\text{B.6})$$

Eq. (B.6) suggests that the potential part of the heat flux,  $\mathbf{Q}^\alpha$ , is obtained from the temperature gradient through an effective heat conductivity,  $\lambda_{\text{eff}} = \kappa/(1 + 3m^2\ell^2)$ .

The time evolution of the temperature profile depends on  $\mathbf{Q}^\alpha$  only, as it can be seen from the energy conservation law:

$$c_v \frac{\partial T}{\partial t} + \nabla \mathbf{Q} = 0, \quad (\text{B.7})$$

where  $c_v$  is the specific heat per unit volume. Noting that  $\nabla \mathbf{Q}^\beta = 0$  and  $\nabla \mathbf{Q}^\alpha = -m^2\Phi$  and using Eq. (B.6), one obtains:

$$c_v \frac{\partial T}{\partial t} + \frac{\kappa m^2}{1 + 3m^2\ell^2} T = 0. \quad (\text{B.8})$$

The temperature profile decay can be obtained directly from Eq. (B.8) as

$$\gamma = \frac{\kappa m^2 / c_v}{1 + 3m^2\ell^2}. \quad (\text{B.9})$$

For a purely one dimensional initial profile,  $T(x, y, t = 0) = \sin(\zeta x)$ , in an unbounded medium in the  $X$  and  $Y$  directions one has that Eq. (B.9) leads to Eq. (B.7). However, if this initial profile is imposed in a membrane of smaller

thickness in the  $Y$  direction, a dependence of the solution on the transverse coordinate will appear, which needs to be taken into account through a different value from 0.

The rotational contribution to the heat flux can be described through the stream function. From Eq. (B.5), equation for  $\psi$  is obtained as:

$$(1 + m^2 \ell^2) \psi = 0, \quad (\text{B.10})$$

which shows that the stream function is not vanishing only if  $m^2 = -1/\ell^2$ . Therefore some components of  $\mathbf{m}$  must be complex. Assuming that  $m_x = \zeta$  is real, then  $m_y = \pm i \sqrt{\zeta^2 + 1/\ell^2}$ , and one has

$$\psi \propto e^{i\zeta x \pm \beta(\zeta)y}, \text{ where } \beta(\zeta) = \sqrt{\zeta^2 + 1/\ell^2}. \quad (\text{B.11})$$

This function decays exponentially in a length of the order of  $\beta^{-1}$ . The vorticity, which is proportional to  $\psi$ , also decays in a length of order of  $\beta^{-1}$ .

Finally, for a complete determination of the heat flux, the differential equations in Eq. (B.1) must be supplemented with suitable boundary conditions. Each condition imposed on the components of the heat flux will introduce a coupling between the potential  $\mathbf{Q}^\alpha$  and rotational  $\mathbf{Q}^\beta$  contributions to the flux. According to the definitions of  $\Phi$  and  $\psi$ , the components of the heat flux are given by

$$Q_x = \frac{\partial \Phi}{\partial x} - \frac{\partial \psi}{\partial y} \text{ and} \quad (\text{B.12})$$

$$Q_y = \frac{\partial \Phi}{\partial y} + \frac{\partial \psi}{\partial x}. \quad (\text{B.13})$$



# Appendix C

## Longitudinal heat transport in a thin film

A membrane of width  $h$  described by the coordinate  $y \in [-h/2, h/2]$  with finite extension along the  $X$  direction and an initial temperature profile  $T(x, y, t = 0) = \sin(\zeta x)$  is considered.

The evolution of the system for  $t > 0$  is given by Eq. (B.1) and Eq. (B.7) together with boundary conditions at both surfaces of the film,  $y = \pm h/2$ :

- Insulating boundary conditions,  $Q_y(y \pm h/2) = 0$ . According to Eq. (B.13):

$$\frac{\partial \Phi}{\partial y} \Big|_{y=\pm h/2} + \frac{\partial \psi}{\partial x} \Big|_{y=\pm h/2} = 0 . \quad (\text{C.1})$$

- Slip boundary condition,  $Q_x = C\ell \partial Q_x / \partial y$ , where  $C$  is a slip coefficient, and the orientation towards the interior of the film is taken as positive in the derivative; this slip condition is analogous to the one employed in hydrodynamics [34]. Using Eq. (B.12) leads to:

$$\frac{\partial \Phi}{\partial x} \Big|_{y=\pm h/2} - \frac{\partial \psi}{\partial y} \Big|_{y=\pm h/2} = \pm C\ell \nabla^2 \psi \Big|_{y=\pm h/2} . \quad (\text{C.2})$$

To obtain the right hand side of this equality it has been used that the first boundary condition,  $Q_y = 0$  at  $y = \pm h/2$ , applies to all  $x$  values, so  $\partial Q_y / \partial x = 0 = \partial^2 \Phi / \partial x \partial y + \partial^2 \psi / \partial x^2$  at the boundaries. The solution to this problem can be obtained as a combination of the previously obtained separable solutions. According to the symmetry of the problem, the contributions to the temperature field must be of the form

$$T_m(x, y, t) = A_m e^{-\gamma_m t} \sin(\zeta x) \cos(m_y y) , \quad (\text{C.3})$$

where the decay rate  $\gamma_m$  is given by Eq. (B.9) with  $m^2 = \zeta^2 + m_y^2$ . The differential equation fixes this temporal dependence for the functions  $T_m$ , and also for  $\Phi_m$ . According to Eq. (B.6) one has:

$$\Phi_m(x, y, t) = B_m e^{-\gamma_m t} \sin(\zeta x) \cos(m_y y), \quad (\text{C.4})$$

with  $B_m = -\kappa A_m / (1 + 3m^2 \ell^2)$ . The form  $\psi_m$ , according to Eq. (B.11) and the symmetries of the problem, is

$$\psi_m(x, y, t) = D_m(t) \cos(\zeta x) \sinh(\beta y). \quad (\text{C.5})$$

The time dependence of Eq. (C.5) will be fixed by the boundary conditions. The first boundary condition (Eq. (C.1)) gives

$$D_m(t) = -B_m e^{-\gamma_m t} \frac{m_y \sin(m_y h/2)}{\zeta \sinh(\beta h/2)}. \quad (\text{C.6})$$

Using the second boundary condition given by Eq. (C.2), the following relation is obtained:

$$m_y \tan(m_y h/2) = -\frac{\zeta^2}{\beta} \frac{\tanh(\beta h/2)}{1 + \frac{C}{2\beta\ell} \tanh(\beta h/2)}. \quad (\text{C.7})$$

This is an eigenvalue for the magnitude  $m_y$ . There is an infinite number of real solutions for  $m_y$ : given that the right-hand-side of the equation is negative, there will be a solution in each of the intervals  $m_y h/2 \in [(n-1/2)\pi, n\pi]$ ,  $n = 1, 2, \dots$ . The decay rate for the  $n$ -th solution increases with  $n$ , because  $m^2 = \zeta^2 + m_y^2$ . However, there exists also an imaginary solution,  $m_y = i\alpha$ , with  $\alpha$  determined by

$$\frac{\alpha h}{2} \tanh(\alpha h/2) = \left(\frac{\zeta h}{2}\right)^2 \frac{\tanh(\beta h/2)}{\frac{\beta h}{2} + \frac{C h}{2\ell} \tanh(\beta h/2)}. \quad (\text{C.8})$$

The solution given by Eq. (C.8) provides the eigenfunction with the slowest decay, since  $m^2 = \zeta^2 - \alpha^2$  takes the smallest value:

$$\gamma = \frac{\kappa \zeta^2}{C} \frac{1 - \alpha^2/\zeta^2}{1 + 3\ell^2 \zeta^2 (1 - \alpha^2/\zeta^2)}. \quad (\text{C.9})$$

Therefore, the change of the decay rate from the bulk expression, Eq. (B.9), due to the finite thickness of the film can be absorbed in a  $\zeta$ -dependent modification of coefficients  $\kappa$  and  $\ell^2$  through the same factor,  $f = 1 - \alpha^2/\zeta^2$ . The effect of the finite thickness is thus to reduce the decay rate as compared to the unbounded case; this is what expected from the viscous-like term in the hydrodynamic heat flux equation.

As Eq. (C.8) shows,  $\alpha$  is a function of  $h$ ,  $\ell$  and  $\zeta$ , and then, for dimensional reasons, the functional form of the correction factor  $f$  is  $f(\zeta h, h/\ell)$ . In the experiments, the values of  $\zeta h$  are always very small (smaller than  $\sim 0.1$ ), so that this quotient is nearly independent of  $\zeta$  (see Fig. C.1):

$$\lim_{\zeta h \rightarrow 0} 1 - \left(\frac{\alpha}{\zeta}\right)^2 = 1 - \left(\frac{2\ell}{h}\right) \frac{\tanh(h/2)\ell}{1 + C \tanh(h/2)\ell} \equiv f_0(h/\ell). \quad (\text{C.10})$$

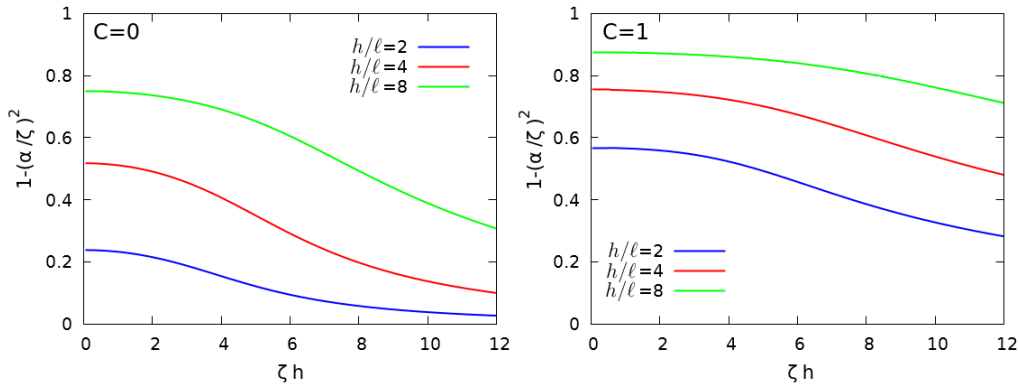


Figure C.1: Correction coefficient  $f$  as a function of  $\zeta h/2$  for different values of  $h/\ell$  and for boundary conditions  $C = 0$  (left) and  $C = 1$  (right). For the experimental range,  $\zeta h < 1$ , the value of  $f$  remains approximately constant.

In the experimental interval one has:

$$\gamma = \frac{\kappa_{\text{eff}} \zeta^2 / C}{1 + 3\ell_e^2 \zeta^2}, \quad (\text{C.11})$$

with  $\kappa_{\text{eff}} = \kappa f(h/\ell)$  and  $\ell_{\text{eff}}^2 = \ell^2 f_0(h/\ell) = \ell^2 \kappa_{\text{eff}} / \kappa$ . The change in the decay rate can be described through the use of an effective reduced conductivity  $\kappa_{\text{eff}}$  and an effective non-local length  $\ell_{\text{eff}}$ . In all the applications a general slip condition  $C=1$  is used, which is related to the specularity of boundaries [34].





# Bibliography

- [1] C. De Tomas, A. Cantarero, A. F. Lopeandia, and F. X. Alvarez, *From kinetic to collective behavior in thermal transport on semiconductors and semiconductor nanostructures*, J. Appl. Phys **115**, (2014).
- [2] C. De Tomas, A. Cantarero, A. F. Lopeandia, and F. X. Alvarez, *Enhancing of optic phonon contribution in hydrodynamic phonon transport*, J. Appl. Phys **118**, (2015).
- [3] P. Torres, A. Torello, J. Bafaluy, J. Camacho, X. Cartoixà, and F. X. Alvarez, *First principles Kinetic-Collective thermal conductivity of semiconductors*, Phys. Rev. B **95**, 165407 (2016).
- [4] J. A. Johnson, A. A. Maznev, J. Cuffe, J. K. Eliason, A. J. Minnich, T. Kehoe, C. M. S. Torres, G. Chen, and K. A. Nelson, *Direct measurement of room-temperature nondiffusive thermal transport over micron distances in a silicon membrane*, Phys. Rev. Lett. **110**, 025901 (2013).
- [5] M. E. Siemens, Q. Li, R. Yang, K. K. A. Nelson, E. H. Anderson, M. M. Murnane, and H. C. Kapteyn, *Quasi-Ballistic thermal transport from nanoscale interfaces observed using ultrafast coherent soft X-ray beams*, Nat. Mater. **9**, 26 (2010).
- [6] A. J. Minnich, J. A. Johnson, A. J. Schmidt, K. Esfarjani, M. S. Dresselhaus, K. A. Nelson, and G. Chen, *Thermal conductivity spectroscopy technique to measure phonon mean free paths*, Phys. Rev. Lett. **107**, (2011).
- [7] K. T. Regner, D. P. Sellan, Z. Su, C. H. Amon, A. J. H. McGaughey, and J. Malen, *Broadband phonon mean free path contributions to thermal conductivity measured using frequency domain thermoreflectance.*, Nature Comm. **4**, 1640 (2013).
- [8] R. B. Wilson and D. G. Cahill, *Anisotropic failure of Fourier theory in time-domain thermoreflectance experiments*, Nature Comm. **5**, 5075 (2014).

- 
- [9] Y. Hu, L. Zeng, A. J. Minnich, M. S. Dresselhaus, and G. Chen, *Spectral mapping of thermal conductivity through nanoscale ballistic transport*, Nat. Nanotechnol. **10**, 701 (2015).
- [10] K. M. Hoogeboom-Pot, J. N. Hernandez-Charpak, X. Gu, T. D. Frazer, E. H. Anderson, W. Chao, R. W. Falcone, R. Yang, M. M. Murnane, H. C. Kapteyn, and D. Nardi, *A new regime of nanoscale thermal transport: Collective diffusion increases dissipation efficiency*, Proc. Natl. Acad. Sci. **112**, 201503449 (2015).
- [11] B. Vermeersch, A. M. S. Mohammed, G. Pernot, Y. R. Koh, and A. Shakouri, *Thermal interfacial transport in the presence of ballistic heat modes*, Phys. Rev. B **90**, 1 (2014).
- [12] B. Vermeersch and A. Shakouri, *Nonlocality in microscale heat conduction*, arXiv:1412.6555 1 (2014).
- [13] A. Cepellotti, G. Fugallo, L. Paulatto, M. Lazzeri, F. Mauri, and N. Marzari, *Phonon hydrodynamics in two-dimensional materials*, Nature Comm. **6**, 1 (2015).
- [14] S. Lee, D. Broido, K. Esfarjani, and G. Chen, *Hydrodynamic phonon transport in suspended graphene.*, Nature Comm. **6**, 6290 (2015).
- [15] R. A. Guyer and J. A. Krumhansl, *Solution of the linearized phonon boltzmann equation*, Phys. Rev. **148**, 766 (1966).
- [16] D. Jou, G. Lebon, and M. Criado-Sancho, *Variational principles for thermal transport in nanosystems with heat slip flow*, Phys. Rev. E **82**, 1 (2010).
- [17] F. X. Alvarez, D. Jou, and A. Sellitto, *Phonon hydrodynamics and phonon-boundary scattering in nanosystems*, J. Appl. Phys **105**, (2009).
- [18] L. Boltzmann, *Weitere studien über das wärmeleichgewicht unter gasmolekülen*, Sitzungsberichte der Akademie der Wissenschaften, Wien 66 (1872).
- [19] J. Ziman, *Electrons and Phonons The Theory of* (Oxford University Press, Oxford, 2001).
- [20] J. Callaway, *Model for lattice thermal conductivity at low temperatures*, Phys. Rev. **113**, 1046 (1959).

- 
- [21] L. Chaput, *Direct solution to the linearized phonon boltzmann equation*, Phys. Rev. Lett. **110**, 1 (2013).
- [22] A. Cepellotti and N. Marzari, *Thermal Transport in Crystals as a Kinetic Theory of Relaxons*, Phys. Rev. X **6**, 041013 (2016).
- [23] P. B. Allen, *Improved Callaway model for lattice thermal conductivity*, Phys. Rev. B **88**, 144302 (2013).
- [24] W. Li, N. Mingo, L. Lindsay, D. A. Broido, D. A. Stewart, and N. A. Katcho, *Thermal conductivity of diamond nanowires from first principles*, Phys. Rev. B **85**, 1 (2012).
- [25] L. Chaput, *Supplementary Material*, Phys. Rev. Lett. **110**, 1 (2013).
- [26] R. A. Guyer and J. A. Krumhansl, *Thermal conductivity, second sound, and phonon hydrodynamic phenomena in nonmetallic crystals*, Phys. Rev. **148**, 778 (1966).
- [27] C. De Tomas, A. Cantarero, a. F. Lopeandia, and F. X. Alvarez, *Thermal conductivity of group-IV semiconductors from a kinetic-collective model*, Proc. R. Soc. A **470**, 20140371 (2014).
- [28] B. Vermeersch, J. Carrete, N. Mingo, and A. Shakouri, *Superdiffusive heat conduction in semiconductor alloys. I. Theoretical foundations*, Phys. Rev. B **91**, 085202 (2015).
- [29] B. Vermeersch, A. M. S. Mohammed, G. Pernot, Y. R. Koh, and A. Shakouri, *Superdiffusive heat conduction in semiconductor alloys. II. Truncated Lévy formalism for experimental analysis*, Phys. Rev. B **91**, 085203 (2015).
- [30] K. C. Collins, A. A. Maznev, Z. Tian, K. Esfarjani, K. A. Nelson, and G. Chen, *Non-diffusive relaxation of a transient thermal grating analyzed with the Boltzmann transport equation*, J. Appl. Phys **114**, 104302 (2013).
- [31] E. H. Sondheimer, *Mean Free Path of Electrons in Metals*, Advances in Physics 1 (1952).
- [32] G. L. D. Jou, J. Casas, *Extended Irreversible Thermodynamics* (Springer, Fourth Edition, Berlin, 2010).
- [33] F. X. Alvarez and D. Jou, *Memory and nonlocal effects in heat transport: From diffusive to ballistic regimes*, Appl. Phys. Lett. **90**, 1 (2007).

- [34] A. Sellitto, F. X. Alvarez, and D. Jou, *Second law of thermodynamics and phonon-boundary conditions in nanowires*, J. Appl. Phys **107**, (2010).
- [35] B. Vermeersch and A. Shakouri, *Spatiotemporal flux memory in nondiffusive transport*, arXiv:1412.8517 1 (2014).
- [36] D. G. Cahill and R. O. Pohl, *Thermal conductivity of amorphous solids above the plateau*, Phys. Rev. B **35**, 4067 (1987).
- [37] K. M. Lee, T. Y. Choi, S. K. Lee, and D. Poulikakos, *Focused ion beam-assisted manipulation of single and double beta-SiC nanowires and their thermal conductivity measurements by the four-point-probe 3-omega method.*, Nanotechnology **21**, 125301 (2010).
- [38] Y. K. Koh and D. G. Cahill, *Frequency dependence of the thermal conductivity of semiconductor alloys*, Phys. Rev. B **76**, 075207 (2007).
- [39] D. G. Cahill, *Thermal conductivity measurement from 30 to 750 K: The  $3\omega$  method*, Rev. Sci. Instrum. **61**, 802 (1990).
- [40] G. Nilsson and G. Nelin, *Study of the homology between silicon and germanium by thermal-neutron spectrometry*, Phys. Rev. B **6**, 3777 (1972).
- [41] G. Winterling and W. Heinicke, *Measurements of phonon lifetimes by two successive light pulses*, Phys. Lett. A **27**, 329 (1968).
- [42] B.-L. Huang and M. Kaviani, *Ab initio and molecular dynamics predictions for electron and phonon transport in bismuth telluride*, Phys. Rev. B **77**, 125209 (2008).
- [43] J. Sadhu, H. Tian, J. Ma, B. Azeredo, J. Kim, K. Balasundaram, C. Zhang, X. Li, P. M. Ferreira, and S. Sinha, *Quenched Phonon Drag in Silicon Nanowires Reveals Significant Effect in the Bulk at Room Temperature.*, Nano Lett. (2015).
- [44] T. A. M.C. Payne, M.P. Teter and J. Joannopoulos, *techniques for*, Rev. Mod. Phys **64**, (1992).
- [45] A. Debernardi, *Anharmonic properties of semiconductors from Density-Functional Perturbation Theory*, Thesis disseration (1995).
- [46] P. Hohenberg and W. Kohn, *Inhomogeneous electron gas*, Phys. Rev. **136**, 864 (1964).
- [47] W. Kohn and L. J. Sham, *Self-consistent equations including exchange and correlation effects*, Phys. Rev. **140**, (1965).

- [48] S. Baroni, P. Giannozzi, and A. Testa, *Green's-function approach to linear response in solids*, Phys. Rev. Lett. **58**, 1861 (1987).
- [49] P. Giannozzi, S. Baroni, N. Bonini, M. Calandra, R. Car, C. Cavazzoni, D. Ceresoli, G. L. Chiarotti, M. Cococcioni, I. Dabo, A. Dal Corso, S. de Gironcoli, S. Fabris, G. Fratesi, R. Gebauer, U. Gerstmann, C. Gougoussis, A. Kokalj, M. Lazzeri, L. Martin-Samos, N. Marzari, F. Mauri, R. Mazzarello, S. Paolini, A. Pasquarello, L. Paulatto, C. Sbraccia, S. Scandolo, G. Sclauzero, A. P. Seitsonen, A. Smogunov, P. Umari, and R. M. Wentzcovitch, *QUANTUM ESPRESSO: a modular and open-source software project for quantum simulations of materials.*, J. Phys. Condens. Matter **21**, 395502 (2009).
- [50] K. Esfarjani and H. Stokes, *Method to extract anharmonic force constants from first principles calculations*, Phys. Rev. B **77**, 144112 (2008).
- [51] G. Leibfried and W. Ludwig, *Theory of Anharmonic Effects in Crystals*, Solid State Phys. **12**, 275 (1961).
- [52] M. H. F. Sluiter, M. Weinert, and Y. Kawazoe, *Force constants for substitutional alloys*, Phys. Rev. B **59**, 4100 (1999).
- [53] X. Gonze, *Adiabatic density-functional*, Phys. Rev. A **52**, 1096 (1995).
- [54] G. Deinzer, G. Birner, and D. Strauch, *Ab initio calculation of the linewidth of various phonon modes in germanium and silicon*, Phys. Rev. B **67**, 144304 (2003).
- [55] K. Esfarjani, G. Chen, and H. T. Stokes, *Heat transport in silicon from first-principles calculations*, Phys. Rev. B **84**, 085204 (2011).
- [56] P. E. Blöchl, O. Jepsen, and O. Andersen, *Improved tetrahedron method for Brillouin-zone integrations*, Phys. Rev. B **49**, 16223 (1994).
- [57] P. G. Klemens, *The Scattering of Low-Frequency Lattice Waves by Static Imperfections*, Proc. R. Soc. A **68**, 1113 (1955).
- [58] P. Klemens, *Thermal Resistance due to Point Defects at High Temperatures*, Phys. Rev. **119**, 507 (1960).
- [59] S. I. Tamura, *Isotope scattering of dispersive phonons in Ge*, Phys. Rev. B **27**, 858 (1983).
- [60] W. Capinski, H. Maris, and S. Tamura, *Analysis of the effect of isotope scattering on the thermal conductivity of crystalline silicon*, Phys. Rev. B **59**, 10105 (1999).

- 
- [61] H. Casimir, *Note on the conduction of heat in crystals*, *Physica* **5**, 495 (1938).
- [62] A. V. Inyushkin, A. N. Taldenkov, A. M. Gibin, A. V. Gusev, and H.-J. Pohl, *On the isotope effect in thermal conductivity of silicon*, *Phys. Status Solidi (C)* **1**, 2995 (2004).
- [63] Z. M. Zhang, *Nano/microscale heat transfer* (McGraw-Hill Nanoscience and Technology, New York, 2007).
- [64] B. Liao, B. Qiu, J. Zhou, S. Huberman, K. Esfarjani, and G. Chen, *Significant reduction of lattice thermal conductivity by the electron-phonon interaction in silicon with high carrier concentrations: A first-principles study*, *Phys. Rev. Lett.* **114**, 1 (2015).
- [65] X. Cartoixà, R. Dettori, C. Melis, L. Colombo, and R. Rurali, *Thermal transport in porous Si nanowires from approach-to-equilibrium molecular dynamics calculations*, *Appl. Phys. Lett.* **109**, 013107 (2016).
- [66] J. E. Turney, A. J. H. McGaughey, and C. H. Amon, *In-plane phonon transport in thin films*, *J. Appl. Phys.* **107**, 024317 (2010).
- [67] M. Luisier, *Thermal transport and Matthiessen's rule in ultra-scaled Si nanowires*, *Appl. Phys. Lett.* **103**, 113103 (2013).
- [68] A. Ward, D. A. Broido, D. A. Stewart, and G. Deinzer, *Ab initio theory of the lattice thermal conductivity in diamond*, *Phys. Rev. B* **80**, 1 (2009).
- [69] G. Fugallo, M. Lazzeri, L. Paulatto, and F. Mauri, *Ab initio variational approach for evaluating lattice thermal conductivity*, *Phys. Rev. B* **88**, 045430 (2013).
- [70] L. Bellaïche and D. Vanderbilt, *Virtual crystal approximation revisited: Application to dielectric and piezoelectric properties of perovskites*, *Phys. Rev. B* **61**, 7877 (2000).
- [71] J. Garg, N. Bonini, B. Kozinsky, and N. Marzari, *Role of disorder and anharmonicity in the thermal conductivity of silicon-germanium alloys: A first-principles study*, *Phys. Rev. Lett.* **106**, 1 (2011).
- [72] A. Zunger, S. Wei, L. G. Ferreira, and J. E. Bernard, *Special quasirandom structures*, *Phys. Rev. Lett.* **65**, 353 (1990).
- [73] J. Sanchez, F. Ducastelle, and D. Gratias, *Generalized cluster description of multicomponent systems*, *Physica A* **128**, 334 (1984).

- [74] G. Kresse and J. Furthmüller, *Efficiency of ab-initio total energy calculations for metals and semiconductors using a plane-wave basis set*, Comput. Mater. Sci **6**, 15 (1996).
- [75] G. Kresse and J. Furthmüller, *Efficient iterative schemes for ab initio total-energy calculations using a plane-wave basis set*, Phys. Rev. B **54**, 11169 (1996).
- [76] G. Kresse and J. Hafner, *Ab initio molecular dynamics for liquid metals*, Phys. Rev. B **47**, 558 (1993).
- [77] G. Kresse and J. Hafner, *Ab initio molecular-dynamics simulation of the liquid-metal-amorphous-semiconductor transition in germanium*, Phys. Rev. B **49**, 14251 (1994).
- [78] T. Tadano, Y. Gohda, and S. Tsuneyuki, *Anharmonic force constants extracted from first-principles molecular dynamics : applications to heat transfer simulations*, J. Phys.: Condens. Matter **26**, 225402 (2014).
- [79] A. Togo, L. Chaput, and I. Tanaka, *Distributions of phonon lifetimes in Brillouin zones*, Phys. Rev. B **91**, (2015).
- [80] P. Torres, *Kinetic Collective Model: BTE-based hydrodynamic model for thermal transport*, 2017 (accessed August 20, 2017). Url: <https://physta.github.io/>.
- [81] A. Kokalj, *Computer graphics and graphical user interfaces as tools in simulations of matter at the atomic scale*, Comput. Mater. Sci **28**, 155 (2003).
- [82] J. P. Perdew and A. Zunger, *Self-interaction correction to density-functional approximations for many-electron systems*, Phys. Rev. B **23**, 5048 (1981).
- [83] R. R. A. Dal Corso, S. Baroni and S. de Gironcoli, *Ab initio calculation of phonon dispersions in II-VI semiconductors*, Phys. Rev. B: Condens. Matter. **47**, 3588 (1993).
- [84] J. Warren, J. Yarnell, G. Dolling, and R. Cowley, *Lattice dynamics of diamond*, Phys. Rev. **158**, (1967).
- [85] D. Strauch and B. Dorner, *Phonon dispersion in GaAs* Phonon dispersion in GaAs, J. Phys.: Condens. Matter **2**, 1457 (1990).



- [86] X. Chen, D. Parker, and D. J. Singh, *Acoustic impedance and interface phonon scattering in Bi<sub>2</sub>Te<sub>3</sub> and other semiconducting materials*, Phys. Rev. B **87**, 1 (2013).
- [87] V. I. Ozhogin, a. V. Inyushkin, a. N. Taldenkov, a. V. Tikhomirov, G. É. Popov, E. Haller, and K. Itoh, *Isotope effect in the thermal conductivity of germanium single crystals*, J. Exp. Theor. Phys. Lett. **63**, 490 (1996).
- [88] D. G. Onn, A. Witek, Y. Z. Qiu, T. R. Anthony, and W. F. Banholzer, *Some aspects of the thermal conductivity of isotopically enriched diamond single crystals*, Phys. Rev. Lett. **68**, 2806 (1992).
- [89] A. V. Inyushkin, A. N. Taldenkov, A. Y. Yakubovsky, A. V. Markov, L. Moreno-Garsia, and B. N. Sharonov, *Thermal conductivity of isotopically enriched 71GaAs crystal*, Semicond. Sci. Tech. **18**, 685 (2003).
- [90] D. A. Broido, M. Malorny, G. Birner, N. Mingo, and D. A. Stewart, *Intrinsic lattice thermal conductivity of semiconductors from first principles*, Appl. Phys. Lett. **91**, (2007).
- [91] L. Zeng, K. C. Collins, Y. Hu, M. N. Luckyanova, A. A. Maznev, S. Huberman, V. Chiloyan, J. Zhou, X. Huang, K. A. Nelson, and G. Chen, *Measuring Phonon Mean Free Path Distributions by Probing Quasiballistic Phonon Transport in Grating Nanostructures*, Sci. Rep. **5**, 17131 (2015).
- [92] O. Hellman and D. A. Broido, *Phonon thermal transport in Bi<sub>2</sub>Te<sub>3</sub> from first principles*, Phys. Rev. B **90**, 134309 (2014).
- [93] C. Jeong, S. Datta, and M. Lundstrom, *Full dispersion versus Debye model evaluation of lattice thermal conductivity with a Landauer approach*, J. Appl. Phys **109**, (2011).
- [94] I.-i. Kanamori, X. Fujii, and I.-i. Mizutani, *Thermal diffusivity measurement of rock-forming minerals from 300° to 1100°K*, J. Geophys. Res **73**, 595 (1968).
- [95] Z. Dughaish, *Lead telluride as a thermoelectric material for thermoelectric power generation* Lead telluride as a thermoelectric material for thermoelectric power generation, Physica B: Condens. Matter. **322**, 205 (2002).
- [96] B. Abeles, D. Beers, G. Cody, and J. Dismukes, *Thermal Conductivity of Ge-Si Alloys at High Temperatures*, Phys. Rev. **125**, 44 (1962).

- [97] J. P. Dismukes, L. Ekstrom, E. F. Steigmeier, I. Kudman, and D. S. Beers, *Thermal and electrical properties of heavily doped Ge-Si alloys up to 1300Å°K*, J. Appl. Phys **35**, 2899 (1964).
- [98] M. C. Steele and F. D. Rosi, *Thermal conductivity and thermoelectric power of germanium-silicon alloys*, J. Appl. Phys **29**, 1517 (1958).
- [99] P. D. Maycock, *Thermal Conductivity of Silicon, Germanium, Iii-V Compounds and Iii-V Alloys*, Solid-State Electronics Pergamon Press **10**, 161 (1966).
- [100] W. Kim, J. Zide, A. Gossard, D. Klenov, S. Stemmer, A. Shakouri, and A. Majumdar, *Thermal conductivity reduction and thermoelectric figure of merit increase by embedding nanoparticles in crystalline semiconductors*, Phys. Rev. Lett. **96**, 1 (2006).
- [101] S. Chen, Q. Wu, C. Mishra, J. Kang, H. Zhang, K. Cho, W. Cai, A. A. Balandin, and R. S. Ruoff, *Thermal conductivity of isotopically modified graphene*, Nat. Mater. **11**, 1 (2012).
- [102] Y. Serap, *Electronic thermal conductivity measurements in graphene*, Thesis disseration (2015).
- [103] T. Y. Kim, C.-h. Park, and N. Marzari, *The electronic thermal conductivity of graphene* *The electronic thermal conductivity of graphene*, Nano Lett. **16**, 2439 (2016).
- [104] B. Liao, J. Zhou, B. Qiu, M. S. Dresselhaus, and G. Chen, *Ab initio study of electron-phonon interaction in phosphorene*, Phys. Rev. B **91**, 1 (2015).
- [105] P. Martin, Z. Aksamija, E. Pop, and U. Ravaioli, *Impact of phonon-surface roughness scattering on thermal conductivity of thin Si nanowires*, Phys. Rev. Lett. **102**, 1 (2009).
- [106] M. Asheghi, M. N. Touzelbaev, K. E. Goodson, Y. K. Leung, and S. S. Wong, *Temperature-Dependent Thermal Conductivity of Single-Crystal Silicon Layers in SOI Substrates*, Journal of Heat Transfer **120**, 30 (1998).
- [107] D. Li, Y. Wu, P. Kim, L. Shi, P. Yang, and A. Majumdar, *Thermal conductivity of individual silicon nanowires*, Appl. Phys. Lett. **83**, 2934 (2003).
- [108] A. Jain, Y. J. Yu, and A. J. H. McGaughey, *Phonon transport in periodic silicon nanoporous films with feature sizes greater than 100 nm*, Phys. Rev. B **87**, 1 (2013).

- [109] Z. Tian, K. Esfarjani, J. Shiomi, A. S. Henry, and G. Chen, *On the importance of optical phonons to thermal conductivity in nanostructures*, Appl. Phys. Lett. **99**, (2011).
- [110] M. Muñoz Rojo, B. Abad, C. V. Manzano, P. Torres, X. Cartoixà, F. X. Alvarez, and M. S. Martín-González, *Thermal conductivity of  $\text{Bi}_2\text{Te}_3$  nanowires: How size affects phonon scattering*, Nanoscale **9**, 6741 (2017).
- [111] M. Muñoz Rojo, Y. Zhang, C. V. Manzano, R. Alvaro, J. Gooth, M. Salmeron, and M. Martín-González, *Spatial potential ripples of azimuthal surface modes in topological insulator  $\text{Bi}_2\text{Te}_3$  nanowires*, Sci. Rep. **6**, 19014 (2016).
- [112] E. K. Lee, L. Yin, Y. Lee, J. W. Lee, S. J. Lee, J. Lee, S. N. Cha, D. Whang, G. S. Hwang, K. Hippalgaonkar, A. Majumdar, C. Yu, B. L. Choi, J. M. Kim, and K. Kim, *Large thermoelectric figure-of-merits from SiGe nanowires by simultaneously measuring electrical and thermal transport properties*, Nano Lett. **12**, 2918 (2012).
- [113] A. Sellitto, F. X. Alvarez, and D. Jou, *Temperature dependence of boundary conditions in phonon hydrodynamics of smooth and rough nanowires*, J. Appl. Phys **107**, (2010).
- [114] M. Calvo, M. Hennessy, P. Torres, T. Myers, and F. X. Alvarez, *A slip based model for the size-dependent thermal conductivity in nanowires*, Submitted (2017).
- [115] A. Cepellotti and N. Marzari, *Boltzmann Transport in Nanostructures as a Friction Effect*, NanoLetters (2017).
- [116] L. Zeng, V. Chiloyan, S. Huberman, A. A. Maznev, J.-P. M. Peraud, N. G. Hadjiconstantinou, K. A. Nelson, and G. Chen, *Monte Carlo study of non-diffusive relaxation of a transient thermal grating in thin membranes*, Appl. Phys. Lett. **108**, 063107 (2016).
- [117] A. I. Hochbaum, R. Chen, and R. D. Delgado, *Enhanced thermoelectric performance of rough silicon nanowires*, Nature **451**, 163 (2008).
- [118] A. Jain and A. J. H. McGaughey, *Effect of exchange-correlation on first-principles-driven lattice thermal conductivity predictions of crystalline silicon*, Comput. Mater. Sci **110**, 115 (2015).

- 
- [119] P. Jiang, L. Lindsay, and Y. K. Koh, *Role of low-energy phonons with mean-free-paths  $>0.8 \mu\text{m}$  in heat conduction in silicon*, J. Appl. Phys **119**, 0 (2016).
- [120] Y. J. Han and P. G. Klemens, *Anharmonic thermal resistivity of dielectric crystals at low temperatures*, Phys. Rev. B **48**, 6033 (1993).
- [121] R. Cheaito, J. C. Duda, T. E. Beechem, K. Hattar, J. F. Ihlefeld, D. L. Medlin, M. a. Rodriguez, M. J. Champion, E. S. Piekos, and P. E. Hopkins, *Experimental Investigation of Size Effects on the Thermal Conductivity of Silicon-Germanium Alloy Thin Films*, Phys. Rev. Lett. **109**, 195901 (2012).
- [122] C. Herring, *Role of low-energy phonons in thermal conduction*, Phys. Rev. **95**, 954 (1954).
- [123] J. C. Maxwell, *On the dynamical theory of gases*, The London, Edinburgh, and Dublin Philos. Mag. and J. Sci. **35**, 49 (1868).
- [124] Y.-J. Han, *Intrinsic thermal-resistive process of crystals: Umklapp processes at low and high temperatures*, Phys. Rev. B **54**, 8977 (1996).
- [125] A. Ziabari, P. Torres, B. Vermeersch, X. Cartoixa, A. Torello, Y. Xuan, J.-H. Bahk, Y. Koh, Y. P., F. Alvarez, and A. Shakouri, *Full-field thermal imaging of quasiballistic heat flow enhancement in nanoscale devices*, Submitted to Nature Comm. (2017).
- [126] L. Levitov and G. Falkovich, *Electron viscosity, current vortices and negative nonlocal resistance in graphene*, Nat. Phys. **12**, 672 (2016).